开篇语 / START：

“博学之，审问之，慎思之，明辨之，笃行之。”

“Learn extensively, inquire carefully, think deeply, differentiate clearly, and practice faithfully.”

《礼记·中庸》—《博学之》

Glimpse of Chinese Culture

Intracellular delivery of biopharmaceuticals and contrast agents by VNB photoporation and sizing nanomaterials in bio-fluids by FRAP

Ranhua Xiong

Master of Engineering

Thesis submitted to obtain the degree of
Doctor in Pharmaceutical Sciences

Proefschrift voorgedragen tot het bekomen van de graad van
Doctor in de Farmaceutische Wetenschappen

2017

Faculteit Farmaceutische Wetenschappen

Promotors

Prof. dr. Kevin Braeckmans

Prof.dr.apr. Stefaan De Smedt

Prof. dr. Andre G. Skirtach

Dean

Prof.dr.apr. Jan Van Bocxlaer

Members of the Exam Committee:

Prof. **Filip De Vos (chairman)**	**UGent**
Prof. **Jo Demeester (secretary)**	**UGent**
Prof. **Emmanuel Courtade**	**ULille 1**
Prof. **Johan Hofkens**	**KULeuven**
Prof. **Luc Leybaert**	**UGent**
Dr. **Saskia Lippens**	**VIB**

COPYRIGHT STATMENT

Ghent, 2017

The promotor:	**The author:**
Prof. dr. Kevin Braeckmans	M.S. Ranhua Xiong

The co-promotors:

Prof.dr.apr. Stefaan De Smedt

Prof. dr. Andre G. Skirtach

Table of contents

List of abbreviations

AOTF	acoustic optical tunable filter
AF488	Alexa Fluor 488
AD	Alexa@488-dextran
RD10	Alexa-red dextran 10 kD
BLI	bioluminescence imaging
BSA	bovine serum albumin
IBA	Bremsstrahlung absorption
CB	Carbon black
CdSe QD	CdSe/ZnS core/shell quantum dot
CFSE	Carboxyfluorescein succinimidyl ester
cFRAP	continuous Fluorescence Recovery After Photobleaching
CPP	cell-penetrating peptide
CSF	Cerebrospinal fluid
CW	continuous wavelength
CD	Cy5.5-dextran
DIV	days in vitro
DOL	degree of labeling
DLS	Dynamic light scattering
END	endocytic labeling
BBB	endothelial blood-brain
EGFP	enhanced green fluorescent protein
BCSFB	epithelial blood-CSF barrier
fs	femtosecond
FBS	fetal bovine serum
FD4	FITC-dextran 4 kDa
FD10	FITC-dextran 10 kDa
FD150	FITC-dextran 150 kDa
FD500	FITC-dextran 500 kD
FD	FITC-dextran
FI	fluorescence intensity
cFRAP	continuous Fluorescence Recovery After Photobleaching
FRAP	Fluorescence recovery after photobleaching
fSPT	fluorescence Single Particle Tracking
FLI	fluorescent imaging
FPs	fluorescent proteins
AuNPs	gold nanoparticles
GO	Graphene Oxide
IV	intravenous
InP QD	InP/ZnS core/shell quantum dots
PtK2	kidney epithelial

LSPR	Localized Surface Plasmon Resonance
LPS	lipopolysaccharide
MRI	magnetic resonance imaging
MEM	Maximum Entropy Method
MFI	mean fluorescence intensity
MKs	mononuclear senescent keratinocytes
ns	nanosecond
NHEKs	Normal Human Epidermal Keratinocytes
NPs	NanoParticles
PDI	polydispersity index
ps	picosecond
PKs	polynuclear senescent keratinocytes
PSNE	post-senescence neoplastic emergent
PI	Propidium Iodide
QDs	quantum dots
ROS	Reactive Oxygen Species
ROI	regions of interest
rFRAP	rectangle FRAP
SEM	Scanning electron microscope
SNR	signal to noise ratio
SEC	Size exclusion chromatographic
FBS	fetal bovine serum
siRNA	small interfering RNA
SNAP	Spatially-resolved NAnoparticle-enhanced Photoporation
SPIONs	superparamagnetic iron oxide nanoparticles
SPR	surface plasmon resonance
UV	Ultraviolet
VNBs	vapor nanobubbles

Introduction

CONTEXT

This thesis is divided to two parts (**Part I** and **Part II**). **Part I** is focused on intracellular delivery by photoporation and relevant applications like cell labeling and tracking. In **Part II**, a new FRAP (fluorescence recovery after photobleaching) model is developed for measuring the size distribution of nanomaterials in complex biological fluids and is applied to the characterization of protein aggregates and diagnosis of bio-barrier permeability. Both parts will be introduced separately below.

Part I INTRACELLULAR DELIVERY OF BIOPHARMACEUTICALS AND CONTRAST AGENTS BY VAPOR NANOBUBBLE (VNB) PHOTOPORATION

Cytosolic delivery of foreign nanomaterials into living cells is an important step for cell studies as well as for therapy and bio-imaging. Delivering such nanomaterials into cells requires overcoming the cell membrane, which is a major biological barrier to macromolecules and nanoparticles. Numerous methodologies have been developed to deliver these membrane-impermeable exogenous materials across the cell membrane, which can be broadly classified into biological, chemical and physical methods. In the biological approach, foreign nucleic acids are introduced into cells *via* a viral vector. Although virus-mediated transfection can provide highly efficient and sustainable transgene expression, the major disadvantages of this method are immunogenicity and toxicity. To overcome these shortcomings, chemical vectors, often lipid or polymer based, are being developed. These nanocarriers are generally internalized by cells through endocytosis, which means that they will be sequestered inside endosomes in cell's interior. In many cases, however, the delivered compound should rather reach the cell's cytosol. Yet, escape from the endosomal compartment remains one of the major bottlenecks for non-viral nanocarriers.

Physical approaches for the cytosolic delivery of nanomaterials have attracted considerable interest as well. They typically offer generic applicability to a variety of cell types and enable direct delivery of the exogenous materials across the cell membrane into the cytoplasm. They are primarily used for *in vitro* or *ex vivo* intracellular delivery as their *in vivo* application is typically more limited. Well-known examples of physical delivery methods are micro-injection, electroporation and sonoporation. Another physical delivery method that is receiving more and more attention in recent years is laser-assisted photoporation. Photoporation is based on the generation of transient pores in the cell membrane using laser light. In its traditional form, these pores are formed by focusing a high-energy laser beam on the cell membrane. More recently, however, laser irradiation is combined with sensitizing nanoparticles that amplify the laser effects. Nanoparticle sensitized laser photoporation has the benefit that a lower laser energy can be used and that cells can be photoporated in higher-throughput. Nanoparticle sensitized photoporation, which is the topic in **Part I** of this thesis, is an exciting young research field that is a striking example of the tremendous possibilities that multidisciplinary science has to offer. It combines biophotonics with nanotechnology to enable new and improved biological and biomedical applications, of which several examples will be given in this thesis.

Plasmonic metallic nanoparticles, such as gold nanoparticles (AuNP) are used the most as enhancers of the photoporation effect. Their surface plasmon resonance (SPR) can tremendously enhance laser absorption, leading to distinct phenomena such as heating of the surrounding tissue, acoustic shockwaves, and formation of water vapor nanobubbles (VNBs). As will be demonstrated in **Chapter 2**, the latter effect is of particular interest for photoporation. VNB can be efficiently generated with short laser pulses (< 10 ns) of sufficiently high intensity. Upon absorption of such a laser pulse, the temperature of a nanoparticle (NP) can rapidly increase to several hundred degrees, causing the water surrounding the NP to evaporate. This results in the creation of a VNB around the AuNP surface, with a size ranging from tens to hundreds of nm depending on the laser energy. When the thermal energy of the NP is consumed, the VNB violently collapses and causes local damage by high-pressure shockwaves. Due to the extremely short lifetime of VNBs (<1 μs), the diffusion of heat from the AuNP into the environment is negligible so that almost all energy of the irradiated AuNP is converted to mechanical energy (expansion of the VNB) without heating of the environment. This property makes VNBs an interesting phenomenon to mechanically cause local damage to biological structures such as the cell membrane, without causing aspecific thermal damage to healthy cells or tissue, which is a concern in classic hyperthermia therapies. VNB mediated photoporation is, therefore, an interesting delivery method that deserves further exploration for its use in a variety of applications.

In **Part I**, we first give a detailed review on the history of photoporation and its main principles. Then we investigate specifically VNB mediated photoporation in comparison with the more traditionally used thermal variant of photoporation. Having found that VNB photoporation is the more efficient mechanism for permeabilizing the cell membrane, we make use of it to deliver of imaging contract agents into cells for improved long-term *in vivo* cell tracking. Next we show that VNB photoporation can be used to deliver extrinsic labels into cells for microscopic visualization of subcellular structures of living cells. Finally, we develop a fully automated VNB photoporation platform, for fast and flexible spatially resolved photoporation of selected cells with several unique applications.

Part II SIZING NANOMATERIALS IN BIO-FLUIDS BY FLUORESCENCE RECOVERY AFTER PHOTOPOBLEACHING (FRAP)

FRAP is one of the first fluorescence microscopy based methods for the measurement of molecular mobility in biological tissues and biomaterials. Since its development in the 1970s, FRAP is widely used in the biophysical, pharmaceutical and material sciences to study diffusion of molecules and nanoparticles on the micrometer scale. In a FRAP experiment, the sample is placed on a microscope and the fluorescently labeled molecules or nanoparticles are photobleached in a micron sized area by a powerful excitation pulse. Bleached molecules will diffuse out of the bleach area and will be gradually replaced by intact fluorophores. The fluorescence inside the bleach area will recover at a rate that is proportional to the diffusional rate of the fluorescent species. Typically it is the average fluorescence in the bleach area that is analyzed as a function of time. Fitting of a proper mathematical diffusion model to the fluorescence recovery data yields the local diffusion coefficient of the fluorescently labeled species.

Previous work in our group has shown that the precision and accuracy of FRAP data analysis is improved when the full tempo-spatial information is considered, rather than just the time-progression of the average fluorescence intensity. In this thesis we hypothesize that this extended way of doing FRAP analysis enables the interpretation of FRAP data in terms of continuous distributions of diffusion coefficients, rather than just one apparent average diffusion coefficient. If correct it would extend the capabilities of FRAP to the analysis of polydisperse systems, which is much closer to reality and, therefore, would open up new application possibilities.

In particular our interest goes to the sizing of nanomaterials in complex biological fluids, which is of importance in a wide range of applications in the life sciences. For instance, even though nanomedicine formulations may be stable under normal storage conditions, they may very well aggregate after administration into a biological fluid such as blood. Similarly, there is a growing appreciation that the colloidal stability of therapeutic proteins needs to be tested in blood as protein aggregation after intravenous administration may alter their functionality and induce immunogenic responses. Being able to size nanomaterials in biofluids is of interest to medical diagnosis as well, for instance to determine intestinal or vascular barrier permeability which is related to several pathologies, such as sepsis, liver disease, inflammatory bowel disease and neurodegenerative diseases. Barrier permeability can be assessed by administering inert size probes, e.g. orally or intravenously, followed by quantification of the size and amount of probes that have leaked through the barrier. Despite its relevance, measuring the size of molecules and nanomaterials in complex biological fluids remains a major challenge and still very much needed. In the second part of the thesis we develop a dedicated FRAP method capable of analyzing the distribution of diffusion coefficients of polydisperse systems. These distributions can be converted to size distributions as well since size and diffusion rate are directly linked to one another. After thorough validation we show that our new FRAP method can measure the size distribution of proteins and protein aggregates in undiluted human serum. In addition, we apply the new method to assess intestinal and vascular barrier permeability *in vivo* by measuring the size distribution of probes that permeated through the respective barriers.

AIM

Part I INTRACELLULAR DELIVERY OF BIOPHARMACEUTICALS AND CONTRAST AGENTS BY VAPOR NANOBUBBLE (VNB) PHOTOPORATION

The general aim of first part is to build up a nanoparticle enhanced photoporation setup and optimize the cytosolic delivery efficiency and toxicity for various cell types. It is applied to the delivery of therapeutic biomolecules as well as contrast agents for long-term *in vivo* cell tracking or subcellular microscopic imaging. In addition, technology will be developed to enable high-throughput cell-selective photoporation which opens up several new applications.

As discussed in the review in **Chapter 1**, there are two major mechanisms by which cell membranes can be permeabilized through photoporation. One is by local heating, the other is by mechanical pore formation by vapor nanobubbles. In **Chapter 2** we compare both cell permabilization mechanisms to determine which offers the best efficiency. In addition we intend to show for the first time that photoporation can be used to deliver siRNA into cells for the downregulation of proteins.

In **Chapter 3** we hypothesize that photoporation can be used for the cytosolic delivery of fluorescent contrast agents for *in vivo* cell tracking. Long-term *in vivo* imaging of cells is crucial for the understanding of cellular fate in biological processes in cancer research, immunology or in cell-based therapies. Cell labeling with the desired contrast agent occurs *ex vivo* via endocytosis, which is a variable and slow process. Following endocytic uptake, the contrast agents mostly remain entrapped in the endolysosomal compartment, which leads to signal degradation, cytotoxicity and asymmetric inheritance of the labels upon cell division. Therefore, it is of current interest to develop methods that can circumvent endocytic uptake of labels and instead deliver them directly into the cytoplasm. Here we aim to demonstrate that photoporation is well-suited to deliver fluorescent labels into the cytosol of cells and mitigates the many problems associated with label endocytosis. We will show that the combined advantages will enable substantially improved long-term *in vivo* cell tracking.

Apart from *in vivo* cell tracking, there is great interest in the intracellular delivery of fluorescent labels for high-resolution microscopy of living cells. Quantum Dots (QDs) represent one interesting class of microscopy labels due to some of their unique properties like improved photostability, increased brightness and narrow emission spectra. While they have been used for subcellular labeling of fixed cells, their application to living cells is very limited so far mainly due to inefficient cytosolic delivery of QDs. **Chapter 4** is aimed to demonstrate that VNB photoporation offers the long awaited ability to deliver functionalized QDs efficiently into the cytosol of cells for labeling and microscopic visualization of subcellular structures.

Finally, we aim to exploit arguably the most unique feature of photoporation, which is the capability to deliver compounds into selected cells within a large population of cells. In **Chapter 5** we will develop soft- and hardware to do this and will demonstrate its usefulness in challenging applications which benefit from high-throughput cell-selective delivery. These include sparse labeling of random single neurons in primary hippocampal cultures for automated analysis of spine density, and the labeling and sorting of polynucleic or mononucleic primary keratinocytes that are potentially involved in neoplasm (and tumor) formation.

Part II SIZING NANOMATERIALS IN BIO-FLUIDS BY FLUORESCENCE RECOVERY AFTER PHOTOPOBLEACHING (FRAP)

The second part is aimed at developing a FRAP method capable of analyzing the size distribution of nanomaterials in complex biological fluids in **Chapter 6** and **Chapter 7**. Specifically we aim at developing a FRAP method that can make use of the full time and space information available from FRAP recovery images in **Chapter 6**. By doing so we hypothesize that better precision may be obtained as compared to the traditional FRAP methods that only make use of time information (i.e. the recovery of the average fluorescence intensity in the bleach area over time). We will base our 'continuous' FRAP model (cFRAP) on previous work from our group where a tempo-spatial FRAP method was developed to measure the diffusion of a single component. This single component FRAP model will be implemented in the Maximum Entropy Method (MEM) framework to enable interpretation of the recovery data in terms of a semi-continuous distribution of diffusion coefficients. If the viscosity of the solution is known, which can be measured independently, the distribution of diffusion coefficients can be converted to a distribution of sizes with the Stokes-Einstein equation. The cFRAP method will be thoroughly validated by simulations and biophysical experiments on model systems. Then it will be applied to challenging pharmaceutical and biomedical problems that would benefit from a method that can size nanomaterials in the 1-100 nm range in complex biological fluids **Chapter 7**. First we will demonstrate that cFRAP can be used for size measurements of proteins and protein aggregates in serum. Next, we will investigate to which extent cFRAP could be suitable for a detailed assessment of the permeability of the intestinal or vascular barrier in mice. We propose the oral intake or IV injection of a mixture of FITC-dextrans covering a wide range of sizes. cFRAP can then be used to analyze the size distribution of FITC-dextrans that have entered into the blood circulation after permeation through the intestinal barrier or measure size distribution of FITC-dextrans that permeated into CSF, brain or other organs.

OUTLINE

The PhD thesis is divided to two independent parts as was introduced above. The first and largest part (**Part I**) deals with various unique applications of the cytosolic delivery of nanomaterials enabled by VNB photoporation. This part includes five chapters from **Chapter 1** to **Chapter 5**. The fundamentals, technological advances and applications of laser-assisted photoporation are reviewed in **Chapter 1**. Specifically, it provides a detailed account on the history and current state-of-the-art of photoporation as a physical nanomaterial delivery technique in its various embodiments. This chapter should allow the reader to get a detailed understanding of the most important aspects of photoporation, which will be of benefit to appreciate the subsequent research chapters. In **Chapter 2**, the hypothesis is investigated that VNB photoporation offers more efficient delivery of nanomaterials into cells as compared to the more traditional photothermal photoporation. Both photoporation methods are systematically evaluated in terms of cytotoxicity, cell loading, and siRNA transfection efficiency. Having found that VNB photoporation does offer the expected benefits, it is further applied in **Chapter 3** to deliver fluorescent contrast agents into cells to enable long-term cell tracking *in vitro* and *in vivo*. Specifically it is investigated if the cytosolic delivery of contrast agents by VNB photoporation offers a number of benefits over traditional cell labeling where uptake of the desired contrast agent occurs *via* spontaneous endocytosis. In **Chapter 4**, we demonstrate that VNB photoporation is equally suited to deliver fluorescent contrast agents into cells for subcellular labeling as is needed for microscopic visualization of cells. We show that antibody-functionalized QDs could be successfully delivered into the cytoplasm and successfully targeted the microtubules. Finally, in **Chapter 5**, we explore spatially resolved nanoparticle-enhanced photoporation (SNAP) as the unique possibility of photoporation to deliver nanomaterials into selected cells, rather than a whole population of cells. Soft- and hardware is developed to target the photoporation laser beam to specific cells of interest in a cell culture. Cell-selective photoporation is finally applied to two challenging applications: labeling of single neuron cells and sorting of polynucleic and mononucleic normal human epithelial keratinocytes.

Sizing nanomaterials in complex biological fluids by FRAP is the topic of **Part II** that includes **Chapters 6** and **7**. In **Chapter 6**, we develop a tempo-spatial FRAP methodology to measure continuous distributions of diffusion coefficients. First we present the mathematical derivation of the cFRAP model and examine how certain experimental parameters influence the accuracy and precision of cFRAP experiments. The ability of cFRAP to analyze the diffusion of polydisperse systems is validated by performing FRAP experiments on solutions of FITC-dextran of different molecular weight and mixtures. Thanks to including spatial information in the cFRAP model, we found that the PDI (polydispersity index) of the distributions was significantly less as compared to the apparent PDI measured by DLS or traditional FRAP methods which only take time information into account. Having thoroughly validated the performance of cFRAP, we demonstrate its strength and versatility in a number of challenging sizing applications in **Chapter 7**. As a first proof-of-concept application we demonstrate that the extent of aggregation of therapeutic proteins can be accurately measured in undiluted serum by cFRAP. Next, we show that cFRAP allows detailed investigation of the permeability of the intestinal and vascular barriers *in vivo* following the administration of fluorescent probes spanning 2 orders of magnitude in size. As a single measurement in a microliter sample is sufficient to determine the full size distribution of probes that have leaked through the barrier, the number of animals needed to assess the barrier permeability can be substantially reduced. At the same time unprecedented detailed information is obtained on the size distribution of probes that can permeate through the barrier.

The thesis finally finishes with a dedicated section on the broader context and future perspectives on photoporation and cFRAP.

PART I

INTRACELLULAR DELIVERY OF BIOPHARMACEUTICALS AND CONTRAST AGENTS BY VNB PHOTOPORATION

Chapter 1

Laser-assisted photoporation: fundamentals, technological advances and applications

This chapter is published as:

Laser-assisted photoporation: fundamentals, technological advances and applications

Ranhua Xiong[1,2], Sangram Keshari Samal[1,2], Jo Demeester[1], Andre G. Skirtach[2,3,4], Stefaan C. De Smedt[1] and Kevin Braeckmans[1,2,5,6], Advances in Physics: X, 2016, DOI:10.1080/23746149.2016.1228476

[1]Laboratory of General Biochemistry and Physical Pharmacy, Faculty of Pharmaceutical Sciences, Ghent University, Ghent, Belgium;
[2]Centre for Nano- and Biophotonics, Faculty of Pharmaceutical Sciences, Ghent University, Ghent, Belgium;
[3]Department of Molecular Biotechnology, Ghent University, Ghent, Belgium;
[4]Department of Interfaces, Max-Planck Institute of Colloids and Interfaces, Potsdam, Germany;
[5]Department of Materials and Nanostructures, IEMN, UMR 8520, University Lille 1, University Lille Nord France, Villeneuve D'Ascq, France;
[6]UMR 8523, Lab Phys Lasers Atomes & Mol, University Lille 1, University Lille Nord France, Villeneuve D'Ascq, France

ABSTRACT

Laser-assisted photoporation is a promising technique that is receiving increasing attention for the delivery of membrane impermeable nanoscopic substances into living cells. Photoporation is based on the generation of localized transient pores in the cell membrane using continuous or pulsed laser light. Increased membrane permeability can be achieved directly by focused laser light or in combination with sensitizing nanoparticles for higher throughput. Here, we provide a detailed account on the history and current state-of-the-art of photoporation as a physical nanomaterial delivery technique. We first introduce with a detailed explanation of the mechanisms responsible for cell membrane pore formation, following an overview of experimental procedures for realizing direct laser photoporation. Next, we review the second and most recent method of photoporation that combines laser light with sensitizing NPs. The different mechanisms of pore formation are discussed and an overview is given of the various types of sensitizing nanomaterials. Typical experimental setups to achieve nanoparticlemediated photoporation are discussed as well. Finally, we discuss the biological and therapeutic applications enabled by photoporation and give our current view on this expanding research field and the challenges and opportunities that remain for the near future.

1. INTRODUCTION

The incorporation of foreign materials into living cells is an important step not only for cell studies, but also for therapy and bio-imaging. DNA is for instance introduced into live cells for studying gene expression[1-5], mutation analysis[6], and gene therapy[7]. Similarly, mRNA incorporation into living cells helps to assess cell biological functions[8], while small interfering RNA (siRNA) is introduced for sequence-specific gene silencing[9-13]. Proteins also can be delivered into living cells for bio-imaging and therapies[14-16]. In recent years, the use of inorganic particles as intracellular labels is being investigated, such as superparamagnetic iron oxide nanoparticles (SPIONs) and Gadolinium complexes for magnetic resonance imaging (MRI)[17-19], quantum dots (QDs)[20-22] and upconversion nanoparticles[23] for fluorescence imaging and gold nanoparticles (AuNPs) for photoacoustic imaging[24, 25]. In addition, QDs and AuNPs are also delivered into cells for *in vitro* microscopic imaging of subcellular structures and intracellular biosensing, respectively[26-28].

Delivering such nanomaterials into cells requires overcoming the cell membrane, which is a major biological barrier to charged, noncharged, and polar molecules as well as nanoparticles. Numerous methodologies have been developed to allow these membrane-impermeable exogenous materials to cross the cell membrane, which can be broadly classified into biological, chemical and physical methods[29]. In the biological approach, foreign DNA is introduced into cells *via* a viral vector. Although virus-mediated transfection can provide highly efficient and sustainable transgene expression, the major disadvantages of this method are immunogenicity and toxicity[30, 31]. To overcome these shortcomings of viral vectors, chemical vectors, often lipid or polymer based, are being explored as well[32-35]. These nanocarriers are generally internalized by cells through endocytosis, although the required subsequent escape from the endosomal compartments remains one of the major bottlenecks[36-38].

Physical approaches to permeate the cell membrane have attracted considerable interest as well. They typically offer generic applicability to a variety of cell types and enable direct delivery of the exogenous materials across the cell membrane into the cytoplasm[39-41]. Microinjection is a first example where the compounds of interest are injected into single cells[42-44]. Although it has demonstrated its usefulness for cell biological applications, it is technically challenging and only applicable to a limited number cells. Electroporation is an alternative physical technique that can deliver molecules into a large batch of cells, but the high electric field often results in low cell viability[45-50]. The gene gun is another approach that uses micro- or nano- particles conjugated with e.g. nucleic acids which are shot into cells as a kind of bullets using pressurized gas[51, 52]. More recently, sonoporation has been introduced as a method to permeabilize the plasma cell membrane by making use of ultrasound-responsive microbubbles. The acoustic response of the microbubbles can lead to the formation of micro-jets and shockwaves resulting in cell membrane poration[53-55]. However, the technique is rather developed for *in vivo* applications and less suited for *in vitro* work. It has also been reported that shear forces or elevated temperatures can lead to substantial cell damage and toxicity[39, 56]. The use of a microfluidics device is also reported for the intracellular delivery of therapeutic molecules and labels with high throughput[57-60]. The cells are forced to flow through a narrow constriction in the channel so that pores are created in the cell membrane by friction forces. While it is tremendously fast at one million cells per second, it is limited to cells in suspension and the efficiency remains relatively low.

Photoporation has been developed as a promising alternative technique offering distinct advantages over other physical delivery methods. In its standard form, pores are created in the cell membrane by high-intensity femtosecond laser pulses that are focused precisely with respect to the cell membrane (**Fig. 1**)[61-66]. In the context of this review, the term 'pore' will be used to denote both water-filled holes in the membrane as well as local zones with increased membrane permeability for instance by localized reorganization of lipids. Just like in electroporation and sonoporation, exogenous nanomaterials that are present in the surrounding cell medium can then diffuse into the cell's cytoplasm. Although it has proven to be useful for single cell studies, it requires the use of expensive femtosecond lasers and remains relatively slow since the laser beam needs to be focused exactly in 3-D on the cell membrane and pores are created one at a time. Even by parallelization of laser beams, a limited throughput of only a few cells per second could be achieved[67]. However, by using plasmonic nanoparticles like AuNPs, it has been demonstrated in the last couple of years that photoporation throughput can be immensely enhanced (**Fig. 1**)[68-70]. Most studies so far have used low intensity laser pulses or CW (continuous wavelength) laser light to excite AuNPs[71-74], causing thermal membrane permeabilization by a local phase transition of the lipid bilayer or by denaturation of integral glycoproteins[74]. Instead, the use of more intense laser pulses have shown to cause mechanical membrane poration by the generation of vapor nanobubbles (VNBs)[69, 75]. In a comparative study of thermal vs. VNB mediated membrane poration it has been found that VNB mediated membrane poration actually allows more efficient uptake of exogenous nanomaterials with reduced cytotoxicity as compared to thermal poration at low laser intensity[76]. Although AuNPs are the most widely used for membrane poration, other nanomaterials like titanium nanostructures and carbon based nanomaterials are also currently being evaluated as alternative sensitizing nanoparticles[77-80].

In this review, we provide a detailed account on the history and current state-of-the-art of photoporation as a physical delivery technique. First the historic form of photoporation is introduced with a detailed explanation of the mechanisms responsible for cell membrane pore formation. An overview is given of the most common experimental configurations for realizing direct laser photoporation. Next, we review the second and most recent method of photoporation that combines laser light with sensitizing NPs (NanoParticles). The different mechanisms of pore formation will be discussed and an overview is given of the various types of sensitizing nanomaterials. Typical experimental set-ups to achieve nanoparticle mediated photoporation will be discussed as well. Finally, the biological and therapeutic applications enabled by photoporation will be discussed including nucleic acid transfection, drug delivery and cellular imaging. Taken together it is clear that photoporation is acquiring immense interest and is expected to evolve substantially in the coming years, both in terms of technology and novel applications. Here we give our current view on this expanding research field and the challenges and opportunities that remain for the near future.

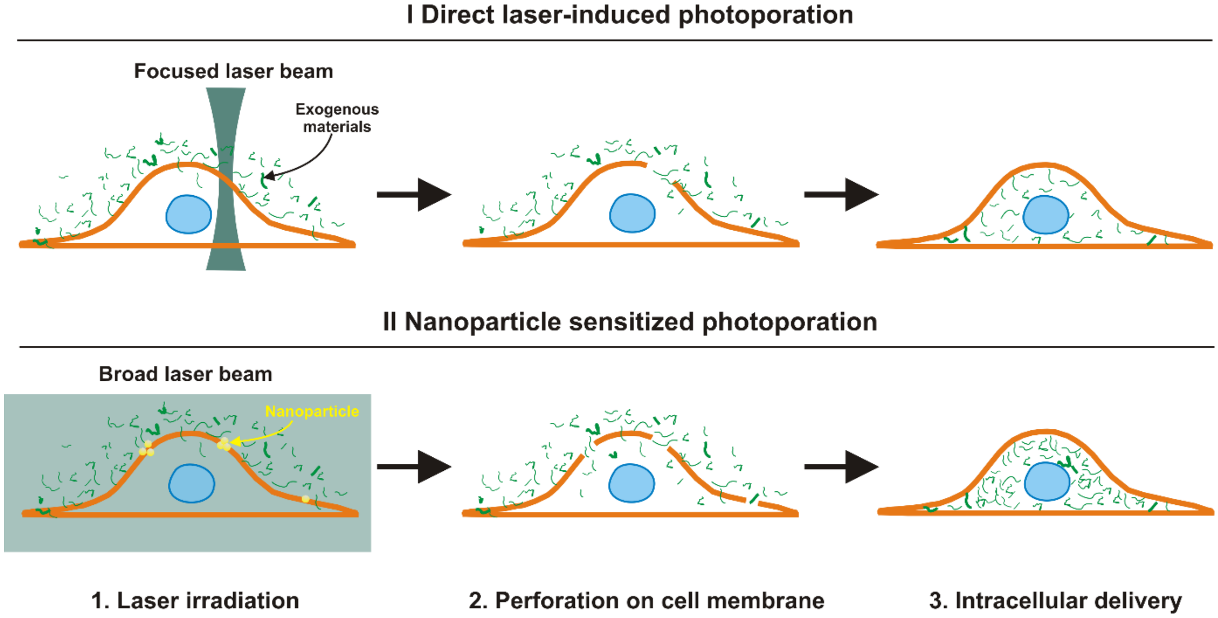

Figure 1. Direct laser-induced photoporation and NP-mediated photoporation. In direct photoporation (I), the laser beam is focused precisely on or slightly above the cell membrane to achieve a locally high photon density. For NP sensitized photoporation (II), the NPs are first incubated with the cells to allow them to adhere to the cell membrane. Notes: A (low intensity) broad laser beam can then be used to photoporate many cells at the same time. Following laser irradiation, exogenous compounds in the cell medium can diffuse through the membrane pore(s) into the cell’s cytoplasm.

2. DIRECT LASER-INDUCED PHOTOPORATION

2.1 Mechanisms

In direct laser induced photoporation, it is crucial to spatiotemporally confine the laser energy to the cell membrane to obtain sufficient laser energy density for the generation of membrane pores. To achieve this, a laser beam is focused to a very small spot size (typically ~1 - 10 µm) through a microscope’s objective lens[81]. Typically, a pulsed laser is used with a pulse duration from nanosecond (ns) down to femtosecond (fs) to achieve a sufficiently high photon density. As schematically shown in **Fig. 2a**, a variety of possible mechanisms may contribute to pore formation, including photothermal, photomechanical and photochemical processes[81-83]. The contribution of each of these processes depends on laser pulse duration, laser wavelength and intensity (which in turn is determined by the laser energy and beam size). In order to control pore formation, it is essential to understand these mechanisms of laser-induced photoporation.

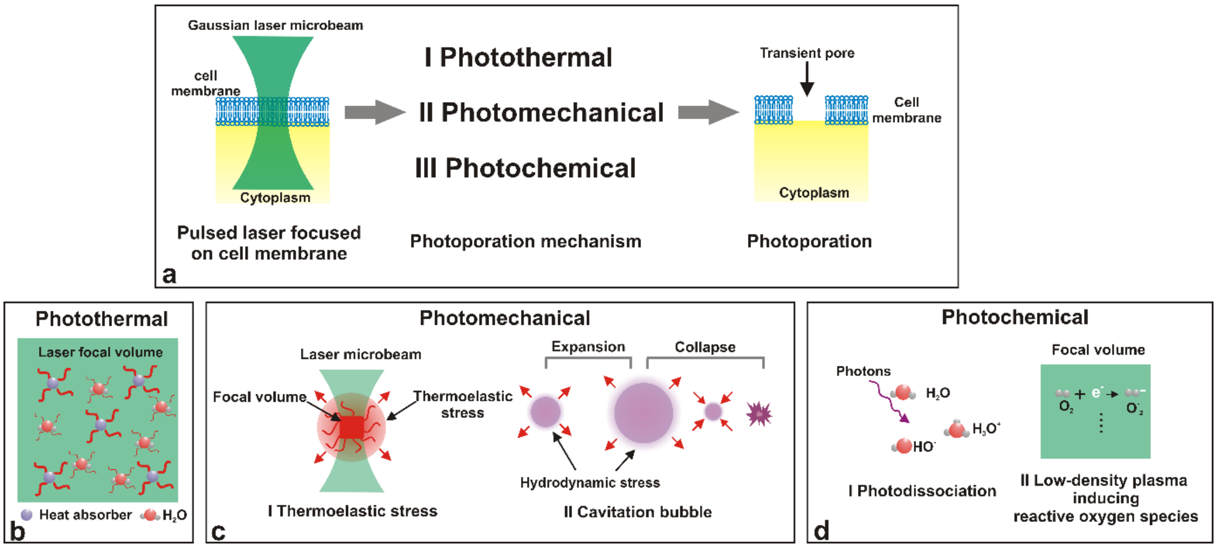

Figure 2. Main mechanisms contributing to direct laser-induced photoporation. (a) A pore (up to hundreds of nm) can be formed in the cell membrane by a focused laser beam through photothermal, photomechanical and photochemical effects. (b) The photothermal effect refers to a temperature increase following absorption of photons by molecules like water, but also proteins or DNA. (c) Under pulsed laser irradiation, thermoelastic stress or cavitation bubbles contribute to photomechanical poration of cell membranes. (d) With fs laser pulses or UV laser light, pores can be formed by photodissociation or the generation of ROS by actively free electrons.

2.1.1 Temporal laser energy confinement

Absorption of light can cause a transition between electronic or vibrational energy levels of the absorbing molecules so that heat is generated upon relaxation to the ground state (**Fig. 2b**). In order to realize a substantial temperature increase in the focal spot, short intense laser pulses are preferred with a duration shorter than the characteristic thermal diffusion time t_d in the focal volume[84]:

$$t_d = \frac{0.124\lambda^2}{\kappa \cdot NA^2} \quad (1)$$

where λ is the laser wavelength, κ is the thermal diffusivity (in water $\kappa = 0.143\, mm^2/s$) and *NA* is the numerical aperture of the objective lens. For example, for a laser operating at λ=1064 nm that is focused through a lens of *NA* = 0.8, the laser pulse duration should be less than 60 ns. Rapid localized heating may lead to a sudden thermal expansion of the medium, resulting in the generation of acoustic waves. In order to generate a substantial amount of this kind of thermoelastic stress, the time scale of laser energy deposition in the focal volume should not be longer than the characteristic time τ_s for acoustic wave propagation out of the focal volume, which is governed by the speed of sound in the medium[82]:

$$\tau_s = \frac{0.61\lambda}{c_w \cdot NA} \quad (2)$$

where c_w is the speed of sound in water (1484 m/s at 20°C). For a typical *NA* in the range of 0.8 and a laser wavelength 1064 nm, the laser duration should be less than 550 ps for stress confinement.

Finally, multi-photon absorption can occur when using focused short laser pulses in the femto- to picosecond range. This may cause ionization of the absorbing molecules and the generation of a low density plasma[85]. Each of these three basic phenomena (heat production, acoustic cavitation and plasma formation) can cause damage to cell membranes in a variety of ways, as will be explained in the following sections.

2.1.2 Photothermal pore formation

The photothermal effect refers to a temperature increase following single photon absorption by molecules like water, but also proteins or DNA (**Fig. 2b**). Absorption in the UV and visible range corresponds to electronic transitions of molecules, while infrared is associated with vibrational transitions. Non-radiative relaxation to the ground state results in heat production. Localized heating can increase the permeability of the cell membrane by a local phase transition of the lipid bilayer or by thermal denaturation of integral proteins[74, 86]. However, it was reported that photothermal heating by single photon absorption alone is not sufficient to effectively form pores in cell membranes[82, 83, 87]. This is mainly because water, lipids and proteins have a relatively low absorption in the 350-1100 nm wavelength range. For that reason dye molecules like phenol red are sometimes used to enhance light absorption and achieve a more efficient temperature increase[88-90].

2.1.3 Photomechanical pore formation

Pores can be created in cell membranes by mechanical stress, which can be induced by acoustic waves (cfr. §2.1.1) or by a phenomenon known as cavitation bubbles. Such bubbles are formed by localized vaporization of water, which can happen in two ways depending primarily on the laser pulse duration. First, cavitation bubbles can be formed with femtosecond (fs) laser pulses which cause plasma formation following a multi-photon absorption process. Free electrons in the plasma thermalize within tens of picoseconds. As this is much shorter than the characteristic time τ_s for acoustic wave propagation out of the focal volume (cfr. Eq. (2)), which is in the order of 0.5 ns, the thermoelastic stress caused by the temperature rise will be confined to the focal volume. Subsequent propagation of the pressure wave causes substantial tensile stress in the centre of the focal volume. If the tensile strength of the liquid (water) is exceeded, a cavitation bubble will be formed. A detailed description of the underlying physics can be found in the article by Vogel and colleagues[81]. The expanding bubble can lead to perforation of the cell membrane by hydrodynamic stress (**Fig. 2c**). Furthermore, when the bubble has expanded to its maximum size, the bubble collapses by the surrounding hydrostatic pressure, inducing liquid jets or shockwaves that can form pores in the cell membrane. Based on SEM imaging, Sankin *et al.* visualized these pores and found that their size ranged from ~200 nm to ~2 µm[91]. A second way by which cavitation bubbles can be formed is by using nanosecond (ns) and picosecond (ps) laser pulses. Also here local plasma formation is involved, although the mechanism is somewhat different as for fs pulses. When using ns or ps laser pulses, only a small number of free 'seed' electrons can be generated following multiphoton absorption. These seed electrons can further absorb photons through a non-resonant process - known as Inverse Bremsstrahlung absorption (IBA) - until their kinetic energy is sufficiently high to produce other free electrons via impact ionization[92]. When the free electrons achieve a critical density, the irradiated material undergoes optical breakdown resulting in bubble formation as explained above. As avalanche ionization takes time to generate a sufficient amount of free electrons via IBA, the laser pulse duration should be typically more than 15 ps. For a pulse duration of tens of ps or even ns, the plasma will be further heated up to several thousands of degrees[93-95]. These high plasma temperatures will cause local evaporation of the medium (mostly water) and expansion of the plasma, which cause the formation of larger and more violent cavitation bubbles as compared to fs laser pulses. Rau. *et al.* measured the bubble size as a function of time with laser fluences between 0.7× and 3× above the threshold (~250 J/cm^2) for plasma formation (t_p=6 ns, λ=532 nm) and measured bubble sizes from ~200 to ~400 µm, which are more than 10 times bigger than those formed by fs laser pulses[85]. The entire process is visualized from plasma formation (bright luminescence in **Fig. 3 a-b**), over thermoelastic stress propagation (**Fig. 3 b-c**) and to bubble expansion and collapse (**Fig. 3c-k**). The violent expansion and collapse of such bubbles could severely damage nearby cells, similar to fs induced cavitation bubbles (**Fig. 3l**).

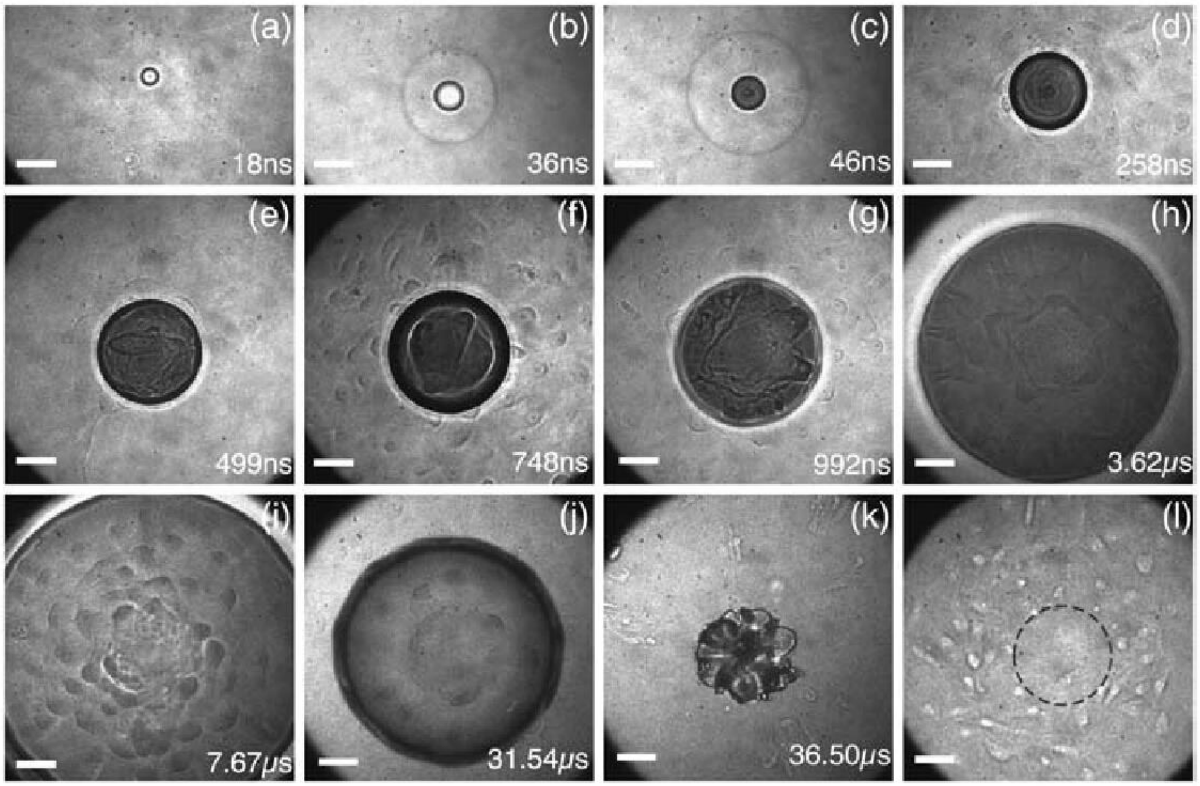

Figure 3. Time-resolved images show the process from plasma formation (a, b) over shock wave propagation (b, c) to cavitation bubble dynamics (c–k) Nearby cells are destroyed by the bubble shear forces (l). Notes: A 6 ns laser pulse (at 532 nm) is used with a fluence three times above the plasma generation threshold (~250 J/cm2). Scale bar is 50 μm and Potorous rat kidney epithelial (PtK2) cells were used (see Ref. 85).

2.1.4 Photochemical pore formation

Photochemical reactions may also contribute to photoporation of cell membranes. When fs laser pulses are used below the threshold for optical breakdown or bubble formation, reactive free electrons can be generated by multiphoton ionization of e.g. water molecules. The resulting highly reactive oxygen species can locally induce cell membrane damage (**Fig. 3d**)[96-98]. Alternatively, pulsed UV (typically ns or ps pulses) may damage the cell membrane by molecular fragmentation after absorption of highly energetic UV photons[83, 99]. Indeed, UV photons have sufficient energy to cause dissociation of many organic molecular bonds[100, 101]. This photo-induced molecular fragmentation plays a significant role in the localized ablation of the cell membrane with wavelengths shorter than 250 nm[83]. However, due to the toxicity of UV light, this process is not so commonly used.

2.2 Experimental procedures for direct laser-induced photoporation.

Several approaches have been developed to achieve laser-induced photoporation. One of the widely used laser configurations makes use of a Gaussian laser beam that is focused on the cell membrane through a microscope objective lens (**Fig. 4a**). In this procedure, pore formation occurs through photomechanical effects induced by thermoelastic stress or cavitation bubbles or photochemical reactions, depending on the laser pulse energy and duration. Here it is crucial to position the focal volume exactly on the cell membrane, not only laterally, but also axially as a miss-focus of only 3 µm could reduce the transfection efficiency by as much as 50%[102]. As careful 3-D positioning of the focal volume is required, the photoporation throughput in this configuration is low at only a few cells/min[103, 104]. It has been demonstrated that throughput can be increased by focusing a ns laser a few micrometers above the cell membrane to generate cavitation bubbles (**Fig. 4b**). Tens of cells can be perforated by a single cavitation microbubble, so that a throughput of hundreds of cells/min can be reached[85, 105]. Another way to increase throughput is the use of a Bessel laser beam that has a large depth of field (with a fluence of typically tens of mJ/cm^2 in the central part of the beam) and, therefore, does not need axial positioning[66, 102]. With an array of multiple Bessel beams generated by a spatial light modulator a throughput of ~100 cells/min could be achieved[67]. The downside of using a non-diffracting Bessel beam is that a high laser intensity is delivered throughout the cell, potentially causing membrane dysfunction and DNA strand breaks, thus leading to apoptosis-like cell death[81, 106].

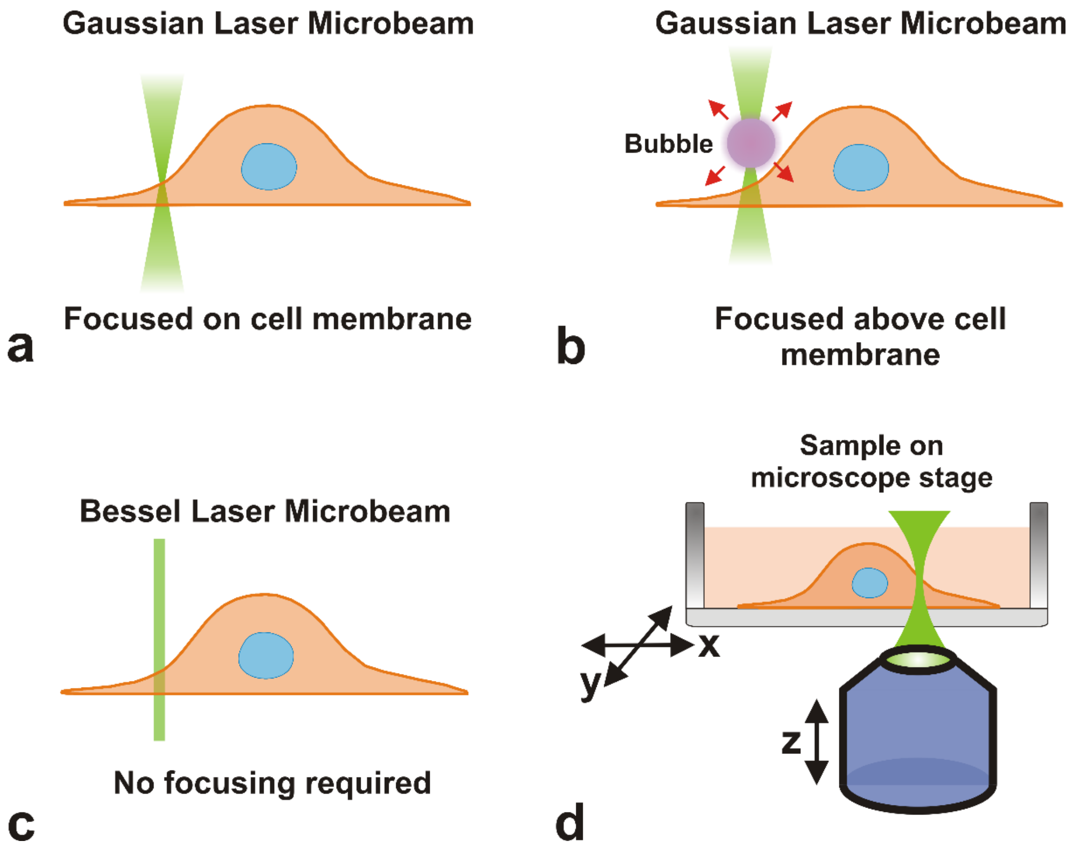

Figure 4. Experimental approaches for direct laser-induced photoporation. (a) A widely used approach in direct photoporation is to focus a Gaussian laser beam directly on the cell membrane. Pore formation in the cell membrane occurs through photomechanical or photochemical effects (b) A nanosecond pulsed laser can be used instead, which is focused a few micrometers above the cell membrane for the generation of micrometer sized vapor bubbles. (c) A non-diffracting Bessel laser beam can be used to enhance photoporation throughput as it does not require careful focusing on the cell membrane. (d) Cells can be photoporated in a sequential fashion by making use of a programmable x-y stage.

Cells can be photoporated in a sequential fashion by scanning the laser beam over the cells with a programmable x-y stage (**Fig. 4d**). With image processing the location of the individual cells can be determined. In combination with an auto-focus system to control the axial position of the photoporation laser beam, this allows cells to be photoporated in an automated fashion[107, 108]. In one example it was demonstrated that ~300 cells/min can be photoporated that way[107]. Finally, a microfluidic approach has also developed in an attempt to increase photoporation throughput, with cells flowing one by one through the focused photoporation laser beam. In this case, a throughput of ~60 cells/min has been obtained[109].

3. NANOPARTICLE (NP) SENSITIZED PHOTOPORATION

Nanomaterials can be used as sensitizers for the photoporation of cell membranes at lower laser energies, as was demonstrated first a little more than a decade ago[110, 111]. While since then gold nanoparticles (AuNP) have been used the most for this purpose, examples of other nanomaterials like titanium nanostructures and carbon based nanomaterials are currently being explored as well. NP sensitized photoporation can offer high throughput since less laser energy density is needed so that the laser beam can be expanded to cover 10s to 100s of cells at the same time. Similar to direct photoporation, sensitizing nanoparticles can lead to pore formation in the cell membrane through thermal, mechanical and photochemical processes, as is discussed in detail in this section.

3.1 Plasmonic NP sensitized photoporation

3.1.1 Laser interaction with plasmonic NP

For metallic nanoparticles like AuNPs, the optical absorption is enhanced by Localized Surface Plasmon Resonance (LSPR). As indicated in **Fig. 5a**, LSPR corresponds to the interaction between a nanostructure and an electromagnetic field, typically laser light. Free electrons in the nanoparticle start to oscillate in synchrony with the incident laser electromagnetic field. These oscillating electrons are called localized surface plasmons. This oscillation generates an electric field opposite to the incident wave and forces the electrons back to their equilibrium position. When the incident laser frequency matches the resonant frequency of the localized surface plasmons, the electrons will oscillate with maximum amplitude, known as localized surface plasmon resonance. The resonant plasmonic frequency depends on the size, shape and composition of the metallic nanoparticle, as well as its environment[112-117]. **Fig. 5b** shows the light scattering, absorption, and extinction cross-section for 50 nm AuNP in water, showing a LSPR peak at ~530 nm.

Due to oscillations of the localized surface plasmons, a series of sequential energy transfer processes occur (**Fig. 5c**). First, the oscillating electrons become thermalized within a hundred of fs through electron-electron interactions[118, 119]. After that, the thermalized electrons transfer their energy to the nanoparticle phonons (i.e. lattice vibrations) by electron-phonon coupling in ~1-5 ps, resulting in an increase of the nanoparticle temperature[120-122]. Finally, thermal equilibration is achieved in ~100 ps inside the NPs, which is followed by heat transfer from the particle to the environment. Furthermore, the plasmon oscillation can also induce an enhanced electric field in the near-field (**Fig. 5d**)[117, 123]. In the intense nearfield photothermal multi-photon absorption effects can happen similar as described for focused fs laser pulses in direct photoporation. These effects will be explained in more detail below.

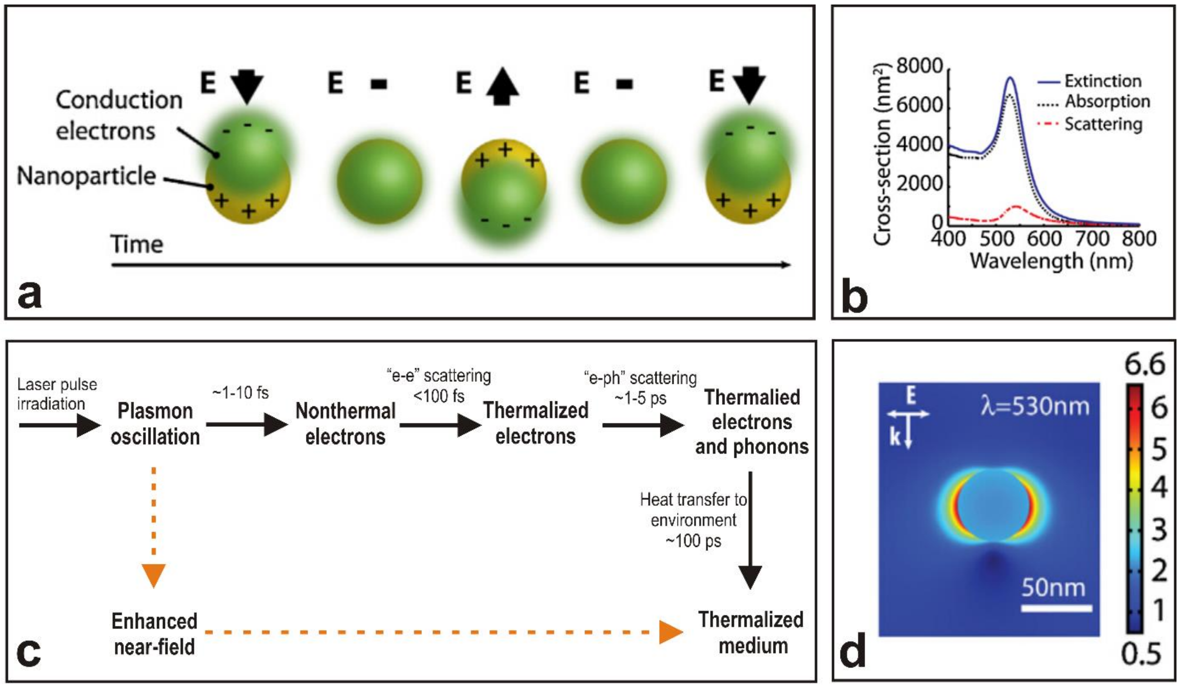

Figure 5. Principle of localized plasmon resonance and mechanisms of energy absorption and dissipation in laser-excited plasmonic NPs. (a) The incident electric field causes displacement of the NP's conduction electrons. Displacement of the electrons relative to the lattice ions creates its own restoration force. The interplay of the driving electric field and the dipole restoration force results in resonant behavior at certain light frequencies. (b) The scattering, absorption and extinction cross-section spectrum is shown for 50 nm NP in water. Localized plasmon resonance occurs around 530 nm. (c) Schematic overview of subsequent effects that happen in a NP upon absorption of incident light. (d) Electric field enhancement distribution around 20 nm AuNP at localized plasmon resonance of 520 nm. A maximum field enhancement of 6.6 along with energy absorption is apparent from the figure. Note: **Fig. 5a, b** and **d** adapted from **Fig. 2**, Ref. 117.

3.1.2 Photoporation by heating of the plasma membrane

Cell membrane perforation can occur through direct heat transfer from the sensitizing NP that are adsorbed to the cell membrane[111]. This is typically achieved with CW (continuous wavelength) laser irradiation or low intensity laser pulses (**Fig. 6a**). A rise in local temperature has been reported ranging from tens to even a few hundreds of degrees[113, 124]. Perforation of the cell membrane happens by a local phase transition of the lipid bilayer or thermal denaturation of integral glycoproteins which leads to opening of transient hydrophilic pores[72, 74, 125]. Heat induced pore sizes have been reported ranging from tens to hundreds of nm depending on the NP size and laser intensity[71, 74]. The main advantage of this approach is that CW lasers are relatively inexpensive and widely available. Throughput is, however, limited since it can take up to tens of seconds or a few minutes to form heat-induced pores.

3.1.3 Nanobubble induced photoporation

When using intense short laser pulses (<100 ps), the NP temperature can reach very high temperatures before heat can diffuse into the environment. In that way the NP temperature can rapidly increase to several hundred or even thousand degrees, leading to evaporation of the water surrounding the NP. The resulting water vapor nanobubble is referred to as a thermo-mediated nanobubble[126-129]. The expansion and collapse of the vapor nanobubbles can create pores in the cell membrane by high-pressure shockwaves or liquid jet formation (**Fig. 6b**). A particular characteristic of this phenomenon is that almost no heat is transferred to the environment due to the insulating effect of the vapor nanobubble[130]. This means that almost all incident laser energy is converted to mechanical energy of the expanding vapor nanobubble. The absence of heat transfer into cells may lead to better cell viability[76]. The size of vapor nanobubbles can be tuned from tens to several hundreds of nm depending on the laser intensity and size of NPs. The application of thermo-mediated nanobubbles for photoporation was pioneered by the Lapotko group. They mostly used 10 ns, 500 ps or 70 ps pulsed laser light to irradiate gold nanospheres, gold nanorods or gold nanoshells[131-133]. They found that the threshold for the formation of thermo-mediated nanobubbles significantly depends on the laser pulse duration and the types of NPs used. The laser intensity threshold for 10 ns pulsed laser light is more than 10-fold higher than for 500 ps pulses. This is due to the fact that thermal equilibration and the onset of heat diffusion in the environment happen on the 100 ps time scale. A large part of nanosecond laser pulses, therefore, do not contribute to the sudden rise in temperature that is needed for nanobubble formation. They also found that gold nano-shells often require much lower laser energy as compared to spherical AuNPs. Although diffusion is likely the predominant mechanism for exogenous compounds to enter cells through the membrane pores, Lukianova-Hleb *et al.* argued that an active flow of extracellular liquid might contribute as well[132]. The latter may be caused by transient nanojets which are formed by asymmetrical expansion and collapse of nanobubbles.

Apart from heat also plasma formation can lead to nanobubbles[123, 134] (**Fig. 6b**). As mentioned before, SPR causes near field enhancement the NP dipole edges. In these regions a plasma can be formed by multiphoton ionization of the medium. The plasma cools down by collision and recombination with water molecules, hence producing a quick temperature and pressure increase and leading to the generation of a water vapor nanobubble around the irradiated nanoparticle. The use of plasma-mediated nanobubbles was first reported by the Meunier group, who used fs pulsed laser (45 fs) irradiation of 100 nm gold nanospheres[123, 134, 135]. Under these conditions they found that the threshold of plasma-mediated nanobubble formation is ~100 mJ/cm^2.

3.1.4 Photochemical induced photoporation

Photochemical processes could occur during laser interaction with nanoparticles, especially in the region where the near field enhancement occurs (**Fig. 6c**). Of special relevance is ionization of water molecules and the generation of Reactive Oxygen Species (ROS)[73, 136, 137]. ROS and free radicals can initiate a damaging chain reaction of lipid peroxidation followed by decreased hydrophobicity of the lipid bilayer[74, 86]. Baumgart *et al.* made use of this process by irradiating 100 nm AuNPs with a fs laser (45 fs pulse, λ = 810 nm) at a laser fluence of 60 mJ/cm^2 [135]. The authors argue that photochemical processes are the predominant photoporation mechanism at these settings since heating is limited by using laser light at a non-resonant wavelength. Similarly, vapor nanobubbles were also thought not to be involved as the fluence was below the bubble threshold of 100 mJ/cm^2. Heisterkamp group performed photoporation experiments under similar conditions (120 fs pulse, λ = 800 nm) using 200 nm AuNPs. Also D. Heinemann and S. Kalies claimed that multiphoton ionization of water was the main photoporation mechanism in their experiments, even though they used substantially longer 850 ps laser pulses (wavelength at 532 nm) in combination with 200 nm AuNPs[73, 138].

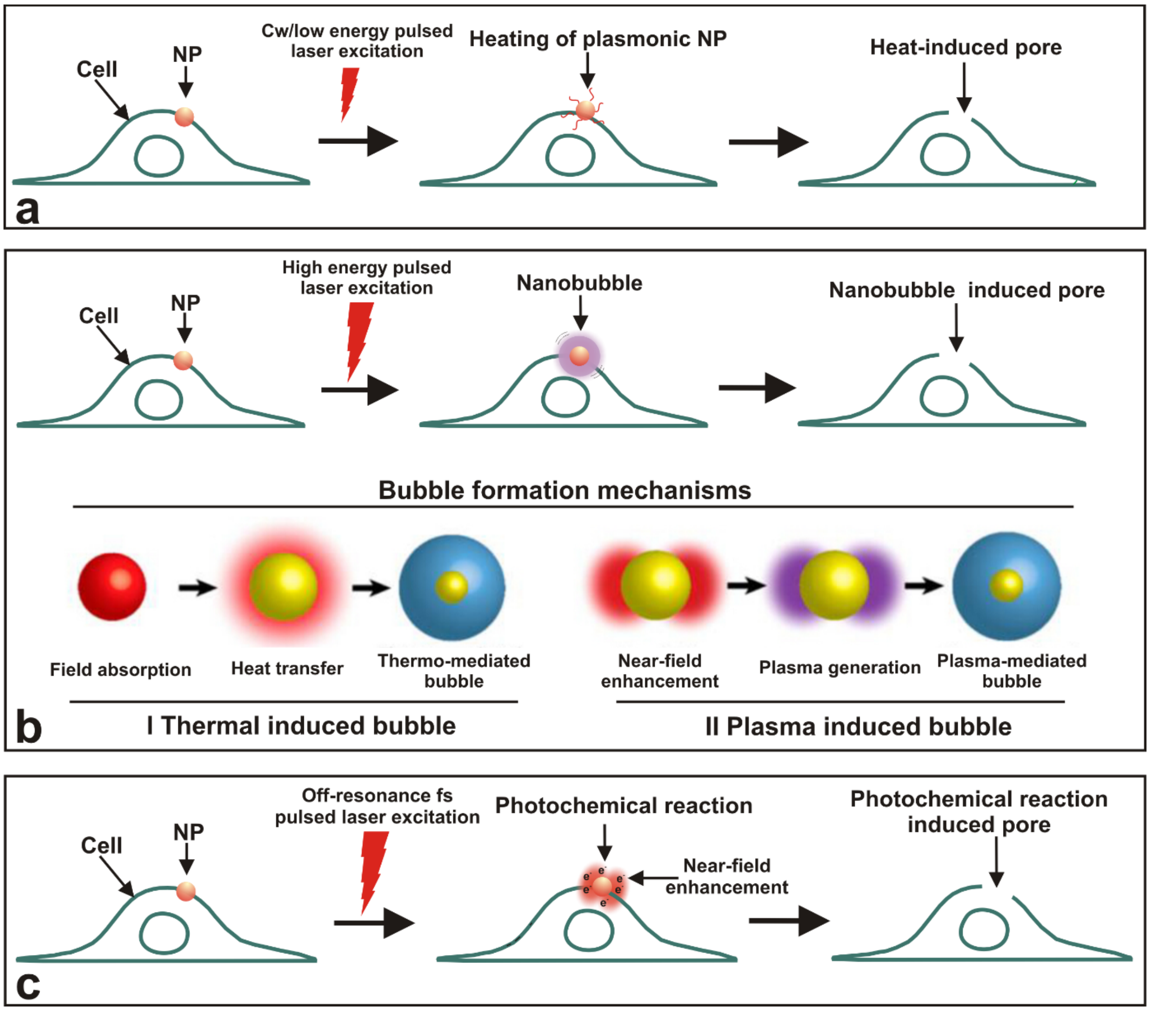

Figure 6. Mechanisms of plasmonic NP-sensitized photoporation. (a) When irradiated with CW laser light or low intensity pulsed laser light, plasmonic NPs become slightly heated and cause small pores in the cell membrane. (b) When short high-intensity laser pulses are used, water vapor nanobubbles can emerge around the NP whose mechanical force can form pores in the cell membrane. Notes: Vapor nanobubbles may be thermally induced or plasma induced. In thermo-mediated nanobubble formation, strong absorption of the incident electric field leads to extreme heating of the NP, which in turn causes vaporization of the surrounding water and the formation of vapor nanobubbles. Alternatively, near-field enhancement around the NP can result in plasma formation via multiphoton ionization of the surrounding water molecules. The plasma relaxes and transfers its energy to the water, in turn leading to nanobubble formation (**Fig. 6 b** down panel adapted from **Fig. 2**, see Refs. 117 and 134). (c) Photoporation of the cell membrane may also be caused by photochemical reactions that are triggered by multiphoton ionization of water and the generation of ROS.

3.2 Carbon nanostructure sensitized photoporation

Recently, carbon nanomaterials were reported as alternative sensitizers for photoporation. Carbon black (CB) NP sensitized photoporation was first reported by the group of Prausnitz[77, 78]. They reported that thermal effects are not the main reason for membrane poration. Instead they explain that a carbon-steam reaction $C(s)+H2O(l)\rightarrow CO(g)+H2(g)$ induces cavitation shockwaves that can perforate the cell membrane[139-141]. Graphene Oxide (GO) is another carbon-based nanomaterial that was demonstrated to improve cell membrane permeability following laser irradiation[142-144]. In combination with CW laser light, the group of Liu reported that heating was the major photoporation mechanism. Also carbon nanotubes have been reported as sensitizers[79, 145, 146], as they are well known to absorb laser energy and achieve high surface temperature upon laser irradiation[147, 148]. The exact photoporation mechanism was not reported and needs further investigation.

3.3 Experimental procedures for nanoparticle sensitized photoporation.

The most frequently used approach to achieve nanoparticle membrane poration is by simple addition of the nanoparticles to the cell medium so that they can adsorb to the cell membrane. There are even demonstrations that nanoparticles can be actively attached to (or even injected through) the cell membrane by optical forces[149, 150]. Laser irradiation can either be provided with a focused beam (**Fig. 7a**) to photoporate single cells or with a broad beam that illuminates several cells at a time (**Fig. 7b**). In the latter case photoporation throughput is significantly enhanced with reported values of $>10^3$ cells/s. To photoporate cells in suspension, Lukianova-Hleb *et al.* used a broad laser beam illuminating cells flowing through an optically transparent cuvette. With this flow set-up a photoporation rate as high as 5×10^4 cells/s was achieved (**Fig. 7c**)[132]. In another approach, to avoid direct adsorption of sensitizing nanoparticles to the cell membrane, sensitizing nanostructures can be incorporated in the substrate onto which cells are grown[80, 151] (**Fig. 7d**). Using AuNPs coated glass substrate, Wu *et al.* showed that gradually more compounds could be delivered into cells with repeated irradiation. The efficiency reached a plateau after 6 pulses probably due to release of the particles from the substrate. A downside of this approach is that the delivery efficiency was not as high as for NPs present on the cell membrane likely due to the fact that molecules have to diffuse through the narrow space underneath the adherent cells. Wu *et al.* tried to deliver calcein (0.6 kDa) and obtained ~58% positive HeLa cells. Instead, with membrane adsorbed AuNP, typically > 80% positive cells are obtained, even when using larger molecules like 10 kDa FITC-dextran[76]. Substrate mediated photoporation could be recently made more efficient by a 'laser-assisted surgery tool' was developed by Wu *et al.* to deliver large cargo in high-throughput in cells[80]. The platform consists of a silicon chip providing an array of micrometer-wide holes whose sides are asymmetrically coated with crescent-shaped titanium thin films (**Fig. 7e**). Underneath, the silicon chip was connected with vertical silicon channels providing pressure-driven fluid passage for cargo delivery. An array of bubbles is generated from the titanium nanostructures by providing pulsed laser irradiation onto the substrate, forming the pores in the adjacent cell membranes. The cargo is then gently driven into cells by pressurized flow. This platform has been used to deliver large cargos including bacteria, enzymes, antibodies and nanoparticles into various cell types with high efficiency and viability. A similar platform was recently presented for spatially, temporally and quantitatively controlled delivery of a broad range of molecules into selected cells *via* plasmonic nanobtubes[152]. The delivery is achieved by a planar substrate with an array of protruding microfabricated gold nanotubes onto which cells are grown. By laser-irradiation of the gold nanotubes heating emerge from the tips that perforate the cell membrane. Compounds can then enter into the cells through the tubes that are directly connected to a microfluidic channel underneath.

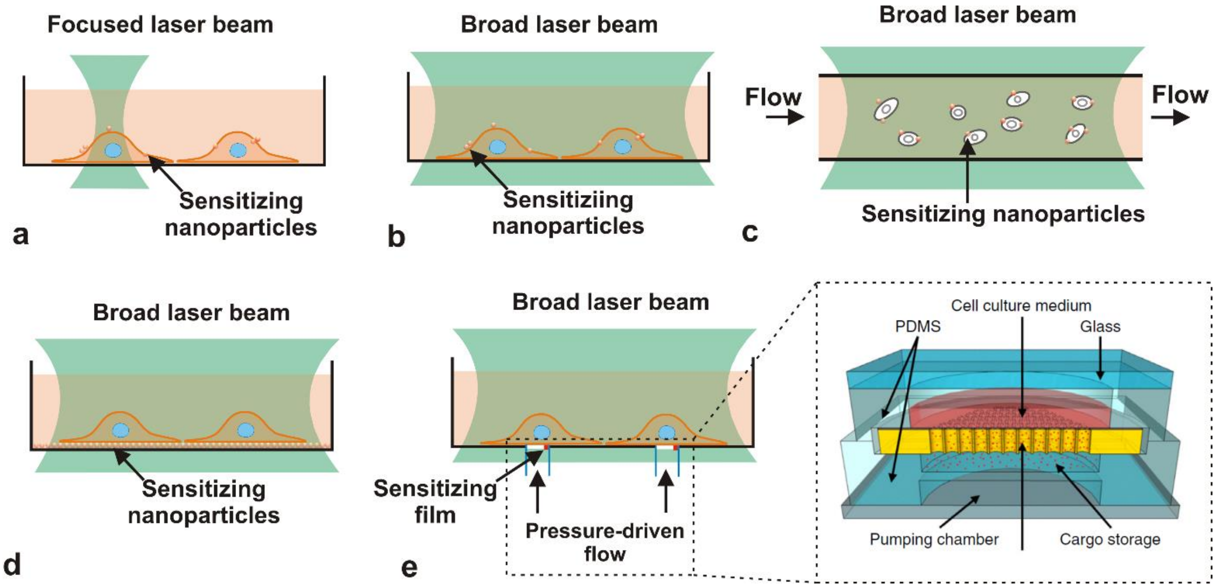

Figure 7. Approaches of NP-sensitized photoporation. (a) A focused laser beam can be applied to photoporate single cells. (b) Due to the sensitizing action of NPs, also a broad (low-energy) laser beam can be used to photoporate several cells at the same time so as to increase throughput. (c) A flow method was developed to photoporate cells in suspension. (d) Sensitizing NPs can be coated on the substrate onto which cells are grown. Pores are formed upon laser irradiation in the adherent part of the cell membrane. (e) Cells are grown on an array of micrometer-wide holes whose sides are asymmetrically coated with crescent-shaped titanium thin films. Notes: The inset shows the microfluidic chip in more detail (**Fig. 7e** Zoom-in figure adapted from Ref. [80]). Vapor bubbles are formed from the titanium structures upon laser irradiation, which form pores in the cell membrane. Cargo is then delivered into the cells by a pressurized fluid flow.

4. RESEALING OF TRANSIENT PORES AFTER PHOTOPORATION

Following photoporation, cells reseal the membrane pores in a matter of tens of seconds to a few minutes, depending on the pore size. The repair mechanism is based on Ca^{2+} influx that induces exocytosis of lysosomes for 'patching' of the pores[153, 154]. Based on inflow of fluorescent dextran after photoporation, the group of Kalies noticed that pores in the membrane (with a size of ~50 nm) were resealed in 15 s[136]. Daisuke Yamane reported a sealing time of 1 or 2 minutes after vapor nanobubble pore formation by using an electrical impedance sensor[155]. R. Palankar found that transient nanopores in lipid membranes generated by photothermal heating of nanorods were resealed in tens of seconds. However, micrometer sized pores could not be repaired [156]. It is consistently observed that higher laser fluences (inducing large pores) or high concentration of NPs (inducing more pores) cause higher toxicity[73, 132, 135, 138]. Therefore, careful optimization of photoporation parameters (like laser fluence, number of NPs) is needed in order to balance delivery efficiency with cell toxicity.

5. APPLICATIONS OF PHOTOPORATION

5.1 Direct laser photoporation

Photoporation has been extensively explored for transfection of cells with nucleic acids (DNA, mRNA or siRNA) as well as with proteins. Direct laser-induced photoporation (wavelength of 355 nm with 5 ns pulse duration) was already shown 30 years ago to enable efficient and contact-free delivery of DNA into cells[157]. Later on, fs-pulsed lasers were used to transfect cells with DNA with better efficiency and low cytotoxicity[62]. Spatially controlled introduction of mRNAs into specific regions (cell body or dendrites region) of primary rat neurons was reported by Barrett. et.al using fs-pulsed direct laser photoporation[8]. Interestingly, they found that delivery of mRNA in dendrites produced cell death, whereas mRNA introduced in cell bodies did not cause cell death, shedding light on the importance of the dendritic environment on protein function. Recently, Dhakal et al. reported the use of a fs laser for the targeted transfection of single and multiple opsin-encoding genes into selected retinal cells *in vitro*[158]. They found that cells transfected with multiple opsins had a significantly higher white-light induced photocurrent than cells expressing a single opsin, paving the way toward the restoration of lost vision in retinitis pigmentosa and age-related macular degeneration. Direct laser induced photoporation was furthermore reported for transfecting ions, small molecules, siRNA, plasmid DNA, and semiconductor nanocrystals into several cell types[105]. In recent years, cellular imaging by direct laser photoporation for delivery of dyes into live cells is being explored as a new and promising application. In particular, fs laser assisted direct photoporation was used to deliver actin-staining fluorophores into rat cortical neurons for visualizing the cytoskeleton of dendrites[159].

5.2 NP sensitized photoporation

Nanoparticle sensitized photoporation has been used for high-throughput transfection of cells with DNA, siRNA and proteins[110]. The group of M. Meunier has explored photoporation of naked DNA into human cancer cells by plasma induced nanobubbles with a fs laser and found much higher transfection efficiency with very low toxicity compared to conventional lipofection[135]. Similarly, Lukianova-Hleb *et al.* used a pico-second laser for high-throughput transfection of 'hard-to-transfect' T-cells with GFP plasmids[132]. More studies are needed, however, to fully explore the potential of delivering large macromolecules like mRNA or pDNA in a variety of cell types by NP sensitized photoporation. Xiong et al. compared the transfection efficiency of thermal induced pores versus pores created by thermo-induced vapor nanobubbles and found that nanobubble mediated poration allows more efficient entry of siRNA into cells[76]. Using carbon black sensitizing nanoparticles, small molecules, proteins and DNA can be successfully delivered into living cells[77]. Titanium thin films were used as sensitizers to deliver large cargo like bacteria, enzymes, antibodies and nanoparticles into diverse cell types with high efficiency, cell viability and high-throughput[80]. Anti-cancer drugs have been delivered by photoporation into cancer cells for an enhanced chemotherapeutic effect[160]. The same group showed that direct delivery of the anti-cancer drug into the cell's cytoplasm by photoporation substantially enhanced the effect of chemoradiation *in vivo*[161]. Also GO nanoparticles were used to deliver a photosensitiser into cells for enhanced photodynamic therapy efficacy against the cancer cells *in vitro*[142]. While photoporation is mostly used to deliver compounds into cells, it has also been shown that it can be used to release compounds from cells, which could be an interesting concept for light triggered drug release[74].

6. PERSPECTIVES AND CONCLUSION

Although photoporation has already been shown to be an exciting technology for efficient intracellular delivery of membrane-impermeable exogenous materials into living cells, there still lay plenty of challenges and opportunities ahead. On a fundamental level it is of interest to get a better insight in the loading mechanism of molecules into the cytoplasm, especially for large and charged molecules like pDNA or mRNA. Translocation of molecules into the cytoplasm is mostly thought to happen by diffusion through the membrane pores. However, it has also been proposed that there might be an active 'nano-jet' mechanism involved as well under certain conditions like the nanobubble induced photoporation[132]. In order to be able to better control and predict the influx of molecules of various sizes and charges into the cytoplasm, the loading mechanisms need to be studied in more detail. Similarly it is of fundamental interest to get a better view on the pore size, lifetime and repair mechanisms for the various photoporation approaches. While there have been a few studies along these lines, the reported values are quite different (e.g. pore lifetimes ranging from tens of seconds to tens of minutes), which is likely caused by differences in photoporation conditions, different cell types and different ways how the measurements are perforated. Therefore, more systematic studies are needed on this which in turn will be helpful to better understand and predict the loading process for different types of cells and molecules. Also systematic and in-depth cytotoxicity studies are needed, especially for NP sensitized photoporation since there is the additional concern of NP induced toxicity. Although simple cytotoxicity measurements are typically included in current research articles, in-depth understanding of the factors contributing to cytotoxicity is needed to expedite acceptance of photoporation as one of the standard transfection methods by the wider scientific community.

For NP sensitized photoporation there clearly lay opportunities on the material size as well. While AuNPs have clearly been used the most till now, it is of interest to look for NPs that are better resistant to the illumination conditions used in photoporation, especially when using pulsed laser light. Indeed, due to the substantial temperature increase the AuNP might melt and change shape (e.g. rods becoming spheres) which alters there wavelength-dependent absorption characteristics. Fragmentation of AuNP has been reported too, which renders them useless already after one laser pulse[69, 76]. Carbon nanomaterial sensitized photoporation was recently explored as a promising alternative class of sensitizing nanoparticles with superior thermal stability, facile synthesis, easily tunable surface functionalization and good biocompatibility. Further studies are needed to explore the potential functional benefits compared to AuNPs with cytotoxicity studies being performed in parallel.

Although photoporation has proven its value for delivering compounds into cells in culture, exploration of its *in vivo* potential has only just been started. Recently, the Lapotko group applied for the first time AuNP sensitized photoporation of chemotherapeutics to *in vivo* cancer treatment[161]. The same group recently showed *in vivo* elimination of residual head and neck cancer cells by tumor targeting gold colloids[162]. Undoubtedly more examples of *in vivo* applications of photoporation will follow in the near future. Here it will be of interest to develop biocompatible sensitizing materials because of the toxicity concerns in relation to the *in vivo* usage of colloidal nanoparticles[163]. In a recent report it was, for instance, shown that vapor nanobubbles can be formed by irradiating hemozoin crystals (malaria related organic crystals) in the blood circulation with laser light[164]. This shows that there might be opportunities to look for organic materials that could replace inorganic nanoparticles.

Apart from certain *in vivo* applications, we do see a bright future for photoporation as a very flexible *in vitro* transfection technology, especially in combination with sensitizing NPs which enable high-throughput treatment. After about a decade of initial developments, we expect that photoporation will gradually become a more mature and widely available intracellular delivery technology. The portable photoporation device developed by the Heisterkamp group is a good example of this[73], as well as some first attempts to perform automated photoporation in a microfluidics device[109, 165]. As cytotoxicity is typically limited under optimized conditions, we believe that photoporation may complement or in some cases even replace standard methods like electroporation which are well-known to induce substantial cell toxicity. Importantly, photoporation offers the unique possibility for spatially controlled delivery into cells as the laser beam can be easily tuned in size and position [152]. The possibility to transfect selected cells in a cell culture offers unprecedented opportunities not possible with any other of the current transfection technologies. One can imagine that this unique feature will be of benefit to study, for instance, cell bystander effects or to transfect one cell type in a co-culture of cells as is of interest for tissue engineering.

Taken together we can conclude that laser-assisted photoporation is a maturing promising technique for unprecedented flexible intracellular delivery of membrane impermeable substances that, thanks to its unique capabilities, will secure its place next to the more established intracellular delivery methods.

Acknowledgements

Financial support by the Ghent University Special Research Fund (Centre for Nano- and Biophotonics) is acknowledged with gratitude. RX gratefully acknowledges the financial support from China Scholarship Council (CSC). KB would like to acknowledge the Research Foundation Flanders (FWO Vlaanderen). KB also acknowledges financial support from the European Research Council (ERC) under the European Union's Horizon 2020 research and innovation program (grant agreement No 648124).

7. REFERENCES

1. Jones, D.C. et al. Regulation of adult bone mass by the zinc finger adapter protein Schnurri-3. *Science* **312**, 1223-1227 (2006).
2. Leftowitz, R.J. & Shenoy, S.K. Transduction of receptor signals by beta-arrestins. *Science* **308**, 512-517 (2005).
3. Glatt, S.J. et al. Comparative gene expression analysis of blood and brain provides concurrent validation of SELENBP1 up-regulation in schizophrenia. *P Natl Acad Sci USA* **102**, 15533-15538 (2005).
4. Pastinen, T. & Hudson, T.J. Cis-acting regulatory variation in the human genome. *Science* **306**, 647-650 (2004).
5. Ashkenazi, A. & Dixit, V.M. Death receptors: Signaling and modulation. *Science* **281**, 1305-1308 (1998).
6. Bienko, M. et al. Ubiquitin-binding domains in Y-family polymerases regulate translesion synthesis. *Science* **310**, 1821-1824 (2005).
7. Gottgens, B. et al. Genome-wide identification of cis-regulatory sequences controlling blood and endothelial development. *Blood* **104**, 449a-449a (2004).
8. Barrett, L.E. et al. Region-directed phototransfection reveals the functional significance of a dendritically synthesized transcription factor. *Nat Methods* **3**, 455-460 (2006).
9. Davidson, B.L. & McCray, P.B. Current prospects for RNA interference-based therapies. *Nat Rev Genet* **12**, 329-340 (2011).
10. Hong, J.H. et al. TAZ, a transcriptional modulator of mesenchymal stem cell differentiation. *Science* **309**, 1074-1078 (2005).
11. McManus, M.T. et al. Small interfering RNA-mediated gene silencing in T lymphocytes. *J Immunol* **169**, 5754-5760 (2002).
12. Sen, G.L. & Blau, H.M. A brief history of RNAi: the silence of the genes. *Faseb J* **20**, 1293-1299 (2006).
13. Xia, H.B., Mao, Q.W., Paulson, H.L. & Davidson, B.L. siRNA-mediated gene silencing in vitro and in vivo. *Nat Biotechnol* **20**, 1006-1010 (2002).
14. Takeuchi, T. et al. Direct and rapid cytosolic delivery using cell-penetrating peptides mediated by pyrenebutyrate. *Acs Chem Biol* **1**, 299-303 (2006).
15. Sakakibara, D. et al. Protein structure determination in living cells by in-cell NMR spectroscopy. *Nature* **458**, 102-U110 (2009).
16. Du, Q.S. & Macara, I.G. Mammalian pins is a conformational switch that links NuMA to heterotrimeric G proteins. *Cell* **119**, 503-516 (2004).
17. Himmelreich, U. & Dresselaers, T. Cell labeling and tracking for experimental models using Magnetic Resonance Imaging. *Methods* **48**, 112-124 (2009).
18. Xu, C.J. et al. Tracking Mesenchymal Stem Cells with Iron Oxide Nanoparticle Loaded Poly(lactide-co-glycolide) Microparticles. *Nano Lett* **12**, 4131-4139 (2012).
19. Guzman, R. et al. Long-term monitoring of transplanted human neural stem cells in developmental and pathological contexts with MRI. *P Natl Acad Sci USA* **104**, 10211-10216 (2007).
20. Wegner, K.D. & Hildebrandt, N. Quantum dots: bright and versatile in vitro and in vivo fluorescence imaging biosensors. *Chem Soc Rev* **44**, 4792-4834 (2015).
21. Michalet, X. et al. Quantum dots for live cells, in vivo imaging, and diagnostics. *Science* **307**, 538-544 (2005).
22. Gao, X.H., Cui, Y.Y., Levenson, R.M., Chung, L.W.K. & Nie, S.M. In vivo cancer targeting and imaging with semiconductor quantum dots. *Nat Biotechnol* **22**, 969-976 (2004).
23. Chen, G.Y., Qju, H.L., Prasad, P.N. & Chen, X.Y. Upconversion Nanoparticles: Design, Nanochemistry, and Applications in Theranostics. *Chemical Reviews* **114**, 5161-5214 (2014).
24. Yang, X.M., Stein, E.W., Ashkenazi, S. & Wang, L.H.V. Nanoparticles for photoacoustic imaging. *Wires Nanomed Nanobi* **1**, 360-368 (2009).

25. Li, W.W. & Chen, X.Y. Gold nanoparticles for photoacoustic imaging. *Nanomedicine-Uk* **10**, 299-320 (2015).
26. Wong, C.L. et al. Photothermal imaging (PTI) system for the imaging of gold nano-particles and cellular organelles. *Adv Mat Res* **74**, 45-48 (2009).
27. Boyer, D., Tamarat, P., Maali, A., Lounis, B. & Orrit, M. Photothermal imaging of nanometer-sized metal particles among scatterers. *Science* **297**, 1160-1163 (2002).
28. Xu, J.M. et al. Nanoblade Delivery and Incorporation of Quantum Dot Conjugates into Tubulin Networks in Live Cells. *Nano Lett* **12**, 5669-5672 (2012).
29. Kim, T.K. & Eberwine, J.H. Mammalian cell transfection: the present and the future. *Anal Bioanal Chem* **397**, 3173-3178 (2010).
30. Pfeifer, A. & Verma, I.M. Gene therapy: Promises and problems. *Annu Rev Genom Hum G* **2**, 177-211 (2001).
31. Verma, I.M. & Somia, N. Gene therapy - promises, problems and prospects. *Nature* **389**, 239-242 (1997).
32. Feng, X.L., Tang, Y.L., Duan, X.R., Liu, L.B. & Wang, S. Lipid-modified conjugated polymer nanoparticles for cell imaging and transfection. *J Mater Chem* **20**, 1312-1316 (2010).
33. Dheur, S. et al. Polyethylenimine but not cationic lipid improves antisense activity of 3'-capped phosphodiester oligonucleolides. *Antisense Nucleic A* **9**, 515-525 (1999).
34. Luo, D. & Saltzman, W.M. Enhancement of transfection by physical concentration of DNA at the cell surface. *Nat Biotechnol* **18**, 893-895 (2000).
35. Midoux, P., Pichon, C., Yaouanc, J.J. & Jaffres, P.A. Chemical vectors for gene delivery: a current review on polymers, peptides and lipids containing histidine or imidazole as nucleic acids carriers. *Brit J Pharmacol* **157**, 166-178 (2009).
36. Martens, T.F., Remaut, K., Demeester, J., De Smedt, S.C. & Braeckmans, K. Intracellular delivery of nanomaterials: How to catch endosomal escape in the act. *Nano Today* **9**, 344-364 (2014).
37. Varkouhi, A.K., Scholte, M., Storm, G. & Haisma, H.J. Endosomal escape pathways for delivery of biologicals. *J Control Release* **151**, 220-228 (2011).
38. Raemdonck, K., Naeye, B., Hogset, A., Demeester, J. & De Smedt, S.C. Prolonged gene silencing by combining siRNA nanogels and photochemical internalization. *J Control Release* **145**, 281-288 (2010).
39. Lakshmanan, S. et al. Physical energy for drug delivery; poration, concentration and activation. *Adv Drug Deliver Rev* **71**, 98-114 (2014).
40. Prentice, P., Cuschierp, A., Dholakia, K., Prausnitz, M. & Campbell, P. Membrane disruption by optically controlled microbubble cavitation. *Nat Phys* **1**, 107-110 (2005).
41. Mehier-Humbert, S. & Guy, R.H. Physical methods for gene transfer: Improving the kinetics of gene delivery into cells. *Adv Drug Deliver Rev* **57**, 733-753 (2005).
42. Auerbach, A.B. Production of functional transgenic mice by DNA pronuclear microinjection. *Acta Biochim Pol* **51**, 9-31 (2004).
43. Gordon, J.W., Scangos, G.A., Plotkin, D.J., Barbosa, J.A. & Ruddle, F.H. Genetic-Transformation of Mouse Embryos by Micro-Injection of Purified DNA. *P Natl Acad Sci-Biol* **77**, 7380-7384 (1980).
44. Capecchi, M.R. High-Efficiency Transformation by Direct Micro-Injection of DNA into Cultured Mammalian-Cells. *Cell* **22**, 479-488 (1980).
45. Murphy, R.C. & Messer, A. Gene transfer methods for CNS organotypic cultures: A comparison of three nonviral methods. *Mol Ther* **3**, 113-121 (2001).
46. Canatella, P.J. & Prausnitz, M.R. Prediction and optimization of gene transfection and drug delivery by electroporation. *Gene Ther* **8**, 1464-1469 (2001).
47. Goto, T. et al. Highly efficient electro-gene therapy of solid tumor by using an expression plasmid for the herpes simplex virus thymidine kinase gene. *P Natl Acad Sci USA* **97**, 354-359 (2000).
48. Mir, L.M. et al. High-efficiency gene transfer into skeletal muscle mediated by electric pulses. *P Natl Acad Sci USA* **96**, 4262-4267 (1999).

49. Muramatsu, T., Mizutani, Y., Ohmori, Y. & Okumura, J. Comparison of three nonviral transfection methods for foreign gene expression in early chicken embryos in ovo. *Biochem Bioph Res Co* **230**, 376-380 (1997).
50. Yi, J., Barrow, A.J., Yu, N. & O'Neill, B.E. Efficient electroporation of liposomes doped with pore stabilizing nisin. *J Liposome Res* **23**, 197-202 (2013).
51. Gan, W.-B., Grutzendler, J., Wong, W.T., Wong, R.O.L. & Lichtman, J.W. Multicolor “DiOlistic” Labeling of the Nervous System Using Lipophilic Dye Combinations. *Neuron* **27**, 219-225 (2000).
52. Klein, T.M., Wolf, E.D., Wu, R. & Sanford, J.C. High-velocity microprojectiles for delivering nucleic acids into living cells. *Nature* **327**, 70-73 (1987).
53. Lentacker, I., De Cock, I., Deckers, R., De Smedt, S.C. & Moonen, C.T.W. Understanding ultrasound induced sonoporation: Definitions and underlying mechanisms. *Adv Drug Deliver Rev* **72**, 49-64 (2014).
54. Fan, Z., Kumon, R.E. & Deng, C.X. Mechanisms of microbubble-facilitated sonoporation for drug and gene delivery. *Therapeutic delivery* **5**, 467-486 (2014).
55. Kudo, N. & Yamamoto, K. Sonoporation: Mechanisms of cell membrane perforation and rapid resealing. *The Journal of the Acoustical Society of America* **120**, 3229-3229 (2006).
56. Park, D. et al. Sonophoresis Using Ultrasound Contrast Agents for Transdermal Drug Delivery: An in Vivo Experimental Study. *Ultrasound Med Biol* **38**, 642-650 (2012).
57. Kollmannsperger, A. et al. Live-cell protein labeling with nanometre precision by cell squeezing. *Nat Commun* **7** (2016).
58. Sharei, A. et al. A vector-free microfluidic platform for intracellular delivery. *P Natl Acad Sci USA* **110**, 2082-2087 (2013).
59. Lee, J. et al. Nonendocytic Delivery of Functional Engineered Nanoparticles into the Cytoplasm of Live Cells Using a Novel, High-Throughput Microfluidic Device. *Nano Lett* **12**, 6322-6327 (2012).
60. Sharei, A. et al. Ex Vivo Cytosolic Delivery of Functional Macromolecules to Immune Cells. *Plos One* **10** (2015).
61. He, H., Kong, S.K., Lee, R.K.Y., Suen, Y.K. & Chan, K.T. Targeted photoporation and transfection in human HepG2 cells by a fiber femtosecond laser at 1554 nm. *Opt Lett* **33**, 2961-2963 (2008).
62. Tirlapur, U.K. & Konig, K. Cell biology - Targeted transfection by femtosecond laser. *Nature* **418**, 290-291 (2002).
63. Wu, T.H. et al. Pulsed laser triggered high speed microfluidic fluorescence activated cell sorter. *Lab Chip* **12**, 1378-1383 (2012).
64. Sibbett, W., Lagatsky, A.A. & Brown, C.T.A. The development and application of femtosecond laser systems. *Opt Express* **20**, 6989-7001 (2012).
65. Waleed, M. et al. Single-cell optoporation and transfection using femtosecond laser and optical tweezers. *Biomed Opt Express* **4**, 1533-1547 (2013).
66. Stevenson, D.J., Gunn-Moore, F.J., Campbell, P. & Dholakia, K. Single cell optical transfection. *J R Soc Interface* **7**, 863-871 (2010).
67. Antkowiak, M. et al. Fast targeted gene transfection and optogenetic modification of single neurons using femtosecond laser irradiation. *Sci Rep-Uk* **3** (2013).
68. Sapsford, K.E. et al. Functionalizing Nanoparticles with Biological Molecules: Developing Chemistries that Facilitate Nanotechnology. *Chemical Reviews* **113**, 1904-2074 (2013).
69. Qin, Z.P. & Bischof, J.C. Thermophysical and biological responses of gold nanoparticle laser heating. *Chem Soc Rev* **41**, 1191-1217 (2012).
70. Zijlstra, P. & Orrit, M. Single metal nanoparticles: optical detection, spectroscopy and applications. *Rep Prog Phys* **74** (2011).
71. Sun, X.H. et al. Enhanced drug delivery via hyperthermal membrane disruption using targeted gold nanoparticles with PEGylated Protein-G as a cofactor. *Nanomed-Nanotechnol* **9**, 1214-1222 (2013).
72. Kalies, S. et al. Gold nanoparticle mediated laser transfection for high-throughput antisense applications. *Medical Laser Applications and Laser-Tissue Interactions Vi* **8803** (2013).

73. Heinemann, D. et al. Gold Nanoparticle Mediated Laser Transfection for Efficient siRNA Mediated Gene Knock Down. *Plos One* **8** (2013).
74. Delcea, M. et al. Nanoplasmonics for Dual-Molecule Release through Nanopores in the Membrane of Red Blood Cells. *Acs Nano* **6**, 4169-4180 (2012).
75. Skirtach, A.G. et al. The role of metal nanoparticles in remote release of encapsulated materials. *Nano Lett* **5**, 1371-1377 (2005).
76. Xiong, R.H. et al. Comparison of Gold Nanoparticle Mediated Photoporation: Vapor Nanobubbles Outperform Direct Heating for Delivering Macromolecules in Live Cells. *Acs Nano* **8**, 6288-6296 (2014).
77. Chakravarty, P., Qian, W., El-Sayed, M.A. & Prausnitz, M.R. Delivery of molecules into cells using carbon nanoparticles activated by femtosecond laser pulses. *Nat Nanotechnol* **5**, 607-611 (2010).
78. Sengupta, A., Kelly, S.C., Dwivedi, N., Thadhani, N. & Prausnitz, M.R. Efficient Intracellular Delivery of Molecules with High Cell Viability Using Nanosecond-Pulsed Laser-Activated Carbon Nanoparticles. *Acs Nano* **8**, 2889-2899 (2014).
79. Hong, G.S., Diao, S.O., Antaris, A.L. & Dai, H.J. Carbon Nanomaterials for Biological Imaging and Nanomedicinal Therapy. *Chemical Reviews* **115**, 10816-10906 (2015).
80. Wu, Y.C. et al. Massively parallel delivery of large cargo into mammalian cells with light pulses. *Nat Methods* **12**, 439-+ (2015).
81. Vogel, A., Noack, J., Huttman, G. & Paltauf, G. Mechanisms of femtosecond laser nanosurgery of cells and tissues. *Appl Phys B-Lasers O* **81**, 1015-1047 (2005).
82. Quinto - Su, P.A. & Venugopalan, V. in Methods in Cell Biology, Vol. Volume 82 111-151 (Academic Press, 2007).
83. Vogel, A. & Venugopalan, V. Mechanisms of pulsed laser ablation of biological tissues. *Chemical Reviews* **103**, 577-644 (2003).
84. Dierickx, C.C., Michael Casparian, J., Venugopalan, V., Farinelli, W.A. & Rox Anderson, R. Thermal Relaxation of Port-Wine Stain Vessels Probed In Vivo: The Need for 1-10-Millisecond Laser Pulse Treatment. *Journal of Investigative Dermatology* **105**, 709-714 (1995).
85. Rau, K.R., Quinto-Su, P.A., Hellman, A.N. & Venugopalan, V. Pulsed laser microbeam-induced cell lysis: Time-resolved imaging and analysis of hydrodynamic effects. *Biophys J* **91**, 317-329 (2006).
86. Ivanov, I.T., Brähler, M., Georgieva, R. & Bäumler, H. Role of membrane proteins in thermal damage and necrosis of red blood cells. *Thermochimica Acta* **456**, 7-12 (2007).
87. Peng, Q. et al. Lasers in medicine. *Rep Prog Phys* **71** (2008).
88. Palumbo, G. et al. Targeted gene transfer in eucaryotic cells by dye-assisted laser optoporation. *J Photoch Photobio B* **36**, 41-46 (1996).
89. Schneckenburger, H., Hendinger, A., Sailer, R., Strauss, W.S.L. & Schmitt, M. Laser-assisted optoporation of single cells. *J Biomed Opt* **7**, 410-416 (2002).
90. Fabian, J., Nakazumi, H. & Matsuoka, M. Near-Infrared Absorbing Dyes. *Chemical Reviews* **92**, 1197-1226 (1992).
91. Sankin, G.N., Yuan, F. & Zhong, P. Pulsating Tandem Microbubble for Localized and Directional Single-Cell Membrane Poration. *Phys Rev Lett* **105** (2010).
92. Ridley, B.K. Quantum processes in semiconductors. (Oxford University Press, 2013).
93. Vogel, A. et al. Energy balance of optical breakdown in water at nanosecond to femtosecond time scales. *Appl Phys B-Lasers O* **68**, 271-280 (1999).
94. Juhasz, T., Hu, X.H., Turi, L. & Bor, Z. Dynamics of Shock-Waves and Cavitation Bubbles Generated by Picosecond Laser-Pulses in Corneal Tissue and Water. *Laser Surg Med* **15**, 91-98 (1994).
95. Zysset, B., Fujimoto, J.G. & Deutsch, T.F. Time-Resolved Measurements of Picosecond Optical-Breakdown. *Ber Bunsen Phys Chem* **93**, 260-265 (1989).
96. Garrett, B.C. et al. Role of water in electron-initiated processes and radical chemistry: Issues and scientific advances. *Chemical Reviews* **105**, 355-389 (2005).

97. Tirlapur, U.K., Konig, K., Peuckert, C., Krieg, R. & Halbhuber, K.J. Femtosecond near-infrared laser pulses elicit generation of reactive oxygen species in mammalian cells leading to apoptosis-like death. *Exp Cell Res* **263**, 88-97 (2001).
98. Nikogosyan, D.N., Oraevsky, A.A. & Rupasov, V.I. Two-photon ionization and dissociation of liquid water by powerful laser UV radiation. *Chemical Physics* **77**, 131-143 (1983).
99. Yannas, I.V. Collagen and Gelatin in the Solid State. *Journal of Macromolecular Science, Part C* **7**, 49-106 (1972).
100. Srinivasan, R. Ablation of Polymers and Biological Tissue by Ultraviolet-Lasers. *Science* **234**, 559-565 (1986).
101. Srinivasan, R. & Leigh, W.J. Ablative photodecomposition: action of far-ultraviolet (193 nm) laser radiation on poly(ethylene terephthalate) films. *Journal of the American Chemical Society* **104**, 6784-6785 (1982).
102. Tsampoula, X. et al. Femtosecond cellular transfection using a nondiffracting light beam. *Appl Phys Lett* **91** (2007).
103. Tao, W., Wilkinson, J., Stanbridge, E.J. & Berns, M.W. Direct Gene-Transfer into Human Cultured-Cells Facilitated by Laser Micropuncture of the Cell-Membrane. *P Natl Acad Sci USA* **84**, 4180-4184 (1987).
104. Davis, A.A., Farrar, M.J., Nishimura, N., Jin, M.M. & Schaffer, C.B. Optoporation and Genetic Manipulation of Cells Using Femtosecond Laser Pulses. *Biophys J* **105**, 862-871 (2013).
105. Clark, I.B. et al. Optoinjection for efficient targeted delivery of a broad range of compounds and macromolecules into diverse cell types. *J Biomed Opt* **11** (2006).
106. Tirlapur, U.K., König, K., Peuckert, C., Krieg, R. & Halbhuber, K.-J. Femtosecond Near-Infrared Laser Pulses Elicit Generation of Reactive Oxygen Species in Mammalian Cells Leading to Apoptosis-like Death. *Exp Cell Res* **263**, 88-97 (2001).
107. Breunig, H.G., Uchugonova, A., Batista, A. & Konig, K. Software-aided automatic laser optoporation and transfection of cells. *Sci Rep-Uk* **5** (2015).
108. Cappelleri, D.J. et al. Toward a Fully Automated High-Throughput Phototransfection System. *Jala-J Assoc Lab Aut* **15**, 329-341 (2010).
109. Marchington, R.F., Arita, Y., Tsampoula, X., Gunn-Moore, F.J. & Dholakia, K. Optical injection of mammalian cells using a microfluidic platform. *Biomed Opt Express* **1**, 527-536 (2010).
110. Heinemann, D. et al. Delivery of proteins to mammalian cells via gold nanoparticle mediated laser transfection. *Nanotechnology* **25** (2014).
111. Pitsillides, C.M., Joe, E.K., Wei, X.B., Anderson, R.R. & Lin, C.P. Selective cell targeting with light-absorbing microparticles and nanoparticles. *Biophys J* **84**, 4023-4032 (2003).
112. Hatef, A. & Meunier, M. Plasma-mediated photothermal effects in ultrafast laser irradiation of gold nanoparticle dimers in water. *Opt Express* **23**, 1967-1980 (2015).
113. Hatef, A., Fortin-Deschenes, S., Boulais, E., Lesage, F. & Meunier, M. Photothermal response of hollow gold nanoshell to laser irradiation: Continuous wave, short and ultrashort pulse. *Int J Heat Mass Tran* **89**, 866-871 (2015).
114. Bayazitoglu, Y., Kheradmand, S. & Tullius, T.K. An overview of nanoparticle assisted laser therapy. *Int J Heat Mass Tran* **67**, 469-486 (2013).
115. Pustovalov, V.K., Smetannikov, A.S. & Zharov, V.P. Photothermal and accompanied phenomena of selective nanophotothermolysis with gold nanoparticles and laser pulses. *Laser Physics Letters* **5**, 775-792 (2008).
116. Ghosh, S.K. & Pal, T. Interparticle coupling effect on the surface plasmon resonance of gold nanoparticles: From theory to applications. *Chemical Reviews* **107**, 4797-4862 (2007).
117. Boulais, E., Lachaine, R., Hatef, A. & Meunier, M. Plasmonics for pulsed-laser cell nanosurgery: Fundamentals and applications. *J Photoch Photobio C* **17**, 26-49 (2013).
118. Link, S. & El-Sayed, M.A. Spectral properties and relaxation dynamics of surface plasmon electronic oscillations in gold and silver nanodots and nanorods. *J Phys Chem B* **103**, 8410-8426 (1999).
119. Sun, C.K., Vallee, F., Acioli, L.H., Ippen, E.P. & Fujimoto, J.G. Femtosecond-Tunable Measurement of Electron Thermalization in Gold. *Phys Rev B* **50**, 15337-15348 (1994).

120. Khlebtsov, N.G. & Dykman, L.A. Optical properties and biomedical applications of plasmonic nanoparticles. *J Quant Spectrosc Ra* **111**, 1-35 (2010).
121. Link, S. & El-Sayed, M.A. Shape and size dependence of radiative, non-radiative and photothermal properties of gold nanocrystals. *International Reviews in Physical Chemistry* **19**, 409-453 (2000).
122. Schoenlein, R.W., Lin, W.Z., Fujimoto, J.G. & Eesley, G.L. Femtosecond studies of nonequilibrium electronic processes in metals. *Phys Rev Lett* **58**, 1680-1683 (1987).
123. Boulais, E., Lachaine, R. & Meunier, M. Plasma Mediated off-Resonance Plasmonic Enhanced Ultrafast Laser-Induced Nanocavitation. *Nano Lett* **12**, 4763-4769 (2012).
124. Yashchenok, A. et al. Optical Heating and Temperature Determination of Core-Shell Gold Nanoparticles and Single-Walled Carbon Nanotube Microparticles. *Small* **11**, 1320-1327 (2015).
125. Urban, A.S. et al. Controlled Nanometric Phase Transitions of Phospholipid Membranes by Plasmonic Heating of Single Gold Nanoparticles. *Nano Lett* **9**, 2903-2908 (2009).
126. Plech, A., Ibrahimkutty, S., Issenmann, D., Kotaidis, V. & Siems, A. Ultrafast x-ray scattering on nanoparticle dynamics. *11th International Conference on Synchrotron Radiation Instrumentation (Sri 2012)* **425** (2013).
127. Lindenberg, A.M. et al. X-ray diffuse scattering measurements of nucleation dynamics at femtosecond resolution. *Phys Rev Lett* **100** (2008).
128. Merabia, S., Shenogin, S., Joly, L., Keblinski, P. & Barrat, J.L. Heat transfer from nanoparticles: A corresponding state analysis. *P Natl Acad Sci USA* **106**, 15113-15118 (2009).
129. Siems, A., Weber, S.A.L., Boneberg, J. & Plech, A. Thermodynamics of nanosecond nanobubble formation at laser-excited metal nanoparticles. *New J Phys* **13** (2011).
130. Xiong, R., Nikiforov, A.Y., Vanraes, P. & Leys, C. Characteristics of an underwater direct current discharge in bubbles and the temperature distribution in the bubbles. *Physics of Plasmas* **19**, 023501 (2012).
131. Lukianova-Hleb, E.Y., Mutonga, M.B.G. & Lapotko, D.O. Cell-Specific Multifunctional Processing of Heterogeneous Cell Systems in a Single Laser Pulse Treatment. *Acs Nano* **6**, 10973-10981 (2012).
132. Lukianova-Hleb, E.Y., Wagner, D.S., Brenner, M.K. & Lapotko, D.O. Cell-specific transmembrane injection of molecular cargo with gold nanoparticle-generated transient plasmonic nanobubbles. *Biomaterials* **33**, 5441-5450 (2012).
133. Lapotko, D. Optical excitation and detection of vapor bubbles around plasmonic nanoparticles. *Opt Express* **17**, 2538-2556 (2009).
134. Lachaine, R., Boulais, E. & Meunier, M. From Thermo- to Plasma-Mediated Ultrafast Laser-Induced Plasmonic Nanobubbles. *Acs Photonics* **1**, 331-336 (2014).
135. Baumgart, J. et al. Off-resonance plasmonic enhanced femtosecond laser optoporation and transfection of cancer cells. *Biomaterials* **33**, 2345-2350 (2012).
136. Kalies, S. et al. Plasmonic laser treatment for Morpholino oligomer delivery in antisense applications. *J Biophotonics* **7**, 825-833 (2014).
137. Krpetic, Z. et al. Inflicting Controlled Nonthermal Damage to Subcellular Structures by Laser-Activated Gold Nanoparticles. *Nano Lett* **10**, 4549-4554 (2010).
138. Kalies, S. et al. Enhancement of extracellular molecule uptake in plasmonic laser perforation. *J Biophotonics* **7**, 474-482 (2014).
139. Chen, H.X., McGrath, T. & Diebold, G.J. Laser chemistry in suspensions: New products and unique reaction conditions for the carbon-steam reaction. *Angew Chem Int Edit* **36**, 163-166 (1997).
140. Chen, H. & Diebold, G. Chemical Generation of Acoustic Waves: A Giant Photoacoustic Effect. *Science* **270**, 963-966 (1995).
141. Löwen, H. & Madden, P.A. A microscopic mechanism for shock ‐ wave generation in pulsed ‐ laser ‐ heated colloidal suspensions. *The Journal of Chemical Physics* **97**, 8760-8766 (1992).
142. Tian, B., Wang, C., Zhang, S., Feng, L.Z. & Liu, Z. Photothermally Enhanced Photodynamic Therapy Delivered by Nano-Graphene Oxide. *Acs Nano* **5**, 7000-7009 (2011).

143. Yoo, J.M., Kang, J.H. & Hong, B.H. Graphene-based nanomaterials for versatile imaging studies. *Chem Soc Rev* **44**, 4835-4852 (2015).
144. Zhang, Z.J., Wang, J. & Chen, C.H. Near-Infrared Light-Mediated Nanoplatforms for Cancer Thermo-Chemotherapy and Optical Imaging. *Adv Mater* **25**, 3869-3880 (2013).
145. Smith, A.M., Mancini, M.C. & Nie, S.M. BIOIMAGING Second window for in vivo imaging. *Nat Nanotechnol* **4**, 710-711 (2009).
146. O'Connell, M.J. et al. Band gap fluorescence from individual single-walled carbon nanotubes. *Science* **297**, 593-596 (2002).
147. Link, S., Burda, C., Nikoobakht, B. & El-Sayed, M.A. Laser-induced shape changes of colloidal gold nanorods using femtosecond and nanosecond laser pulses. *J Phys Chem B* **104**, 6152-6163 (2000).
148. Sun, X. et al. Investigation of an optical limiting mechanism in multiwalled carbon nanotubes. *Appl Optics* **39**, 1998-2001 (2000).
149. Urban, A.S., Pfeiffer, T., Fedoruk, M., Lutich, A.A. & Feldmann, J. Single-Step Injection of Gold Nanoparticles through Phospholipid Membranes. *Acs Nano* **5**, 3585-3590 (2011).
150. Li, M., Lohmuller, T. & Feldmann, J. Optical Injection of Gold Nanoparticles into Living Cells. *Nano Lett* **15**, 770-775 (2015).
151. Wu, T.H., Kalim, S., Callahan, C., Teitell, M.A. & Chiou, P.Y. Image patterned molecular delivery into live cells using gold particle coated substrates. *Opt Express* **18**, 938-946 (2010).
152. Messina, G.C. et al. Spatially, Temporally, and Quantitatively Controlled Delivery of Broad Range of Molecules into Selected Cells through Plasmonic Nanotubes. *Adv Mater* **27**, 7145-+ (2015).
153. Andrews, N.W., Almeida, P.E. & Corrotte, M. Damage control: cellular mechanisms of plasma membrane repair. *Trends Cell Biol* **24**, 734-742 (2014).
154. Defour, A., Sreetama, S.C. & Jaiswal, J.K. Imaging Cell Membrane Injury and Subcellular Processes Involved in Repair. *Jove-J Vis Exp* (2014).
155. Yamane, D. et al. Electrical Impedance Monitoring of Photothermal Porated Mammalian Cells. *Jala-J Assoc Lab Aut* **19**, 50-59 (2014).
156. Palankar, R. et al. Nanoplasmonically-Induced Defects in Lipid Membrane Monitored by Ion Current: Transient Nanopores versus Membrane Rupture. *Nano Lett* **14**, 4273-4279 (2014).
157. Tsukakoshi, M., Kurata, S., Nomiya, Y., Ikawa, Y. & Kasuya, T. A Novel Method of DNA Transfection by Laser Microbeam Cell Surgery. *Appl Phys B-Photo* **35**, 135-140 (1984).
158. Dhakal, K., Batabyal, S., Wright, W., Kim, Y.T. & Mohanty, S. Optical delivery of multiple opsin-encoding genes leads to targeted expression and white-light activation. *Light-Sci Appl* **4** (2015).
159. Dhakal, K., Black, B. & Mohanty, S. Introduction of impermeable actin-staining molecules to mammalian cells by optoporation. *Sci Rep-Uk* **4** (2014).
160. Lukianova-Hleb, E.Y., Ren, X.Y., Zasadzinski, J.A., Wu, X.W. & Lapotko, D.O. Plasmonic Nanobubbles Enhance Efficacy and Selectivity of Chemotherapy Against Drug-Resistant Cancer Cells. *Adv Mater* **24**, 3831-3837 (2012).
161. Lukianova-Hleb, E.Y. et al. On-demand intracellular amplification of chemoradiation with cancer-specific plasmonic nanobubbles. *Nat Med* **20**, 778-784 (2014).
162. Lukianova-Hleb, E.Y. et al. Intraoperative diagnostics and elimination of residual microtumours with plasmonic nanobubbles. *Nat Nanotechnol* **11**, 525-+ (2016).
163. Shibata, A., Yada, S. & Terakawa, M. Biodegradability of poly(lactic-co-glycolic acid) after femtosecond laser irradiation. *Sci Rep-Uk* **6**, 27884 (2016).
164. Lukianova-Hleb, E.Y. & Lapotko, D.O. Malaria Theranostics using Hemozoin-Generated Vapor Nanobubbles. *Theranostics* **4**, 761-769 (2014).
165. Rendall, H.A. et al. High-throughput optical injection of mammalian cells using a Bessel light beam. *Lab Chip* **12**, 4816-4820 (2012).

Chapter 2

Comparison of gold nanoparticle mediated photoporation: vapor nanobubbles outperform direct heating for delivering macromolecules in live Cells

This chapter is published as:

Comparison of gold nanoparticle mediated photoporation: vapor nanobubbles outperform direct heating for delivering macromolecules in live Cells

Ranhua Xiong[1,2], Koen Raemdonck[1], Karen Peynshaert[1], Ine Lentacker[1], Ine De Cock[1], Jo Demeester[1], Stefaan C. De Smedt[1], Andre G. Skirtach[2,3,4], Kevin Braeckmans[1,2]. ACS Nano, 2014, DOI: 10.1021/nn5017742.

[1]Laboratory of General Biochemistry and Physical Pharmacy, Ghent University,
Harelbekestraat 72, 9000 Ghent, Belgium
[2]Centre for Nano- and Biophotonics, Harelbekestraat 72, 9000 Ghent, Belgium
[3]Department of Molecular Biotechnology, Ghent University, 9000 Ghent, Belgium
[4]Max-Planck Institute of Colloids and Interfaces, 14424 Potsdam, Germany

ABSTRACT

There is a great interest in delivering macromolecular agents into living cells for therapeutic purposes, such as siRNA for gene silencing. Although substantial effort has gone into designing nonviral nanocarriers for delivering macromolecules into cells, translocation of the therapeutic molecules from the endosomes after endocytosis into the cytoplasm remains a major bottleneck. Laser-induced photoporation, especially in combination with gold nanoparticles,is an alternative physical method that is receiving increasing attention for delivering macromolecules in cells. By allowing gold nanoparticles to bind to the cell membrane, nanosized membrane pores can be created upon pulsed laser illumination. Depending on the laser energy, pores are created through either direct heating of the AuNPs or by vapor nanobubbles (VNBs) that can emerge around the AuNPs. Macromolecules in the surrounding cell medium can then diffuse through the pores directly into the cytoplasm. Here we present a systematic evaluation of both photoporation mechanisms in terms of cytotoxicity, cell loading, and siRNA transfection efficiency. We find that the delivery of macromolecules under conditions of VNBs is much more efficient than direct photothermal disturbance of the plasma membrane without any noticeable cytotoxic effect. Interestingly, by tuning the laser energy, the pore size could be changed, allowing control of the amount and size of molecules that are delivered in the cytoplasm. As only a single nanosecond laser pulse is required, we conclude that VNBs are an interesting photoporation mechanism that may prove very useful for efficient high-throughput macromolecular delivery in live cells.

1. INTRODUCTION

For many therapeutic applications, macromolecules need to be delivered into living cells[1]. For example, to allow sequence-specific gene silencing on the post-transcriptional level, small interfering RNA (siRNA) needs to be delivered into the target cell's cytoplasm[2]. This is typically achieved by means of formulating the siRNA into non-viral lipid or polymer nanocarriers. As these are generally internalized by cells through endocytosis, escape from the endosome and subsequent siRNA release is needed. However, to date endosomal escape remains one of the major bottlenecks hampering safe and efficient delivery of therapeutic macromolecules into the cytosol[3, 4].

As an alternative strategy, physical approaches to permeate the cell membrane has attracted considerable interest, especially for *in vitro* applications. They typically offer generic applicability to a variety of cell types and grant macromolecular agents such as siRNA direct access into the cytoplasm[5-7]. A first example is microinjection, a conventional tool to directly inject compounds into single cells[8-10]. However, this technique can only be applied to a limited number of cells and typically requires a skilled person to perform. Electroporation is another common physical technique to deliver molecules into cells *in vitro* and *in vivo*. While it has shown to lead to good transfection efficiencies[11-15], the high electric field often results in low cell viability[16, 17]. More recent, sonoporation has been introduced as a method to permeabilize the plasma cell membrane by making use of ultrasound-responsive microbubbles. The acoustic response of the microbubbles can lead to the formation of micro-jets and shockwaves resulting in cell membrane poration[18, 19]. However, shear forces or elevated temperatures can lead to substantial cell damage and toxicity[20, 21].

Photoporation is an alternative physical approach that has received increasing attention in recent years. In its most straightforward form, cell membrane permeability is obtained by focusing high-intensity femtosecond laser pulses onto individual cells[22-28]. By attaching plasmonic nanoparticles, such as gold nanoparticles (AuNPs), to the cell membrane, the photoporation effect can be achieved at lower laser intensities. This means that throughput can be increased since non-focused laser light can be used to illuminate a large amount of cells[29-31]. This is thanks to the AuNP surface plasmon resonance (SPR), which depends on the size, shape and surface coating of the particles, tremendously enhances laser absorption[30, 32, 33], leading to distinct phenomena such as heating of the surrounding tissue, acoustic shockwaves, and formation of water vapor nanobubbles (VNBs)[30, 34]. Recently, it has been shown that both heating and VNBs can be used to permeate the plasma membrane and deliver cell impermeable compounds into the cytosol[35-37]. For heating of the plasma membrane, both continuous wave (CW) and low intensity pulsed laser light have been employed to heat membrane-adsorbed AuNPs, resulting in pore formation by a local phase transition of the lipid bilayer or by thermal denaturation of integral glycoproteins[35-38].

However, diffusion of heat throughout the cell can result in hyperthermia-induced cell stress, substantially decreasing cell viability[35, 37]. When using short laser pulses (< 10 ns) of sufficiently high intensity, the temperature of a AuNP can rapidly increase to several hundred degrees due to which the water surrounding the AuNP evaporates, resulting in a VNB that emerges around its surface[30, 39]. The size of a VNB can be tuned from ten to several hundreds of nanometers depending on the laser intensity[32, 40]. When the thermal energy of the AuNP is consumed, the VNB violently collapses and causes local damage by high-pressure shockwaves. Due to the extremely short lifetime of VNBs (<1 μs), the diffusion of heat from the AuNP into the environment is negligible so that almost all energy of the irradiated AuNP is converted to mechanical energy (expansion of the VNB) without heating of the environment. This property makes VNBs an interesting phenomenon to cause local mechanical damage, without causing thermal damage to the surrounding healthy tissue. It has been shown that VNBs can induce membrane pores through which compounds can diffuse into the cell[41, 42]. Thus, direct heating and VNB formation by laser irradiated AuNPs are two distinct photothermal effects that can be used to deliver cell impermeable compounds directly into the cytosol. However, to date it remains unclear which of both effects is preferred in terms of delivery efficiency and cytotoxicity. Neither has it been evaluated if VNB-induced membrane poration can be used to deliver siRNA into cells.

Here we report on a systematic comparison of AuNP-mediated photoporation for delivering macromolecules in cells by direct heating and VNB generation. Despite the fact that it requires higher laser energies, surprisingly we find that VNBs allow more efficient cellular uptake of compounds with little or no cytotoxicity as compared to direct heating. Furthermore, we successfully show that VNB photoporation can more efficiently transfect cells with small interfering RNA (siRNA) compared to direct heating, resulting in enhanced target gene silencing. Finally, we show that pores of different sizes can be created depending on the laser energy, thus enabling size-selective delivery of macromolecules in cells. Based on these results we envisage that VNB photoporation can offer unique opportunities for drug delivery in live cells.

2. MATERIALS AND METHODS

2.1 Materials

Cationic AuNPs with 70 nm were purchased from NanoPartz™ (#C2159, Nanopartz Inc., Loveland, USA). These AuNPs had a zeta potential of 30 mV as measured by dynamic light scattering (NanoSizer, Malvern, UK). FITC-dextrans with Mw of 10 kD and 500 kD were purchased from Sigma-Aldrich (Belgium). Calcein red-orange AM (#C34851,CellTrace™ Calcein Red-Orange) and Alexa Fluor 647 labeled dextran of 10 kD (#D-22914, Dextran, Alexa Fluor® 647) were obtained from Invitrogen™ (Belgium). Twenty-one nucleotide siRNA duplexes targeting the enhanced green fluorescent protein (siEGFP) and negative control duplexes (siCTRL) were purchased from Eurogentec (Seraing, Belgium). siEGFP: sense strand = 5′-CAAGCUGACCCUGAAGUUC**tt**-3′; antisense strand= 5′-GAACUUCAGGGUCAGCUUG**tt**-3′. siCTRL: sense strand = 5′-UGCGCUACGAUCGACGAUG**tt**-3′; antisense strand = 5′-CAUCGUCGAUCGUAGCGCA**tt**-3′ (lower case bold letters represent 2′-deoxyribonucleotides, capital letters are ribonucleotides). For fluorescence experiments, siCTRL duplex was labeled with a Cy®5 dye at the 5′ end of the sense strand (Eurogentec).

2.2 Cell Experiments

HeLa cells as a generally used cell model were employed in this study and H1299 cells stably expressing EGFP were used for siRNA knockdown experiment. Before laser treatment, HeLa cells (1×10^4 cells/well) were grown in cell medium of DMEM/F-12 with 2 mM glutamine, 10% heat-inactivated fetal bovine serum (FBS, Hyclone) and 100 U/mL penicillin/streptomycine, and H1299_EGFP cells (1×10^4 cells/well) were cultured in 96 wells (#92096,TPP®, Switzerland) at 37°C in RPMI 1640, supplemented with 2 mM glutamine, 10% heat-inactivated fetal bovine serum (FBS, Hyclone) and 100 U/mL penicillin/streptomycine at 37 °C in a humidified atmosphere containing 5% CO_2 for 24 hours before treatment. For laser treatment, the cells were incubated with AuNPs for 30 min at concentrations as indicated in the text. Following incubation with AuNPs, the cells were washed to remove any remaining free AuNPs in solution. Just prior to the laser scanning treatment, the solution of extracellular agents (dextrans or siRNA) was added to the cells. After the laser treatment, the cells were washed and supplied with fresh cell medium. CellTrace® calcein red-orange AM was added to the samples for 45 min incubation at room temperature to stain living cells for quantifying cell viability. The prepared cell samples were taken images by confocal microscope (C1-si, Nikon, Japan) for quantifying the molecular loading efficiency and cell viability. The samples were also prepared for the measurement of flow cytometer. The cells were washed with PBS, trypsinized (trypsin / EDTA 0.25 %) and diluted with complete cell culture medium. Following centrifugation (7 min, 300 g), the cell pellet was resuspended in flow buffer (PBS supplemented with 1% BSA and 0.1% sodium azide) and placed on ice until flow cytometric analysis. A minimum of 10^4 cells was analyzed in each measurement, using a BD Biosciences FACSCalibur™ flow cytometer.

2.3 Generation and Detection of AuNP Heating and VNB Formation

A homemade setup including optical system and electric timing system was used to generate and detect the AuNPs heating or VNBs. As shown in **Figure S2**, a pulsed laser with pulse duration of ~7 ns was tuned at wavelength of 561 nm (Opolette™ HE 355 LD, OPOTEK Inc., Faraday Ave, CA, USA) and used for illumination of AuNPs. The setup has two modes for detecting AuNP heating or VNB formation, respectively. The time-response mode is used for detecting both of AuNP heating and VNBs. It makes use of a photo detector (APD110A, Thorlabs) that monitors a change in transmitted light of a CW red laser (Spectra-Physics Excelsion-640, Santa Calara, CA, US) due to changes in refractive index upon heating.[43] VNBs on the other hand can be very well detected by dark-field microscopy as they efficiently scatter light. As VNBs typically have a very short lifetime (< 1 μs), depending on their size, we synchronized the camera (EMCCD camera, Cascade II: 512, Photometrics, Tucson, USA) with the pulsed laser by an electronic pulse generator (BNC575, Berkeley Nucleonics Corporation, CA, USA). The pulse laser sends a Q-switch signal to trigger pulse generator and it will trigger the camera at a setting delay.

For treating large areas of cells, such as an entire well of a 96 well-plate, an electronic microscope stage was used to scan the laser beam (20 Hz pulse frequency) line by line across the entire sample. The scanning speed was 2 mm/s and the distance between subsequent lines was 0.1 mm (diameter of laser beam). This way each location in the sample receives a single laser pulse, with a total treatment time of ~3.6 min per well. The laser pulse energy was monitored by an energy meter (J-25MB-HE&LE, Energy Max-USB/RS sensors, Coherent) synchronized with the pulsed laser. The intensity of exciting pulse laser was calculated the average pulse energy divided by the area of the laser beam. Individual pulsed were observed to deviate up to 10% from the average value.

2.4 Quantification of Cell Loading and Viability

After laser treatment, at least 5 confocal images were acquired with a confocal laser scanning microscope (C1si, Nikon, Japan). Using a 10× lens (CFI Plan Apochromat, Nikon, Badhoevedorp, The Netherlands), each image has a field of view of 1.35 mm by 1.35 mm with several hundreds to a thousand cells for each image. Each image consists of three channels, one for green fluorescence (505-550 nm), one for orange-red fluorescence (575-620 nm) and one for the transmission image. A Matlab (The matworks, Natick, MA, USA) program was written for automated quantification of cell loading and cell viability. First, the average intensity per cell was measured in both fluorescence channels. Green fluorescence resembles cell loading, and orange-red fluorescence is used for quantifying cell viability. Untreated cells are used to define the threshold for positive cell loading, where the threshold value is defined as the 95% level of untreated cells. Similarly, cells are considered as alive when the orange-red fluorescence intensity is higher than the 95% level of dead cells.

For calculating siRNA gene silencing efficiency, EGFP knockdown efficiency was quantified as the average fluorescence intensity of cells treated with anti-EGFP siRNA divided by the average intensity of cells treated with negative control siRNA under identical experimental conditions as flowing equation

$$Knockdown\ efficiency\ (\%) = 1 - \frac{MFI\ siEGFP}{MFI\ siCTRL} \times 100\%$$

with MFI siEGFP indicating the mean fluorescence intensity of cells incubated with anti-EGFP siRNA and MFI siCTRL indicating the mean fluorescence intensity of cells incubated with negative control siRNA. For flow cytometry, data analysis was performed by using the BD CellQuest Pro analysis software.

3. RESULTS AND DISCUSSION

3.1 Cell Adsorbed AuNPs Mediate Distinct Photothermal Effects as a Function of Laser Fluence.

The experimental procedure to load cells with cell impermeable molecules is shown in **Fig. 1**. First, AuNPs are adsorbed onto the cell's surface by which they can act as mediators of nanopore formation. In this study, positively charged AuNPs (70 nm) were used to facilitate interaction with the negatively charged cell membrane. Following incubation of HeLa cells with 3 different AuNP concentrations (4.1×10^7, 8.2×10^7 and 16.5×10^7 particles/ml) during half an hour at 37°C, the number of cell-attached AuNPs was quantified from confocal images in reflection mode. As shown in **Figure S1a-c**, more AuNPs adsorbed to the cells with increasing concentrations of AuNPs, ranging from 4 to approx. 15 particles per cell. In the second step of the procedure, the non-adherent AuNPs are removed and the cell impermeable molecules are added to the cells just prior to the laser treatment. A low laser energy will lead to heating of the cell membrane, while VNBs are formed at higher laser energies. The two effects can be monitored by detecting the transmitted intensity of a CW laser focused on the sample (**Figure S2**)[32]. Heating of a AuNP induces a local change in refractive index[43]. This 'thermolensing' effect can cause a refocusing of the CW laser on the pinhole in front of the detector (as shown in **Figure S2**), resulting in an increase of the detected transmitted CW laser light. A laser pulse with energy below the VNB threshold will cause heating of the AuNP, after which this heat diffuses into the environment. The corresponding intensity profile of the transmitted laser light is shown in **Figure S3a**. The long tail is indicative of heat diffusion and heating of the environment. At a pulse energy above the VNB threshold, VNBs are created with a size and lifetime that is proportional to the laser energy (**Figure S3b** and **S3c**). The absence of a heat diffusion tail at high pulse energies clearly demonstrates that VNB generation does not cause heat transfer to the environment. Alternatively, VNBs can be detected by dark field microscopy, as demonstrated in **Figure S3d-f**[44]. From these experiments we can conclude that VNBs could be clearly generated at a laser fluence of 1.02 J/cm^2 , while 0.38 J/cm^2 only resulted in heating of the surrounding medium. This result is in agreement with the threshold of VNB generation as reported before under similar conditions[32]. It is of note that the medium surrounding the AuNPs can affect the threshold for the generation of gas bubbles[45].

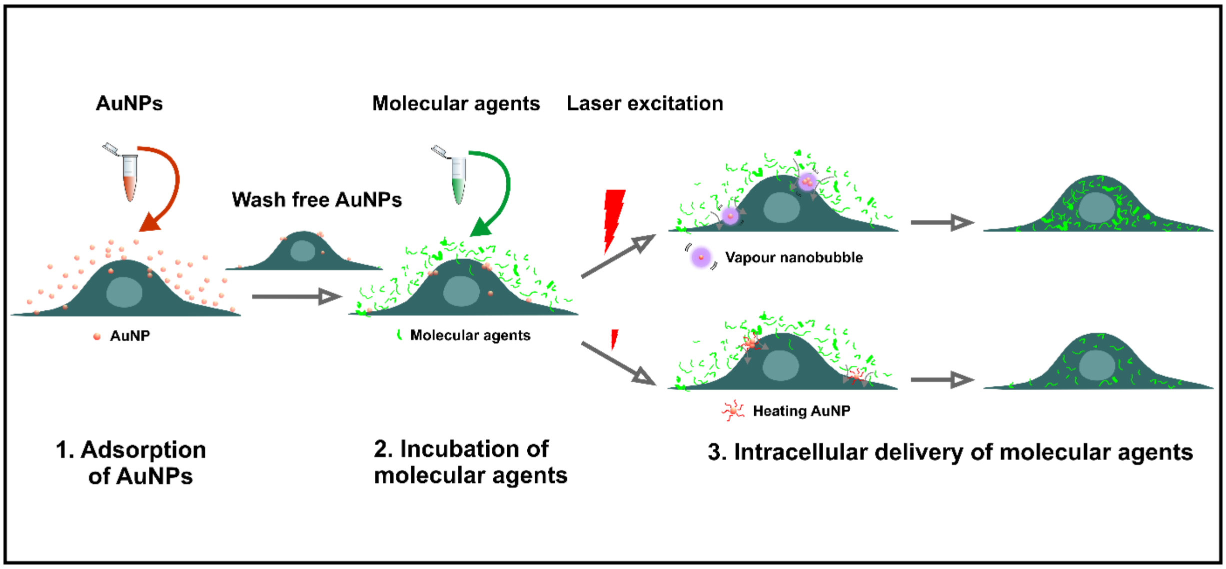

Figure 1. Schematic overview of the experimental procedure. 1. Cells are incubated with AuNPs that are adsorbed to the cell membrane; 2. The non-adherent AuNPs are removed in a washing step, after which the solution of molecular agents is added to the cells just prior to the laser treatment; 3. Laser treatment causes pore formation either by VNBs that mechanically puncture the cell membrane (high laser energy) or by heating of the cell membrane (low laser energy). The extracellular molecules are finally expected to diffuse into the cells via the created pores.

3.2 Intracellular Delivery of Macromolecules and Cell Viability *via* Local Heating or VNB Generation.

FITC-dextran with a molecular weight of 10 kDa (FD10) was used as a model macromolecule to compare cell loading by direct heating or VNB generation. We use the term 'cell loading' to signify delivery of macromolecules into cells across the plasma membrane by VNB-induced membrane pores. For an AuNP concentration of 8.2×10^7 particles/ml (*i.e.* approx. 8 AuNPs per cell; **Figure S1d**), two different laser fluence levels were tested, *i.e.* one below (0.38 J/cm^2) and one above the VNB threshold (2.04 J/cm^2). All cells in a well of a 96-well titer plate were treated with a single laser pulse of the indicated energy. After laser treatment the cells were washed immediately to remove the remaining extracellular FITC-dextran and fresh cell medium was added to avoid the endositosis of FITC-dextran. Just as for other poration techniques (microinjection, electroporation, sonoporation, direct photoporation) the pores generated by the bubbles are also quickly repaired in a few tens of seconds as shown in very recently studied for vapor bubble mediated poration[46]. Calcein red- orange AM was added to the cells to quantify cell viability. The images presented in **Fig. 2** clearly show that FITC-dextran loading was much more efficient when mediated by VNBs than by direct heating of the plasma membrane. Interestingly, neither of both procedures caused any noticeable cytotoxicity. Next, cell loading with FITC-dextran and cell viability were systematically evaluated for different laser intensities (**Fig. 3**). No appreciable cell loading occurred by AuNP or laser treatment alone. Instead, approximately 40% of the treated cells were loaded with FITC-dextran at a laser fluence of 0.38 J/cm^2. Increasing the laser fluence levels above the VNB threshold resulted in more positive cells and a much higher loading efficiency as can be seen from the higher FITC-dextran signal per cell. At 2.04 J/cm^2 an optimum was found with >85% positive cells and a loading efficiency that is ~6 times higher than by AuNP heating at 0.38 J/cm^2. More levels of low laser fluence heating AuNP show no significant improvement of loading efficiency (**Figure S4**). There was no noticeable decrease in cell viability up to 2.04 J/cm^2. Further increasing the laser fluence to 4.08 J/cm^2 reduced the number of positive cells, likely due to the onset of cytotoxic effects as the VNBs are becoming rather large and damage the cells[39]. When increasing the AuNP concentration to 16.5×10^7 particles/ml a similar trend was found, although here the percentage of positive and viable cells already decreased ~1.5 times at a laser fluence of 2.04 J/cm^2 (**Figure S5**). This shows that photoporation by VNBs also requires careful optimization of the concentration of AuNPs used. Based on these results, we decided to continue with 8.2×10^7 particles/ml, corresponding to approx. 8 AuNPs per cell. These results obtained from confocal microscopy could be confirmed by flow cytometry analysis in a set of independent experiments (**Figure S6**). At 0.38 J/cm^2 ~50% of positive cells were found, while this increased to ~90% at 2.04 J/cm^2. The average intensity per cell again increased by a factor of ~6, while no signs of cytotoxicity could be found.

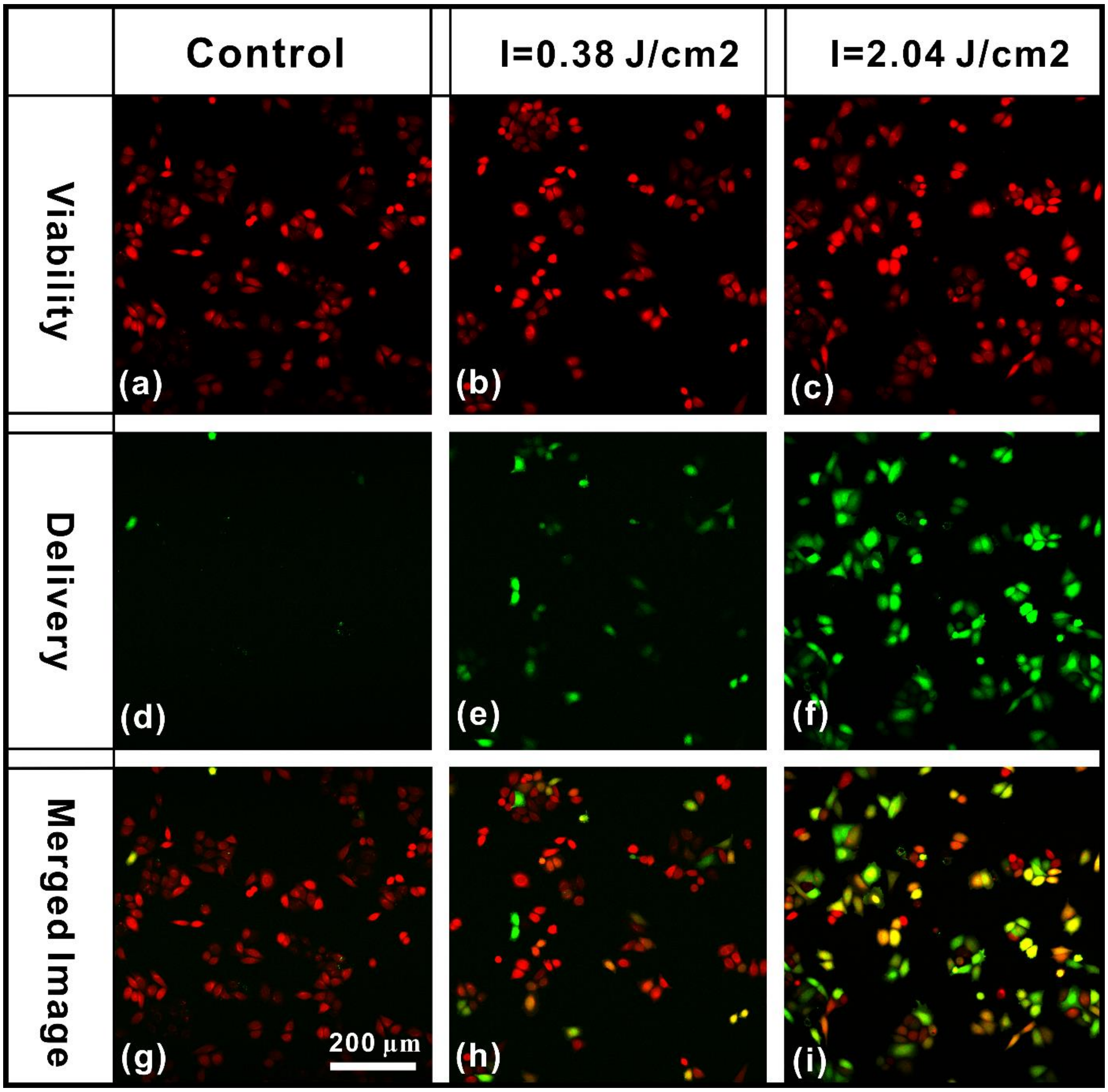

Figure 2. Confocal images showing the viability of HeLa cells labeled with calcein red-orange AM (a-c) and the intracellular delivery of FITC-dextran 10 kDa after laser treatment (d-f). The bottom row shows an overlay of both colors (g-i). At a laser fluence of 2.04 J/cm^2, VNBs are induced that perforate the cell membrane and allow more efficient uptake of FITC-dextran as compared to a low laser fluence (0.38 J/cm^2) that causes heating of the AuNPs and the plasma membrane.

To further evaluate the effect of the number of laser pulses on the delivery efficiency, the cells were scanned multiple times with pulsed laser illumination. As shown in **Fig. 4**, no significant improvement of the loading efficiency was obtained both for direct heating and VNBs. This could be caused by melting of AuNPs and breaking up into smaller fragments[47]. Fragmentation of AuNPs has been reported at a laser fluence as low as 0.08 J/cm^2 for 40 nm particles[48-50]. Based on these results, we will perform further comparisons with single laser pulse treatment only.

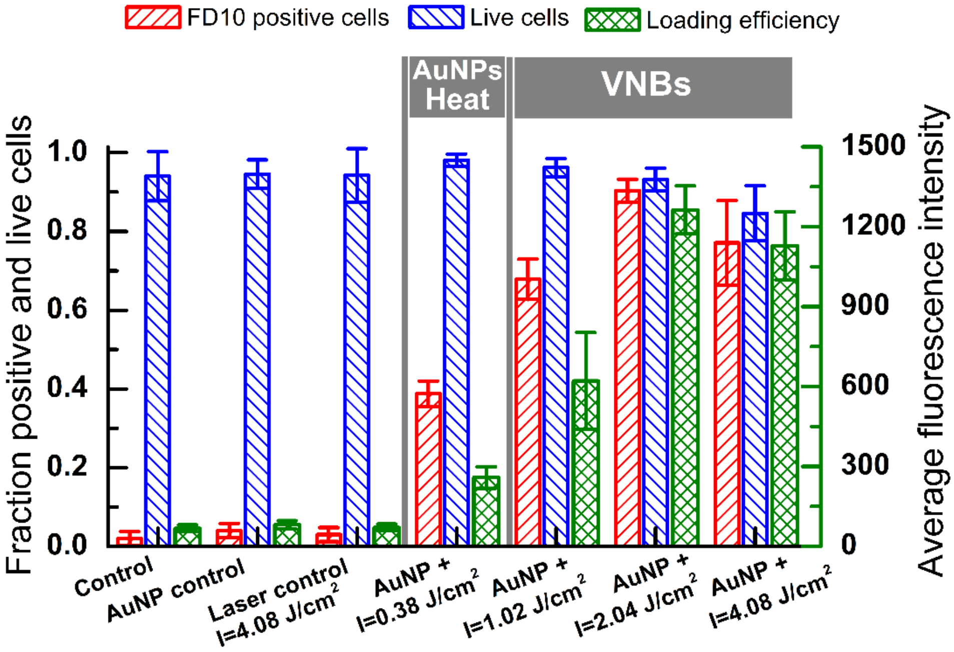

Figure 3. Cell viability and delivery efficiency of FITC-dextran 10 kDa (FD10) as quantified by imaging processing of confocal images. HeLa cells were incubated with 70 nm cationic AuNPs at a concentration of 8.25×10^7 particles/ml corresponding to approx. 8 AuNPs per cell. The laser fluence was adjusted to compare heating of the plasma membrane (0.38 J/cm^2) with pore formation by VNBs (1.02, 2.04 and 4.08 J/cm^2). Red bars are the fraction of FD10 positive cells, blue bars are the fraction of live cells and olive bars are the average fluorescence intensity. The average FD10 fluorescence per cell is a measure for the loading efficiency. The data shown are the result from 3 independent experiments.

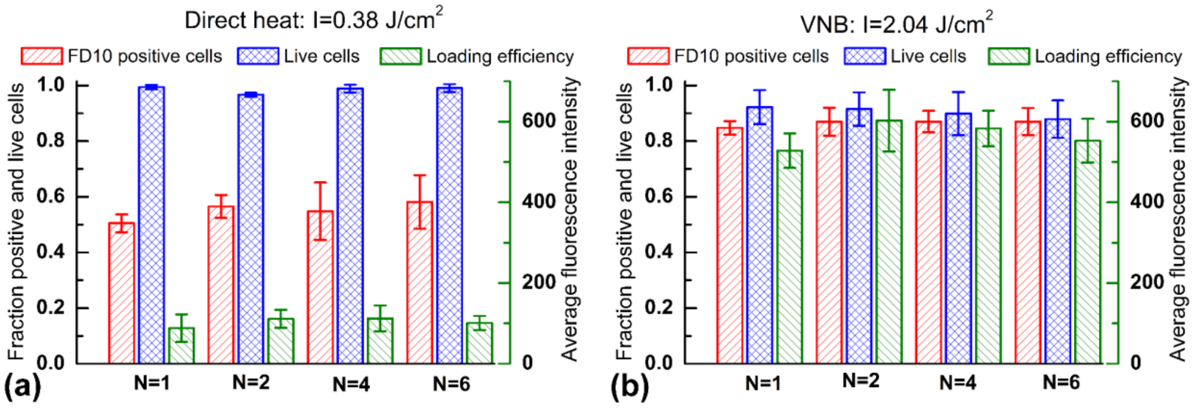

Figure 4. Positive cells, cell viability and loading of FD10 using 8.25×10^7 AuNP/ml in function of the number of laser pulses (N). Different laser fluences are compared: (a) 0.38 J/cm^2 (below the VNB threshold) and (b) 2.04 J/cm^2 (above the VNB threshold). No increase in loading efficiency is found by increasing the number of laser pulses for either of both conditions.

3.3 Evaluation of Intracellular siRNA Delivery and Gene Silencing *via* Local Heating and VNB Generation.

Next to the delivery of FITC-dextran as a model macromolecule, the applicability of photoporation for delivering macromolecular therapeutic agents, such as small interfering RNA (siRNA), was assessed. Recently, siRNA was shown to be delivered into cells using AuNPs and photoporation by direct heating of the plasma membrane[37]. Considering our finding that VNBs are more efficient for loading cells with FITC-dextrans, we continued our comparative study toward siRNA gene silencing.

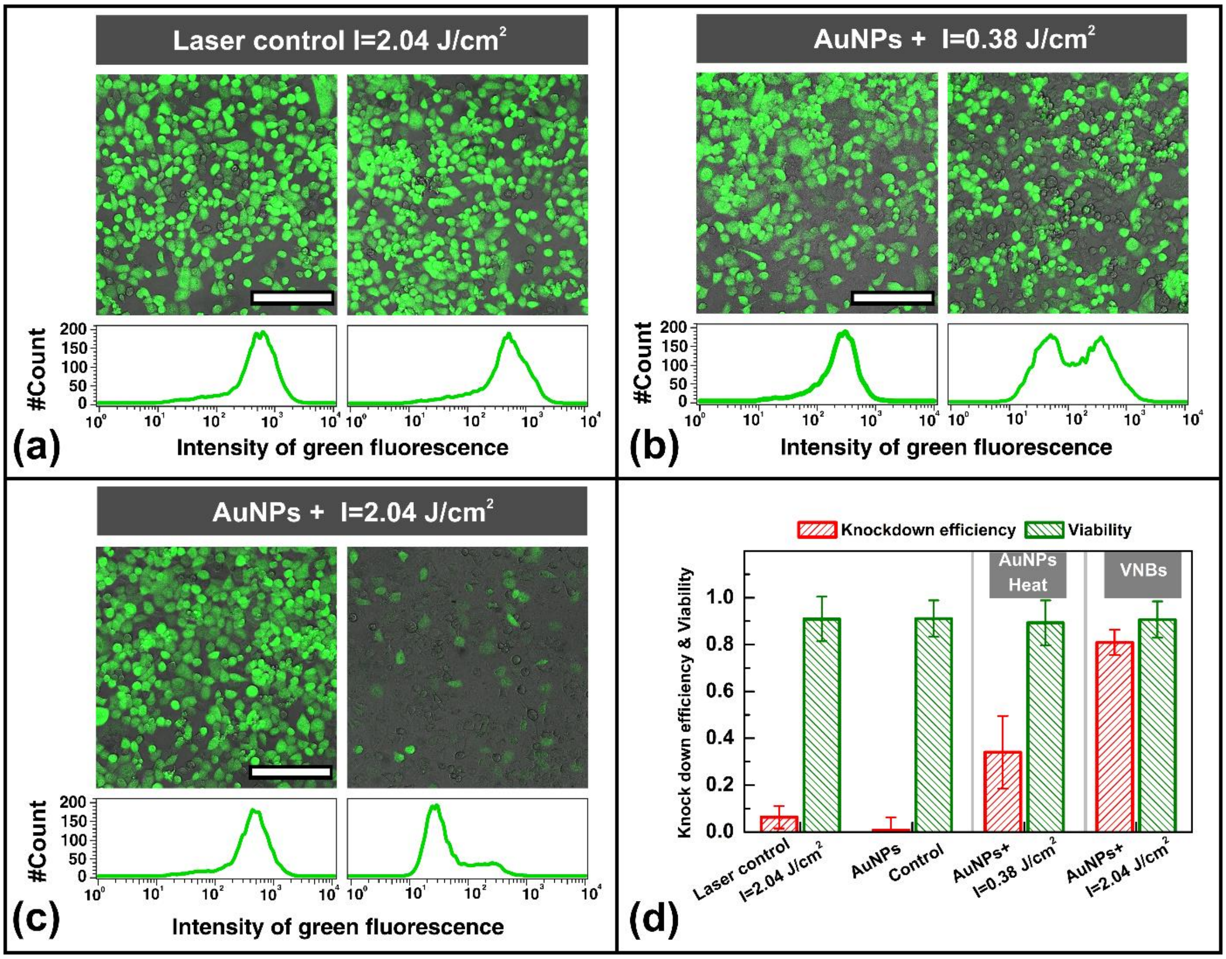

Figure 5. Photoporation of H1299 EGFP cells with varying laser intensity for siRNA gene silencing. Following the adsorption of AuNPs (positively charged, 70 nm, 8.25X10^7 particles/ml) to the cell surface, photoporation was initiated in the presence of siRNA. Twenty-four hours after treatment, the cellular EGFP expression was visualized by confocal microscopy and quantified with flow cytometry. The left and right microscopy images in (a-c) represent cells that are incubated with negative control siRNA and anti-EGFP siRNA, respectively, at a laser fluence of 2.04 J/cm^2 without incubation of AuNPs (a) and 0.38 J/cm^2 (b) and 2.04 J/cm^2 (c) with incubation of AuNPs. The corresponding flow cytometry histograms in (a-c) show the distributions of the cells' EGFP fluorescence. The cell viability and knockdown efficiency are quantified by flow cytometry (n=3) (d). The scale bars shown in (a-c) correspond to 200 µm.

First, loading of HeLa cells with Alexa Fluor 488 (AF488)-labeled siRNA was evaluated by adding it to the cell medium prior to laser treatment. In analogy with previous experiments, the cells were incubated with a AuNP concentration of 8.25×10^7 particles/ml (*i.e.* ~8 particles per cell). As shown in **Figure S7**, similar to our findings for FITC-dextran, direct heating of the plasma membrane (0.38 J/cm^2) is less efficient in delivering siRNA to the cytosol than pore formation by VNBs (2.04 J/cm^2). Cell viability and cellular delivery were again quantified by imaging processing (**Figure S8**). More than 90% of the cells were loaded with a detectable amount of siRNA with no signs of cytotoxicity at a laser fluence of 2.04 J/cm^2. Although heating of the plasma membrane also didn’t cause any cytotoxicity, the percentage of siRNA containing cells was much less (~40%). Furthermore, the average fluorescence per cell was 4-fold higher in case of VNB pore formation as compared to direct heating.

In a next step the knockdown efficiency of anti-EGFP siRNA delivered *via* the photoporation approach was evaluated in a human non-small cell lung carcinoma cell line (H1299) that stably expresses EGFP. The knockdown efficiency and cell viability were measured by both confocal microscopy and flow cytometry. As shown in **Fig. 5a-c**, the knockdown efficiency was about ~40% for direct heating of the plasma membrane (0.38 J/cm^2) as compared to >80% for VNB induced pore formation (2.04 J/cm^2). No significant knockdown was observed in case the cells received exactly the same treatment (2.04 J/cm^2) but without AuNPs or when the same protocol was performed (~8 AuNPs per cell) but without laser exposure. Quantification of cell viability did not reveal any signs of cytotoxicity for any of the experiments. Taken together, it can be concluded that VNB-induced pore formation allows much more efficient cellular uptake of siRNA and target gene silencing as compared to cellular delivery *via* heating of the plasma membrane.

3.4 Tuning the Incident Laser Fluence Allows Size-Selective Intracellular Delivery.

As demonstrated before, the size of a VNB is governed by the intensity of the incident laser beam.[32] Here we evaluated the hypothesis that the cell membrane pore size is thus also proportional to the incident laser fluence, meaning that large molecules can only be delivered *via* the pores formed by VNBs with a high intensity laser light, while smaller molecules can be delivered already at lower intensities such as for direct heating. To investigate this, immediately prior to the laser treatment, a mixture of two fluorescent dextrans of different molecular weight was added to HeLa cells, being red fluorescent 10 kD Alexa-red dextran (RD10) and green fluorescent 500 kD FITC-dextran (FD500). The cells were treated either with a laser fluence of 0.38 J/cm^2 or 2.04 J/cm^2, after which the cells were washed and supplied with fresh cell medium. As can be seen from the confocal images in **Fig. 6a-c**, at the lowest laser fluence the red fluorescent dextrans with low molecular weight could enter the cells quite efficiently. On the other hand, only a few cells had taken up the larger green fluorescent dextrans. At the highest laser fluence, clearly both small and large dextrans were delivered into the cells. By image analysis it was quantified that ~50 % of treated cells were found to have taken up 10 kDa dextran at the lowest laser fluence, while this increased to ~90% at the highest laser fluence. However, for the larger 500 kDa dextrans less than 10% of the cells showed detectable uptake, which increased to >80% for the highest laser fluence. The average green fluorescence per cell for FD500 was only ~2 fold more than the control sample in case of the lowest laser fluence, which increased to more than 10 fold at the highest laser fluence. Although more work is needed to investigate this relationship in more detail, these experiments show that the pore size can be easily changed by tuning the laser energy of the photoporation procedure.

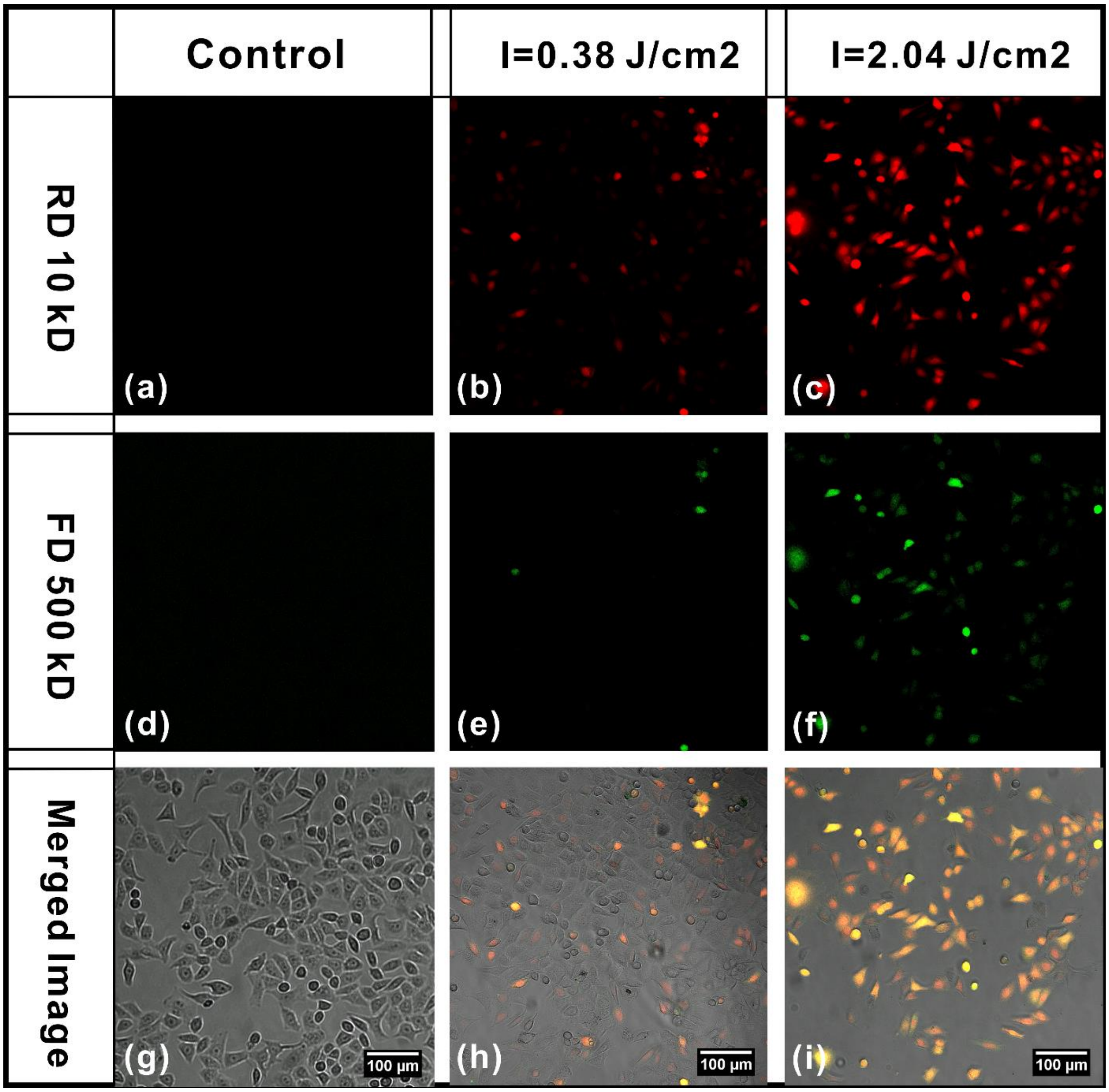

Figure 6. Size-selective delivery of fluorescently-labeled dextrans is demonstrated in HeLa cells. Cells are supplied with a mixture of red fluorescent Tex-dextran of 10 kDa (RD10) and green fluorescent FITC-dextran of 500 kDa (FD500). (a-c) Confocal images showing the delivery of RD10 in HeLa cells that received laser treatment of 0.38 J/cm2 or 2.04 J/cm2. (d-f) Confocal images showing the delivery of FD500. (g-i) Merged confocal images of green and red fluorescence with transmission images.

4. CONCLUSIONS

It was demonstrated that delivering macromolecules across the plasma membrane in cells is more efficient when pores are created by VNBs rather than by direct heating. This is likely caused by a larger pore size in case of VNBs due to which more molecules can diffuse into the cell. When delivering siRNA, this might result in more efficient gene knockdown as well. Despite the fact that VNB generation requires a higher laser energy, it did not result in increased toxicity. This is likely due to the fact that VNB generation is an almost purely mechanical effect that does not lead to heat diffusion into the surrounding tissue. Interestingly, by tuning the laser energy and hence the size of the VNBs, it is possible to tune the size of the pores that are created. This in turn allows to control the amount of molecules that are delivered into the cytosol, as well as the maximum size of molecules that are allowed to pass through. Combined with the general applicability of the approach and the fact that this procedure can be applied to large cell numbers by scanning of the laser beam, we are convinced that VNB photoporation is a promising alternative physical technique to efficiently deliver compounds into cells with little or no toxicity. In future research it will be of interest to further investigate the influence of AuNP size and cell type on pore size and drug delivery efficiency.

Acknowledgements

Financial support by the Ghent University Special Research Fund (Centre for Nano- and Biophotonics) is acknowledged with gratitude. R. Xiong gratefully acknowledges the financial support from China Scholarship Council (CSC). K. Raemdonck and I. Lentacker are postdoctoral fellows of the Research Foundation-Flanders (FWO-Vlaanderen).

5. REFERENCES

1. Mann, S. Life as a nanoscale phenomenon. *Angew Chem Int Edit* **47**, 5306-5320 (2008).
2. Davidson, B. L.; McCray, P. B., Jr. Current prospects for rna interference-based therapies. *Nat Rev Gene* **12**, 329-40 (2011).
3. Varkouhi, A. K.; Scholte, M.; Storm, G.; Haisma, H. J. Endosomal escape pathways for delivery of biologicals. *J Control Release* **151**, 220-228 (2011).
4. Raemdonck, K.; Naeye, B.; Hogset, A.; Demeester, J.; De Smedt, S. C. Prolonged gene silencing by combining sirna nanogels and photochemical internalization. *J Control Release* **145**, 281-8 (2010).
5. Prentice, P.; Cuschierp, A.; Dholakia, K.; Prausnitz, M.; Campbell, P. Membrane disruption by optically controlled microbubble cavitation. *Nat Phys* **1**, 107-110 (2005).
6. Mehier-Humbert, S.; Guy, R. H. Physical methods for gene transfer: improving the kinetics of gene delivery into cells. *Adv Drug Deliver Rev* **57**, 733-753 (2005).
7. Lai, B. H.; Chen, D. H. Lab6 nanoparticles with carbon-doped silica coating for fluorescence imaging and near-ir photothermal therapy of cancer cells. *Acta Biomater* **9**, 7556-63 (2013).
8. Auerbach, A. B. Production of functional transgenic mice by dna pronuclear microinjection. *Acta Biochim Pol* **51**, 9-31 (2004).
9. Gordon, J. W.; Scangos, G. A.; Plotkin, D. J.; Barbosa, J. A.; Ruddle, F. H. Genetic-transformation of mouse embryos by micro-injection of purified dna. *P Natl Acad Sci-Biol* **77**, 7380-7384 (1980).
10. Capecchi, M. R. High-efficiency transformation by direct micro-injection of dna into cultured mammalian-cells. *Cell* **22**, 479-488 (1980).
11. Murphy, R. C.; Messer, A. Gene transfer methods for cns organotypic cultures: a comparison three nonviral methods. *Mol Ther* **3**, 113-121 (2001).
12. Canatella, P. J.; Prausnitz, M. R. Prediction and optimization of gene transfection and drug delivery by electroporation. *Gene Ther* **8**, 1464-1469 (2001).
13. Goto, T.; Nishi, T.; Tamura, T.; Dev, S. B.; Takeshima, H.; Kochi, M.; Yoshizato, K.; Kuratsu, J.; Sakata, T.; Hofmann, G. A.; et al. Highly efficient electro-gene therapy of solid tumor by using an expression plasmid for the herpes simplex virus thymidine kinase gene. *P Natl Acad Sci USA* **97**, 354-359 (2000).
14. Mir, L. M.; Bureau, M. F.; Gehl, J.; Rangara, R.; Rouy, D.; Caillaud, J. M.; Delaere, P.; Branellec, D.; Schwartz, B.; Scherman, D. High-efficiency gene transfer into skeletal muscle mediated by electric pulses. *P Natl Acad Sci USA* **96**, 4262-4267 (1999).
15. Muramatsu, T.; Mizutani, Y.; Ohmori, Y.; Okumura, J. Comparison of three nonviral transfection methods for foreign gene expression in early chicken embryos in ovo. *Biochem Bioph Res Co* **230**, 376-380 (1997).
16. Yi, J.; Barrow, A. J.; Yu, N.; O'Neill, B. E. Efficient electroporation of liposomes doped with pore stabilizing nisin. *J Liposome Res* **23**, 197-202 (2013).
17. Rubinsky, B. Irreversible electroporation in medicine. *Tech Canc Res Treat* **6**, 255-60 (2007).
18. Lentacker, I.; De Cock, I.; Deckers, R. ; De Smedt, S.C.; Moonen, C.T.W. Understanding ultrasound induced sonoporation: definitions and underlying mechanisms. *Adv Drug Deliver Rev* **72**, 49-64 (2013).
19. Lentacker, I.; De Smedt, S. C.; Sanders, N. N. Drug loaded microbubble design for ultrasound triggered delivery. *Soft Matter* **5**, 2161-2170 (2009).
20. Lakshmanan, S.; Gupta, G. K.; Avci, P.; Chandran, R.; Sadasivam, M.; Jorge, A. E.; Hamblin, M. R. Physical energy for drug delivery; poration, concentration and activation. *Adv Drug Deliv Rev* **71**, 98-114 (2013).
21. Park, D.; Ryu, H.; Kim, H. S.; Kim, Y. S.; Choi, K. S.; Park, H.; Seo, J. Sonophoresis using ultrasound contrast agents for transdermal drug delivery: an in vivo experimental study. *Ultrasound Med Biol* **38**, 642-50 (2012).
22. Wu, T. H.; Chen, Y.; Park, S. Y.; Hong, J.; Teslaa, T.; Zhong, J. F.; Di Carlo, D.; Teitell, M. A.; Chiou, P. Y. Pulsed laser triggered high speed microfluidic fluorescence activated cell sorter. *Lab Chip* **12**, 1378-1383 (2012).

23. Sibbett, W.; Lagatsky, A. A.; Brown, C. T. A. The development and application of femtosecond laser systems. *Opt Express* **20**, 6989-7001 (2012).
24. Baumgart, J.; Humbert, L.; Boulais, E.; Lachaine, R.; Lebrun, J. J.; Meunier, M. Off-resonance plasmonic enhanced femtosecond laser optoporation and transfection of cancer cells. Biomaterials **33**, 2345-2350 (2012).
25. Stevenson, D. J.; Gunn-Moore, F. J.; Campbell, P.; Dholakia, K. Single cell optical transfection. *J R Soc Interface* **7**, 863-871 (2010).
26. Chakravarty, P.; Qian, W.; El-Sayed, M. A.; Prausnitz, M. R. Delivery of molecules into cells using carbon nanoparticles activated by femtosecond laser pulses. *Nat Nanotechnol* **5**, 607-611 (2010).
27. Jain, T.; Muthuswamy, J. Bio-chip for spatially controlled transfection of nucleic acid payloads into cells in a culture. *Lab Chip* **7**, 1004-1011 (2007).
28. Tirlapur, U. K.; Konig, K. Cell biology - targeted transfection by femtosecond laser. *Nature* **418**, 290-291 (2002).
29. Sapsford, K. E.; Algar, W. R.; Berti, L.; Gemmill, K. B.; Casey, B. J.; Oh, E.; Stewart, M. H.; Medintz, I. L. Functionalizing nanoparticles with biological molecules: developing chemistries that facilitate nanotechnology. *Chem Rev* **113**, 1904-2074 (2013).
30. Qin, Z. P.; Bischof, J. C. Thermophysical and biological responses of gold nanoparticle laser heating. *Chem Soc Rev* **41**, 1191-1217 (2012).
31. Zijlstra, P.; Orrit, M. Single metal nanoparticles: optical detection, spectroscopy and applications. *Rep Prog Phys* **74**, 106401 (2011).
32. Lapotko, D. Optical excitation and detection of vapor bubbles around plasmonic nanoparticles. *Opt Express* **17**, 2538-2556 (2009).
33. Ghosh, S. K.; Pal, T. Interparticle coupling effect on the surface plasmon resonance of gold nanoparticles: from theory to applications. *Chem Rev* **107**, 4797-4862 (2007).
34. Skirtach, A. G.; Dejugnat, C.; Braun, D.; Susha, A. S.; Rogach, A. L.; Parak, W. J.; Mohwald, H.; Sukhorukov, G. B. The role of metal nanoparticles in remote release of encapsulated materials. *Nano Lett* **5**, 1371-1377 (2005).
35. Sun, X. H.; Zhang, G. D.; Keynton, R. S.; O'Toole, M. G.; Patel, D.; Gobin, A. M. Enhanced drug delivery via hyperthermal membrane disruption using targeted gold nanoparticles with pegylated protein-g as a cofactor. *Nanomed Nanotech Biol Med* **9**, 1214-1222 (2013).
36. Kalies, S.; Heinemann, D.; Schomaker, M.; Birr, T.; Ripken, T.; Meyer, H. Gold nanoparticle mediated laser transfection for high-throughput antisense applications. *Medical Laser Applications And Laser-Tissue Interactions Vi* **8803**,1-5 (2013).
37. Heinemann, D.; Schomaker, M.; Kalies, S.; Schieck, M.; Carlson, R.; Escobar, H. M.; Ripken, T.; Meyer, H.; heisterkamp, a. Gold nanoparticle mediated laser transfection for efficient sirna mediated gene knock down. *Plos One* **8**, e58604 (2013).
38. Delcea, M.; Sternberg, N.; Yashchenok, A. M.; Georgieva, R.; Baumler, H.; Mohwald, H.; Skirtach, A. G. Nanoplasmonics for dual-molecule release through nanopores in the membrane of red blood cells. *Acs Nano* **6**, 4169-4180 (2012).
39. Lukianova-Hleb, E. Y.; Mutonga, M. B. G.; Lapotko, D. O. Cell-specific multifunctional processing of heterogeneous cell systems in a single laser pulse treatment. *Acs Nano* **6**, 10973-10981 (2012).
40. Lapotko, D. Plasmonic nanoparticle-generated photothermal bubbles and their biomedical applications. *Nanomedicine-Uk* **4**, 813-845 (2009).
41. Lukianova-Hleb, E. Y.; Wagner, D. S.; Brenner, M. K.; Lapotko, D. O. Cell-specific transmembrane injection of molecular cargo with gold nanoparticle-generated transient plasmonic nanobubbles. *Biomaterials* **33**, 5441-5450 (2012).
42. Lukianova-Hleb, E. Y.; Ren, X. Y.; Zasadzinski, J. A.; Wu, X. W.; Lapotko, D. O. Plasmonic nanobubbles enhance efficacy and selectivity of chemotherapy against drug-resistant cancer cells. *Adv Mater* **24**, 3831-3837 (2012).
43. Zharov, V. P.; Lapotko, D. O. Photothermal imaging of nanoparticles and cells. *Ieee J Sel Top Quant* **11**, 733-751 (2005).

44. Lukianova-Hleb, E. Y.; Lapotko, D. O. Influence of transient environmental photothermal effects on optical scattering by gold nanoparticles. *Nano Lett* **9**, 2160-2166 (2009).
45. Huhn, D.; Govorov, A.; Gil, P. R.; Parak, W. J. Photostimulated au nanoheaters in polymer and biological media: characterization of mechanical destruction and boiling. *Adv Funct Mater* **22**, 294-303 (2012).
46. Yamane, D.; Wu, Y. C.; Wu, T. H.; Toshiyoshi, H.; Teitell, M. A.; Chiou, P. Y. Electrical impedance monitoring of photothermal porated mammalian cells. *Jala-J Lab Autom* **19**, 50-59 (2014).
47. Yao, C. P.; Qu, X. C.; Zhang, Z. X.; Huttmann, G.; Rahmanzadeh, R. Influence of laser parameters on nanoparticle-induced membrane permeabilization. *J Biomed Opt* **14**, 054034 (2009).
48. Kotaidis, V.; Plech, A. Cavitation dynamics on the nanoscale. *Appl Phys Lett* **87**, 213102 (2005).
49. Takami, A.; Kurita, H.; Koda, S. Laser-induced size reduction of noble metal particles. J *Phys Chem B* **103**, 1226-1232 (1999).
50. Kurita, H.; Takami, A.; Koda, S. Size reduction of gold particles in aqueous solution by pulsed laser irradiation. *Appl Phys Lett* **72**, 789-791 (1998).

6. SUPPLEMENTARY INFORMATION

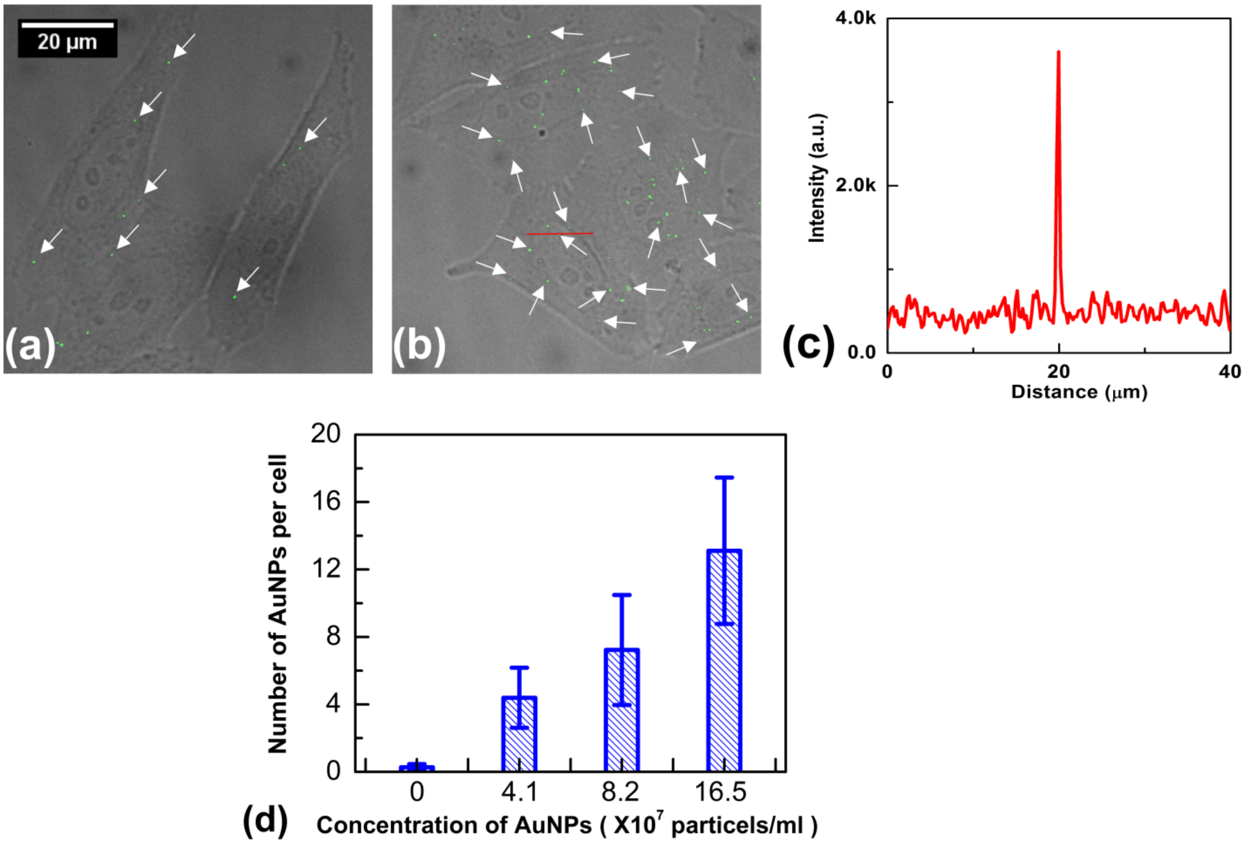

Figure S1. Cationic AuNPs (70 nm) are incubated with HeLa cells at 37 °C for 30 min, after which non-attached AuNPs are washed away. (a-b) CLSM images are obtained from AuNPs in reflection mode (depicted in green, some examples indicated by the arrows)) and merged with the transmission images. CLSM images are shown of cells incubated with (a) a AuNP concentration of 4.1 X 107 particles/ml and (b) a 4-fold higher concentration. (c) The intensity profile across a AuNP adsorbed onto the plasma cell membrane shows that they can be visualized with high contrast. (d) The average number of adsorbed AuNPs per cell is quantified for different AuNPs concentrations by image processing of >200 cells (n = 3).

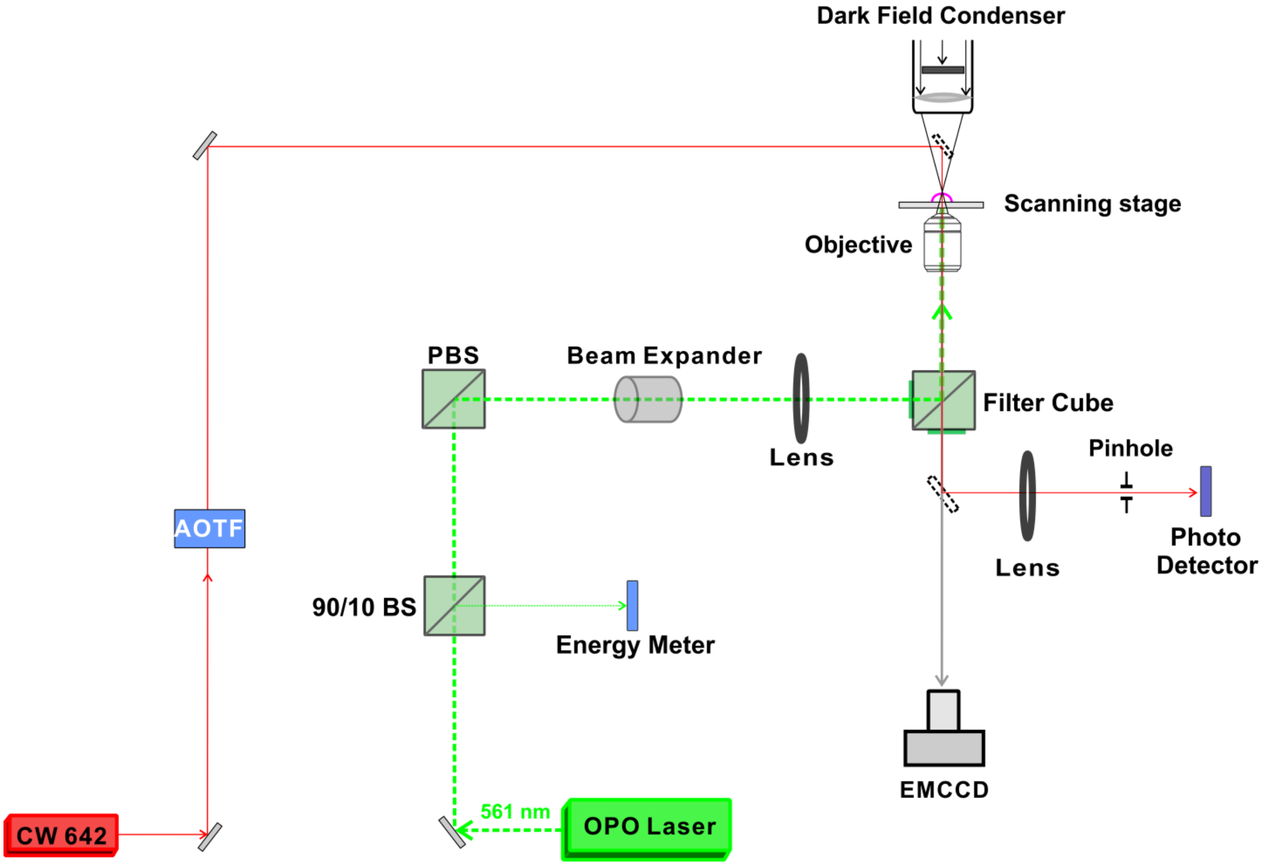

Figure S2. Optical layout for photoporation and detection of VNBs. AOTF: acousto-optic modulator for controlling the power of the continuous wave laser; OPO Laser: pulsed laser with ~7 ns pulses equipped with an Optic Parametric Oscillator that allows to tune the wavelength from 410 nm to 2200 nm; 90/10 BS: laser beam splitter reflecting 10% and transmitting 90% of the laser light; PBS: polarization beam splitter.

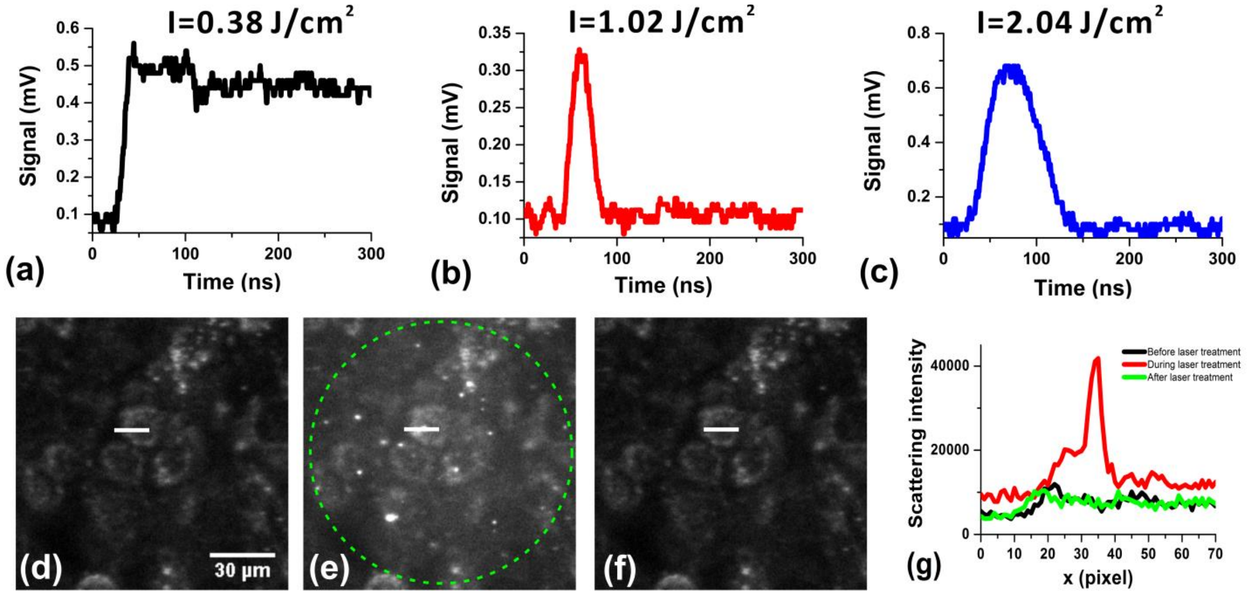

Figure S3. Heating of AuNPs or the formation of VNBs can be monitored with a photodiode that detects transmitted laser light. (a) A typical photothermal singal of AuNPs excited by a laser pulse with a fluence below the VNB threshold shows fast heating of AuNPs with a long tail arrising from heat diffusion into the surrounding medium. (b) At intermediate laser fluence, small VNBs can be generated with a lifetime < 50 ns. (c) At a higher laser pulse fluence, larger VNBs are created with a longer lifetime (~100 ns). The VNB photothermal traces nicely show that there is no heat transferred into the environment. Instead, all energy is consumed by the VNB and is converted to mechanical energy. (d-f) VNBs can also be detected by dark field microscopy. HeLa cells are shown in dark field mode before laser illumination (d), during laser illumination, showing VNBs (bright spots) (e) and after laser illumination (f). The green circle in (e) marks the laser illumation area of approx. 100 µm diameter. (g) the scattering intensity profiles along the lines in d-f.

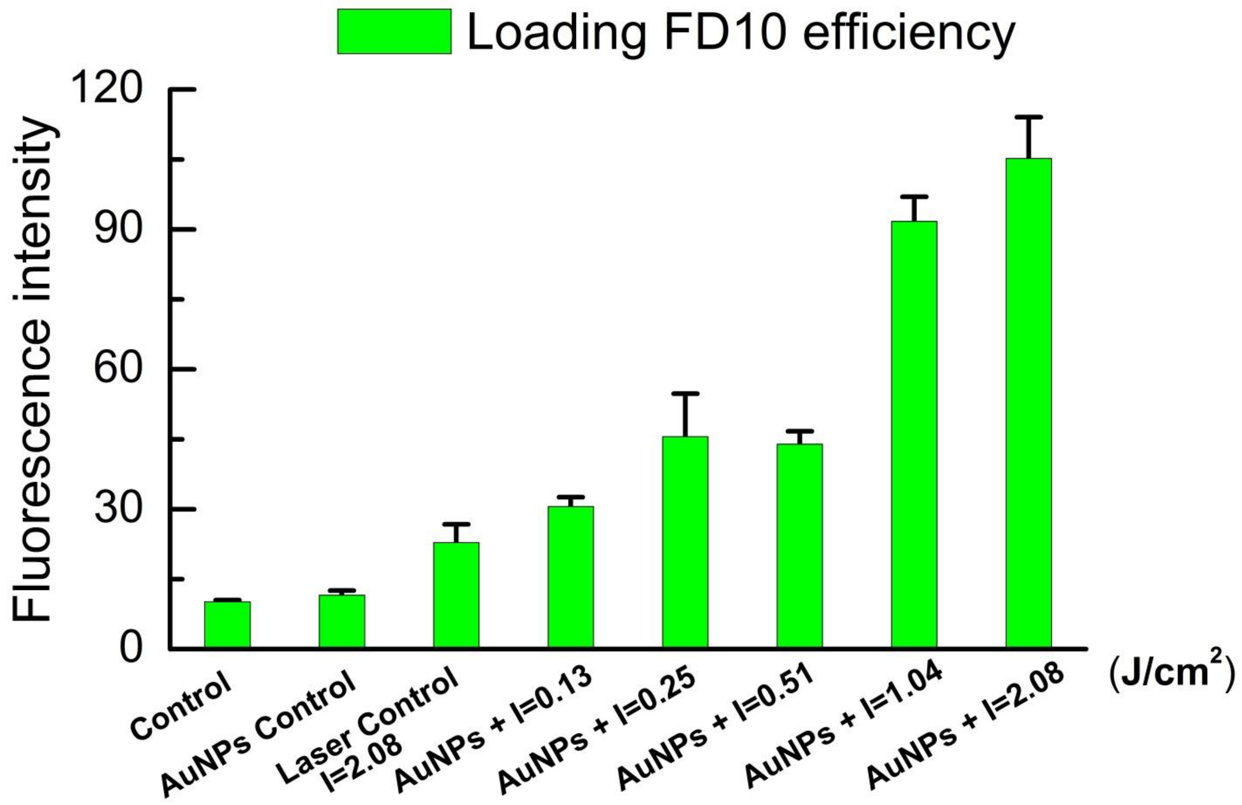

Figure S4. FITC-dextran delivery efficiency is quantified by imaging processing of cells incubated with 8.2x10^7 particles/ml of AuNPs and illuminated with different laser fluences from 0.13, 0.25 and 0.51 J/cm^2 (below the VNB threshold) to 1.02 and 2.04 J/cm^2 (above the VNB threshold).

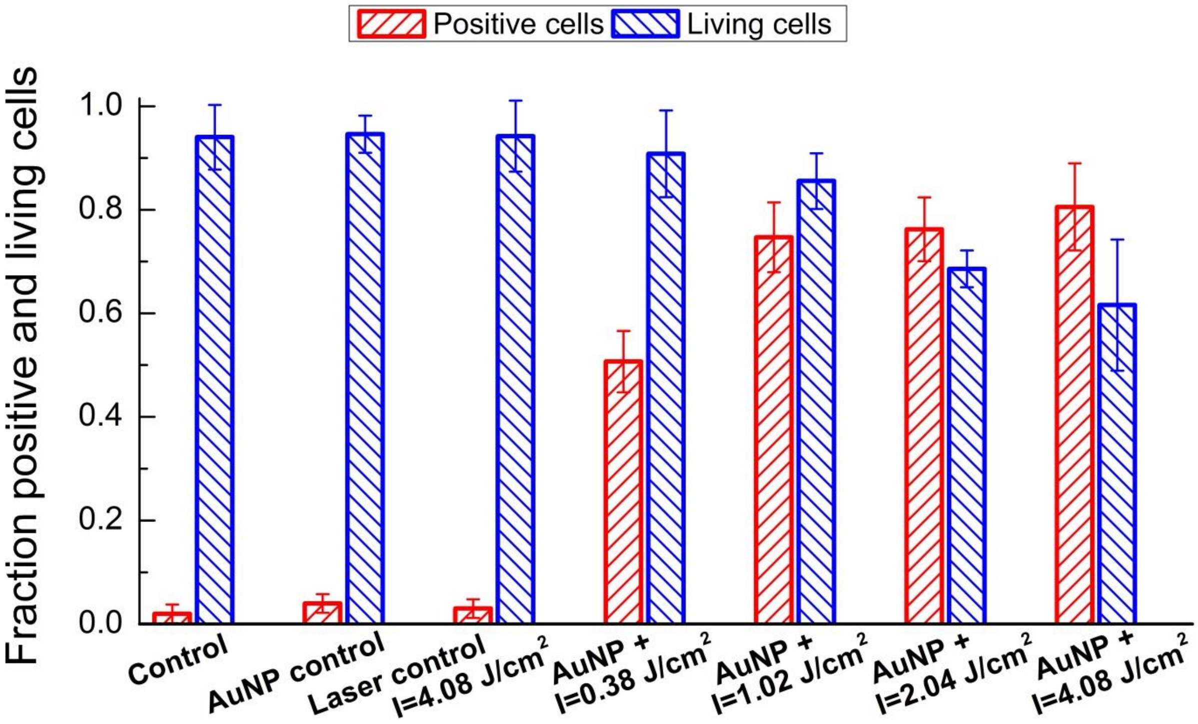

Figure S5. Cell viability and FITC-dextran delivery efficiency are quantified by imaging processing of cells incubated with 16.5x107 particles/ml of AuNPs and illuminated with different laser fluences from 0.38 J/cm2 (below the VNB threshold) to 1.02, 2.04 and 4.08 J/cm^2 (above the VNB threshold). Red bars indicate the fraction of FD10 positive cells, blue bars represent the fraction of live cells.

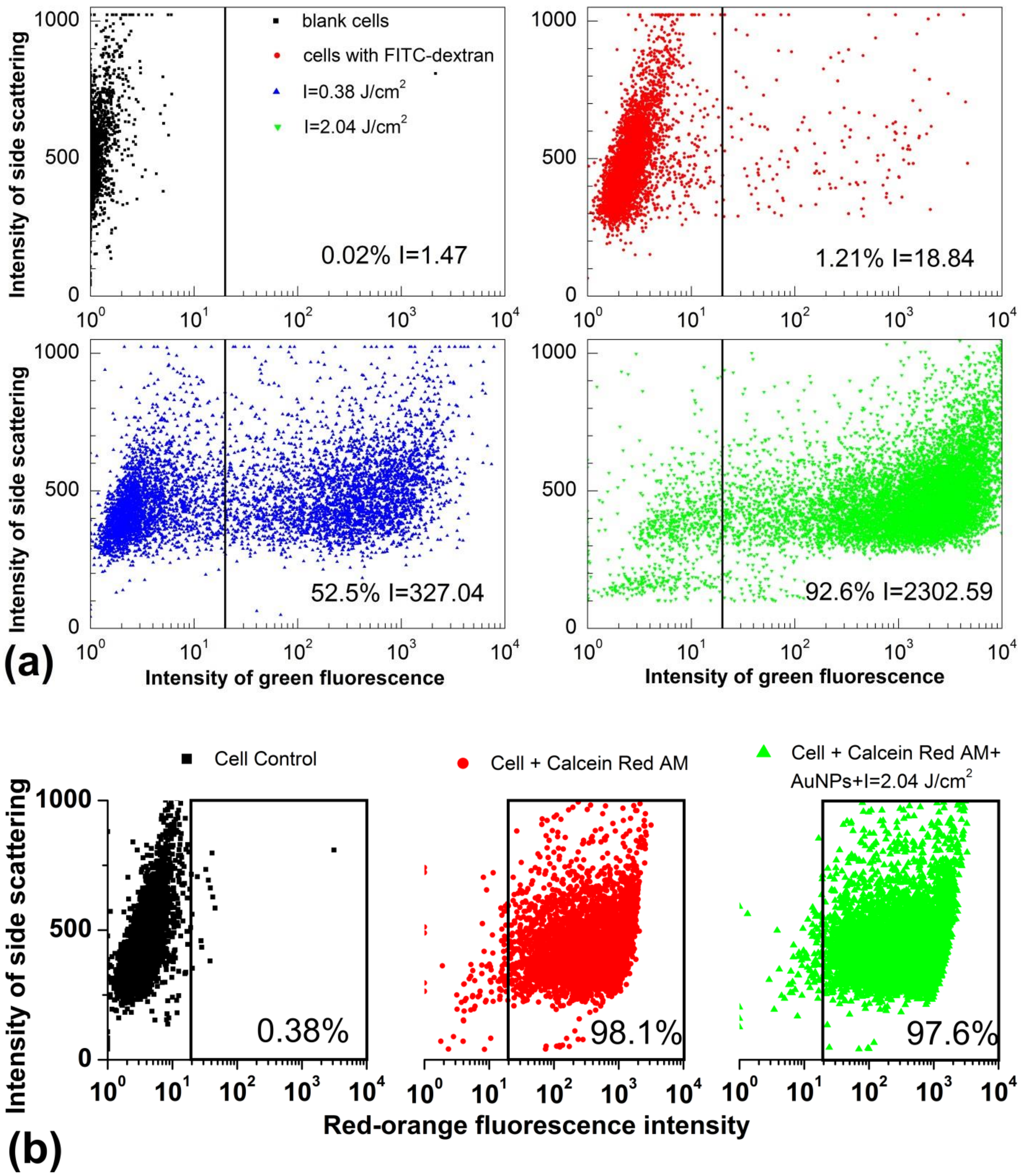

Figure S6. Cell loading with FITC-dextran and viability was evaluated by flow cytometry. HeLa cells were incubated with 70 nm cationic AuNPs at a concentration of 8.25×107 particles/ml corresponding to approx. 8 AuNPs per cell. (a) 52.5% of positive cells are obtained when using 0.38 J/cm2 (direct heating of cell membrane) as compared to 92.6% at 2.04 J/cm2 (pore formation by VNBs). (b) Cell viability is estimated by flow cytometer for blank cells without staining by calcein red-orange AM (left figure), control cells with staining calcein red-orange AM (middle figure) and the cells after laser treatment with the fluence of 2.04 J/cm2 . The rectangles in the figures represent the percentage of living cells.

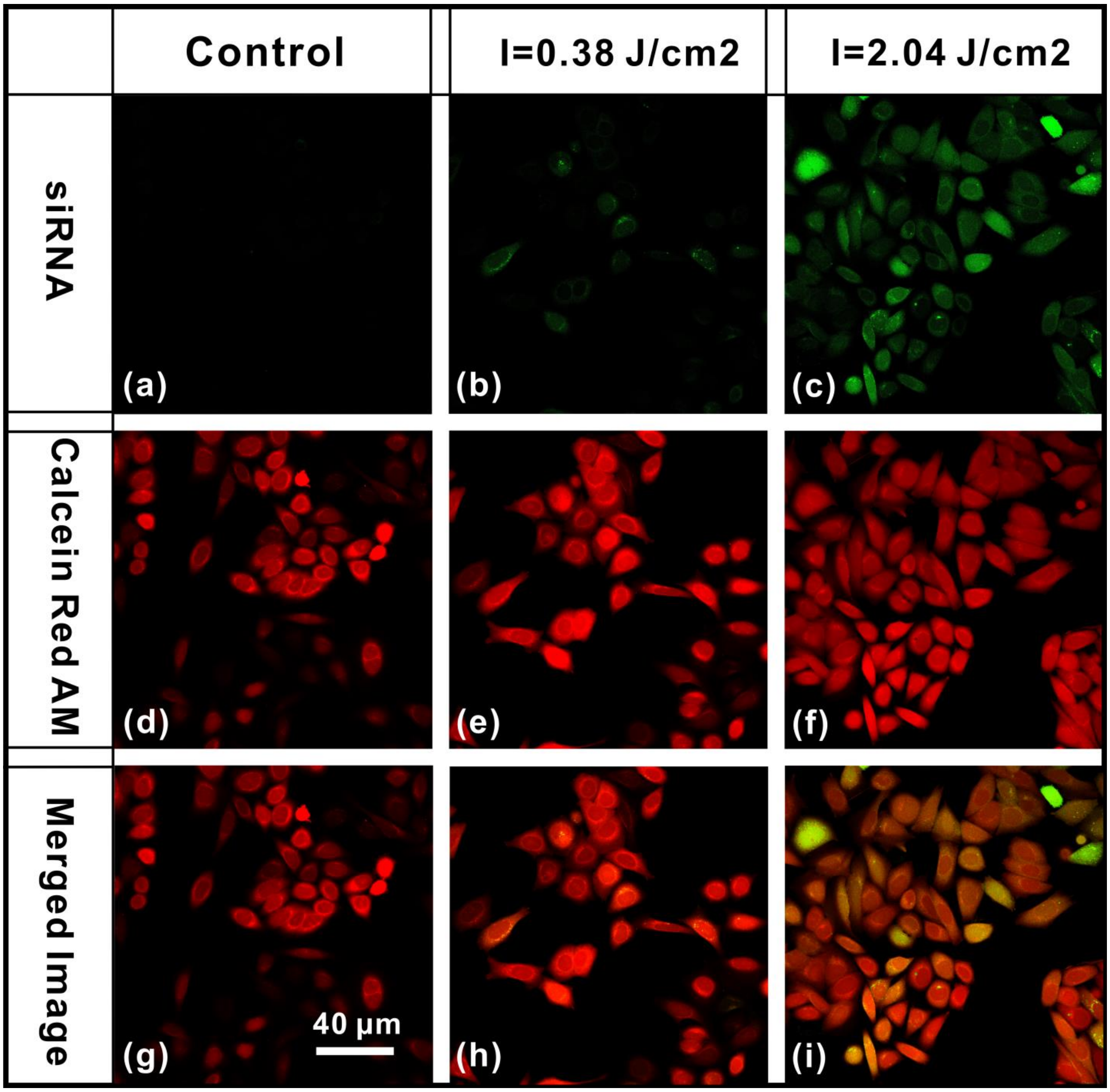

Figure S7. Fluorescently labeled siRNA was delivered into HeLa cells by photoporation. Also for siRNA it is found that cell loading is more efficient by VNB pore formation (2.04 J/cm2) as compared to direct heating of the plasma membrane (0.38 J/cm2).

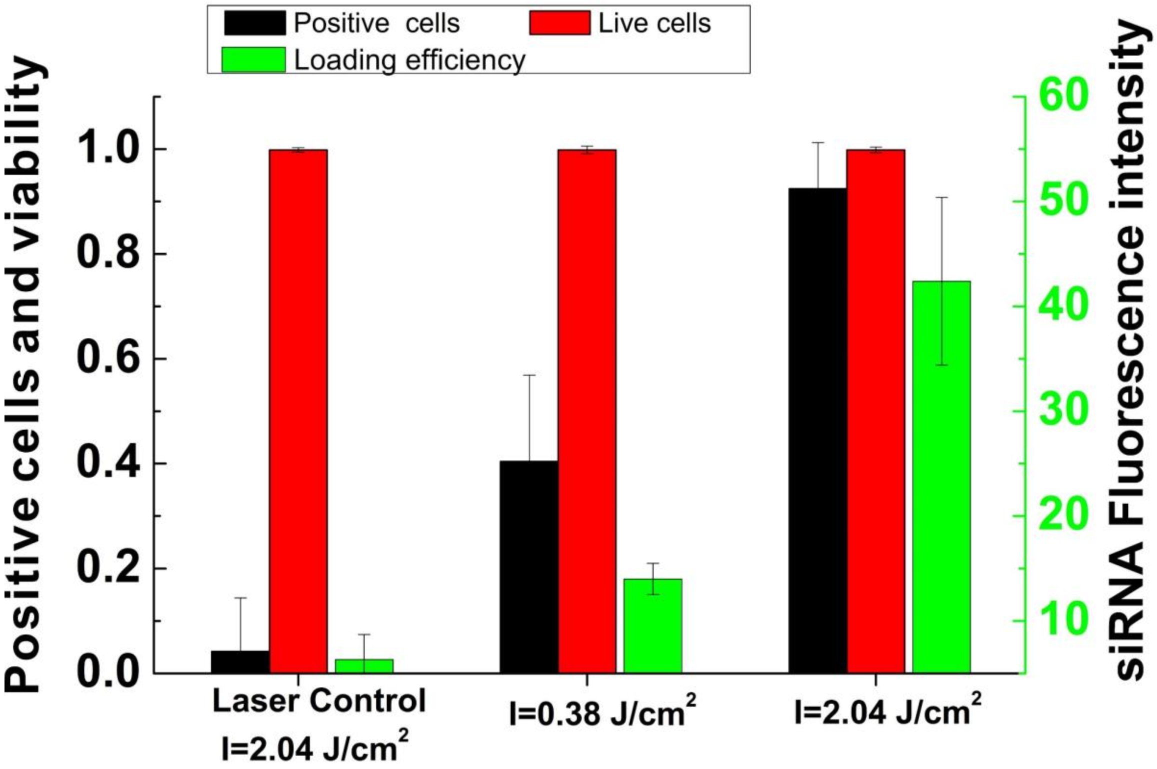

Figure S8. Cell viability and siRNA delivery efficiency was quantified by confocal imaging. HeLa cells were incubated with a AuNP concentration of 8.25×107 particles/ml. Immediately prior to laser treatment, siRNA was added to the cell medium at a concentration of 1 µM. Black bars are the fraction of cells containing a detectable amount of siRNA, green bars show the average fluorescence per cell, and red bars indicate cell viability. The data shown are the result from 3 independent repeats.

Chapter 3

Cytosolic delivery of nano-labels by photoporation prevents their asymmetric inheritance and enables extended quantitative in vivo cell imaging

This chapter is published as:

Cytosolic delivery of nano-labels by photoporation prevents their asymmetric inheritance and enables extended quantitative *in vivo* cell imaging

Ranhua Xiong[1,2], Freya Joris[1], Sayuan Liang[3], Riet De Rycke[4,5], Saskia Lippens[4,5], Jo Demeester[1], Andre Skirtach[6,7], Koen Raemdonck[1], Uwe Himmelreich[3], Stefaan C. De Smedt[1], Kevin Braeckmans[1,2,8,9], Nano Letters, 2016, DOI: 10.1021/acs.nanolett.6b01411

[1]Laboratory of General Biochemistry and Physical Pharmacy, Ghent University, Ghent, Belgium
[2]Centre for Nano- and Biophotonics, Ghent University, 9000 Ghent, Belgium
[3]Biomedical NMR Unit, Faculty of Medicine, Katholieke Universiteit Leuven, 3000 Leuven, Belgium
[4]Inflammation Research Center, Image Core Facility, VIB, 9052 Ghent, Belgium;
[5]Department of Biomedical Molecular Biology, Ghent University, 9052 Ghent, Belgium.
[6]Department of Molecular Biotechnology, Ghent University, 9000 Ghent, Belgium
[7]Max-Planck Institute of Colloids and Interfaces, 14424 Potsdam, Germany
[8]Univ Lille 1, Univ Lille Nord France, IEMN, UMR 8520, 59652 Villeneuve Dascq, France
[9]Univ Lille 1, Univ Lille Nord France, Lab Phys Lasers Atomes & Mol, UMR 8523, 59655 Villeneuve Dascq, France

ABSTRACT

Long-term in vivo imaging of cells is crucial for the understanding of cellular fate in biological processes in cancer research, immunology or in cell-based therapies such as beta cell transplantation in type I diabetes or stem cell therapy. Traditionally, cell labeling with the desired contrast agent occurs ex vivo via spontaneous endocytosis, which is a variable and slow process that requires optimization for each particular label-cell type combination. Following endocytic uptake, the contrast agents mostly remain entrapped in the endolysosomal compartment, which leads to signal instability, cytotoxicity and asymmetric inheritance of the labels upon cell division. Here, we demonstrate that these disadvantages can be circumvented by delivering contrast agents directly into the cytoplasm via vapour nanobubble photoporation. Compared to classic endocytic uptake, photoporation resulted in 50 and 3 times higher loading of fluorescent dextrans and quantum dots, respectively, with improved signal stability and reduced cytotoxicity. Most interestingly, cytosolic delivery by photoporation prevented asymmetric inheritance of labels by daughter cells over subsequent cell generations. Instead, unequal inheritance of endocytosed labels resulted in a dramatic increase in polydispersity of the amount of labels per cell with each cell division, hindering accurate quantification of cell numbers in vivo over time. The combined benefits of cell labeling by photoporation resulted in a marked improvement in long-term cell visibility in vivo where an insulin producing cell line (INS-1E cell line) labeled with fluorescent dextrans could be tracked for up to two months in Swiss Nude mice compared to two weeks for cells labeled by endocytosis.

1. INTRODUCTION

There is great interest in monitoring *in vivo* transplanted cells for research and therapeutic purposes. In cancer research, for instance, it is of importance to visualize cancer cells in real time to study their metastatic potential in animal models[1]. *In vivo* tracking of cells is also desired for cell therapies to follow-up on treatment efficacy[2]. Examples are stem cells in regenerative medicine[3, 4], β-cells for the treatment of type I diabetes[5] and immune cells such as T-cells in immunotherapy[6].

For *in vivo* cell tracking, the cells need to be labeled before transplantation, for which two main strategies are being explored. One is to transfect the cells with a reporter gene[2, 7] and follow-up on their proliferation through optical imaging, positron emission tomography or magnetic resonance imaging[8-10]. This strategy, however, requires a rather time-consuming transfection procedure that may lead to undesired phenotypical alterations and abnormalities in the transplanted cells in comparison to the native cells[11-13]. The second strategy is to label the cells with exogenous contrast agents, being either organic probes or inorganic nanoparticles (NPs)[14, 15]. Examples are fluorescently labeled dextrans[16, 17] and quantum dots (QD) for optical fluorescence imaging[18-20], or superparamagnetic iron oxide NPs and Gadolinium complexes for magnetic resonance imaging (MRI)[4, 21, 22]. Traditionally, these contrast agents are simply incubated with the cells, in some cases in combination with transfecting agents, so that they are internalized primarily by endocytic uptake. Despite its simplicity and widespread use, several disadvantages are connected to this way of labeling cells. First, as endocytosis is a highly cell-type dependent process, the labeling procedure needs to be optimized for each particular nanomaterial-cell type combination. In addition, several cell types such as T-cells have difficulties in internalizing extracellular compounds through endocytosis[23]. In other cases, problems may arise for cells that have a limited life span in culture, such as pancreatic islets, as efficient cell labeling through endocytic uptake is a rather slow process[24]. A second problem is that entrapment of contrast agents in the acidic endolysosomes may lead to increased cytotoxicity, for instance by creating reactive groups on the NP surface or by leaching of toxic metal ions, such as Cd^{2+} in case of QDs[25-27]. A third disadvantage of endocytic cell labeling is that the vast majority of the contrast agents are trafficked to the endolysosomes where they are exposed to an acidic and overall degrading environment[26, 28]. This can lead to degradation of the contrast agent, lowering the signal intensity, as reported for fluorescent labels[28-30] as well as MRI contrast agents[31-33]. In addition, it has been reported that nanomaterials trapped in endolysosomal vesicles are not distributed equally over daughter cells upon cell division[30, 34, 35]. While this process has been proposed to be a protective mechanism where the daughter cell with the highest NP load can be sacrificed in favour of the daughter cell with the lowest NP content[29, 36], recent findings show that asymmetric inheritance of vesicles is an inherent cell-biological phenomenon[37]. For quantitative cell tracking applications asymmetric inheritance of contrast agents over daughter cells is disadvantageous as it hinders accurate quantification of cell numbers over time, apart from the fact that the brightest signals are coming from cells that are suffering from the highest cytotoxicity.

In this work, we hypothesized that direct delivery of contrast agents into the cytosol could alleviate the many difficulties related to endocytic cell labeling. Evidently, this requires a technology that is able to deliver a broad range of contrast agents across the cell membrane in a fast, efficient and non-toxic manner. Vapour nanobubble (VNB) photoporation is an interesting and relatively new method that is receiving increasing interest in recent years to deliver nanomaterials into cells[38-41]. It is based on the usage of plasmonic nanoparticles, typically gold nanoparticles (AuNP), adsorbed to the plasma membrane of cells that are illuminated with pulsed laser light. If a short laser pulse (< 10 ns) of sufficiently high intensity is absorbed by an AuNP, its temperature can rapidly increase to several hundred degrees due to efficient heat confinement[42]. If the AuNP is located in hydrated tissue, like in cell culture, the water surrounding the AuNP will evaporate. This results in the generation of an expanding VNB around the AuNP surface, with a size ranging from tens to hundreds of nm depending on the laser pulse intensity. When the thermal energy of the AuNP is consumed, the VNB violently collapses causing local damage to the surrounding tissue by high-pressure shock waves. Due to the extremely short lifetime of VNBs (<1 μs), the diffusion of heat from the AuNP into the environment is negligible so that almost all energy of the irradiated AuNP is converted to mechanical energy (expansion of the VNB). This property makes VNB photoporation an interesting technology to mechanically perforate the cell membrane, without causing unspecific thermal damage to cells. Building forth on recent successes with the cytosolic delivery of therapeutic molecules[43-45], here we show that vapour nanobubble photoporation is a well-suited technology for cytosolic cell labeling in a fast and non-toxic manner. First, we demonstrate efficient and safe loading of fluorescent dextran and QD in different cell types by photoporation. Compared to endocytic uptake, cell loading with photoporation was 50 and 3 times more efficient for FITC-dextran (FD) and QD, respectively. Combined with reduced toxicity, this enabled extended cell visualization *in vitro* over 10 generations for FD and 3 generations for QD. This shows that old-school labeled dextrans are excellent inexpensive and bio-compatible labels for cell tracking when delivered by photoporation as compared to much more expensive and toxic QDs. We demonstrate for the first time that asymmetric inheritance of fluorescent labels can be avoided by cytosolic delivery *via* photoporation. As a result, the cell intensity polydispersity remains identical over multiple cell divisions, while it rapidly increases for endocytic loading (already factor 10 after 6 divisions). Finally, we show extended *in vivo* imaging of an insulin producing cell line (INS-1E cell line) labeled with Cy5.5-dextran by photoporation. Cells labeled by photoporation could be imaged up to two months instead of only two weeks in case of endocytic labeling.

2. MATERIALS AND METHODS

Materials. 520 (±10) nm CdSe/ZnS quantum dots and 690 (±25) nm InP/ZnS fluorescent nanocrystals coated with a thiol oligomer, surface functionalized with -COOH groups (PEG-coated QD) were purchased from Mesolight, Inc. (#CdSe/ZnS-PEG-COOH-520 and #InP/ZnS-PEG-COOH-690, Mesolight, Inc., Little Rock Arkansas, USA). 520 (+/-15) InP/ZnS nm QD, functionalized with -COOH groups, were purchased from AC Diagnostics, Inc. (#CAIPS-520-P-1, AC Diagnostics, Inc., Fayetteville, AR, USA). 70 nm cationic AuNPs were purchased from NanoPartz (#CU11-70-P30-50, Nanopartz Inc., Loveland, CO, USA). These AuNPs had a zeta potential of 30 mV as measured by dynamic light scattering (NanoSizer, Malvern, UK). FITC-dextrans (FD) with a molecular weight of 10 kDa were purchased from Sigma-Aldrich (Belgium). Alexa Fluor @488 labeled 10 kDa dextrans (AD) (#D-22910, Molecular Probes®), Propidium Iodide (#P1304MP, Molecular Probes®) and Hoechst (cell nuclei labeling, #H3570, Molecular Probes®) were obtained from Invitrogen (Belgium). Cy5.5 labeled 10 kDa dextrans (CD) were purchased from Interchim (#FP-DZ2581, France).

Cell culture. Three different cell lines were applied in this work, namely the HeLa, C17.2 and INS-1E cell line. HeLa cells were obtained from ATCC (CCL-2) and cultured in complete cell medium which consisted of DMEM/F-12 supplemented with 10% heat-inactivated foetal bovine serum (FBS), 2 mM glutamine and 100 U/mL penicillin/streptomycin. The C17.2 neural progenitor cell line was retrieved from Sigma (Belgium) and cultured in DMEM containing 10% FBS, 5% horse serum, 2mM L-Glutamine and 100 U/mL penicillin/streptomycin. Finally, the LV-transduced INS-1E cells were cultured in RPMI completed with 10% FBS, 2mM L-Glutamine, 100 U/mL penicillin/streptomycin, 1% 100mM sodium pyruvate, 0.1% 50mM 2-mercaptoethanol and 10 mM Hepes. All cells were cultured at 37°C in a humid atmosphere containing 5% CO_2. All cell culture products were obtained from Invitrogen (Belgium) unless specifically stated otherwise.

Detection of AuNPs by confocal reflectance imaging and TEM. HeLa cells were cultured as described above. Cells were incubated with AuNPs for 30 min at 37°C at a fixed concentration of $\sim 5\times10^7$ particles/ml. Cells were washed to remove unbound AuNPs. For confocal imaging the plasma membrane was stained with red fluorescent CellMask (#C10046, ThermoFisher Scientific). Confocal images were acquired with a Nikon C1si confocal laser scanning microscope using a 60× oil lens with 1.4 numerical aperture. AuNP were detected by the reflected laser light and false-colored in green. For TEM imaging, cell sections were placed on carbon-coated Cu grids (200-mesh) and visualized by a JEM 1400plus transmission electron microscope (JEOL, Tokyo, Japan) operating at 60 kV.

Generation and detection of vapour nanobubble. A homemade setup, including an optical and electrical timing system, was used to generate and detect the vapour nanobubble[37]. A pulsed laser (~7 ns) tuned at a wavelength of 561 nm (Opolette™ HE 355 LD, OPOTEK Inc., Faraday Ave, CA, USA) was applied to illuminate the AuNPs in order to generate vapour nanobubbles. Under these conditions the initial AuNP temperature will be in the order of 500 K upon absorption of a single laser pulse. Here we have taken into account that only the first 0.5 ns of the laser pulse is most efficiently absorbed since after that there is efflux of heat energy to form the vapour nanobubble and the emerging nanobubble scatters (partly) the subsequently incoming light. For a more detailed theoretical framework the reader is referred to the work by Pustovalov et al.[42]. Finally, the setup has a time-response and light scattering mode to allow detection of VNB formation[43].

Cell labeling *via* endocytosis. HeLa and C17.2 cells were seeded in 96 well plates at a density of 15000 cells/well while for INS-1E cells a density of 100000 cells/well was respected. Cells were allowed to settle overnight prior to treatment. Typically, for endocytosis experiments the cells were incubated with 2 mg/ml FITC-dextrans (FD) / Alexa@488-dextran (AD) / Cy5.5-dextran (CD) or 400 nM QDs (CdSe/ZnS @ 520 nm, InP/ZnS @ 520 nm, InP/ZnS @ 690 nm) during 1 hour at 37°C. In viability experiments also 100 and 200 nM QD dispersions were included. Subsequently cells were washed once with PBS (Invitrogen, Belgium) before performing further analysis.

Cell labeling *via* vapour nanobubble photoporation. For laser treatment, the cells were seeded at the same densities as for endocytic cell loading. Here, cells were initially incubated with AuNPs during 30 min at 37°C at a fixed concentration of $\sim 5\times10^7$ particles/mL for HeLa and C17.2 cells and $\sim 1\times10^8$ particles/mL for the INS-1E cells. Next, the cells were washed to remove remaining free AuNPs and a 2 mg/ml dextran dispersion (FD, AD or CD), or 1 µM QD dispersion (CdSe/ZnS @ 520 nm, InP/ZnS @ 520 nm or InP/ZnS @ 690 nm) was added just prior to the laser scanning. After the laser treatment, the cells were washed once with PBS and supplied with fresh cell medium before continuing with further analysis.

Measuring fluorescence intensity (FI) by fluorescence microscopy. Cells were imaged in a stage-top cell incubator (37°C with 5% CO_2 supplied, Tokai heat) for ~ 48 hours using a swept field confocal microscope (SFC & Eclipse Ti, Nikon, Japan). Each hour, cells were imaged with a 60× oil immersion lens (CFI Plan Apo VC 60×oil, Nikon, Japan) over a large area by stitching 25 by 25 images, thus covering ~2.15 mm by ~2.15 mm with ~1500 cells. The microscope's autofocus system was used to maintain a constant focus position on the cells. ImageJ software was used to segment the cells and calculate the fluorescence of each cell. The FI of each cell was calculated as follows:

$$FI = (FI_{cell} - FI_{BG}) \times \beta \ (1)$$

where FI_{cell} is the total fluorescence intensity of a cell as measured by ImageJ, and FI_{BG} is the total background fluorescence intensity within the area of one cell. β used to compensate for photobleaching and was defined as $\beta = \bar{I}_0/\bar{I}_i$ where $\bar{I}_0$ is the initial average fluorescence intensity and $\bar{I}_i$ is the average fluorescence intensity after *i* times of laser scanning.

Measuring mean fluorescence intensity (MFI) by flow cytometry. Following labeling with either fluorescently labeled dextrans or QD *via* endocytosis or photoporation, cells were detached by trypsin-EDTA (Invitrogen, Belgium) treatment and collected by centrifugation. Following resuspension in flow buffer (PBS supplemented with 5% FBS) the samples were measured by flow cytometry (FACS Calibur, BD, Belgium) and 10000 events were detected per sample. The cells were excited with a 488 nm laser and fluorescence was recorded in the 530/30 channel. For a certain time t_i after labeling, the normalized $\overline{MFI}_{t_i}$was obtained by normalizing the population MFI (MFI_{t_i}) to the MFI of cells immediately after labeling (MFI_{t_0}):

$$\overline{MFI}_{t_i} = \frac{MFI_{t_i} - MFI_{t_i}^{ctrl}}{MFI_{t_0} - MFI_{t_0}^{ctrl}} \quad (2)$$

where $MFI_{t_i}^{ctrl}$ is the MFI of untreated cells (*i.e.* correction for contribution by autofluorescence). The following mono-exponential decay model was used to obtain the cell division time τ:

$$\overline{MFI} = 2^{-(\frac{t}{\tau})} \quad (3)$$

Finally, the relative MFI of a cell population was calculated by dividing the MFI at a certain time after labeling by the MFI of untreated cells at the same time point.

Evaluation of cell viability following cell labeling. Cells were seeded and loaded according to methods described above. Subsequently, cells were washed once with PBS, fresh medium was added and cells were allowed to recover two hours before performing the MTT assay. To this end 30 µl of a 5 mg/ml 3-(4,5-dimethylthiazol-2-yl)-2,5-diphenyltetrazolium bromide (MTT, Sigma, Belgium) solution was added to each well. Following an incubation period of three hours at 37°C the MTT containing cell medium was removed and cells were lysed using dimethylsulfoxide (Sigma, Belgium). When the formazan crystals were completely dissolved, the absorbance in each well was measured at 570 and 650 nm using an Envision Xcite multilabel reader (PerkinElmer LAS, Boston, MA). NP containing cell medium was included as a control to allow correction for the possible interaction of the NPs with the assay. Additionally, we evaluated cell viability following vapour nanobubble generation without contrast agent loading. In this way we could differentiate to what extent effects on viability were stemming from the loading method. All data are expressed as the mean ± SD (n=3).

Statistical model to describe the inheritance of contrast agents over subsequent cell generations. As reported previously, the redistribution of endocytosed NPs over daughter cells can be modelled by a convolution product of the original cell distribution with a binomial partitioning probability function[30]:

$$n_{t_1}(N_1) = \sum_N n_{t_0}(N) \times T(N, N_1) \quad (4)$$

$$T(N, N_1) = (1 - f)\delta(N_1 = N) + f[binomial(N, N_1, p) + binomial(N, N - N_1, p)] \; (5)$$

Here, *T* is the transfer function and includes two binomial functions, describing the probability of N_1 endo-lysosomal vesicles containing NPs being inherited by one of the daughter cells upon division of the mother cell with *N* vesicles. Parameter *p* describes the probability of endolysosomal vesicles being allocated to a specific daughter cell during division. *p* = 0.5 signifies 50% chance that the daughter cell will receive the vesicle, while *p* = 1 means that all of the vesicles will be inherited by the daughter cell. While this model was developed for describing the repartitioning of a small number of NP containing endolysosomal vesicles (typically<100), in our work we are dealing with much higher numbers (typically $>10^5$ particles). When the statistical samples are large enough (typically N>100), the binomial distribution can be approximated by a normal distribution. This means that the convolution probability distribution can be approximated by a normal distribution. Similarly, the fluorescence intensity distributions of daughter cells can be convoluted by the transfer function implemented with a normal probability function:

$$F(I_1) = \sum_I F_{t_0}(I) \times T(I, I_1) \quad (6)$$

Here, I is the fluorescence intensity of a mother cell and I_1 is the fluorescence intensity inherited by one of the daughter cells after cell division. The transfer function $T(I, I_1)$ can be expressed with two normal distribution functions which describe the probability that a mother cell with intensity I transfers its contrast agents over its daughter cells in a ratio $I_1/I-I_1$:

$$T(I, I_1) = (1 - f)\delta(I_1 = I - I_1) + f[N(I_1, \mu_1, \sigma) + N(I_1, \mu_2, \sigma)] \; (7)$$

Here, *f* is the fraction of cells that have undergone mitosis and *N* is the normal distribution function.

$$N(I_1, \mu_i, \sigma) = \frac{1}{\sigma\sqrt{2\pi}} \exp\left[-\frac{(I_1 - \mu_i)^2}{2\sigma^2}\right] \quad (8)$$

The mean μ_1 and μ_2, and the standard deviation σ are defined as

$$\mu_1 = I \cdot p, \mu_2 = I \cdot (1 - p\,), \sigma = \sqrt{I \cdot p \cdot (1 - p\,)} \quad (9)$$

where p is the probability that a contrast agent is inherent by one particular daughter cell upon cell division and I is the mother cell fluorescence intensity.

***In vivo* experiments long-term cell tracking post injection in mice.** All animal experiments were executed in accordance with national and European regulations and approved by the local Animal Ethics Committee. Swiss Nude mice (7-9 weeks old, Charles River, Chatillon-sur-Chalaronne, France) received 1 million LV-transduced (fLuc expression for bioluminescence) INS-1E cells suspended in 100 µL cell culture medium subcutaneously into both the hind limbs (left side: unlabelled control cells; right side: labeled cells). During cell transplantation, animals were anesthetized with 2% isoflurane (Isoflurane ISP, Rothacher, Basel, Switzerland) in 100% oxygen, at a flow rate of 2 L/minute. For both *in vivo* bioluminescence imaging (BLI) and fluorescent imaging (FLI), the animals were anesthetized with 2% isoflurane in 100% oxygen, at a flow rate of 2 L/minute. All the images were acquired using an IVIS *in vivo* optical imaging system (PerkinElmer, Massachusetts, U.S.A). For the BLI, D-luciferin, dissolved in PBS (15 mg/mL), was injected intraperitoneally (126 mg/kg body weight) prior to the imaging sessions. Consecutive frames were acquired each minute until the maximum signal intensity was reached. For the FLI acquisition, the EPI mode was used with an excitation wavelength at 673 nm and an emission wavelength at 707 nm for Cy5.5 according to its default value set in the system software (Living Imaging, Perkin Elmer). All reported BLI and FLI images were superimposed by a grey-scale photographic image with anatomical information and a pseudocolor image with functional/optical information. The BLI/FLI signals were expressed as total photon flux (p/s/sr) from circular region of interests (ROI) using the Living Imaging software. The FLI signals of average radiance were also quantified in the ROI by this software (Perkin Elmer). No samples or animals were excluded from the analysis. The quantification data are expressed in average radiance of FLI or BLI with the mean ± SD (n=3). The data was compared by one-way ANOVA.

3. RESULTS

3.1 Photoporation enables efficient cytosolic delivery of contrast agents with reduced cytotoxicity.

The procedure of delivering contrast agents into the cytosol of cells by vapour nanobubble photoporation is illustrated in **Fig. 1a**. Cells are first incubated with plasmonic NPs, such as gold NPs (AuNPs), for 15-30 min. During that time the AuNP can adsorb to the cells and are internalized just below the plasma membrane by endocytic uptake (see TEM images in **Figure S1**). On average ~8 AuNPs are associated per cell as determined by confocal reflection imaging (**Figure S1** and **Supporting Movie 1**). After washing the cells to remove the unbound AuNPs, the contrast agent is added and the cells are irradiated with ns (nanosecond) pulsed laser light. When a laser pulse of sufficiently high intensity is applied, the temperature of the AuNPs increases to several hundred degrees causing the water surrounding the AuNPs to evaporate.[46] This in turn results in the formation of vapour nanobubbles that expand and collapse, thereby inducing pores in the cell membrane and allowing the contrast agent to diffuse into the cytoplasm. In our set-up, the cells are grown in a 96-well plate and the laser beam covers a circular area of ~150 µm diameter. The laser pulses are synchronized with a programmed motorized stage to assure that each cell in the culture dish receives one or two laser pulse. Scanning of the entire well takes approximately three minutes, which is essentially limited by the laser repetition rate (20 Hz). The generation of vapour nanobubbles can be confirmed with dark field microscopy (**Figure S1c**), or in time-resolved transmitted light mode (**Figure S1b**). To confirm successful photoporation of the cell membrane, we *in-situ* recorded the cytoplasmic accumulation of the cell impermeable dye Propidium Iodide (PI) (**Supporting Movie 2**, Supporting Information). To assess the size of VNB induced membrane pores, we measured the delivery efficiency of FITC-dextran of 10 kDa (FD10), 150 kDa (FD150) and 500 kDa (FD500), which have a hydrodynamic diameter of respectively 4, 17 and 31 nm. The photoporation procedure was carried out at 3 different laser fluence settings (1, 2 and 4 J/cm²). It is expected that bigger VNB are formed with higher laser fluences, which should result in bigger membrane pores as well. The data in **Figure S2a** and **S2b** show that all three probes could be delivered into 80-95% of the cells although the amount per cell is clearly less for the bigger probes. By increasing the laser fluence a slight increase in delivery efficiency was observed, indicative of slightly bigger pores. Based on FD500 delivery we conclude that pores created under the illumination conditions used in this study can have a size of at least 30 nm diameter. We also tried to estimate the pore lifetime by adding the FITC-dextran probes as a function of time after photoporation to the cells. The data in **Figure S2c** and **S2d** show that already after 1 min most of the cells have been completely resealed considering that only about 25% still show uptake of the smallest probe (FD10). And even in those cells the remaining pores must have been very small since the amount of FD10 taken up in those cells is about 100 fold less as when the probe is present during photoporation. Looking at FD500, there is no more uptake after 1 min, showing that all pores have become smaller than 30 nm after 1 min. After 3 min there is no further influx of any of the probes, indicating that all pores are resealed in less than 3 min after photoporation.

Since both organic probes and inorganic NPs receive much attention for long-term cell tracking, we selected FITC-dextran (FD) and CdSe/ZnS core/shell quantum dot (CdSe QD) as exemplary contrast agents. For both labels we performed a systematic comparison between endocytic labeling and cytosolic delivery by photoporation in HeLa cells in terms of uptake efficiency and cell viability. Endocytic labeling was performed by incubating the cells for 1 h with increasing concentrations of the contrast agent. Note that a 1 h incubation time was selected since QD induced toxicity became too high for longer incubation times (**Figure S3**). Photoporation was performed with a fixed concentration of contrast agents (2 mg/ml for FD and 1 μM for CdSe QD), but with increasing laser fluence settings (all above the vapour nanobubble generation threshold of ~1 J/cm^2)[43]. From the confocal images in **Fig. 1b** (END for endocytic labeling, VNB for vapour nanobubble photoporation labeling) the difference in intracellular labeling pattern is immediately clear. As expected, endocytic labeling results in a punctuate pattern due to endosomal sequestration of the contrast agent, while a uniform cytosolic labeling is obtained by photoporation. Image quantification (upper panels in **Fig. 1c**, **d**) shows that endocytic labeling results in nearly 100% of the cells with a detectable signal. For photoporation approximately 80% of the cells have a detectable signal at the lowest laser fluence of 1 J/cm^2, which becomes >90% for higher fluences. The difference in efficiency between both labeling methods, however, becomes apparent when looking at the total signal per cell, expressed as the relative mean fluorescence intensity rMFI (rMFI = MFI labeled cells / MFI control cells) (middle panel in **Fig. 1c, d**). For instance, at a laser fluence of 4 J/cm^{2,} cells labeled with FD by photoporation are as much as 50 times brighter as compared to endocytic labeling at the highest concentration tested. While the difference was less pronounced in case of CdSe QD, still a 3 times higher labeling intensity was found in case of photoporation. In terms of cytotoxicity (lower panels in **Fig. 1c, d**), endocytic uptake of FD did not have any effect on the cells. For photoporation the cell viability was close to 90% regardless of the laser fluence used. Endocytic uptake of CdSe QD resulted in a concentration dependent cytotoxicity. Only for the lowest concentration (100 nM) >80% cell viability was obtained. A similar concentration dependent toxicity was found for VNB photoporation with CdSe QD. 80% cell viability was obtained at an intermediate laser fluence of 2 J/cm^2. Notably, the signal per cell for this condition is 5 times higher as compared to endocytic labeling at the non-toxic concentration of 100 nM. Similar experiments were carried out for INS-1E cells, which is a type insulin producing cell under investigation for the treatment of type I diabetes[5]. As can be seen from the results in **Figure S4**, the findings on HeLa cells could be confirmed for INS-1E cells, indicating that the results are independent of the cell type.

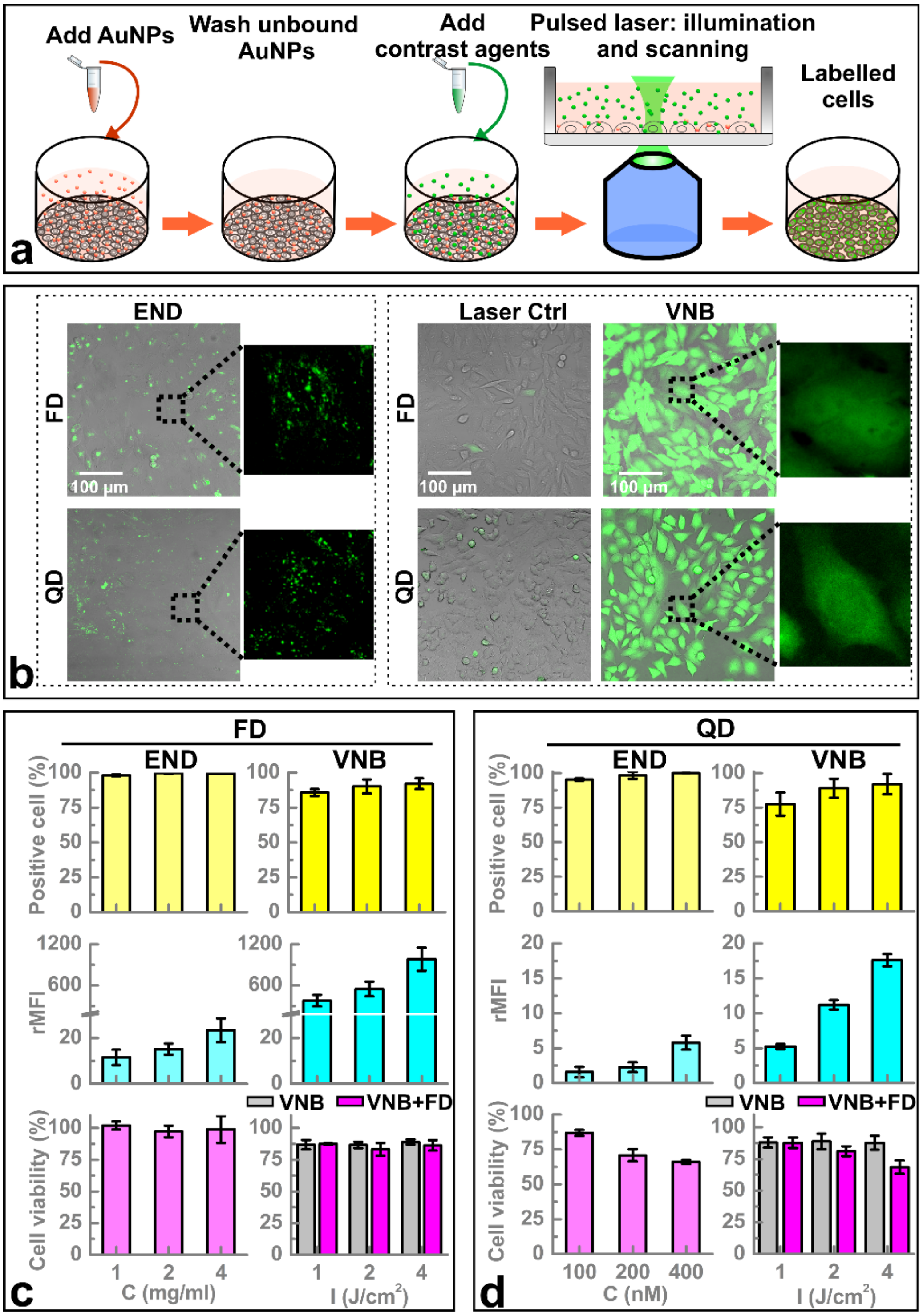

Figure 1. Cell labeling by photoporation vs. endocytic uptake of contrast agents. a, Schematic overview of the experimental procedure to label cells by photoporation. b, Confocal images show successful cell labeling with FD and CdSe QD by endocytic uptake (END) and photoporation (VNB). Control images are shown for cells incubated with FD and CdSe QD, which received laser treatment without AuNPs and VNB formation. This shows that photoporation is not induced by the laser irradiation alone. c-d, Quantification of the percentage of positive cells (yellow), the labeling intensity per cell (cyan) and cell viability (magenta) as a function of label concentration in case of endocytic labeling and as a function of laser fluence from 1 to 4 J/cm2 for photoporation. The cell viability is also shown for cells treated with photoporation but without addition of contrast agents, showing that the photoporation procedure in itself induces very little toxicity. (n=3)

3.2 Cell labeling by photoporation enables extended cell tracking in vitro.

So far we have shown that photoporation allows a much higher amount of label to be delivered into (the cytoplasm of) cells. Combined with the fact that endolysosomal degradation or quenching of the label is avoided when contrast agents are directly delivered to the cytoplasm, we hypothesized that those cells can be imaged over an extended number of cell generations as compared to cells labeled by endocytosis. In the following experiments, a laser fluence of 2 J/cm^2 was used, for which the cell viability remains above 80% for both FD and CdSe QD (cfr. **Fig. 1c, d**). Following photoporation with the FD or CdSe QD, we monitored the mean fluorescence intensity (MFI) of the labeled cells over multiple generations by flow cytometry. The data in **Fig. 2a** and **b** show the decrease in cell intensity over time relative to the MFI at $t = 0$ (i.e. immediately after labeling). The signal decrease for the photoporated cells (**Fig. 2a, b**) is solely due to dilution of the contrast agent upon subsequent cell divisions. Indeed, with a mono-exponential fit we obtained a cell division time of ~25 h for HeLa cells, which is in perfect agreement with reported values[47]. To corroborate this finding, a similar test was performed on faster (C17.2 cells) and slower (INS-1E cells) dividing cell lines, resulting in the expected doubling times of ~17 and ~39 h, respectively (**Figure S5**). Importantly, a signal decrease that is only attributed to dilution by cell division is the best one can achieve for extrinsic contrast agents. Instead, cells labeled by endocytosis exhibited a much more rapid decrease of the cell signal (**Fig. 2a, b**), due to other processes than cell division alone, most importantly label degradation (CdSe QD) or fluorescence quenching (FD) in the acidic endolysosomes[26, 28].

To more precisely quantify the gain in long-term cell visibility of photoporated cells, we determined the percentage of detectable cells, i.e. cell with an intensity higher than unlabelled control cells, over multiple cell generations by flow cytometry (**Fig. 2c, d**). Although both delivery methods resulted in more than 90% positive cells immediately after cell loading, the number of detectable cells quickly decreased in case of endocytic labeling for both FD and CdSe QD. Already after one cell division 20% of FD labeled cells became undetectable, and after 5 cell divisions the cells could no longer be detected. Instead, when cells were loaded with FD by photoporation, nearly 100% of the cells remained visible for 5 generations. Even after 7 divisions more than 80% of these cells were still detectable. Similar results were found for CdSe QD loaded cells. After one cell division only ~30% of cells labeled by endocytosis could be detected, while this was still >90% for photoporated cells. After three cell divisions >70% of photoporated cells could still be detected, while this was <10% for endocytic labeling. The main reason why FD labeled cells can be detected for much longer time as compared to CdSe QD labeled cells is due to a higher loading efficiency of FD by photoporation (cfr. **Fig. 1c, d**).

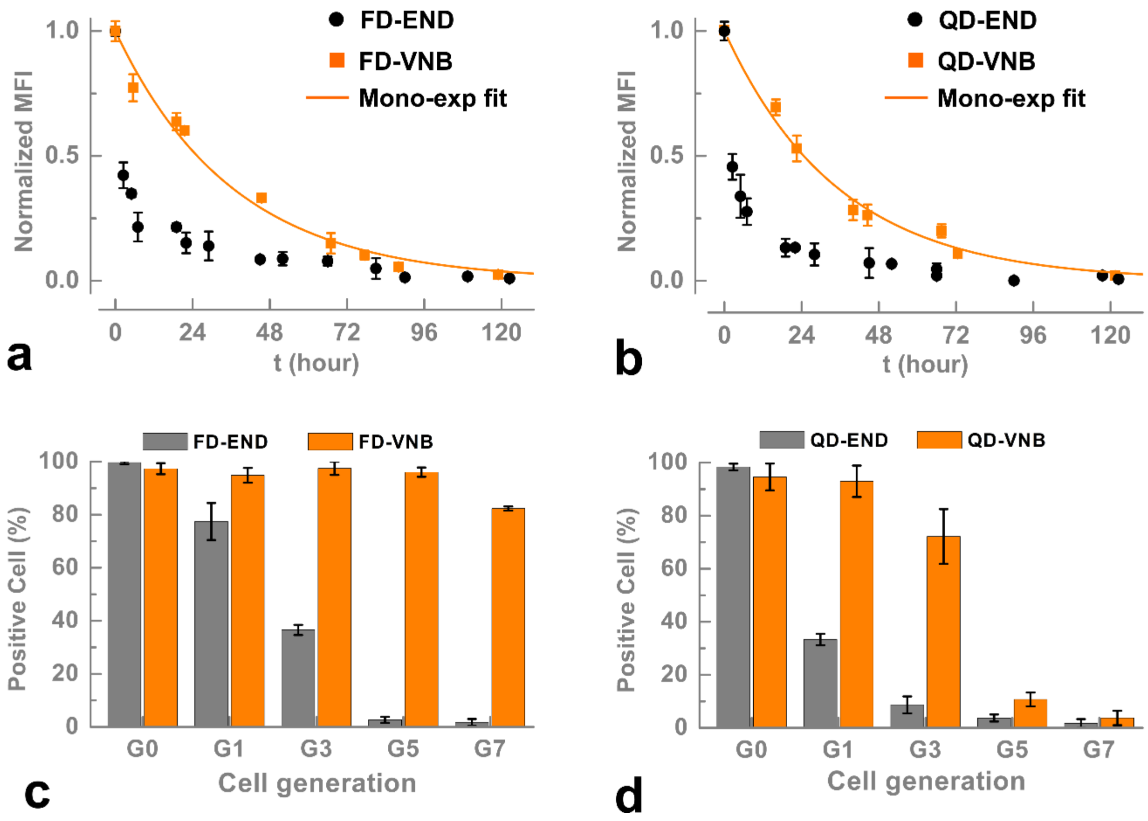

Figure 2. Long-term visibility of HeLa cells labeled by photoporation vs. endocytic labeling. a-b, The normalized MFI is shown in function of time after labeling for cells loaded with FD (a) and CdSe QD (b) via both photoporation (VNB, orange squares in a and b) and endocytic labeling (END, black circles in a and b). Each data point belongs to one of three independent biological repeats; each data point is the average of three technical repeats. A mono-exponential decay function was fitted to the photoporation data to calculate the mean cell division time (orange lines in a and b). c-d, The percentage of detectable cells is shown over several cell generations for respectively FD (c) and CdSe QD (d) labeled cells. Endocytic labeling (END, grey bars in c and d) is compared with cell labeling via photoporation (VNB, orange bars in c and d). (n=3)

Similar experiments were performed with the INS-1E cell line (**Figure S6**). For FD labeled cells the results were identical to those obtained in HeLa cells. For CdSe QD labeled cells the difference between labeling by endocytosis and photoporation were even more pronounced. Almost no cells could be detected after one generation in case of endocytic loading, likely due to the long residence time in the degradative endolysosomes of the slow division rate. Instead, when CdSe QDs were delivered into the cytosol by photoporation, it was only after eight cell divisions that the signal was lost. Taken together, we conclude that delivering labels into the cytosol by photoporation significantly enhances the long-term cell visibility, with a signal decay that is solely determined by cell division. Due to the high loading capacity we find that old-school FDs clearly outperform CdSe QDs for this purpose.

3.3 Cytosolic delivery of contrast agents avoids asymmetric inheritance over daughter cells and the concomitant increase in cell labeling polydispersity.

It is known that contrast agents residing in endocytic vesicles are partitioned unequally between daughter cells during cell division[30, 37]. This results in an increasingly heterogeneous population of labeled cells with each cell division, which confounds quantification of cell numbers in *in vivo* applications. We hypothesized that this drawback can be countered by directly delivering contrast agents into the cell cytoplasm. For a quantitative comparison between endocytosis and photoporation, we selected Alexa fluro@488 labeled dextran (AD) and InP/ZnS core/shell quantum dots (InP QD) which should be less affected by the acidic and degradative environment of the endolysosomes. This is confirmed by **Figure S7** showing that the signal decay over cell generations is only due to cell division after endocytic uptake. Hence, changes in cell intensity are only due to cell division, as is required for these experiments.

In first instance, the mitotic partitioning of the intracellular fluorescent labels in individual HeLa cells was imaged by fluorescence microscopy for two subsequent cell divisions, with pictures being taken every hour. Representative images in **Fig. 3a, b** (also see **Supporting Movie 3-6**) show that the fluorescent labels are diluted upon each imaged cell division. The punctate pattern observed in the cells labeled by endocytosis (END, left panels in **Fig. 3a, b**) is in stark contrast with the homogenous labeling of the entire cell cytoplasm in photoporated cells (VNB, right panels in **Fig. 3a, b**). However, one can still notice a slight punctuate pattern on top of the homogeneous cytosolic labeling after photoporation (see **Supporting Movie 4 and 6**). This is due to a small amount of label endocytosed during the three minutes laser treatment, as confirmed by control experiments where cells were incubated for the three minute with AD and InP QD (**Figure S8**). After two cell divisions the asymmetric partitioning of endocytosed contrast agents over daughter cells can already be noticed on sight (compare for instance D_{11} with D_{12} in **Fig. 3b**).

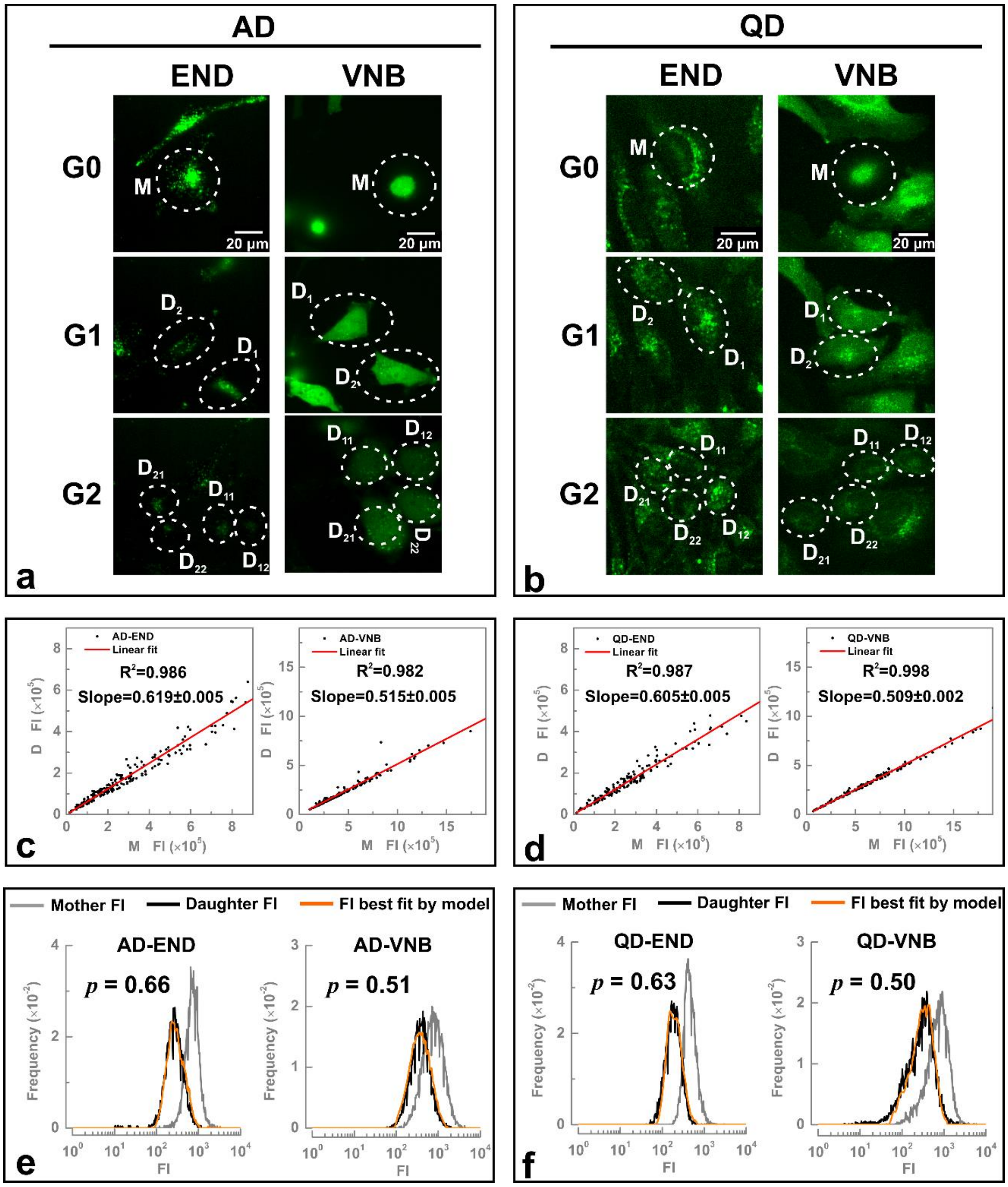

Figure 3. Inheritance of contrast agents in cells labeled by endocytosis or photoporation. a-b, Representative confocal time-lapse images show the redistribution of contrast agents (AD and InP QD) over daughter cells after two subsequent cell divisions. Endocytosed contrast agents are located inside endosomes (punctuate pattern) and are unequally partitioned over daughter cells, e.g. compare D11 and D12 of InP QD labeled cells (END, left panels in a and b). Photoporation results in uniform cytoplasmic labeling and equal distribution of the contrast agents over daughter cells (VNB, right panels in a and b). c-d, Based on image quantification of confocal time lapse images, the fluorescence intensity (FI) of mother cells (n=210 for AD-END, n=205 for AD-VNB, n=172 for InP QD-END, n=155 for InP QD-VNB) is plotted against the FI of their brightest daughter cell. Linear regression shows a slope of ~0.5 for photoporated cells (equal redistribution) and ~0.6 for cells labeled by endocytosis (unequal redistribution). e-f, Flow cytometry was used to quantify the FI of cells immediately after labeling (grey line) and after one cell division (black line). A statistical inheritance model was fitted to the data (orange line) confirming equal inheritance (p = 0.50-0.51) in case of photoporated cells (VNB, right panels in e and f) as opposed to cells labeled by endocytosis (p = 0.63-0.66) (END, left panels in e and f).

To more precisely quantify and characterize the mitotic inheritance of contrast agents in daughter cells, we calculated the fluorescence intensity (FI) for 155-210 mother cells and their respective daughter cells. The FI of the brightest daughter cell is plotted in **Fig. 3c** and **d** against the FI of the mother cell. In case of symmetric division, one expects each daughter cell to contain 50% of the original fluorescence. This is exactly what is observed for the photoporated cells, whose data show a slope of 0.515 for AD and 0.509 for InP QD respectively. In contrast, for cells labeled by endocytosis, the slope is 0.619 for AD and 0.605 for InP QD, implying that one of the daughter cells receives ~60% of the contrast agents (while the other receives ~40%).

To confirm these results, we went on to investigate statistically the inheritance of contrast agents by daughter cells using flow cytometry. The FI was measured immediately after labeling and after one cell division (respectively the grey and black lines in **Fig. 3e-f**). To interpret these results, we developed a statistical model describing the inheritance of materials over daughter cells. The model was applied to the experimental data to obtain the distribution that best matches the observed daughter distribution starting from the mother distribution. The result of the fitting is a parameter *p* that expresses the extent of asymmetry, with 0.5 indicating perfect symmetry. As expected from the microscopy data and in accordance with our hypothesis, for photoporated cells a *p* value of 0.50 and 0.51 was found for AD and InP QD, respectively. This result is independent of the cell type as the same observation was made in a second cell line (C17.2 cells, **Figure S9**). On the contrary, an unequal distribution of endocytosed contrast agents could be confirmed with *p* values of 0.66 for AD and 0.63 for the InP QD.

While an asymmetric division of 40/60 may not seem substantial in the first generation, it does introduce tremendous polydispersity in cell intensity over multiple cell divisions. This can be seen in **Fig. 4** where the FI distributions are shown over multiple generations for endocytic labeling (**Fig. 4a**) and labeling by photoporation (**Fig. 4b**). The polydispersity is plotted as a function of cell generation in **Fig. 4c**, clearly showing that it remains unchanged for cytosolic delivery but increases rapidly for endocytic uptake. Additionally, we applied the statistical inheritance model to the mother distributions (*p* = 0.51 for photoporation and *p* = 0.64 for endocytosis) and found that it accurately predicts the observed polydispersity trend.

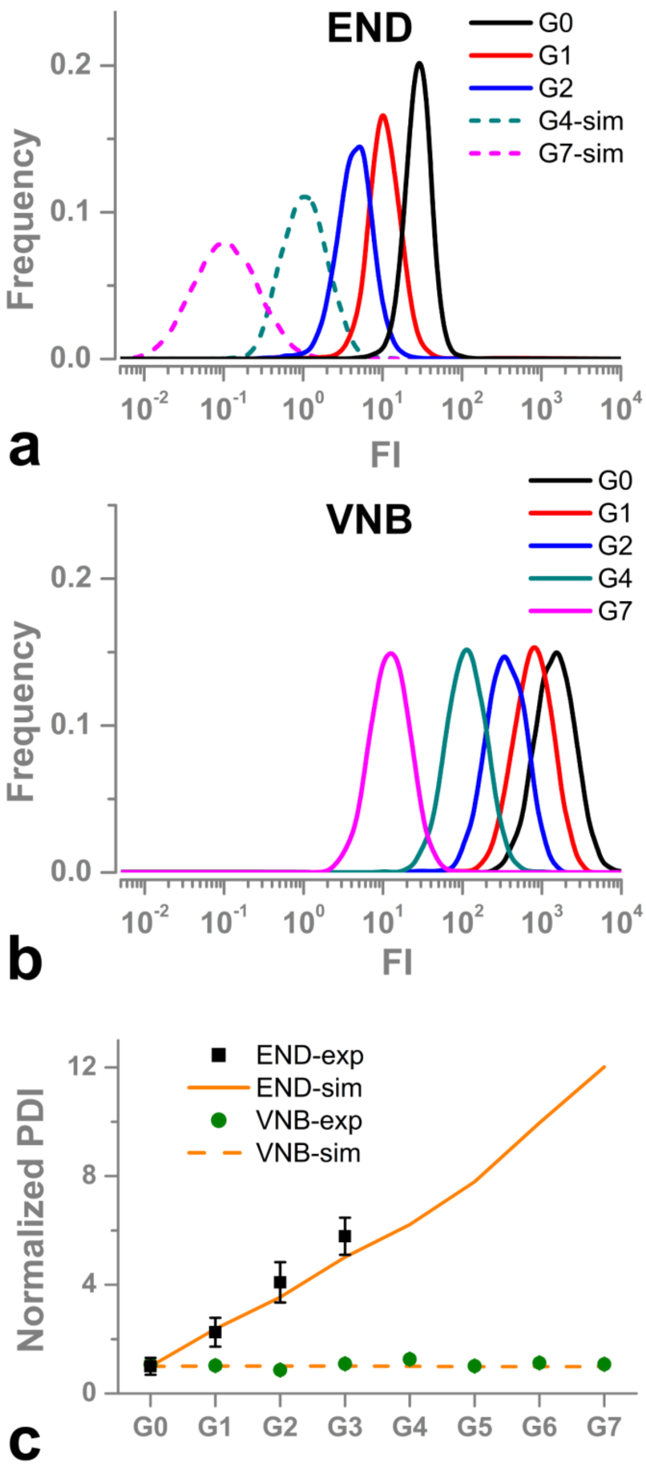

Figure 4. Asymmetric inheritance, leading to highly heterogeneous cell labeling over multiple generations, can be avoided by photoporation. a-b, Distributions of the cell fluorescence intensity (FI) is shown over multiple cell generations (G0-G7) for cells labeled with AD by endocytosis (END) (a) and photoporation (VNB) (b). As for endocytosis the intensity is close to the background after 3 divisions, the statistical inheritance model was applied (p = 0.64) to the mother distribution (G0) to simulate the distributions for G4 and G7 (dashed lines). c, The polydispersity $PDI = (\sigma/\bar{I})^2$ of the distributions remains the same in case of cells labeled by photoporation, while it rapidly increases in case of endocytic labeling. The data is well predicted by the statistical inheritance model with p = 0.64 for endocytosis and p = 0.51 for photoporation.

3.3 Cell labeling by photoporation enables prolonged *in vivo* cell imaging.

Cell transplantation has been proposed as an attractive therapy in a multitude of pathologies. One example is type I diabetes, where insulin producing cells transplantation is a promising strategy to replenish insulin production[48]. In order to visualize whether the transplanted cells reach and remain at their target site, appropriate labeling techniques are required that enable long-term cell tracking. To confirm if the *in vitro* benefits of cell labeling by photoporation are valid *in vivo*, we labeled INS-1E cells with Cy5.5-dextrans and InP/ZnS QD (@690nm) by photoporation and endocytosis. 1 million INS-1E cells were subcutaneously injected in the hind limbs of seven to nine weeks old Swiss Nude mice (left side: unlabelled control cells, right side: labeled cells). Fluorescence and bioluminescence images of the mice were recorded up to 55 days post injection. The fluorescent signal from InP QD labeled cells could not be distinguished from the background for either labeling methods (**Figure S10**) due to the limited loading as compared to fluorescent dextrans (*vide supra*). In contrast, the fluorescent signal of Cy5.5-dextran labeled INS-1E cells could be detected immediately post transplantation (day 0) for cells labeled by both methods **(Fig. 5).** Over time, the fluorescent signal gradually decreased, which resulted in complete signal loss for the cells labeled by endocytosis at day ~15 post injection (**Fig. 5a**). Strikingly, even after 55 days post injection, vapour nanobubble photoporated cells remained clearly detectable (**Fig. 5b**). In addition, the bioluminescent signal remained present at the injection site, which shows that the cells remained alive during the experiment (**Figure S11**). No detectable bioluminescent signal was found in other parts of the mouse bodies, indicating that no substantial amounts of viable cells (> 100) migrated away from the injection site. Note that a gradually increasing signal intensity is visible in the 'upper left part' of the mouse, which is most likely coming from the spleen and may be due to Cy5.5-dextrans that have been cleared from dead or dying cells over the time course of the experiment (two months). Overall, we can conclude that cytosolic cell labeling by photoporation clearly outperforms the classical endocytosis method for long-term *in vivo* cell tracking. Due to its higher loading capacity, we furthermore find that old-school labeled dextrans are better suited for long-term cell imaging than the newer class of more expensive and often cytotoxic QDs.

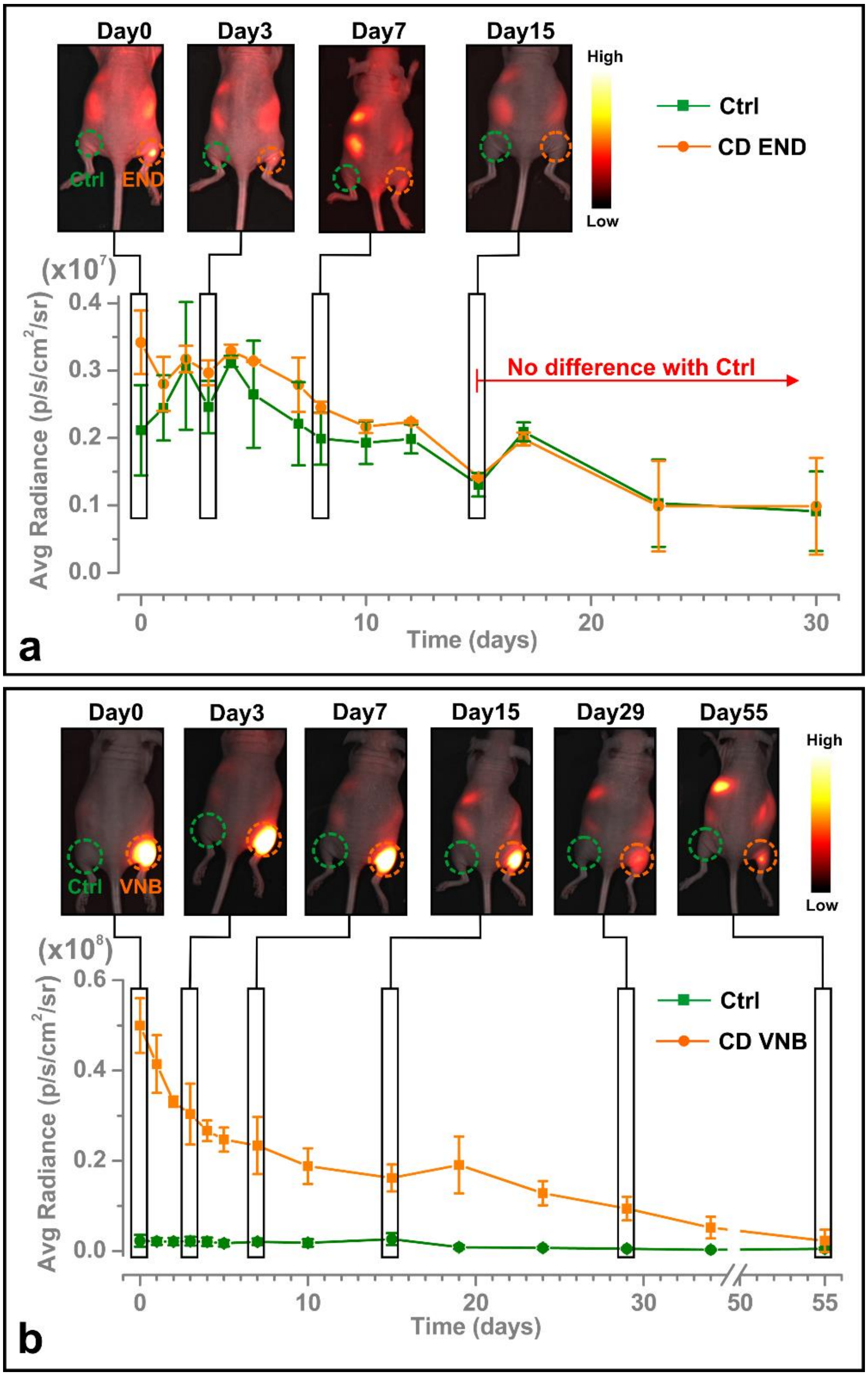

Figure 5. Long term in vivo imaging of transplanted INS-1E cells labeled by either photoporation or endocytosis. INS-1E cells were labeled with Cy5.5-dextran (CD) by (a) endocytic uptake (END) or (b) photoporation (VNB). labeled cells were subcutaneously injected right hind limb of Swiss Nude mice. Unlabelled control cells were injected at left side. For three independent repeats, the fluorescence was quantified over time of labeled (orange) and unlabelled (green) cells in the indicated regions of interest (ROI). Photoporated cells were still clearly visible after 55 days, as opposed to cells labeled by endocytosis which disappeared already after 15 days.

4. DISCUSSION

For *in vivo* imaging of transplanted cells, labeling with the desired contrast agents is classically performed *via* simple incubation and subsequent internalization by endocytosis. This means that the contrast agent will typically be sequestered in endolysosomes, which is associated with a number of potential drawbacks. Endocytic uptake is typically time-consuming, has limited loading capacity, may lead to quenching or degradation of labels with concomitant increased cytotoxicity, and results in asymmetric division over daughter cells. In this work we hypothesized that these shortcomings could be largely alleviated by delivering contrast agents directly into the cytosol. Photoporation was chosen to this end, as it was recently shown by our group and others to be a fast, efficient and non-toxic method to deliver therapeutic agents into the cytosol of cells, independent of cell type[40, 43, 45]. Following adsorption of a small number of gold nanoparticles to the cell membrane (~8 per cell), cells receive a single ns laser pulse so as to induce transient membrane pores by the mechanical force of vapour nanobubbles. Exogenous labels that are supplied in the cell medium can then diffuse through the pores into the cytoplasm. A particular benefit of photoporation by vapour nanobubbles is that there is no net heat transfer to the cellular environment. This means that cells experience less cytotoxicity as compared to the more traditional photothermal treatment at lower laser intensities in which case small pores are induced by heating of the cell membrane[43, 49].

As a single ns pulse per cell is sufficient, the photoporation procedure is essentially limited by the laser repetition rate. The laser used in this work had a (limited) repetition rate of 20 Hz which resulted in a treatment time of 3 min for a single well of a 96 well plate. While this is already much faster than endocytic labeling, we expect that speed can be increased further in the future by at least one order of magnitude by switching to a picosecond laser with higher repetition rate[40].

As contrast agents can be distributed throughout the entire cytoplasm, photoporation allows much higher cell labeling efficiency as compared to endocytic uptake, where contrast agents are restrained to the endolysosomal compartments. For 10 kDa FITC-dextran we observed a 50-fold increase in cell loading compared to endocytosis independent of cell type. As QDs are larger (slower diffusion) and can only be supplied in a lower molar concentration (due to cost and toxicity), the difference in loading capacity was less pronounced, but photoporation was still 3 times more efficient than endocytic uptake of CdSe QD.

When analysing the fluorescence intensity of cells labeled by endocytosis over multiple generations, we noticed that the signal intensity rapidly decreased for both FITC-dextran and CdSe QD labeled cells. Sequestration in the acidic and degradative endolysosomes results in quenching of the fluorescein label (which is strongly pH dependent) and degradation of the CdSe QD[29]. Instead, when the same labels were delivered into the cytosol by photoporation, the signal decrease over multiple cell generations was only due to dilution in the daughter cells. Again these results were cell-independent since the same observations were made for three different cell types, including therapeutically relevant insulin producing INS-1E cells. In addition, endosomal sequestration of CdSe QD resulted in noticeable concentration-dependent toxicity, which could be largely avoided when delivered in the cytosol by photoporation. This is in agreement with a recent publication where metallic NPs were found to cause cell injury when sequestered in endosomes, but not when delivered straight into the cytoplasm[50].

Nanomaterials, like QDs, present in the endolysosomes are known to be distributed unevenly over daughter cells upon cell division[30]. Here we could confirm this observation and report for the first time that it is equally true for endocytosed molecular agents like Alexa Fluor dextran. This is perhaps not so surprising in light of the recent finding that asymmetric inheritance of vesicles is a naturally occurring cellular process[37]. Indeed, asymmetric cell division appears to be a crucial biological feature that does not only provide protection against exogenous materials, but is also involved in differentiation towards various lineages[51, 52]. Here, we hypothesized that asymmetric inheritance of contrast agents could be avoided by delivering the labels directly into the cell cytoplasm. In that case the labels are homogeneously distributed throughout the cytoplasm and there is no active mechanism that the cell can use anymore (such as motor proteins in case of endosomes) to shuttle the nanomaterials preferentially to one of the daughter cells. This was confirmed with labeling by photoporation independent of label and cell type. In contrast, in case of endocytosis, labels were divided over daughter cells in a 40/60 ratio. While this may not seem like a major problem on first sight, it does pose problems for accurate quantification of cell numbers in *in vivo* imaging after multiple cell divisions. Indeed, already after 6 generations the label polydispersity will have increased 10-fold so that it becomes increasingly difficult to accurately relate the detected signal to cell numbers. Instead, equal inheritance after cytosolic loading by photoporation ensures that the polydispersity does not increase over cell generations. This means that signal quantification remains equally accurate over time in long-term cell tracking studies, which is of major importance for instance for following-up on cell therapies. To our knowledge, this is the first time that it is shown that asymmetric inheritance of exogenous materials can be avoided by delivering labels directly into the cytosol.

Finally, we imaged INS-1E cells *in vivo* labeled by photoporation or endocytosis. Following the injection of labeled cells in seven to nine weeks old Swiss Nude mice, we found that cells labeled with Cy5.5-dextran by photoporation can be imaged up to two months. Instead, cells labeled by endocytosis completely lost their fluorescent signal after two weeks. Due to less efficient loading with InP QD, the fluorescent signal from InP QD labeled cells could not be distinguished from the background for neither labeling method. This shows that old-school fluorescent dextrans are excellent labels for cell tracking *in vivo*, especially in combination with photoporation. Taken together, we can state that we developed a highly efficient and safe method to label cells that enables straightforward long term cell tracking.

Here, photoporation was selected for the cytosolic delivery of contrast agents into live cells since it has been shown to enable efficient loading at high throughput and with low toxicity. Although it needs to be demonstrated in future research, it could be expected that similar findings on long-term visibility and symmetric inheritance in daughter cells may be obtained with other methods that enable cytosolic delivery of contrast agents. For instance, electroporation could be explored to this end, although it is typically associated with high cell death[53] and for QD it was reported to result in marked aggregation[54]. Also molecular approaches are developed to this end where contrast agents are conjugated to ligands that – hopefully – can translocate the contrast agents into the cytoplasm, either directly across the cell membrane or across endosomal membranes after endocytic uptake. Examples are CFSE (Carboxyfluorescein succinimidyl ester)[55], but also CPP (cell-penetrating peptide) conjugates[56]. Yet it is clear that such strategies require special development of conjugates for each type of label, apart from the fact that the efficiency may be very much cell-dependent. Instead, a fast and efficient method like photoporation is entirely independent of the type of label or cell type used, and we expect that this method will see quickly increasing applications for intracellular delivery in general.

5. CONCLUSIONS

Direct cytosolic delivery of nano-sized contrast agents by photoporation opens up exciting avenues for improved long-term quantitative *in vivo* cell tracking. Apart from much more efficient cell loading and prolonged cell visibility *in vitro* and *in vivo* as compared to endocytic labeling, we show for the first time that asymmetric inheritance of labels can be avoided by delivering the labels directly into the cytosol through photoporation. As photoporation is independent of the cell type and contrast agent used, we expect that it will be a major benefit for improved long-term cell tracking studies. While this study focused on fluorescence labels, it will be of interest to evaluate in the future cell labeling with e.g. superparamagnetic iron oxide nanoparticles or Gd-complexes for magnetic resonance imaging.

6. REFERENCES

1. Taylor, A., Wilson, K.M., Murray, P., Fernig, D.G. & Levy, R. Long-term tracking of cells using inorganic nanoparticles as contrast agents: are we there yet? *Chem Soc Rev* **41**, 2707-2717 (2012).
2. Brader, P., Serganova, I. & Blasberg, R.G. Noninvasive Molecular Imaging Using Reporter Genes. *J Nucl Med* **54**, 167-172 (2013).
3. Tabar, V. & Studer, L. Pluripotent stem cells in regenerative medicine: challenges and recent progress. *Nat Rev Genet* **15**, 82-92 (2014).
4. Himmelreich, U. & Dresselaers, T. Cell labeling and tracking for experimental models using Magnetic Resonance Imaging. *Methods* **48**, 112-124 (2009).
5. Sherry, N.A., Tsai, E.B. & Herold, K.C. Natural history of beta-cell function in type 1 diabetes. *Diabetes* **54**, S32-S39 (2005).
6. Zou, W.P. Regulatory T cells, tumour immunity and immunotherapy. *Nat Rev Immunol* **6**, 295-307 (2006).
7. Cao, F. et al. In vivo visualization of embryonic stem cell survival, proliferation, and migration after cardiac delivery. *Circulation* **113**, 1005-1014 (2006).
8. McCracken, M.N. et al. Long-term in vivo monitoring of mouse and human hematopoietic stem cell engraftment with a human positron emission tomography reporter gene. *P Natl Acad Sci USA* **110**, 1857-1862 (2013).
9. Bhaumik, S. & Gambhir, S.S. Optical imaging of Renilla luciferase reporter gene expression in living mice. *P Natl Acad Sci USA* **99**, 377-382 (2002).
10. Vande Velde, G., Himmelreich, U. & Neeman, M. Reporter gene approaches for mapping cell fate decisions by MRI: promises and pitfalls. *Contrast Media Mol I* **8**, 424-431 (2013).
11. Nguyen, P.K., Riegler, J. & Wu, J.C. Stem Cell Imaging: From Bench to Bedside. *Cell Stem Cell* **14**, 431-444 (2014).
12. Ransohoff, J.D. & Wu, J.C. Imaging Stem Cell Therapy for the Treatment of Peripheral Arterial Disease. *Curr Vasc Pharmacol* **10**, 361-373 (2012).
13. Gu, E., Chen, W.Y., Gu, J., Burridge, P. & Wu, J.C. Molecular Imaging of Stem Cells: Tracking Survival, Biodistribution, Tumorigenicity, and Immunogenicity. *Theranostics* **2**, 335-345 (2012).
14. Dean, K.M. & Palmer, A.E. Advances in fluorescence labeling strategies for dynamic cellular imaging. *Nat Chem Biol* **10**, 512-523 (2014).
15. Sutton, E.J., Henning, T.D., Pichler, B.J., Bremer, C. & Daldrup-Link, H.E. Cell tracking with optical imaging. *Eur Radiol* **18**, 2021-2032 (2008).
16. Walter, G.C., Phillips, R.J., Baronowsky, E.A. & Powley, T.L. Versatile, high-resolution anterograde labeling of vagal efferent projections with dextran amines. *J Neurosci Meth* **178**, 1-9 (2009).
17. Clarke, J.W. in Molecular Embryology, Vol. 461. (eds. P. Sharpe & I. Mason) 351-361 (Humana Press, 2009).
18. Wegner, K.D. & Hildebrandt, N. Quantum dots: bright and versatile in vitro and in vivo fluorescence imaging biosensors. *Chem Soc Rev* **44**, 4792-4834 (2015).
19. Michalet, X. et al. Quantum dots for live cells, in vivo imaging, and diagnostics. *Science* **307**, 538-544 (2005).
20. Gao, X.H., Cui, Y.Y., Levenson, R.M., Chung, L.W.K. & Nie, S.M. In vivo cancer targeting and imaging with semiconductor quantum dots. *Nat Biotechnol* **22**, 969-976 (2004).
21. Xu, C.J. et al. Tracking Mesenchymal Stem Cells with Iron Oxide Nanoparticle Loaded Poly(lactide-co-glycolide) Microparticles. *Nano Lett* **12**, 4131-4139 (2012).
22. Guzman, R. et al. Long-term monitoring of transplanted human neural stem cells in developmental and pathological contexts with MRI. *P Natl Acad Sci USA* **104**, 10211-10216 (2007).
23. Irvine, D.J., Swartz, M.A. & Szeto, G.L. Engineering synthetic vaccines using cues from natural immunity. *Nat Mater* **12**, 978-990 (2013).
24. Jirak, D. et al. MRI of transplanted pancreatic islets. *Magnet Reson Med* **52**, 1228-1233 (2004).

25. Oh, E. et al. Meta-analysis of cellular toxicity for cadmium-containing quantum dots. *Nat Nano* **advance online publication** (2016).
26. Soenen, S.J. et al. The effect of nanoparticle degradation on poly(methacrylic acid)-coated quantum dot toxicity: The importance of particle functionality assessment in toxicology. *Acta Biomater* **10**, 732-741 (2014).
27. Su, Y.Y. et al. The cytotoxicity of CdTe quantum dots and the relative contributions from released cadmium ions and nanoparticle properties. *Biomaterials* **31**, 4829-4834 (2010).
28. Martens, T.F., Remaut, K., Demeester, J., De Smedt, S.C. & Braeckmans, K. Intracellular delivery of nanomaterials: How to catch endosomal escape in the act. *Nano Today* **9**, 344-364 (2014).
29. Soenen, S.J., Demeester, J., De Smedt, S.C. & Braeckmans, K. The cytotoxic effects of polymer-coated quantum dots and restrictions for live cell applications. *Biomaterials* **33**, 4882-4888 (2012).
30. Summers, H.D. et al. Statistical analysis of nanoparticle dosing in a dynamic cellular system. *Nat Nanotechnol* **6**, 170-174 (2011).
31. Terreno, E. et al. Effect of the intracellular localization of a Gd-based imaging probe on the relaxation enhancement of water protons. *Magnet Reson Med* **55**, 491-497 (2006).
32. Strijkers, G.J., Hak, S., Kok, M.B., Springer, C.S. & Nicolay, K. Three-Compartment T(1) Relaxation Model for Intracellular Paramagnetic Contrast Agents. *Magnet Reson Med* **61**, 1049-1058 (2009).
33. Gianolio, E. et al. Photochemical Activation of Endosomal Escape of MRI-Gd-Agents in Tumor Cells. *Magnet Reson Med* **65**, 212-219 (2011).
34. Yan, Y. et al. Particles on the Move: Intracellular Trafficking and Asymmetric Mitotic Partitioning of Nanoporous Polymer Particles. *Acs Nano* **7**, 5558-5567 (2013).
35. Walczak, P., Kedziorek, D.A., Gilad, A.A., Barnett, B.P. & Bulte, J.W.M. Applicability and limitations of MR tracking of neural stem cells with asymmetric cell division and rapid turnover: The case of the shiverer dysmyelinated mouse brain. *Magnet Reson Med* **58**, 261-269 (2007).
36. Errington, R.J. et al. Single cell nanoparticle tracking to model cell cycle dynamics and compartmental inheritance. *Cell Cycle* **9**, 121-130 (2010).
37. Derivery, E. et al. Polarized endosome dynamics by spindle asymmetry during asymmetric cell division. *Nature* **528**, 280-+ (2015).
38. Shao, J. et al. Near-Infrared-Activated Nanocalorifiers in Microcapsules: Vapor Bubble Generation for In Vivo Enhanced Cancer Therapy. *Angewandte Chemie International Edition* **54**, 12782-12787 (2015).
39. Wu, Z. et al. Near-Infrared Light-Triggered “On/Off” Motion of Polymer Multilayer Rockets. *Acs Nano* **8**, 6097-6105 (2014).
40. Lukianova-Hleb, E.Y., Wagner, D.S., Brenner, M.K. & Lapotko, D.O. Cell-specific transmembrane injection of molecular cargo with gold nanoparticle-generated transient plasmonic nanobubbles. *Biomaterials* **33**, 5441-5450 (2012).
41. Boulais, E., Lachaine, R. & Meunier, M. Plasma Mediated off-Resonance Plasmonic Enhanced Ultrafast Laser-Induced Nanocavitation. *Nano Lett* **12**, 4763-4769 (2012).
42. Pustovalov, V.K., Smetannikov, A.S. & Zharov, V.P. Photothermal and accompanied phenomena of selective nanophotothermolysis with gold nanoparticles and laser pulses. *Laser Phys Lett* **5**, 775-792 (2008).
43. Xiong, R. et al. Comparison of Gold Nanoparticle Mediated Photoporation: Vapor Nanobubbles Outperform Direct Heating for Delivering Macromolecules in Live Cells. *Acs Nano* **8**, 6288-6296 (2014).
44. Lukianova-Hleb, E.Y. et al. On-demand intracellular amplification of chemoradiation with cancer-specific plasmonic nanobubbles. *Nat Med* **20**, 778-784 (2014).
45. Baumgart, J. et al. Off-resonance plasmonic enhanced femtosecond laser optoporation and transfection of cancer cells. *Biomaterials* **33**, 2345-2350 (2012).
46. Skirtach, A.G. et al. The role of metal nanoparticles in remote release of encapsulated materials. *Nano Lett* **5**, 1371-1377 (2005).

47. Berger, S.M. et al. Quantitative analysis of conditional gene inactivation using rationally designed, tetracycline-controlled miRNAs. *Nucleic Acids Res* **38** (2010).
48. Wu, Z. et al. In Vivo Imaging of Transplanted Islets with 64Cu-DO3A-VS-Cys40-Exendin-4 by Targeting GLP-1 Receptor. *Bioconjugate Chem* **22**, 1587-1594 (2011).
49. Lukianova-Hleb, E.Y., Mutonga, M.B.G. & Lapotko, D.O. Cell-Specific Multifunctional Processing of Heterogeneous Cell Systems in a Single Laser Pulse Treatment. *Acs Nano* **6**, 10973-10981 (2012).
50. Guarnieri, D. et al. Transport across the cell-membrane dictates nanoparticle fate and toxicity: a new paradigm in nanotoxicology. *Nanoscale* **6**, 10264-10273 (2014).
51. Knoblich, J.A. Asymmetric cell division: recent developments and their implications for tumour biology. *Nat Rev Mol Cell Bio* **11**, 849-860 (2010).
52. Coumailleau, F., Furthauer, M., Knoblich, J.A. & Gonzalez-Gaitan, M. Directional Delta and Notch trafficking in Sara endosomes during asymmetric cell division. *Nature* **458**, 1051-1055 (2009).
53. Rubinsky, B., Onik, G. & Mikus, P. Irreversible electroporation: A new ablation modality - Clinical implications. *Technol Cancer Res T* **6**, 37-48 (2007).
54. Derfus, A.M., Chan, W.C.W. & Bhatia, S.N. Intracellular delivery of quantum dots for live cell labeling and organelle tracking. *Adv Mater* **16**, 961-+ (2004).
55. Hawkins, E.D. et al. Measuring lymphocyte proliferation, survival and differentiation using CFSE time-series data. *Nat Protoc* **2**, 2057-2067 (2007).
56. Erazo-Oliveras, A. et al. Protein delivery into live cells by incubation with an endosomolytic agent. *Nat Methods* **11**, 861-867 (2014).

7. SUPPLEMENTARY INFORMATION

Supporting Figures

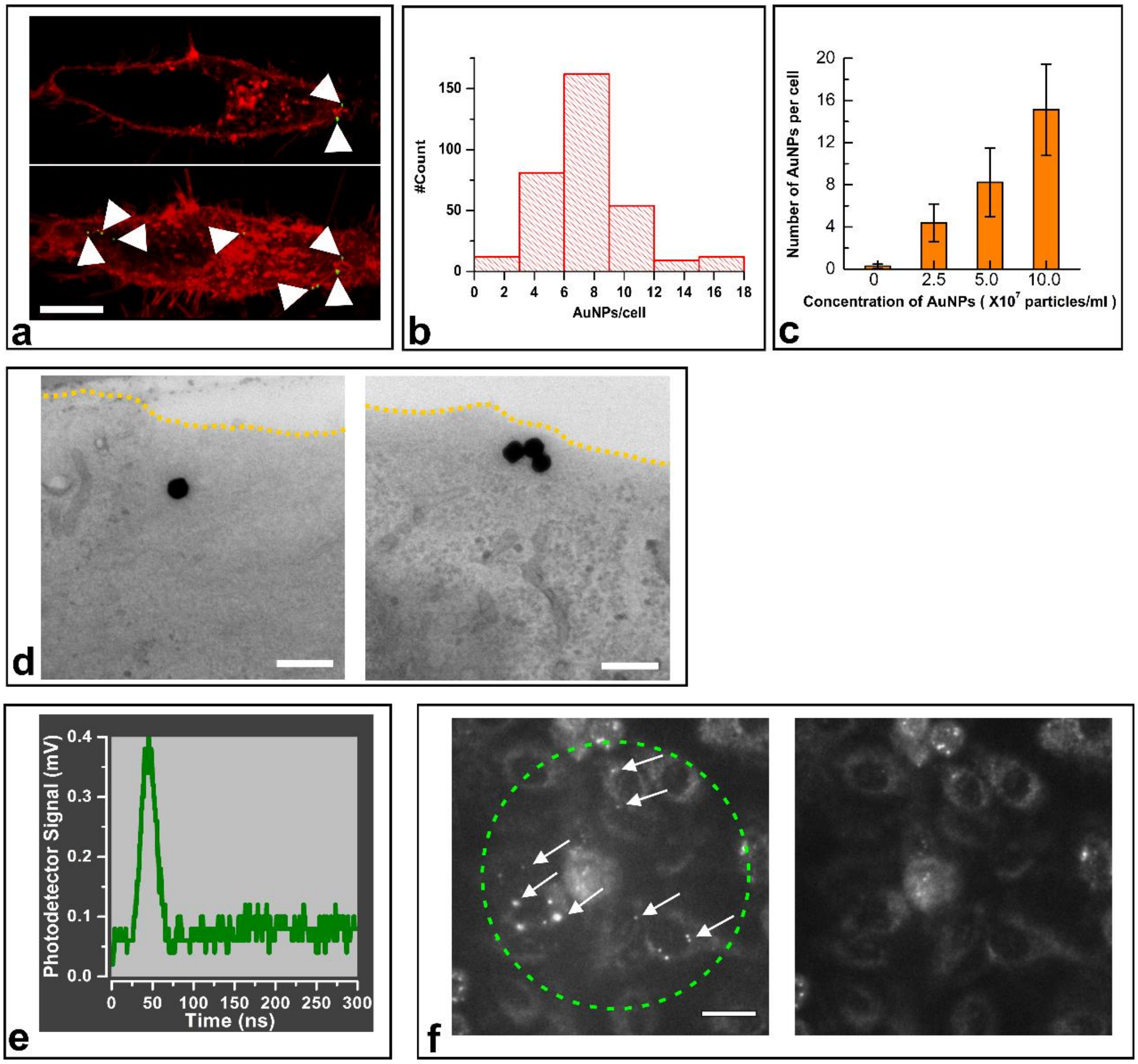

Figure S1. Detection of cell associated AuNPs and laser-induced VNB (vapour nanobubble). a, Cell associated AuNPs are visualized by confocal microscopy. HeLa cells are labeled with red fluorescent CellMask, which stains lipid membranes. AuNP are detected in confocal reflectance mode, false-colored in green and indicated by white arrow heads. The confocal section at the top shows that AuNP are located close to the plasma membrane. The bottom image is a z-projection of an entire cell showing all cell-associated AuNP. Scale bar is 5 µm. b, By analyzing confocal z-projections of 330 cells, the number of AuNP per cell was determined for cells incubated with 5×107 particles/ml. c, The average number of cell associated AuNP can be controlled by changing the concentration of AuNP in the cell medium (n = 3). d, TEM images show that AuNP are internalized just below the plasma membrane (indicated by the yellow dashed line). Scale bars are 200 nm. e, Laser-induced VNB formation can be detected with a photodiode that detects transmitted laser light. A change in transmitted light occurs due to changes in refractive index upon VNB formation. This method allows to monitor the lifetime of the laser-induced VNBs, which was ~40 ns in the example shown. f, VNBs can be also be detected by dark-field microscopy as the bubbles efficiently scatter light. The green circle indicates the area in which the laser pulse is applied and the white arrows indicate VNBs (Scale bar is 20 µm). The right image shows the same cells when the VNBs have disappeared.

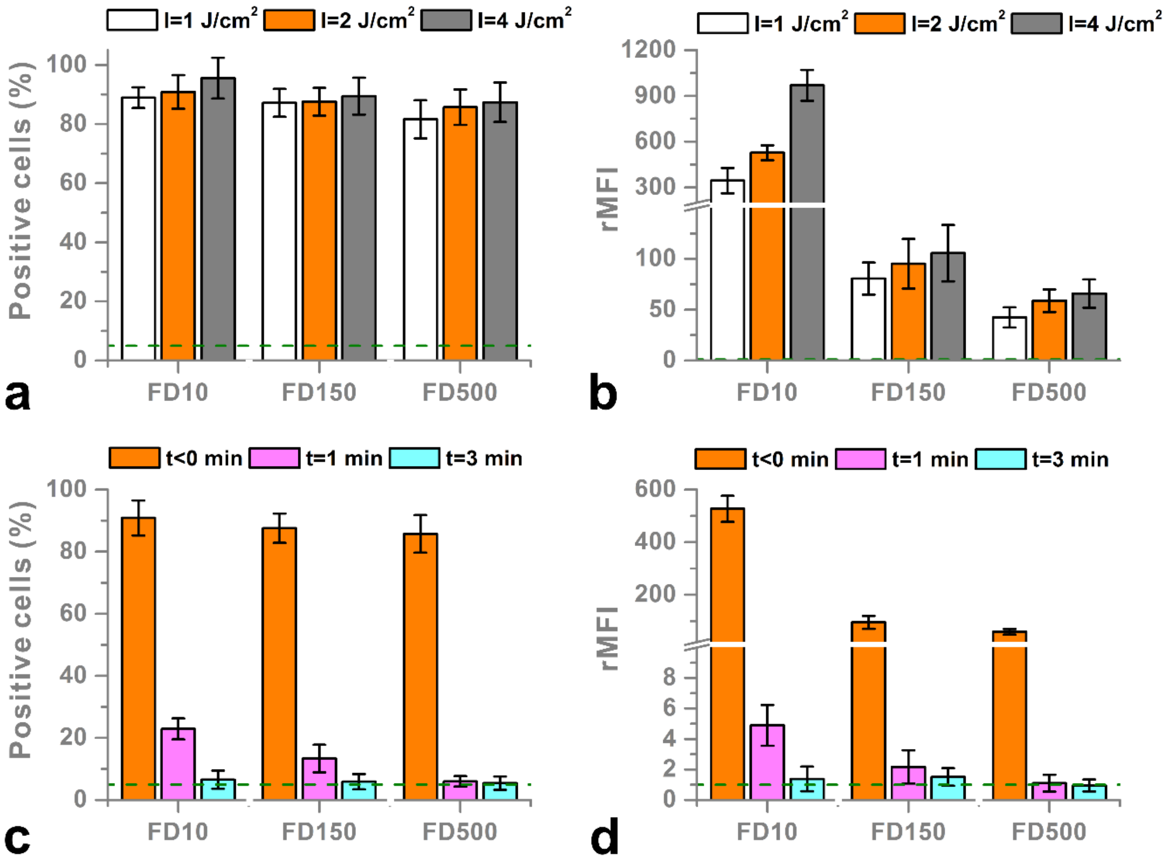

Figure S2. Investigation of the size and lifetime of VNB induced membrane pores. a-b, FD10, FD150 and FD500 was delivered by VNB mediated photoporation using three different laser fluences and quantified in terms of the percentage of positive cells and the relative mean fluorescence intensity per cell (rMFI). While >80% of the cells become positively loaded with any of the probes for all laser fluence conditions, the rMFI clearly shows that the delivery efficiency decreases substantially as the probes increase in size. The rMFI increases slightly with increasing laser fluence, likely due to bigger pores being formed when larger VNBs are generated. c-d, To assess the lifetime of the transient membrane pores, photoporation was performed at a laser fluence of 2 J/cm2 in the presence of the probes, or with probes added 1 or 3 min after the photoporation procedure. To keep the photoporation time to a minimum, an area of 1.5 by 1.5 mm in a 96-well plate was treated, taking only ~7 s in total. The green dashed line shows the percentage of negative control cells (i.e. same treatment but without AuNPs added to cells). These data show that pores are quickly closing in a matter of 1-2 min and that bigger probes are, consequently, excluded faster from entry than smaller ones. (n=3)

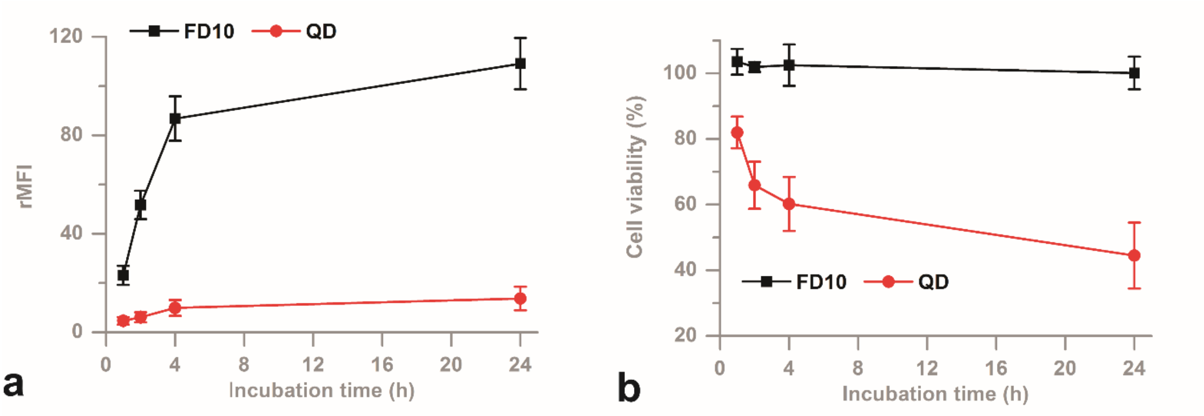

Figure S3. a, Both FD10 and QDs are increasingly internalized over longer incubation times. b, Cell viability measurements show that QD toxicity becomes too high for incubation times exceeding 1h.

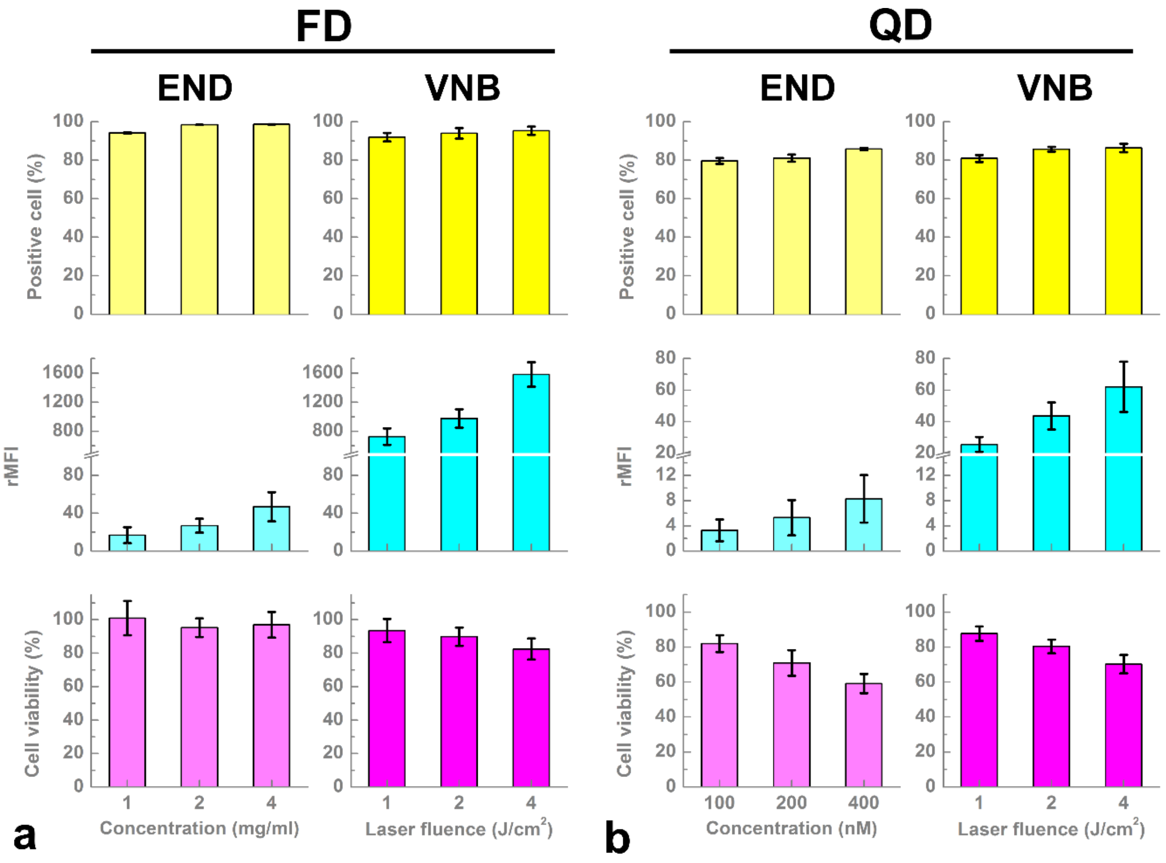

Figure S4. Loading of contrast agent into INS-1E cells by photoporation and endocytosis. Quantification of FD (a) or CdSe QD (b) positive cells as a function of incubation concentration for endocytic labeling (END, light yellow bars of top left panels in a and b) and laser fluence from 1 to 4 J/cm^2 for photoporation (VNB, yellow bars in top right panels in a and b), respectively. The loading amount labels of FD and CdSe QD by photoporation as a function of laser fluence ranged from 1 to 4 J/cm^2 (cyan of middle right panels in a and b) compared with the endocytic uptake with function of labels concentration (light cyan bars of middle left panels in a and b). The effect of VNB loading FD and CdSe QD in conjunct with both labels present in cytosol on the cell viability (magenta of bottom right panels in a and b), in comparison with the cell viability induced by classically labeling method of endocytosis as a function of the labels of FD and CdSe QD incubation concentration (light magenta bars of bottom right panels in a and b). The data were shown as mean of three times of measurements with SD.

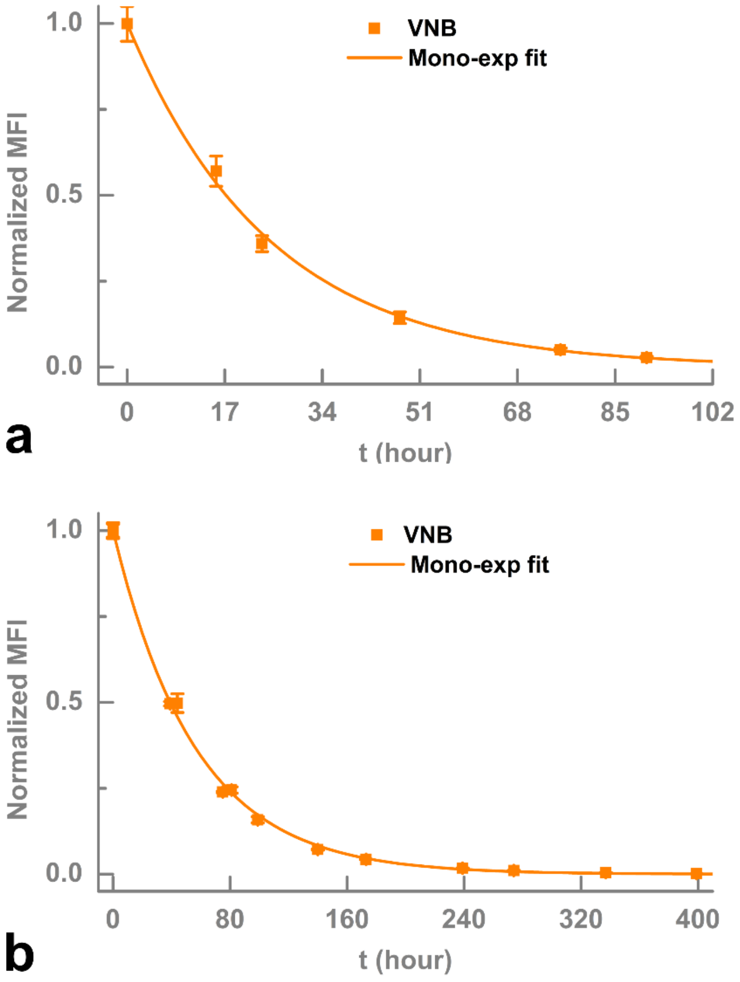

Figure S5. Long-term visibility of C17.2 and INS-1E cells labeled with FD by photoporation. A cell line C17.2 with fast cell division time (a) and INS-1E with slow cell division time (b) were used to further validate that the fluorescence intensity decay is mainly caused by partitioning of the fluorescent nanomaterials present in cytosol. MFI for each type of cell was measurement by flow cytometer with 10000 cells at each time points indicated in figure. The data point was shown as the average of three times measurement. The formula (2) was used to normalized the MFI to obtain the y-axis normalized MFI. Finally, the data points were fitted by mono-exponential (formula (3), $\overline{MFI} = 2^{-(\frac{t}{\tau})}$) to calculate the average of cell division time and yielded τ=17.2 h ± 1.8 for C17.2 and τ=39.0 h ± 4.2.

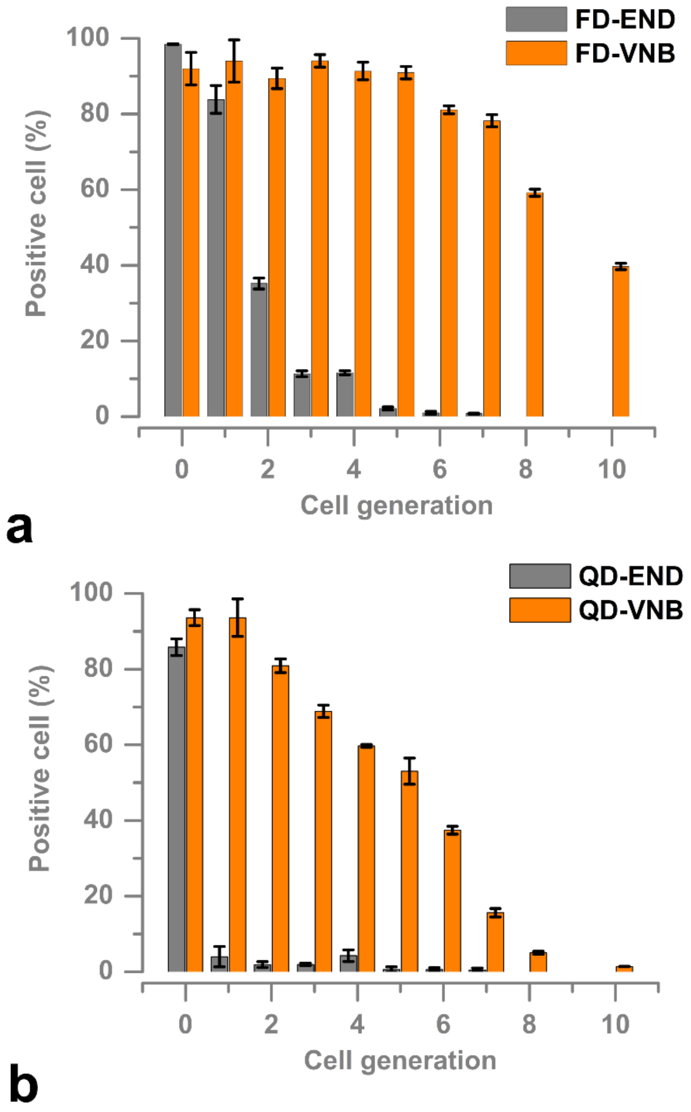

Figure S6. INS-1E cell visibility over multiple cell generations in vitro. The INS-1E cells were labeled with FD (a) and CdSe QD (b) by photoporation (VNB) and endocytosis (END). The percentage of detectable cells was quantified by flow cytometry. The data are shown as the mean of three independent repeats. The error bars indicate the corresponding standard deviation.

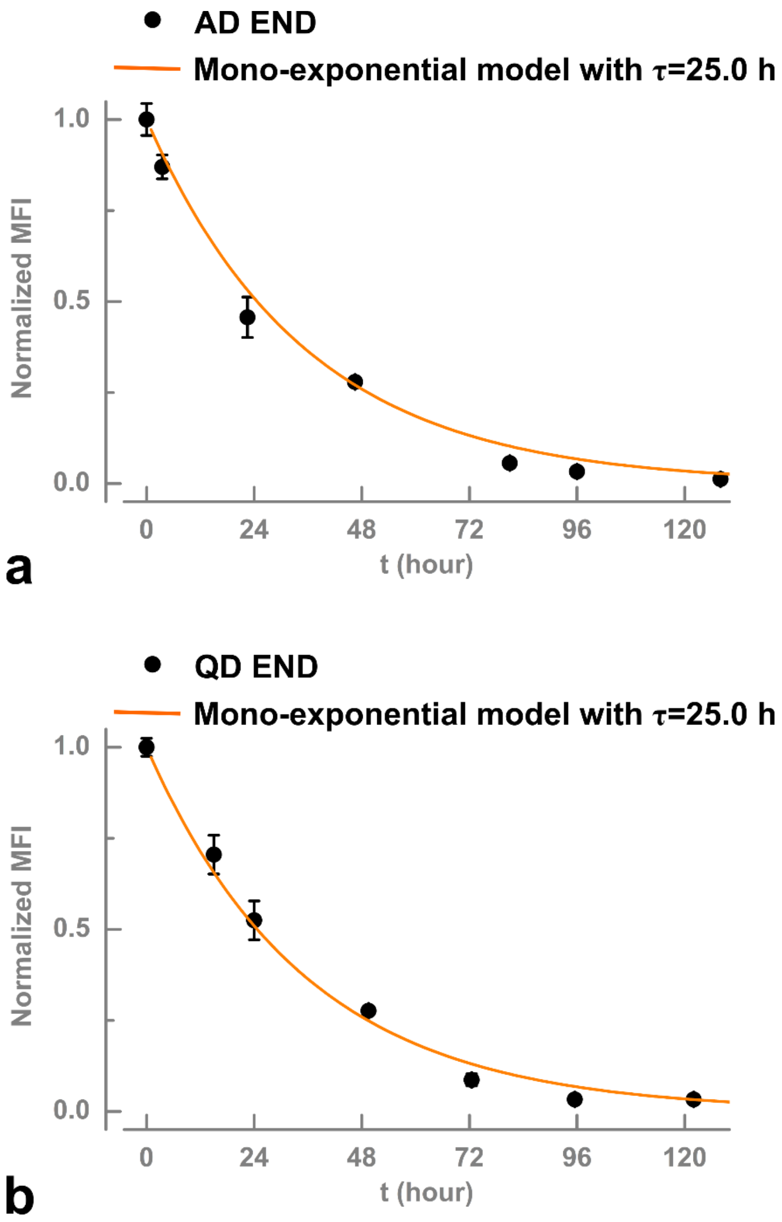

Figure S7. Long-term visibility of HeLa cells labeled with AD (Alexa Fluor dextran) and InP/ZnS QD by endocytosis. The mean fluorescence was determined by flow cytometry over multiple cell generations. A mono-exponential model with a mean cell division time of τ=25 h describe the data well, as expected for HeLa cells. This demonstrates that these labels are not affected by the degradative environment of the endo-lysosomes and that the decrease in contrast is due to dilution of daughter cells only.

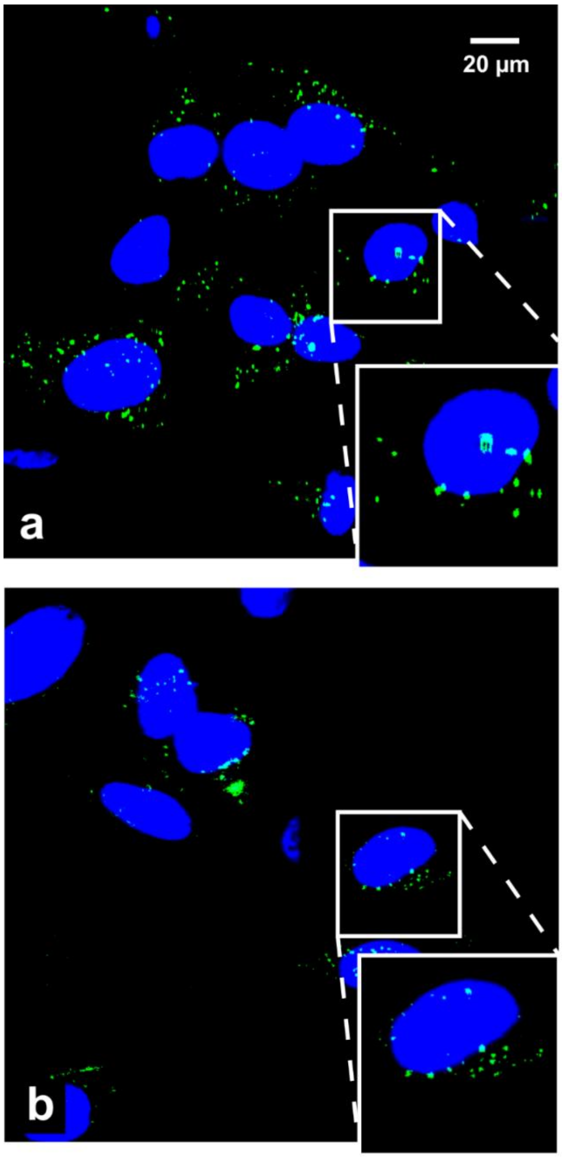

Figure S8. Endocytosis of AD and InP QD during laser treatment. To check the amount of labels that are internalized through endocytosis during the laser treatment for photoporation, cells were incubated with AD (2 mg/ml) and InP QD (1 µM) for 3 min at room temperature. This is the time needed to photoporate a whole well of cells in a 96-well plate. A small amount of labels is internalized during that time, which explains the slight punctuate pattern that can be seen in **Supporting Movie 4, 6** after photoporation.

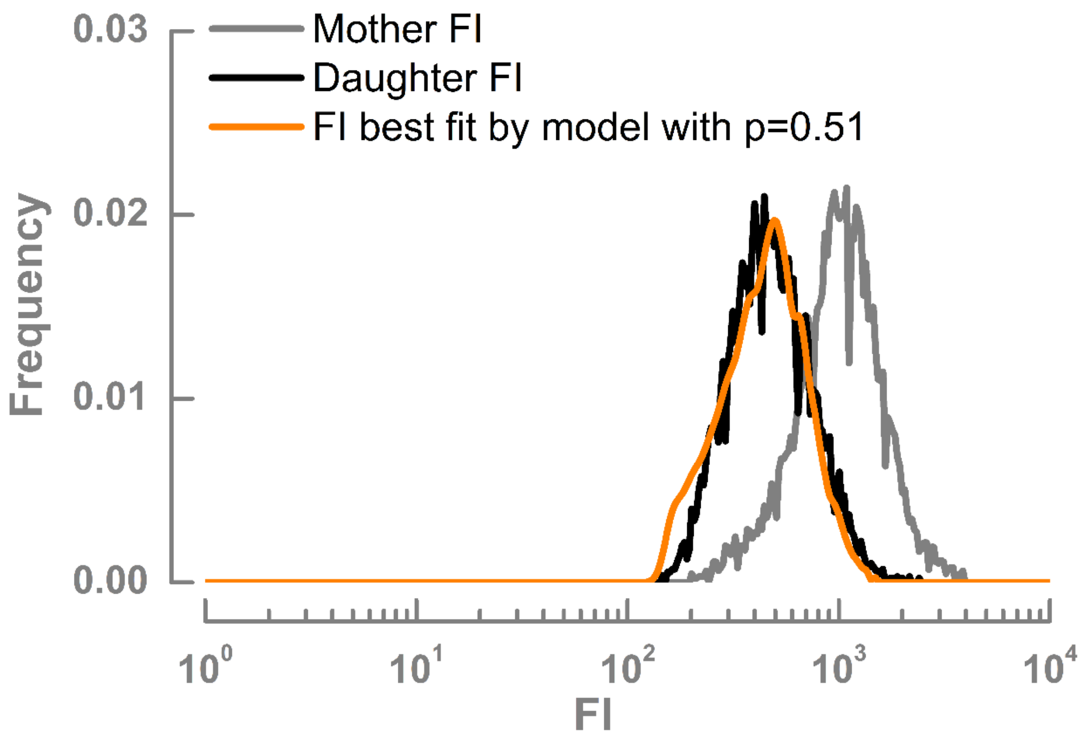

Figure S9. Symmetric or equal redistribution of nanomaterials directly delivered into cytosol over cell division was again validated by C17.2 cell line. FI (fluorescence intensity) distribution of mother cells measured by flow cytometry after photoporation labeling cells (grey line) and FI distributions of first generation of daughter cell populations by experimental measurement (black line). The orange line in the figure show FI distributions of the daughter cells by the best fitting binomial probability of 0.51 with experimentally measured FI distributions.

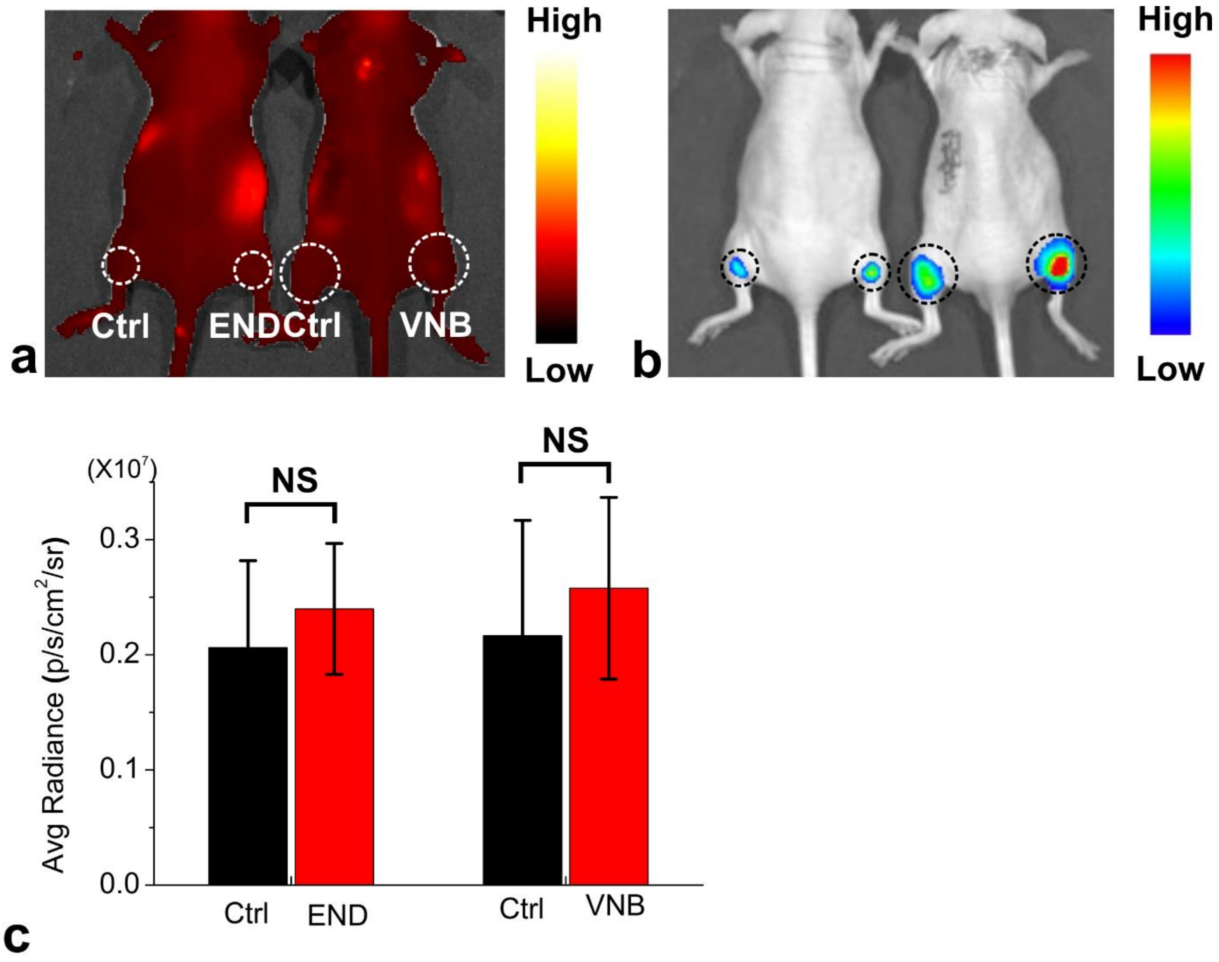

Figure S10. In vivo tracking of INS-1E cells labeled by InP QD with either photoporation or endocytosis. a-b, In vivo fluorescence (a) and bioluminescence images (b) of the cells labeled by InP QD via photoporation (VNB) and endocytosis (END) at immediately post transplantation. c,The quantified fluorescence signals in region of interest (ROI) transplanted site indicated by cycles in a (n=3). No significant differences were found between control and labeling samples. The data was compared by one-way ANOVA.

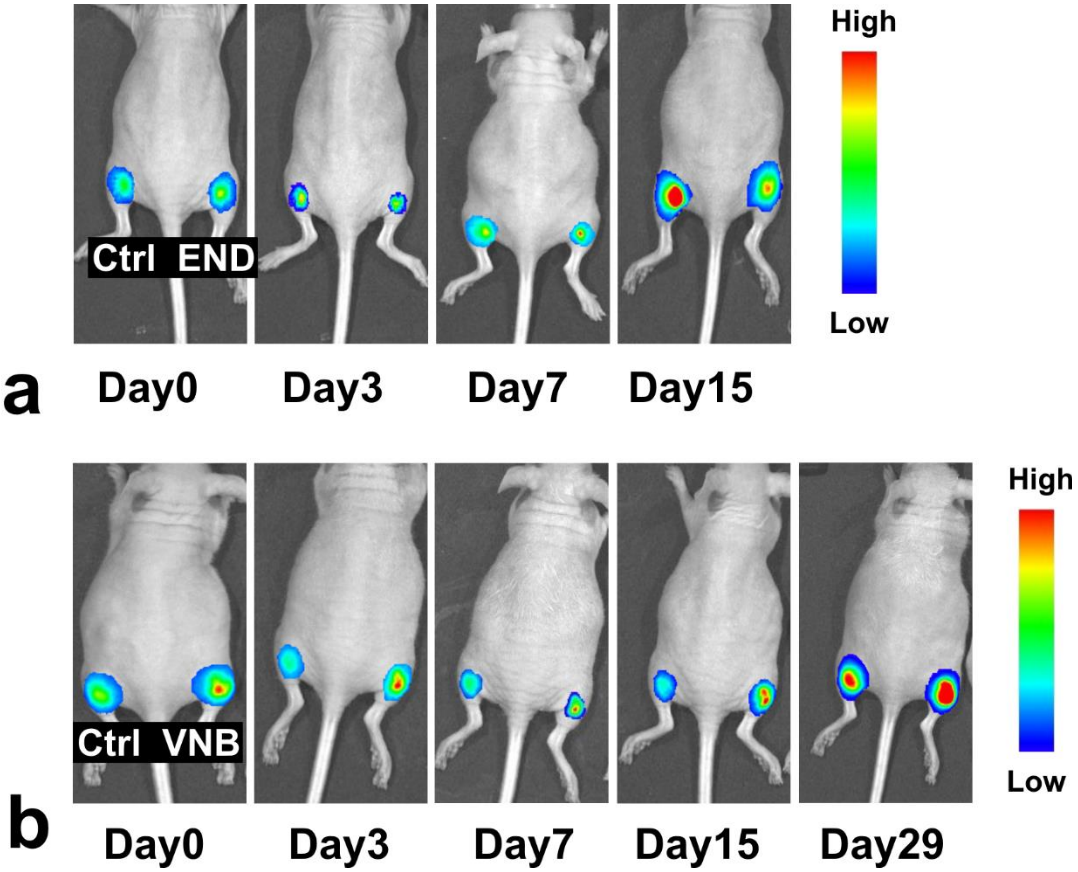

Figure S11. Bioluminescence of INS-1E cells over time. Representative in vivo bioluminescence images of the cells labeled by Cy5.5-dextran via endocytosis (END, a) or photoporation (VNB, b) at the indicated post transplantation days.

Supporting Movies

Supporting Movie 1. Cell associated AuNPs are visualized by confocal microscopy. HeLa cells are labeled with red fluorescent CellMask, which stains lipid membranes. AuNP are detected in confocal reflectance mode, false-colored in green. (https://figshare.com/s/f7109f56fe250a430d10)

Supporting Movie 2. To validate cytosolic delivery by photoporation, the cytoplasmic accumulation of cell impermeable dye of Propidium Iodide (PI) was in situ recorded by fluorescence microscopy before and after photoporation. A laser fluence of 2 J/cm2 was used and the laser irradiation region was indicated with a white circle in the movie. Images were recorded at a rate of 1 s/frame. A single laser pulse was applied between t = 12 s and 13 s, after which PI influx can be clearly seen at distinct locations in the irradiated cells. The view of movie is ~120 µm by ~120 µm. (https://figshare.com/s/f86b0aad38c2ac61fddc)

Supporting Movie 3. Redistribution of endocytosed AD in HeLa cells over two cell divisions. The cells were incubated with 2 mg/ml AD for one hour at 37 °C. After washing, cells were imaged in a stage-top cell incubator (37 °C) with confocal microscopy for 28 hours. (https://figshare.com/s/a2176d03678ab60f8583)

Supporting Movie 4. Redistribution of AD in HeLa cells labeled by photoporation over two cell divisions. Cells were labeled with AD by photoporation. After washing the AD, cells were imaged in a stage-top cell incubator (37 °C) with confocal microscopy for 41 hours. (https://figshare.com/s/5fc2713e1ea74771886b)

Supporting Movie 5. Redistribution of endocytosed InP QD in HeLa cells over two cell divisions. The cells were incubated with 400 nM InP QD for one hour at 37 °C. After washing, cells were imaged in a stage-top cell incubator (37 °C) with confocal microscopy for 33 hours. (https://figshare.com/s/5bcfb8c8abc52864e34f)

Supporting Movie 6. Redistribution of InP QD in HeLa cells labeled by photoporation over two cell divisions. Cells were labeled with InP QD by photoporation. After washing the QD, cells were imaged in a stage-top cell incubator (37 °C) with confocal microscopy for 43 hours. (https://figshare.com/s/7a5db6309df4ee0888e9)

Chapter 4

Subcellular labeling with functionalized QDs enabled by VNB photoporation

ABSTRACT

There is considerable interest in using Quantum Dots (QDs) as fluorescent probes for cellular imaging due to some of their unique properties. In comparison with conventional molecular dyes they offer improved photostability, increased brightness and narrow emission peaks. While they have been used for subcellular labeling of fixed cells, their application to living cells is very limited so far mainly due to inefficient cytosolic delivery of QDs. Here, we demonstrate that VNB photoporation offers the long awaited ability to deliver functionalized QDs efficiently into the cytosol of cells for labeling of subcellular structures. First we confirm highly efficient delivery of PEG-coated QDs into living cells. We obtain >80% positive cells, while the cell viability remains as high as ~85%. Next, we show that antibody functionalized QDs targeted to the microtubules can be delivered into the cytoplasm of living cells. While the final contrast is limited due to the presence of unbound QDs, microtubules can be visualized by confocal microscopy. Although clearly further work is needed to better control the amount of QDs that are delivered into the cells, it does show the potential of VNB photoporation to become a versatile tool for the delivery of exogenous labels for subcellular microscopic visualization.

1. INTRODUCTION

Quantum Dots (QDs) have attracted considerable interest as fluorescent probes in many biological and biomedical applications, especially for cellular imaging[1-10]. In comparison with conventional organic dyes, QDs have several unique advantages such as broad absorption with narrow emission spectra, high resistance to photobleaching, and size-tunable fluorescent emission spectra[11-14]. Although QDs have been already been applied to subcellular labeling of fixed cells, their application to live cell imaging is virtually non-existent. Their use for live cell imaging has remained limited to labeling of membrane proteins which can be easily reached from the outside[10, 13, 15, 16]. In order to be used as general intracellular labels, a method is needed to deliver QDs unambiguously into the cytosol of cells[5, 8]. Extensive efforts have gone into developing such intracellular delivery methods for QDs. These include modification of QDs with cell penetrating peptides (CPP)[17, 18], or usage of transfection reagents[19-22]. However, all of these methods suffer from the same problem, which is that only a part of the QDs actually reaches the cytosol, while the majority remains entrapped in endosomes. Indeed, endosomal entrapment is considered as one of the major bottlenecks for the cytosolic delivery of exogenous nanomaterials by means of chemical transfection agents[23]. For that reason more generic physical delivery approaches have been explored, such as electroporation and microinjection. However, a typical problem of electroporation is that it causes high toxicity to the cells or even aggregation of the QDs[24]. While microinjection can be used for the cytosolic delivery of QDs[24-27], it is a slow and demanding technique which is not suited to label a large number of cells. Recently, a new microfluidic device was introduced where friction forces are used for cell membrane permeabilization. It was demonstrated that it could be used to deliver QDs into live cells with limited cytotoxicity, although the efficiency was limited to about 50% positive cells[28]. In any case it was not used for subcellular labeling with functionalized QDs. In addition, this method can only be applied to cells in suspension, while for microscopy cells are typically adherent. Therefore, it is clear that there still is the need to develop a generic technology for the cytosolic delivery of QDs into live adherent cells with high efficiency, high throughput, low toxicity.

Since in **chapter 3** we demonstrated efficient delivery of QDs in living cells for in vivo cell tracking, here we explored if VNB photoporation allows to deliver antibody functionalized QDs into living cells for subcellular labeling. First we confirm that PEG-coated QDs can be delivered efficiently and with low toxicity in living HeLa cells by VNB photoporation. Next we repeat this for antibody functionalized QDs targeted to microtubules and show successful confocal visualization of those structures. While further optimization is certainly needed, it does demonstrate that VNB photoporation is a promising method for that purpose.

2. MATERIALS AND METHODS

Materials. 530 (+/-10) nm CdSe/ZnS Fluorescent nanocrystals coated with thiol oligomer and surface functionalized with -COOH groups (PEG-coated QDs) was purchased from AC Diagnostics, Inc. (#CAQD-530-P-1, AC Diagnostics, Inc., Fayetteville, AR, USA). The SiteClick™ Qdot® 525 Antibody Labeling Kit was purchased from Invitrogen (#S10449, Molecular Probes®, Belgium). SiteClick™ labeling specifically attaches the heavy chains of an IgG antibody to the QDs ensuring that the antigen binding domains remain available for binding to the antigen target. This is achieved by targeting the carbohydrate domains present on essentially all IgG antibodies regardless of isotype and host species. The primary mouse anti-α-Tubulin antibody (#32-2500, Novex®, Belgium) and the secondary Alexa Fluor® 546 goat anti-mouse IgG antibody (#A11003, Belgium) were also purchased from Invitrogen. Cationic AuNPs of 70 nm were purchased from NanoPartz (#C2159, Nanopartz Inc., Loveland, CO, USA). These AuNPs had a zeta potential of 30 mV as measured by dynamic light scattering (NanoSizer, Malvern, UK). FITC-dextrans with molecular weight of 500 kDa were purchased from Sigma-Aldrich (Belgium). Calcein red AM (#C34851, CellTrace, Belgium) was obtained from Invitrogen.

Cell experiments. The proof-of-concept study in this chapter was performed on HeLa cells. Before laser treatment, HeLa cells (1.5×10^4 cells/well) were grown in DMEM/F-12 cell medium with 2 mM glutamine, 10% heat-inactivated fetal bovine serum (FBS, Hyclone) and 100 U/mL penicillin/streptomycine. Cells were cultured in 96 well plates (#655892, Greiner Bio-One, Germany) at 37° in a humidified atmosphere containing 5% CO_2 for 24 hours before photoporation. For photoporation, the cells were incubated with AuNPs for 30 min at a fixed concentration of 5.0×10^8 nps/mL (corresponding to ~8 nps/cell). The cells were subsequently washed to remove any remaining free AuNPs in solution. Just prior to starting the laser irradiation, the solution of extracellular agents was added to the cells. After laser treatment, the cells were washed and supplied with fresh cell medium. CellTrace® Calcein red AM was added to the samples for 45 min at room temperature to stain living cells for quantifying cell viability.

For validation of the live cell labeling experiments, immunolabeling of fixed cells was performed as well. First, cells were seeded for one day in an 8-well chamber at a density of 40000 cells/well. Next, cells were washed two times with PBS and fixed by 4% paraformaldehyde for 10 min at room temperature. Afterwards, cells were washed two times again and permeabilized with 0.1% Triton for 5 min at room temperature. Blocking solution of 3% BSA in PBS was added for 1h at room temperature to reduce non-specific binding of antibodies followed by two times washing. Then, anti-α-Tubulin antibody functionalized QDs were added at a concentration of 10 µg/ml for 2 hours at room temperature. Next, the secondary antibody was added at 50 µg/ml in PBS during 1h at room temperature. Finally, confocal images were recorded of the stained cells with 60× water-immersion lens (Plan Apo VC 60× WI, Nikon, Badhoevedorp, The Netherlands).

Generation and detection of VNBs. A homemade setup including optical system and electronic timing system was used to generate and detect the generation of VNBs[29].

Imaging of the samples after photoporation. After photoporation, to estimate the delivery efficiency and cell viability, at least 5 confocal images were acquired with a confocal laser scanning microscope (C1si, Nikon, Japan). Using a 10× lens (CFI Plan Apochromat, Nikon, Badhoevedorp, The Netherlands), each image has a field of view of 1.27 mm by 1.27 mm with several hundreds to more than a thousand cells per image. Imaging was performed in three channels, one for green fluorescence (505/520 nm) for label detection (dextrans or QDs), one for red fluorescence (575/620 nm) for imaging of the cell viability probe, and one for the transmission image. A Matlab (#R2007b, The MathWorks, Natick, MA, USA) program was written for automated quantification of cell fluorescence and viability (Calcein Red AM). First, the mean fluorescence intensity of each cell was measured in both fluorescence channels. Green fluorescence resembles cell loading of extracellular agents, and red fluorescence is used for quantifying cell viability. Untreated cells are used to define the threshold for positive cells, where the threshold value is defined as the 95% level of untreated cells. Similarly, cells are considered to be alive when the red fluorescence intensity is higher than the 95% level of dead cells. A 60× water-immersion lens was used for high-resolution imaging of microtubules stained with QD.

3. RESULTS AND DISCUSSION

3.1 Intracellular delivery of PEG-QDs into live cells.

First we evaluated the delivery of PEG-coated QDs into live cells. Four laser irradiation conditions were evaluated: 026, 0.52, 1.04 and 2.08 J/cm^2. In line with the findings from **Chapter 2**, the results in **Fig. 1** show that VNB photoporation is more efficient than photothermal treatment with lower laser intensity. By repeating the VNB photoporation procedure two times, even more QDs could be loaded into the cells. No obvious toxicity was observed based on the fluorescence of the cell viability probe Calcein AM. Quantification shows that ~60% positive cells were obtained with one round of VNB photoporation, which increased to more than 80% after the second photoporation treatment (**Fig. 1**). At the same time the mean fluorescence intensity (MFI) was more than three times higher for VNB photoporation as compared to photothermal treatment. The MFI increased by another factor of 2-3 when VNB photoporation was carried out two times. From quantification of the Calcein AM signal, it was found that cell viability was as high as ~85% for 2x VNB photoporation. The results can further confirmed by the confocal imaging results (**Fig. 1**). From these results we can conclude that PEG-coated QDs can be efficiently delivered into live cells with limited toxicity by a double VNB photoporation treatment.

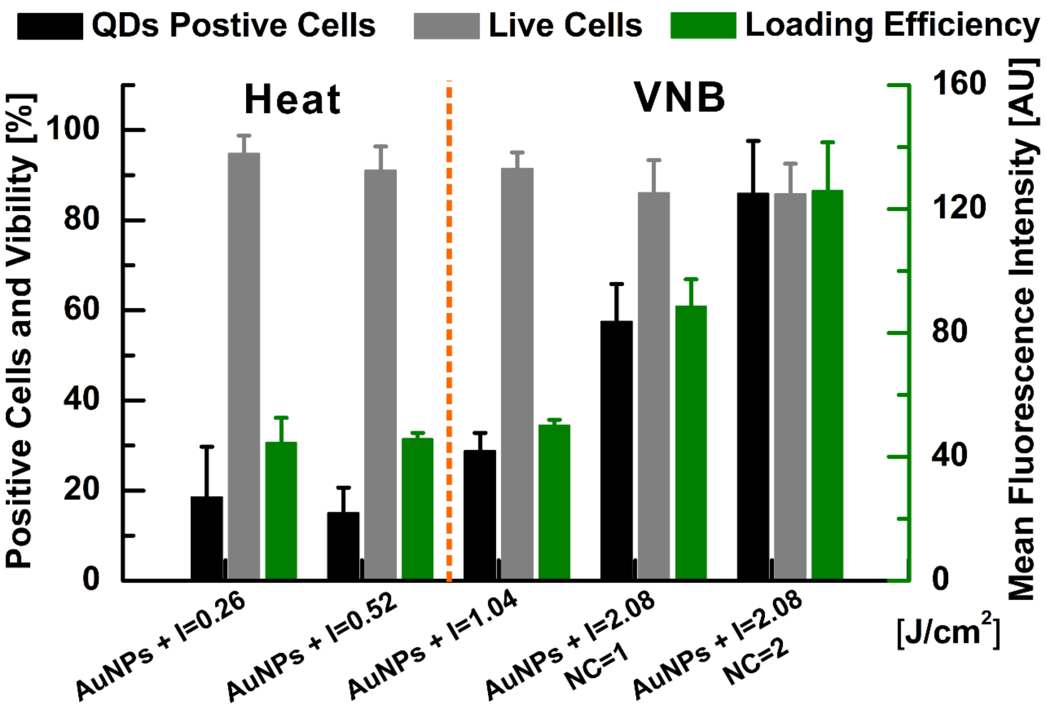

Figure 1. Delivery efficiency of QDs and cell viability for different photoporation conditions. Black bars are the percentage of positive cells, gray bars are the percentage of live cells and green bars are the mean fluorescence intensity (MFI) per cell. The MFI is a measure for the amount of QDs that are delivered per cell. The data shown are the results from three independent experiments.

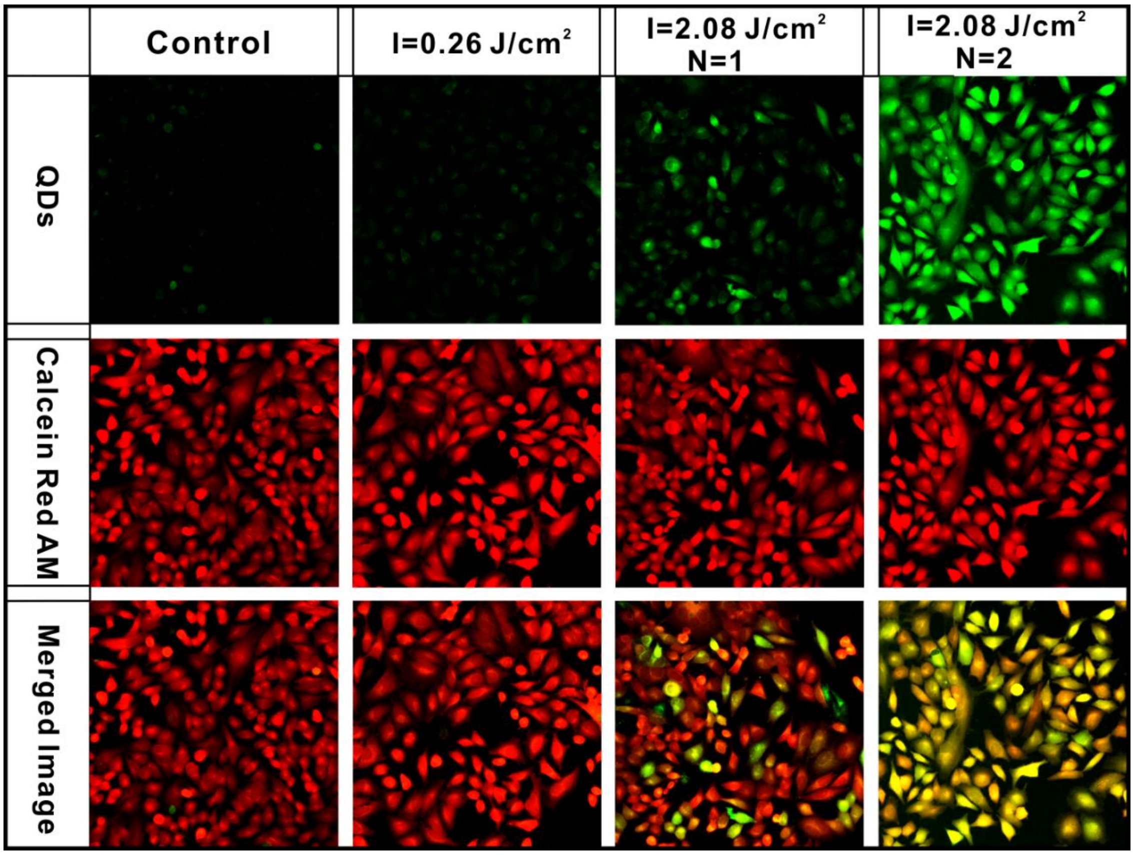

Figure 2. Confocal images showing the delivery of PEG-coated QDs in the green channel and the viability of HeLa cells labeled with calcein red AM in the red channel. Cells were treated with different photoporation conditions as indicated in the figure. The control cells underwent exactly the same procedure as for 1x treatment at a fluence of 2.08 J/cm^2, but in the absence of AuNPs. The field of view of these images is 410 µm by 410 µm.

3.2 Delivery of QDs targeted to microtubules in living cells.

First, green-fluorescent QDs were conjugated to IgG antibody (mouse anti-ɑ-Tubulin) by the SiteClick^{TM} method as explained in the methods section. To confirm successful functionalization, a control experiment was performed where fixed cells were immunolabeled with both the functionalized QDs and red-fluorescent antibodies. Cells were at first fixed and permeabilzed, and subsequently incubated with a primary antibody against the microtubules (mouse anti-ɑ-Tubulin). Next, the orange-red fluorescent secondary antibody (goat anti-mouse IgG antibody) was added which binds to the primary antibody. Finally, the cells were incubated with the functionalized QDs. Confocal images confirmed good colocalization of the functionalized QDs with the labeled antibodies (**Fig. 3**). Filamentous structures could be clearly seen as expected for microtubules, thus confirming successful functionalization of QDs with the primary antibody.

Next, the antibody functionalized QDs were delivered into live cells by VNB photoporation (double photoporation with laser fluence of 2.08 J/cm^2). As shown in **Fig. 4**, filamentous microtubule structures can be clearly observed indicating successful delivery and binding of the QDs to their target. Contrast is rather limited, though, likely due to the presence of unbound QDs in the cytosol. Judging from the Calcein Red AM signal the cells are still alive after the photoporation procedure (inset **Fig. 4A**). As a negative control, non-functionalized PEG-coated QDs were delivered into HeLa cells as well, showing not any subcellular structures (**Fig. 5**). This proof-of-concept experiment shows that antibody functionalized QDs can be very well targeted to subcellular structures in living cells.

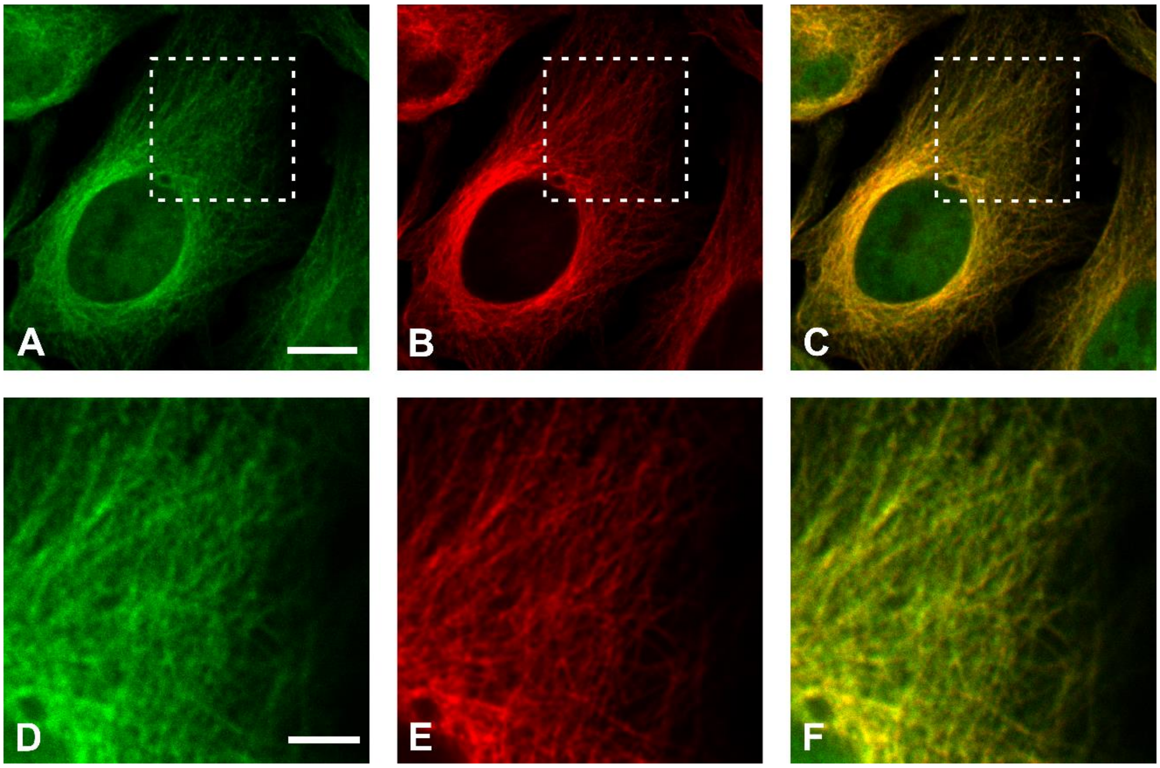

Figure 3. Confocal images showing microtubules in fixed and permeabilized HeLa cells. A comparison is made between QDs functionalized with a primary antibody against α-Tubulin and standard immuno-labeling with a primary and secondary (labeled) antibody. A. Confocal image in green channel showing the green fluorescence of the QDs functionalized with the primary antibody. B. Confocal image of red-labelled microtubules with primary and secondary antibody.. The overlay of green and red channel is shown in C. D-F. Zoomed-in images corresponding to the rectangular regions in A, B and C, respectively. Scale bars are 20 µm(A) and 5 µm(D), respectively.

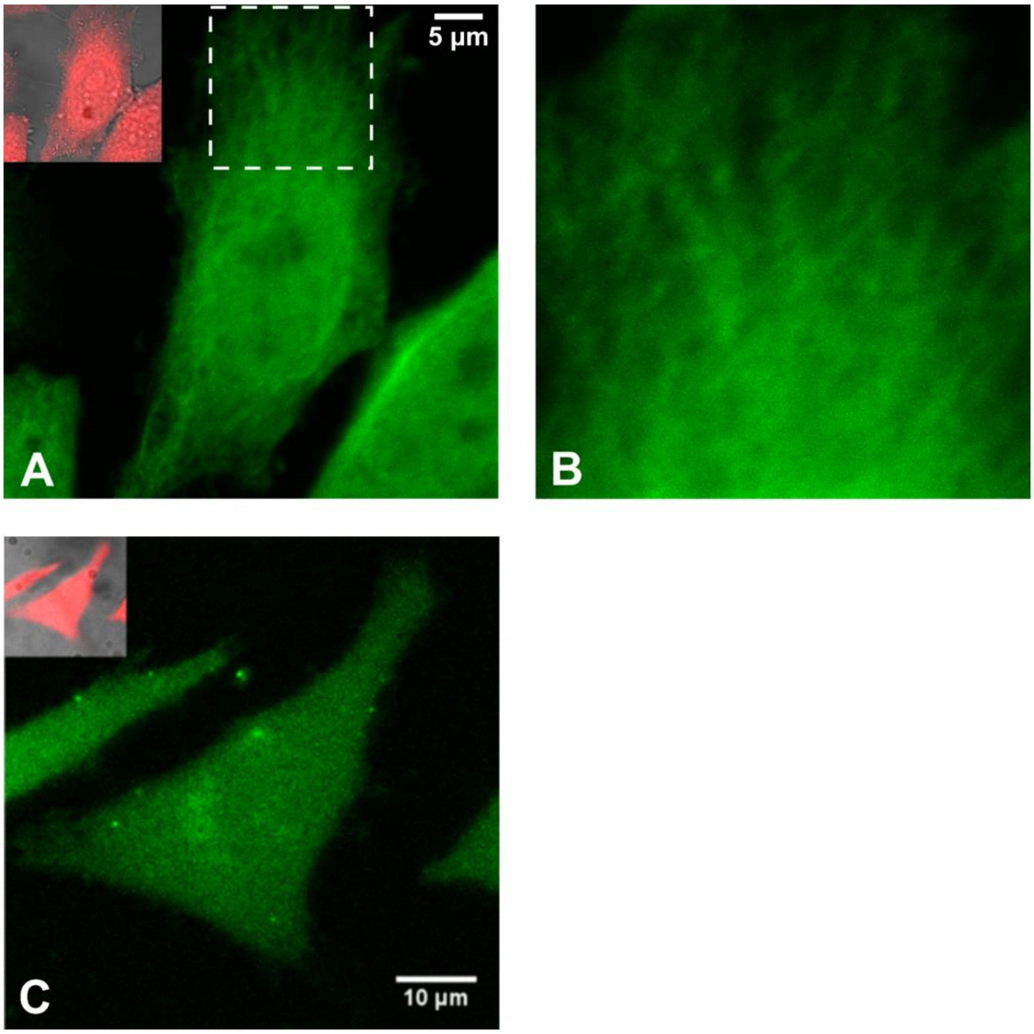

Figure 4. Green fluorescent QDs functionalized with anti-α-Tubulin antibodies are delivered into live HeLa cells by VNB photoporation. A. Confocal image showing filamentous structures as expected for microtubules. The top-left insert is the overlay of the transmission image with the confocal image in red channel showing the viability of the cell (Calcein red AM). B. Zoom-in of the rectangular region in A. C. Green fluorescent PEG-QDs were delivered into live HeLa cells by VNB photoporation. The top-left insert is the overlay of the transmission image with the confocal image in the red channel showing the viability of the cell (Calcein red AM).

4. CONCLUSIONS

In summary, the proof-of-concept study in this chapter demonstrates that VNB photoporation holds promise to become a generic platform for the intracellular delivery of QDs for live cell microscopic imaging. By extension one can imagine that VNB photoporation could be equally used to deliver other types of exogenous labels which were limited to fixed cells until now. Future research in our group will focus on further exploration of this concept.

5. REFERENCES

1. Chan, W.C.W. et al. Luminescent quantum dots for multiplexed biological detection and imaging. *Curr Opin Biotech* **13**, 40-46 (2002).
2. Chinnathambi, S., Chen, S., Ganesan, S. & Hanagata, N. Silicon Quantum Dots for Biological Applications. *Adv Healthc Mater* **3**, 10-29 (2014).
3. Gao, X.H., Cui, Y.Y., Levenson, R.M., Chung, L.W.K. & Nie, S.M. In vivo cancer targeting and imaging with semiconductor quantum dots. *Nat Biotechnol* **22**, 969-976 (2004).
4. Han, M.Y., Gao, X.H., Su, J.Z. & Nie, S. Quantum-dot-tagged microbeads for multiplexed optical coding of biomolecules. *Nat Biotechnol* **19**, 631-635 (2001).
5. He, X.W. & Ma, N. An overview of recent advances in quantum dots for biomedical applications. *Colloid Surface B* **124**, 118-131 (2014).
6. Klarreich, E. Biologists join the dots. *Nature* **413**, 450-452 (2001).
7. Medintz, I.L., Uyeda, H.T., Goldman, E.R. & Mattoussi, H. Quantum dot bioconjugates for imaging, labeling and sensing. *Nat Mater* **4**, 435-446 (2005).
8. Michalet, X. et al. Quantum dots for live cells, in vivo imaging, and diagnostics. *Science* **307**, 538-544 (2005).
9. Smith, A.M., Duan, H.W., Mohs, A.M. & Nie, S.M. Bioconjugated quantum dots for in vivo molecular and cellular imaging. *Adv Drug Deliver Rev* **60**, 1226-1240 (2008).
10. Wu, X.Y. et al. Immunofluorescent labeling of cancer marker Her2 and other cellular targets with semiconductor quantum dots (vol 21, pg 41, 2003). *Nat Biotechnol* **21**, 452-452 (2003).
11. Bruchez, M., Moronne, M., Gin, P., Weiss, S. & Alivisatos, A.P. Semiconductor nanocrystals as fluorescent biological labels. *Science* **281**, 2013-2016 (1998).
12. Chan, W.C.W. & Nie, S.M. Quantum dot bioconjugates for ultrasensitive nonisotopic detection. *Science* **281**, 2016-2018 (1998).
13. Resch-Genger, U., Grabolle, M., Cavaliere-Jaricot, S., Nitschke, R. & Nann, T. Quantum dots versus organic dyes as fluorescent labels. *Nat Methods* **5**, 763-775 (2008).
14. Patterson, G., Davidson, M., Manley, S. & Lippincott-Schwartz, J. Superresolution Imaging using Single-Molecule Localization. *Annu Rev Phys Chem* **61**, 345-367 (2010).
15. Jaiswal, J.K., Mattoussi, H., Mauro, J.M. & Simon, S.M. Long-term multiple color imaging of live cells using quantum dot bioconjugates. *Nat Biotechnol* **21**, 47-51 (2003).
16. Howarth, M. et al. Monovalent, reduced-size quantum dots for imaging receptors on living cells. *Nat Methods* **5**, 397-399 (2008).
17. Ruan, G., Agrawal, A., Marcus, A.I. & Nie, S. Imaging and tracking of tat peptide-conjugated quantum dots in living cells: new insights into nanoparticle uptake, intracellular transport, and vesicle shedding. *J Am Chem Soc* **129**, 14759-14766 (2007).
18. Medintz, I.L. et al. Intracellular delivery of quantum dot-protein cargos mediated by cell penetrating peptides. *Bioconjugate Chem* **19**, 1785-1795 (2008).
19. Buono, C., Anzinger, J.J., Amar, M. & Kruth, H.S. Fluorescent pegylated nanoparticles demonstrate fluid-phase pinocytosis by macrophages in mouse atherosclerotic lesions. *J Clin Invest* **119**, 1373-1381 (2009).
20. Delehanty, J.B. et al. Delivering quantum dot-peptide bioconjugates to the cellular cytosol: escaping from the endolysosomal system. *Integr Biol-Uk* **2**, 265-277 (2010).
21. Yezhelyev, M.V., Qi, L.F., O'Regan, R.M., Nie, S. & Gao, X.H. Proton-sponge coated quantum dots for siRNA delivery and intracellular imaging. *J Am Chem Soc* **130**, 9006-9012 (2008).
22. Bayles, A.R. et al. Rapid Cytosolic Delivery of Luminescent Nanocrystals in Live Cells with Endosome-Disrupting Polymer Colloids. *Nano Lett* **10**, 4086-4092 (2010).
23. Martens, T.F., Remaut, K., Demeester, J., De Smedt, S.C. & Braeckmans, K. Intracellular delivery of nanomaterials: How to catch endosomal escape in the act. *Nano Today* **9**, 344-364 (2014).
24. Derfus, A.M., Chan, W.C.W. & Bhatia, S.N. Intracellular delivery of quantum dots for live cell labeling and organelle tracking. *Adv Mater* **16**, 961-+ (2004).
25. Dubertret, B. et al. In vivo imaging of quantum dots encapsulated in phospholipid micelles. *Science* **298**, 1759-1762 (2002).

26. Delehanty, J.B. et al. Spatiotemporal Multicolor Labeling of Individual Cells Using Peptide-Functionalized Quantum Dots and Mixed Delivery Techniques. *J Am Chem Soc* **133**, 10482-10489 (2011).
27. Xu, J.M. et al. Nanoblade Delivery and Incorporation of Quantum Dot Conjugates into Tubulin Networks in Live Cells. *Nano Lett* **12**, 5669-5672 (2012).
28. Lee, J. et al. Nonendocytic Delivery of Functional Engineered Nanoparticles into the Cytoplasm of Live Cells Using a Novel, High-Throughput Microfluidic Device. *Nano Lett* **12**, 6322-6327 (2012).
29. Xiong, R.H. et al. Comparison of Gold Nanoparticle Mediated Photoporation: Vapor Nanobubbles Outperform Direct Heating for Delivering Macromolecules in Live Cells. *Acs Nano* **8**, 6288-6296 (2014).

Chapter 5

Fast spatial-selective delivery into live cells by nanoparticle-sensitized photoporation

This chapter is submitted for publication:

Ranhua Xiong[1,2], Claire Drullion[3], Peter Verstraelen[4], Jo Demeester[1], Andre G. Skirtach[2,5], Corinne Abbadie[3], Winnok H. De Vos[2,4,5], Stefaan C. De Smedt[1], Kevin Braeckmans[1,2,6,7]

[1]Laboratory of General Biochemistry and Physical Pharmacy, Faculty of Pharmaceutical Sciences, Ghent University, 9000 Ghent, Belgium
[2]Centre for Nano- and Biophotonics, Faculty of Pharmaceutical Sciences, Ghent University, 9000 Ghent, Belgium
[3]Univ. Lille, CNRS, Institut Pasteur de Lille, UMR 8161 – M3T - Mechanisms of Tumorigenesis and Targeted Therapies, 59000 Lille, France
[4]Department of Veterinary Sciences, University of Antwerp, 2020 Antwerp, Belgium
[5]Department of Molecular Biotechnology, Ghent University, 9000 Ghent, Belgium
[6]Univ Lille 1, Univ Lille Nord France, IEMN, UMR 8520, 59652 Villeneuve D'Ascq, France
[7]Univ Lille 1, Univ Lille Nord France, Lab Phys Lasers Atomes & Mol, UMR 8523, 59655 Villeneuve D'Ascq, France

ABSTRACT

We have developed an integrated platform for spatially resolved nanoparticle-sensitized photoporation (SNAP) of cells. SNAP enables high-throughput intracellular delivery of exogenous nanomaterials in selected subpopulations of cells, even down to the single cell level. The versatility of SNAP is demonstrated in two applications, being sparse labeling of neurons for the quantification of dendritic spine density, and the selective labeling and isolation of polynucleic keratinocytes which are potentially involved in neoplasm formation.

1. INTRODUCTION

Intracellular delivery of functional compounds into living cells is of great importance for e.g. cellular imaging[1, 2], therapy[3] and fundamental cell-biology research[4, 5]. For many applications it is sufficient that the compound of interest (being a molecule or nanoparticle) is delivered to the cell population as a whole. In such a case one can choose from a variety of delivery methods, such as lipofection or electroporation[6]. However, there are other applications that would benefit considerably from the possibility of delivering a compound to a certain subpopulation of cells, or even in single cells. For example, delivery of nucleic acids into single cell results in single-cell resolution of gene expression which is beneficial to elucidate gene functions[7]. Cell-selective delivery is also of interest when working with heterogeneous cell cultures. Phenotypic and genomic heterogeneity in a cell population leads to inaccuracy and obscuration of cell differentiation when the population is analyzed as a whole. Delivering inhibitors into individual target cells and analyzing the outcome at the single-cell level allows to accurately regulate and resolve changes in differentiation at the single-cell level[8].

Methods which allow fast and flexible cell-selective intracellular delivery of molecules or nanoparticles are, however, scarce. Microinjection could serve this purpose, but is technically demanding and not amenable to upscaling[9]. Spatially resolved electroporation has been explored as well[10, 11], demonstrating that cells could be selectively transfected by an array of microelectrodes. This method is, however, limited by the fact that transfections are only possible according to the pre-defined layout and size of the electrodes, which, for instance, would not allow transfecting one single cell in a (co-) culture. Photoporation offers a valuable alternative approach to deliver compounds to cells in a targeted manner. Here, selected cells are transiently permeabilized at a particular location of the cell membrane with a precisely focused laser beam[12, 13]. Particular benefits of this approach are that it is a contact free method (as opposed to microinjection) and that the laser beam can be precisely controlled to essentially target any cell[12-14]. While this method was successfully applied to single cell transfections with DNA, or mRNA[12, 13], it is limited in throughput. In a fully automated device with a specially engineered laser beam only a few cells per second could be photoporated[14]. Photoporation throughput can be tremendously sensitized by making use of plasmonic nanoparticles (NPs), like gold nanoparticles (AuNPs), that have a large absorption cross section[15], and are known to raise temperature upon suitable laser irradiation[16]. When adsorbed to the cell membranes they can permeabilize the cell membrane upon laser irradiation through distinct thermally induced phenomena such as local heating, acoustic shockwaves, or the formation of disruptive water vapour nanobubbles (VNB)[17]. NP sensitized photoporation can offer high throughput since less laser energy density is needed so that the laser beam can be expanded to cover tens or even hundreds of cells at the same time. NP sensitized photoporation has proven to be fast

(>1000 cells/s)[18] and efficient at delivering a broad variety of molecules into cells, such as siRNA, pDNA, and proteins[4, 17, 18].

Based on these distinct advantages, here we aimed to explore the unexploited potential of nanoparticle-sensitized photoporation to safely (*i.e.*, in a non-cytotoxic manner) deliver compounds into precisely selected subpopulations of cells, in high-throughput and with great flexibility. Therefore, we developed Spatially-resolved NAnoparticle-sensitized Photoporation (SNAP) according to two different operational modes. In the first mode, cells are selectively photoporated according to a pre-defined pattern. This mode is aimed at experiments where the location rather than the cell type is of importance (**Fig. 1b, c**). In the second mode, cells are photoporated in an image-guided interactive way, where microscopy images are used to (automatically) select the cells of interest (**Fig. 1d, e**). This addresses applications where distinct subtypes of cells need to be transfected which do not have a fixed location in the culture. Each mode has two variants which together should cover most experimental needs (**Fig. 1**). Following detailed characterization of the various SNAP modes, we aimed to apply this new enabling technology to two challenging example applications. First, we show that SNAP can be used to deliver a fluorescent label to a sparse subset of neuronal cells in a dense culture of primary hippocampal neurons so as to enable fast and automated morphological cell analysis. These cells are frequently used readouts for neuronal network connectivity and have been described in numerous neurological disorders, including Alzheimer's disease, schizophrenia, intellectual disabilities and autism spectrum disorders. However, automated image analysis of spines is virtually impossible with current labeling strategies as they stain all cells in the very dense cell culture. Second, we explored SNAP to deliver a non-toxic fluorescent marker into morphologically distinct primary normal human epidermal keratinocytes (NHEKs). In particular, polynucleated or mononucleated NHEKs are separately targeted so that they can be isolated for further downstream molecular and functional analysis in relation to cancer research.

2. MATERIALS AND METHODS

Materials. Cationic AuNPs of 70 nm were purchased from NanoPartz (#CU11-70-P30-50, Nanopartz Inc., Loveland, CO, USA). These AuNPs had a zeta potential of 30 mV as measured by dynamic light scattering (NanoSizer, Malvern, UK). 520 (±10) nm CdSe/ZnS QD coated with a thiol oligomer and surface functionalized with -COOH groups (PEG-coated QDs) were purchased from Mesolight, Inc. (#CdSe/ZnS-PEG-COOH-520, Mesolight, Inc., Little Rock Arkansas, USA). FITC-dextrans with a molecular weight of 10 kDa were purchased from Sigma-Aldrich (Belgium). Cascade Blue dextran (#D-1976, Molecular Probes™), Alexa@647 labelled dextran 10 kDa (#D-22914, Molecular Probes™), and

Propidium Iodide (#P1304MP, Molecular Probes™) were purchased from Invitrogen (Belgium).

Platform for SNAP. The photoporation platform consists of a custom developed setup that includes optical and electrical components to generate and detect vapour nanobubbles (VNB)[17]. The set-up is built around a motorized epi-fluorescence microscope (Nikon Ti) equipped with programmable motorized microscope stage (#H117, Prior Scientific) (**Figure S2**). A pulsed laser (~7 ns pulses @ max. 20 Hz) tuned at a wavelength of 561 nm (Opolette™ HE 355 LD, OPOTEK Inc., Faraday Ave, CA, USA) was applied to illuminate the AuNPs in order to generate VNB. A beam expander (#GBE05-A, Thorlabs) combined with iris diaphragm (#D37SZ, Thorlabs) is used to adjust the laser beam from tens of micrometers to hundreds of micrometers. The setup has time-response and light scattering modes to allow detection of VNB formation as detailed elsewhere[17] (**Figure S1c**). In order to apply a single laser pulse to a selected region in the cell culture, the stage was synchronized with the pulsed laser by a pulse generator (BNC575, Berkeley Nucleonics Corporation, CA, USA). The microscope xy-translation stage is used to move the sample at the desired location into the photoporation laser beam. In this work we used laser fluence level of 2 J/cm^2 (unless specified otherwise) above the vapour nanobubble threshold (~0.5 J/cm^2 @ 561 nm & 7 ns pulse duration) of the 70 nm AuNP used here. This laser fluence was optimized in previous work of ours[17, 19].

Pre-defined pattern SNAP. Photoporation of pre-defined patterns was implemented according to a line-scanning procedure and a pixel-based mode. In the line-scanning mode, the xy-translation stage is moved linearly with constant speed between start and end points of subsequent lines (**Figure S3a**). The laser pulse frequency, laser beam diameter and scanning speed are adjusted so that each location along the line receives a single laser pulse. For example, for a laser beam of 150 µm the pulse frequency is set at 20 Hz with a stage speed of 3 mm/s.

In the pixel-based mode the sample is moved into the photoporation beam according to the pixels of a binary image (**Figure S3c**). The sample receives a single laser pulse for each indicated pixel location. The image pixel coordinates are transformed to global coordinates by:

$$X_i = (x_i - x_0) \cdot \Delta l + X_0 \ (1) \qquad Y_i = (y_i - y_0) \cdot \Delta l + Y_0 \ (2)$$

where x_i, y_i are the coordinates of pixels in the picture, x_0, y_0 are the coordinates of the origin in the image (typically with the top left pixel is chosen as $x_0=0$, $y_0=0$), Δl is the image pixel size which is set as 80% diameter of the photoporation laser beam, X_0, Y_0 are the global coordinates of the origin of the microscope stage (i.e. where the top left pixel from the image corresponds to the desired location in the sample).

Image-guided SNAP. Image-guided photoporation was implemented according to a manual and automated mode. In the manual mode, the cells of interest are manually positioned at the center of the microscope's field of view and receive a single laser pulse. Alternatively, the coordinates of the cells of interest can be determined first manually and used as input for subsequent automated photoporation.

In the automated mode, cells in the culture well are first imaged, typically using a low magnification 10× objective (CFI Plan Apochromat, Nikon, Badhoevedorp, The Netherlands). In case the cells cover a large area, multiple adjacent images can be acquired (**Figure S6**). Dedicated image processing routines can be used to subsequently localize the cells of interest in the recorded images based on morphological features or the presence of a certain (fluorescent) cell marker. The local coordinates of the cells in the images are then transformed to global coordinates of the microscope stage by:

$$X_i^k = (x_i - x_{Laser}) \cdot \Delta l + X^k \quad (3) \qquad Y_i^k = (y_i - y_{Laser}) \cdot \Delta l + Y^k \quad (4)$$

where X_i^k, Y_i^k are the global coordinates of i^{th} cell in k^{th} image, x_i , y_i (in pixel units) are the local coordinates of that cell, x_{Laser}, y_{Laser} (pixel units) are the local coordinates of where the laser beam is centered in the image, Δl is the image pixel size. In this work we used local maxima or minima of the selected cells to define the cell coordinate.

SNAP validation experiments. Pre-defined pattern phtotoporation was validated by SNAP delivery of QDs or fluorescent labeled dextran into HeLa cells cultured in 6-wells plate (~5.0×10^5 cells/well). HeLa cells were obtained from ATCC (CCL-2) and cultured in complete cell medium which consisted of DMEM/F-12 (FBS, Gibco, Invitrogen, Belgium) supplemented with 10% heat-inactivated foetal bovine serum (FBS), 2 mM glutamine and 100 U/mL penicillin/streptomycin (Gibco, Invitrogen, Belgium). Cells were cultured at 37°C in a humid atmosphere containing 5% CO_2. HeLa cells were cultured for 24 hours before laser treatment.

After incubation with AuNPs for 0.5 h, photoporation was performed as described in the main text. Following laser irradiation, the samples were washed a few times with PBS after which new cell medium was added. Next, the cells are put back in the cell incubator for recovery (37°C in humidified atmosphere at 5% CO_2). The cells are finally imaged by confocal microscopy to evaluate the photoporation results.

Preparation of primary neuron cell cultures. Hippocampi were dissected from wild-type E18 Black6 mouse embryos in HEPES (7 mM) buffered Hanks Balanced Salt Solution (HBSS), followed by trypsin digestion (0.05%; 10 min; 37°C) and mechanical dissociation by trituration through 2 fire-polished glass pipettes with decreasing diameter. After centrifugation (5 min at 200 g), the cell pellet was resuspended in Minimal Essential Medium

(MEM) supplemented with 10% heat-inactivated normal horse serum (Innovative Research, Michigan, USA) and 30 mM glucose (MEM-horse medium). Cells were plated in Poly-D-Lysin-coated 96-well plates (Greiner Cell coat, µClear, Wemmel, Belgium), at 45 000 cells per cm², and kept in a humidified CO_2 incubator (37°C; 5% CO_2). After 4 hours, the medium was replaced with B27 supplemented Neurobasal medium, containing Sodium Pyruvate (1 mM), Glutamax (2 mM) and glucose (30 mM). To suppress proliferation of non-neuronal cells, arabinosylcytosine (AraC; 2 µM; Sigma-Aldrich, Bornem, Belgium) was added at the fourth day after plating. The cultures were further grown under control conditions without any further medium replacement until the time of analysis.

Labeling of selected neuronal cells. Primary rat hippocampal cultures were grown in 96-well plates at 37°C in a humidified atmosphere containing 5% CO_2. After the indicated DIV (days *in vitro*), selected neuronal cells were labelled by spatially resolved VNB photoporation with phalloidin (#A12379, Alexa Fluor®, Invitrogen). First, ~100 µl culture medium was removed from the culture well (~50 µl left) and 25 µl of AuNPs with a concentration of $\sim 1.8 \times 10^8$ particles/ml was added to the cells. After 30 min incubation, the nuclear label Hoechst (#H3570, Molecular Probes™) was added to the cells and incubated for another 15 min at room temperature. Next, the cell culture was imaged by confocal laser scanning microscopy (Ex/Em, 405/440). A large field of view image of 1.27 by 1.27 mm was obtained using the microscope's image stitching feature. Nuclei were identified in the image and a sparse selection of distant cells (at least 200 µm apart) was made with a custom written Matlab program. Before starting SNAP treatment, Alexa 488 Phalloidin dissolved in Methanol was added to the cells with final concentration of ~500 nM. After photoporation of the selected cells, the sample was put back in the incubator at least 1 h to allow the cells to recover and the phalloidin to distribute throughout the cells. Imaging of labeled cells was done with confocal laser scanning microscopy using both low (×10) and high (×60 water) magnification lenses. Quantification of dendritic spine density was done with ImageJ software. Dendritic spine density was evaluated from 7 to 21 DIV in primary hippocampal cultures. Three different isolations were used for quantification. For each isolation, ~1000 µm of dendrites was analyzed on 10 selected neurons for each DIV.

Quantifying the delivery efficiency in neurons was performed as following. First, cells in the well are selectively labeled with Phalloidin by SNAP. Next, a series of confocal images is acquired (10x objective lens). The delivery efficiency is quantified as the percentage of cells that show a positive Phalloidin signal in total selected cells. The viability of neuronal cells after SNAP treatment was assessed by Propidium Iodide after ~2 h recovery at 37°C.

It can be noted that it was necessary to make a small change in the photoporation protocol, as the hippocampal cells are very sensitive to washing. Therefore, we decided to leave out the washing step that is normally included to remove unbound AuNPs. Leaving the AuNP in the cell medium during photoporation did not influence photoporation efficiency and neither did it cause substantial toxicity to the cells. With this adapted protocol we achieved an excellent cell viability of more than 90% (**Figure S9b**).

NHEK cell culture. NHEKs (Normal Human Epidermal Keratinocytes) were purchased from Lonza (#192907, Lonza). NHEKs were cultured in KGM-Gold™ Keratinocyte Growth Medium (KGM-Gold BulletKit, #00192060, Lonza) at 37°C with 5% CO_2 atmosphere. 300,000 cells were seeded in a 100 mm dish (cell density ~3800 cells/cm^2) and subcultured at ~70% confluence. The number of population doublings (PD) was calculated at each passage according to[28]: $PD = \log\left(\frac{N_{collected\ cells}}{N_{plate\ cells}}\right)/log2$.

Toxicity measurement of NHEK cells. NHEKs in the exponential growth phase were plated in 24 well plates (5000 cells/well) 24 h before labeling or photoporation. For Hoechst labeling, the cells were incubated with Hoechst 33342 (2 µg/ml) for 15 min at room temperature. For labeling with Alexa 647-dextran with 10 kDa (AD10), cells were incubated with Alexa dextran at a concentration of 20 µg/ml for 24 h at 37°C. Next, cells were incubated with AuNPs at the indicated concentration for 0.5 h, after which photoporation was performed in the cells in the whole well. The samples were finally washed a few times with PBS and supplemented with new cell medium. After labeling or photoporation, cells were cultured for another 4 days at 37°C and 5% CO_2 atmosphere. MTT cytotoxicity measurements were finally performed. Briefly, 30 µl of a 5 mg/ml 3-(4,5-dimethylthiazol-2-yl)-2,5-diphenyltetrazolium bromide (MTT, Sigma, Belgium) solution is added to each well. Following an incubation period of three hours at 37°C the MTT containing cell medium was removed and cells were lysed using dimethylsulfoxide (Sigma, Belgium). When the formazan crystals were completely dissolved and a homogeneous colour was obtained, the absorbance in each well was measured at 570 and 650 nm using an Envision Xcite multilabel reader (PerkinElmer LAS, Boston, MA).

Cell-selective photoporation and isolation of PK and MK cells. NHEKs in the exponential growth phase were plated in 24 well plates with 5000 cells/well before incubation with AD10. 20 µg/mL of AD was added to the cell medium for 24 h at 37°C and 5% CO_2 to label endolysosomes in the perinuclear area. Next, cells were incubated with AuNPs at the relevant concentrations (see main text) for half an hour, followed by washing with PBS. Cells were finally imaged by confocal microscopy with a low magnification 10× objective. 12 by 12 images were recorded to visualize the entire 24-well plate. The location of MK and PK cells was determined by image processing as described in the main text and **Figure S12**. With our Matlab code it typically took 5-10 min to process all the images (144 frames). Finally, FD10 was added to the cells for labeling of the selected cells by photoporation. After laser treatment, cells were washed, supplied with fresh cell medium and imaged again before being put back in the incubator for 24 h. The cells were subsequently collected for sorting by BD FACS Aria III (BD Biosciences, Erembodegem, Belgium). Sorting was based on the presence of FITC signal. After sorting, PK/MK cells were collected for further culture and quantification of isolation levels. The isolation level of PK was defined as,

$$P_{PK} = \frac{N_{PK}}{N} \quad (5)$$

where N_{PK} is the number of PK cells and N is the total number of collected cells. Similarly, MK isolation is defined as,

$$P_{MK} = \frac{N_{MK}}{N} \quad (6)$$

where N_{MK} is the number of MK cells.

Code availability. We provide the Matlab code which was developed SNAP to determine cell positions in the supplementary information.

3. RESULTS AND DISCUSSION

3.1 SNAP

The first step in SNAP is to incubate cells with plasmonic nanoparticles (see **Fig. 1a**). In this work we have used cationic 70 nm AuNPs which have been modified for optimal cell membrane adsorption. After 30 min incubation, cells are typically washed to remove unbound AuNPs, leaving between 5 and 10 AuNP associated per cell, as can be verified with confocal reflection microscopy (**Figure S1a**). The next step is to add the compound of interest into the cell medium, followed by laser irradiation. Here we performed photoporation with VNBs as we have shown it to be a very efficient cell permeabilization mechanism[17]. Briefly, upon absorption of a laser pulse (7 ns) with a fluence above the VNB threshold (here we used 2 J/cm^2 as optimized before[17, 19]) the AuNP's temperature increases sufficiently to let the surrounding water evaporate. This results in the formation of VNBs that expand and collapse, inducing nanopores in the cell membrane and allowing the compound of interest to diffuse into the cell cytoplasm. **Figure S1c** and **Supplementary Movie 1** demonstrate that only irradiated cells become photoporated, in this case with Propidium Iodide (PI). The pores recover in a 1-3 min time frame[19]. In our set-up the diameter of the photoporation laser beam can be adjusted so that either single or multiple cells can be irradiated per laser pulse. A programmed motorized microscope stage is used to move the sample through the laser beam (see **Figure S2** and **Methods**) to photoporate the cells of interest. SNAP was implemented according to two distinct modes: with pre-defined pattern or in an interactive image-guided manner (**Fig. 1b-e**). There are two variants for each mode , as will be explained in detail below.

Pre-defined pattern SNAP

The simplest way to perform SNAP according to a pre-defined pattern is by 'line scanning'. Cells can be photoporated according to simple geometrical shapes by scanning the sample line-by-line through the laser beam, as schematically shown in **Figure S3a**. One example is shown in **Fig. 1b** where HeLa cells were photoporated with quantum dots (QDs). Note that the line width is simply determined by the diameter of the photoporation laser beam. Indeed, as shown in **Figure S3b**, changing the diameter of the laser beam also changes the width of the photoporated lines of cells. With a laser beam of 150 µm and a pulse repetition rate of 20 Hz the stage can move at 3 mm/s, which corresponds to a photoporation rate of about 200 cells/s. Evidently, if a laser with higher pulse repetition rate is used, even higher photoporation rates are possible.

If more complex patterns are desired, a 'pixel-based' approach is more convenient where the photoporation pattern is defined in a binary image. As illustrated in **Figure S3c**, a single laser pulse is applied to the sample according to the black pixels in the binary image. At each of those pixel locations a single laser pulse is applied to locally photoporate the cells. The size of the final pattern in the cell culture essentially depends on the laser beam diameter. The mapping of the image to the cell culture is done such that one image pixel corresponds to 80% of the laser beam diameter. This ensures a small spatial overlap between subsequent photoporation pulses so that all cells are effectively photoporated. An example is shown in **Fig. 1c** where HeLa cells were photoporated with FITC-dextran of 10 kDa (FD10) according to a black-and-white drawing. The zoomed-in images in **Figure S4** clearly show the individually labeled cells. We next delivered different compounds in different regions of the cell culture according to Andy Warhol's painting of Einstein (**Fig. 1c** and **Supplementary Movie 2**). Three rounds of photoporation were subsequently performed with cascade blue-dextran, Alexa 647-dextran and FITC-dextran. Another example is shown in **Figure S5** and **Supplementary Movie 3** where a 6 color 'living painting' was produced in a culture of HeLa cells. With a laser repetition rate of 20 Hz this means that we achieve 20 pixels per second. For instance, both examples in **Fig. 1c** (with about 5000 black pixels and 50000 cells each) did not take more than 5 min to complete.

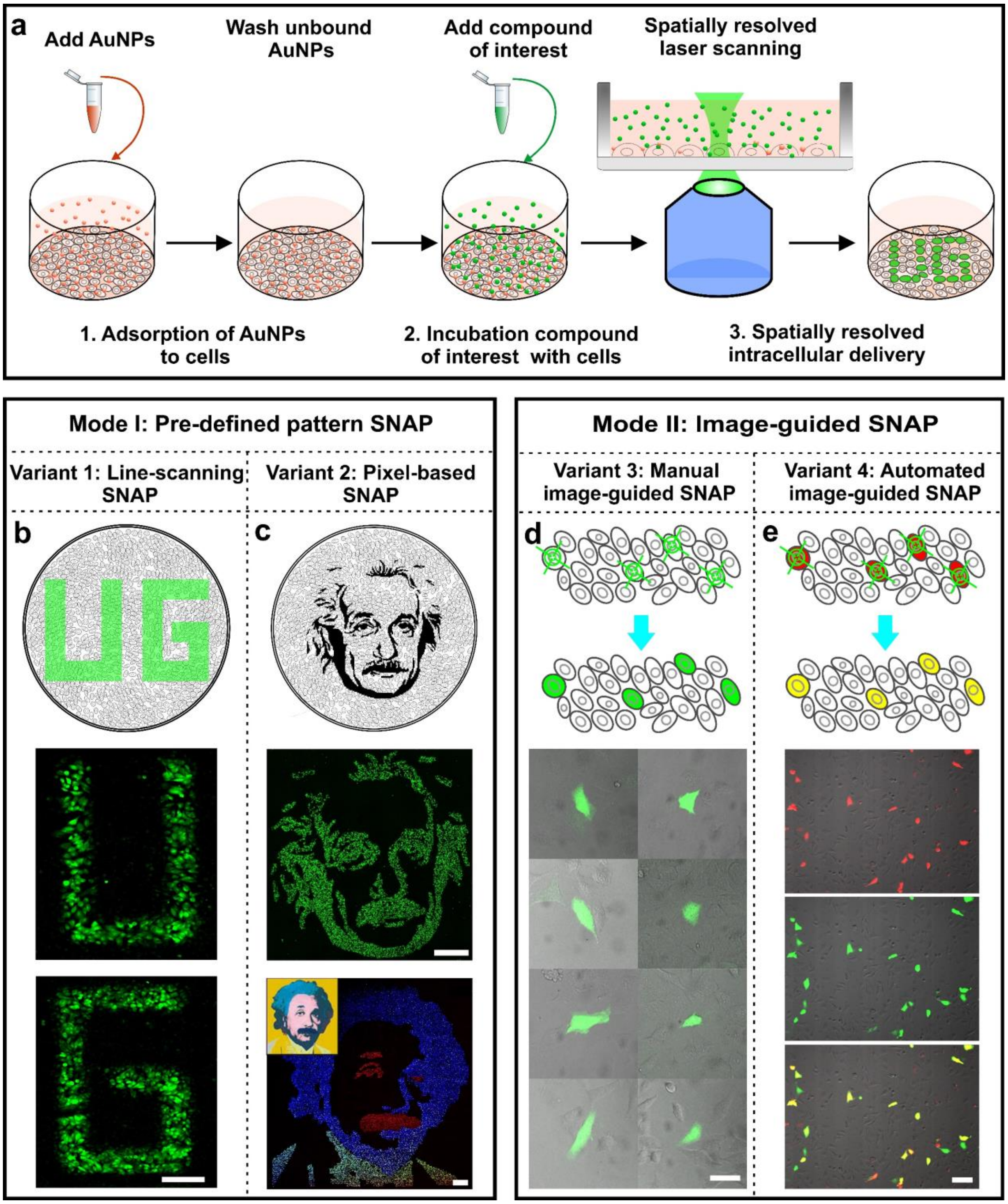

Figure 1. Schematic overview of SNAP. (a) Following AuNP incubation and washing of unbound AuNPs, the compound that should be delivered into the cells is added to the cell medium. An automated xy-stage is used to perform photoporation in selected areas of the cell culture. Only those cells that receive a laser pulse will be photoporated and take up the compound that was added to the medium, while the other cells remain unaffected. (b) By line-scanning of the sample through the photoporation laser beam, HeLa cells were photoporated with quantum dots (QDs) forming the letters 'U' and 'G' in the cell culture. Scale bar is 150 µm. (c) In the pixel-based variant the photoporation beam is directed towards distinct locations in the cell culture according to the pixels of a binary image. HeLa cells were photoporated with FITC-dextran with 10 kDa (FD10) according to the black pixels of a drawing of Albert Einstein. By repeating the photoporation procedure it is possible to deliver different compounds to different regions in the cell culture. As an example,

Andy Warhol's painting of Einstein was reproduced by photoporating HeLa cells sequentially with cascade blue-dextran (blue), FITC-dextran (green) and Alexa 647-dextran (red). Scale bars are 1000 µm. (d) Image-guided cell-selective photoporation is possible by first recording microscopy images of the cell culture. The user can then select manually which cells are of interest and should become photoporated. Here, selected HeLa cells were photoporated with FD10 (green), demonstrating that single cell precision can be achieved. Scale bar is 50 µm. (e) The entire process can be automated if cell selection is done by automated image analysis. Cells of interest may be identified based on morphological features or, as in this example, based on a fluorescent cell marker. Red-labeled HeLa cells were mixed with unlabeled ones in a ratio of 1:5 and automatically localized by image processing for subsequent photoporation with FD10 (green). Scale bar is 100 µm.

Image-guided SNAP

Many applications would benefit from photoporating selected cells according to certain visual features, rather than based on a particular location in a culture well. Distinctive features could be the cell or nuclear morphology, or the presence of a certain (fluorescent) biomarker. Therefore, as a next step, we implemented image-guided photoporation of selected cells with both a manual (**Fig. 1d**) and automated (**Fig. 1e**) cell recognition mode of operation. In the manual mode, the user indicates in the recorded microscopy images which cells should be photoporated after inspection of previously acquired images. As shown in **Fig. 1d**, single cell resolution is easily obtained by reducing the photoporation laser beam diameter to slightly less than the size of a typical cell. Complete automation was achieved by integrating automated image analysis in the pipeline. A proof-of-concept is shown in **Fig. 1e** where the cells of interest have a red fluorescent reporter signal. Here, HeLa cells were first labeled with Alexa 647-dextran (AD) by AuNP sensitized photoporation of all cells in the culture[17]. Next, these cells were trypsinized and reseeded after mixing with unlabeled HeLa cells at a 1:5 ratio. The cell culture was imaged by fluorescence microscopy and the red labeled cells were localized by a simple image processing procedure (**Figure S6**). Subsequently, SNAP was carried out to deliver green fluorescent FD10 into those cells that were stored in the list with coordinates (**Fig. 1e** and **Figure S7a, b**). Colocalization analysis revealed that 70.4 ± 9.7% (n=3) of the red-fluorescent targeted cells were successfully labeled with FD10. About 30% of the cells were incorrectly labeled with FD10. These false positive cells are on the one hand due to a small amount of dead cells into which FD10 can diffuse. On the other hand, false positives also arise from inaccurate positioning of the photoporation laser beam, which is due to two reasons. First, the relatively simple image processing method that we have used to identify the cell's position (based on the maximum intensity) in some cases doesn't indicate the exact center of the cell. Secondly, cells sometimes move or divide between taking the images and the actual photoporation procedure so that they are not at the indicated position anymore. In next generations of the SNAP technology these two shortcomings can be addressed by improving the cell detection algorithm and by combining SNAP with a confocal microscope to minimize the time delay between imaging and photoporation. In case of a fluorescent label these false positives can be reduced by a subsequent targeted photobleaching procedure (**Figure S7c**). After two rounds of photobleaching the false positive cells could be reduced to 5% (true positives increased to 95%) (**Figure S7d**). With automated image-guided SNAP we could achieve a cell photoporation rate of 20 cells/s, as determined by the limited pulse repetition rate of the laser used in this study. While this is already an order of magnitude more than the highest reported rate for standard photoporation[12-14], higher photoporation rates are very well possible with lasers of higher pulse frequency.

3.2 Labeling of a sparse set of individual neurons by automated image-guided SNAP

The unprecedented speed and flexibility of SNAP opens up a whole new range of applications that were not possible before. Here we apply our developed technology to two proof-of-concept applications that benefit from labeling a specific subset of cells. As a first example application, SNAP was used to automatically label a sparse set of living primary hippocampal neuronals in a dense culture for spine density quantification. *In vitro* neuronal networks are frequently used models in studies of neuroplasticity, with synapses, in particular postsynaptic regions known as dendritic spines, serving as sensitive morphological correlates of neuronal connectivity[20]. However, accurate quantification of spine density is difficult with classical labeling strategies. Indeed, the current gold standard consists of the application of hydrophobic dyes such as DiI to the whole cell culture, which suffer from several drawbacks such as lack of control, staining of clustered cells (especially in dense cultures), heterogeneous staining efficiency and artefacts (overstaining, debris) (**Figure S8**). These difficulties preclude automated analysis. Targeted labeling strategies are therefore highly desirable. Although photoactivatable fluorescent proteins (FPs) have recently been explored to highlight individual neuronal cells[21], transfection and overexpression of FPs always comes with the concern of inducing artefacts[22], apart from the fact that transfection and photoconversion processes are both time-consuming processes. Hence, to quickly and automatically label a sparse set of neuronal cells in a hippocampal culture, we made use of automated image-guided SNAP (**Fig. 2a**). First, hippocampal cells were labeled with the nuclear stain Hoechst for facile automated recognition of true neurons (**Fig. 2b**). The nuclei positions were identified by image processing and used as coordinates of the cells. A random selection was made from the list of extracted cell coordinates using the constraint that selected cells should be at least 200 µm apart (**Figure S9a** and **Methods**). The sparse set of selected cells were subsequently labeled by photoporation of Alexa Fluor® 488 phalloidin, a well-known cell impermeable F-actin stain. Each cell received one laser pulse at the indicated position with a beam diameter of ~20 µm. As the photoporation beam was centered onto the nuclear area, phalloidin will initially enter the soma of the cell, after which it will diffuse throughout the cell into the dendrites and label the dendritic spines. A typical result is shown in **Fig. 2b,** where 12 cells were randomly selected to be photoporated out of several hundreds of cells in total. 8 out of 12 selected neuronal cells became successfully labeled with phalloidin which is close to ~70% target efficiency as similarly obtained for HeLa cells (**Figure S9b**). The magnified cell in **Fig. 2b** shows a single neuronal cell in the full field of view of a hippocampal culture. A 3-D confocal image of this cell is shown in **Supplementary Movie 4**. The inset shows that dendritic spines can be unambiguously resolved, thus enabling quantitative morphological analysis. As a proof-of-concept we followed the dendritic spine density over time in culture. In hippocampal cultures of 7, 14 and 21 days *in vitro* (DIV), a sparse set of cells was labeled with phalloidin. An example image is shown in **Fig. 2c** for each time point, with more images being shown in **Figure S10**. Image analysis shows that the spine density increases significantly over time (**Fig. 2d**). This is in good agreement with previous findings based on manual counting in DiI-stained cultures[23]. It opens up the possibility to perform such analyses in an automated fashion in the future since the positions of photoporated cells are precisely known. In addition, the selective labeling can be directed to specific neurons that show particular geno- or phenotypic patterns of interest. These may be neuronal subtypes (e.g. pyramidal- or interneurons) or neurons that show intracellular accumulation of toxic proteins (e.g. alpha-Synuclein or Tau). It is of note that sparse labeling of individual neurons has been attempted before with standard photoporation (*i.e.* without sensitizing nanoparticles). However, the success rate was very low at only ~10% of the cells being successfully labeled, next to the fact that the photoporation rate was relatively low at ~1.7 cells/s[14]. Instead, with automated image-guided SNAP we achieved a more than 10-fold higher throughput of 20 cells/s with seven times better efficiency (~70% success rate).

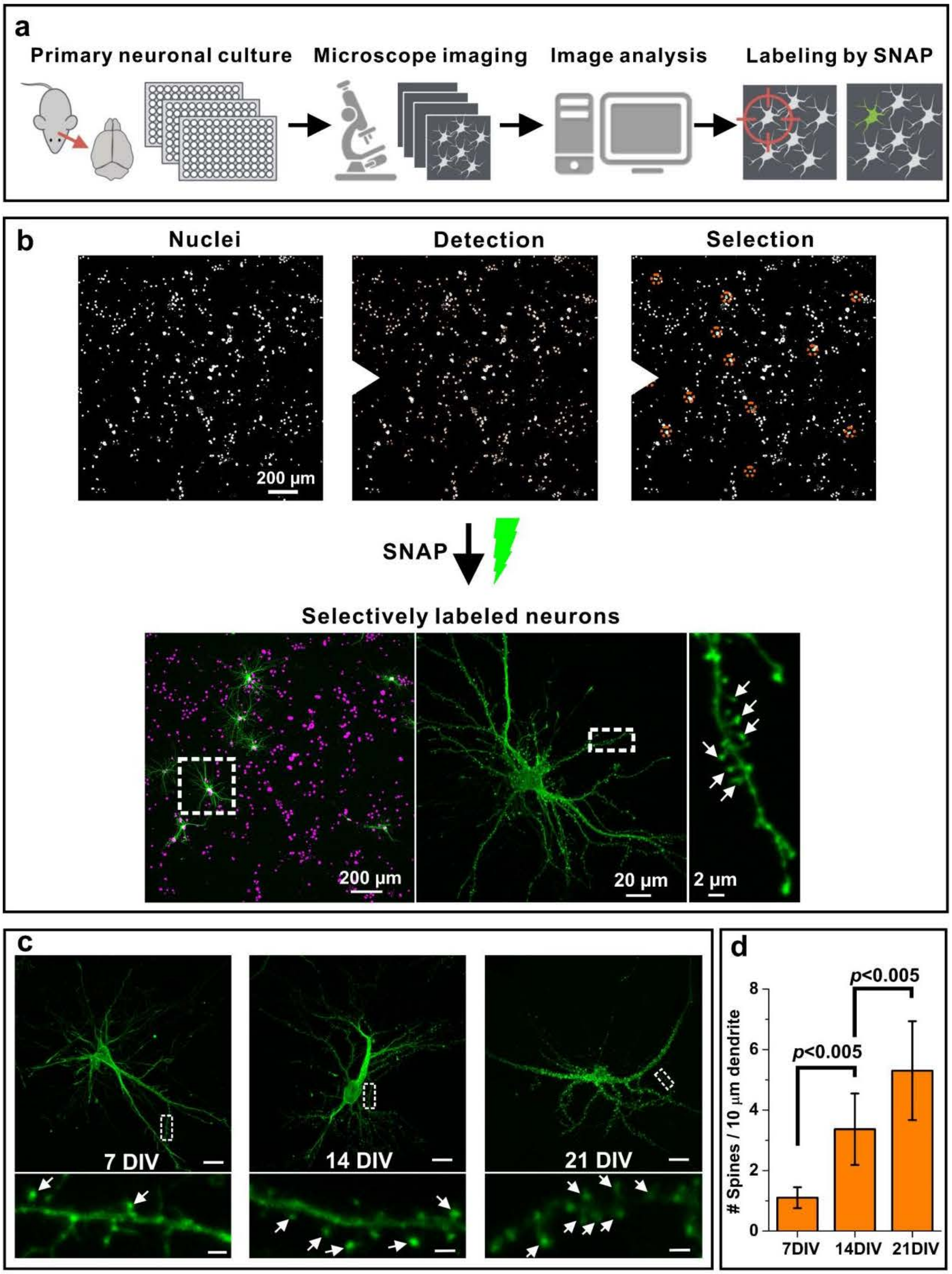

Figure 2. Labeling of a sparse set of individual neurons in a dense primary mouse hippocampal culture by automated image-guided SNAP. (a) Schematic overview of labeling selected neurons by image-guided SNAP. (b) Image recorded with low magnification lens (10×) to locate hippocampal cells labeled with the nuclear stain Hoechst 33342. The position of the nuclei is identified by image processing as indicated by the red dots. A random selection of cells is made that are at least 200 μm apart, here indicated by orange circles. Those positions will be used for subsequent photoporation of the selected cells with AlexaFluor 488

phalloidin. About 70% of the targeted individual neurons become successfully labeled (green fluorescence). A high resolution image of the indicated cell shows that the entire morphology of neuronal cell can be clearly discerned. The inset to the right shows that individual spines (white arrows) along the dendrites can be unambiguously resolved, even though the cell is surrounded by many other (unlabeled) cells. (c) By sparse labelling of individual neurons in primary hippocampal cultures, changes in dendritic spine density could be easily visualized as a function of days *in vitro* (DIV) culture. Example images of single neurons are shown at 7, 14 and 21 DIV. (d) The spine density could be unambiguously quantified by image analysis, showing a significant increase as a function of DIV (n=3). The data were compared with ANOVA test. Scale bars in c are 20 µm (top images) and 2 µm (bottom insets).

3.3 SNAP enabling non-toxic isolation of mononuclear and polynuclear NHEKs

SNAP was next used to enable the isolation of morphologically distinct subpopulations of cells in culture. In particular, we aimed to isolate relatively rare polynucleated from mononucleated primary normal human epidermal keratinocytes (NHEKs). In contrast to cancerous cells, normal diploid cells cannot divide indefinitely, but rather enter a senescent state after a finite number of divisions. While senescence is characterized by an irreversible cell cycle arrest, several studies indicate that this state may not be as stable as generally assumed[24]. Some senescent cells could re-renter the cell cycle and generate precancerous daughter cells, called post-senescence neoplastic emergent (PSNE) cells that are mutated, transformed and tumorigenic[24, 25] (**Figure S11**). Based on microscopy observations it has been suggested that polynucleated senescent cells are the progenitors of PSNE cells[24]. In order to study this important phenomenon in more detail, it is of current interest to isolate polynuclear keratinocytes (PKs) from mononuclear keratinocytes (MKs) in a non-toxic manner to enable further downstream molecular and functional analyses. Initial attempts of ours to sort polynuclear cells with FACS using a cell-permeable nuclear stain like Hoechst, failed due to substantial long-term toxicity, with only 37.2 ±11.9% (n=3) cells surviving after 4 days measured by MTT. Hence we explored if SNAP could be used to selectively label one of both subpopulations with an inert non-toxic fluorescent probe (FD10) that would not cause long-term cytotoxicity. Discriminating PK from MK cells in transmission microscopy images by automated image processing is not easily done. In order to facilitate image analysis, we first incubated the cells with 10 kDa Alexa 647-dextran (AD) for 24 h, which labels the late endosomes and endo-lysosomes in the perinuclear area. At low magnification the nuclei are then visible as dark areas, as can be seen in **Fig. 3**. This type of labeling was found to be completely harmless to NHEKs with 103.7% ± 9.7 cells surviving after 4 days. An image processing protocol was designed to automatically find the location of either PK or MK cells, as outlined in **Figure S12**. These locations were then used to deliver FD10 to the targeted subpopulation by automated image-guided SNAP (**Fig. 3**). An AuNP concentration of 2.5×10^7 nps/ml and a laser fluence of 1.0 J/cm^2 were chosen for the photoporation experiments on NHEKs because under these conditions we achieved >90%

labeling efficiency with ~80% cell viability (**Figure S13**). When targeting PK cells we found that 67.1 ± 9.5% (n=3) of all labeled cells were PK cells, which is close to the ~70% accuracy that we found earlier for HeLa cells and neurons. When targeting MK cells we achieved an accuracy of 95.9 ± 3.2% (n=3). This higher value can be explained by the fact that most of the cells are MKs so that upon mistargeting it is very likely that still a MK is being photoporated. In a next step we tried isolating MK from PK by FACS sorting. The initial cell culture consisted of 17% polynuclear cells and 83% mononuclear cells, based on visual inspection of hundreds of cells. When sorting was done based on labeled PK cells (with unlabeled MK cells), PK cells could be purified to ~65%, which is 4 fold higher than the initial culture (see left panel, **Fig. 3**). At the same time the purity of MK cells increased from 83% to 93%. When cells were sorted based on labeled MK cells, the PK purity could be sensitized from 17% to ~40%, while MK purity increased from 83% to >95%. These results show that the best enrichment of a particular subpopulation is achieved when that particular fraction is labeled. In case, however, one would want to avoid introducing a label into the cells that are of interest for further downstream analysis, the results show that enrichment of a particular subpopulation is still possible by labeling the other subpopulation, although at a lower efficiency. Finally we would like to note that higher purification levels could evidently be reached by simple repetition of the entire procedure. Taken together we conclude that automated image-guided SNAP enabled isolation of PK cells from MK cells without inducing long-term toxicity. This will be very helpful in further research aimed at determining the molecular specificities of PK cells that confer the ability to escape from senescence and generate mutated daughter cells.

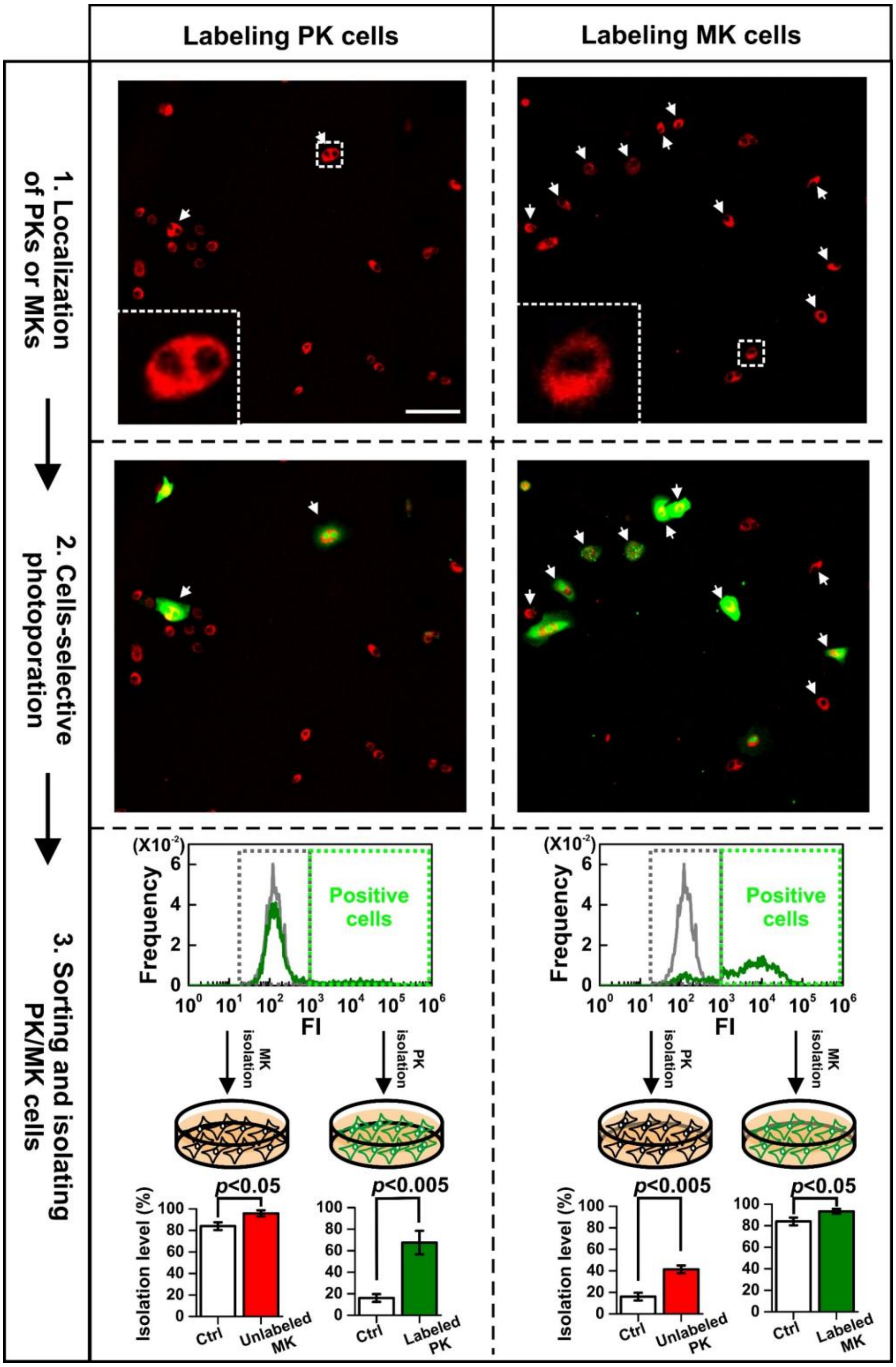

Figure 3. SNAP enables non-toxic isolation of mononuclear and polynuclear NHEKs. Endolysosomes in the perinuclear area are labeled by 24 h incubation of NHEKs with 10 kDa Alexa 647-dextran (red). Following the identification of mononuclear NHEKs (MK) and polynuclear NHEKs (PK) by automated image processing (indicated by white arrows), either of both populations is selectively labeled with FD10 (green) by automated image-guided SNAP. Separation and isolation of both populations is finally done by FACS after trypsinisation of the cells. Cell frequency (n=5000) vs. fluorescence intensity (FI) is shown for photoporated (green) and control (grey) cells. The percentage of PK and MK cells are shown before (white bars) and after (green and red bars) isolation. The results are the mean ± SD of n=3 independent biological repeats. The data are compared with ANOVA test. Scale bar is 100 μm.

4. CONCLUSIONS

In summary, we have developed a methodology that can be used to deliver molecules such as fluorescent labels into living cells in a spatially resolved manner in high throughput, even down to single cell resolution. Spatially selective delivery can be performed according to pre-defined patterns, but most interestingly can be achieved in an interactive image-guide manner as well. By full automation of the procedure we achieved delivery rates that exceed the fastest reported methods by more than one order of magnitude[12, 14]. We expect that speed can be increased by at least another order of magnitude when using a laser with higher pulse frequency. Spatial selective delivery with single cell resolution was recently also demonstrated with a planar arrangement of laser-illuminated gold nanotubes on top of which cells are grown[26]. Throughput was, however, very low as cells had to be manually positioned into the laser beam. In addition, such an approach requires specially microfabricated substrates and is inherently limited to 2-D cell cultures. Instead, SNAP is compatible with normal microscopy samples and may be extended to 3-D cell cultures as well. While we showed two applications where cells were selectively labeled with contrast agents, our platform is equally suited to deliver biologically active molecules, such as nucleic acids or proteins, into selected cells. This could, for instance, be of interests for studying bystander effects or to enable spatially controlled differentiation of stem cells[27].

5. REFERENCES

1. Strack, R. Protein labeling in cells. *Nat Methods* **13**, 33-33 (2016).
2. Zhang, Z.Y., Kenny, S.J., Hauser, M., Li, W. & Xu, K. Ultrahigh-throughput single-molecule spectroscopy and spectrally resolved super-resolution microscopy. *Nat Methods* **12**, 935-938 (2015).
3. D'Astolfo, D.S. et al. Efficient Intracellular Delivery of Native Proteins. *Cell* **161**, 674-690 (2015).
4. Wu, Y.C. et al. Massively parallel delivery of large cargo into mammalian cells with light pulses. *Nat Methods* **12**, 439-+ (2015).
5. Erazo-Oliveras, A. et al. Protein delivery into live cells by incubation with an endosomolytic agent. *Nat Methods* **11**, 861-867 (2014).
6. Stewart, M.P. et al. In vitro and ex vivo strategies for intracellular delivery. *Nature* **538**, 183-192 (2016).
7. Dhakal, K., Batabyal, S., Wright, W., Kim, Y.T. & Mohanty, S. Optical delivery of multiple opsin-encoding genes leads to targeted expression and white-light activation. *Light-Sci Appl* **4** (2015).
8. Chung, J. et al. Single-cell heterogeneity in suppression of PC12 differentiation by direct microinjection of a differentiation inhibitor, U0126. *Cell Biol Int* **38**, 1215-1220 (2014).
9. Remaut, K., Oorschot, V., Braeckmans, K., Klumperman, J. & De Smedt, S.C. Lysosomal capturing of cytoplasmic injected nanoparticles by autophagy: An additional barrier to non-viral gene delivery (vol 195, pg 29, 2014). *J Control Release* **199**, 179-179 (2015).
10. Chang, L.Q. et al. Dielectrophoresis-assisted 3D nanoelectroporation for non-viral cell transfection in adoptive immunotherapy. *Lab Chip* **15**, 3147-3153 (2015).
11. Jain, T. & Muthuswamy, J. Bio-chip for spatially controlled transfection of nucleic acid payloads into cells in a culture. *Lab Chip* **7**, 1004-1011 (2007).
12. Barrett, L.E. et al. Region-directed phototransfection reveals the functional significance of a dendritically synthesized transcription factor. *Nat Methods* **3**, 455-460 (2006).
13. Tirlapur, U.K. & Konig, K. Cell biology - Targeted transfection by femtosecond laser. *Nature* **418**, 290-291 (2002).
14. Antkowiak, M. et al. Fast targeted gene transfection and optogenetic modification of single neurons using femtosecond laser irradiation. *Sci Rep-Uk* **3** (2013).
15. Xiong, R. et al. Laser-assisted photoporation: fundamentals, technological advances and applications. *Advances in Physics: X*, 1-25 (2016).
16. Skirtach, A.G. et al. The role of metal nanoparticles in remote release of encapsulated materials. *Nano Letters* **5**, 1371-1377 (2005).
17. Xiong, R. et al. Comparison of Gold Nanoparticle Mediated Photoporation: Vapor Nanobubbles Outperform Direct Heating for Delivering Macromolecules in Live Cells. *ACS Nano* **8**, 6288-6296 (2014).
18. Lukianova-Hleb, E.Y., Wagner, D.S., Brenner, M.K. & Lapotko, D.O. Cell-specific transmembrane injection of molecular cargo with gold nanoparticle-generated transient plasmonic nanobubbles. *Biomaterials* **33**, 5441-5450 (2012).
19. Xiong, R. et al. Cytosolic Delivery of Nanolabels Prevents Their Asymmetric Inheritance and Enables Extended Quantitative in Vivo Cell Imaging. *Nano Letters* **16**, 5975-5986 (2016).
20. Alvarez, V.A. & Sabatini, B.L. Anatomical and physiological plasticity of dendritic spines. *Annu Rev Neurosci* **30**, 79-97 (2007).
21. Berlin, S. et al. Photoactivatable genetically encoded calcium indicators for targeted neuronal imaging. *Nat Methods* **12**, 852-+ (2015).
22. Shim, S.-H. et al. Super-resolution fluorescence imaging of organelles in live cells with photoswitchable membrane probes. *Proceedings of the National Academy of Sciences* **109**, 13978-13983 (2012).
23. Verstraelen, P. et al. Pharmacological Characterization of Cultivated Neuronal Networks: Relevance to Synaptogenesis and Synaptic Connectivity. *Cell Mol Neurobiol* **34**, 757-776 (2014).

24. Gosselin, K. et al. Senescence-Associated Oxidative DNA Damage Promotes the Generation of Neoplastic Cells. *Cancer Res* **69**, 7917-7925 (2009).
25. Nassour, J. et al. Defective DNA single-strand break repair is responsible for senescence and neoplastic escape of epithelial cells. *Nature Communications* **7**, 10399 (2016).
26. Messina, G.C. et al. Spatially, Temporally, and Quantitatively Controlled Delivery of Broad Range of Molecules into Selected Cells through Plasmonic Nanotubes. *Adv Mater* **27**, 7145-+ (2015).
27. DeForest, C.A. & Tirrell, D.A. A photoreversible protein-patterning approach for guiding stem cell fate in three-dimensional gels. *Nat Mater* **14**, 523-531 (2015).
28. Deruy, E. et al. Level of macroautophagy drives senescent keratinocytes into cell death or neoplastic evasion. *Cell Death Dis* **5** (2014).

6. SUPPLEMENTARY INFORMATION

Supplementary Figures

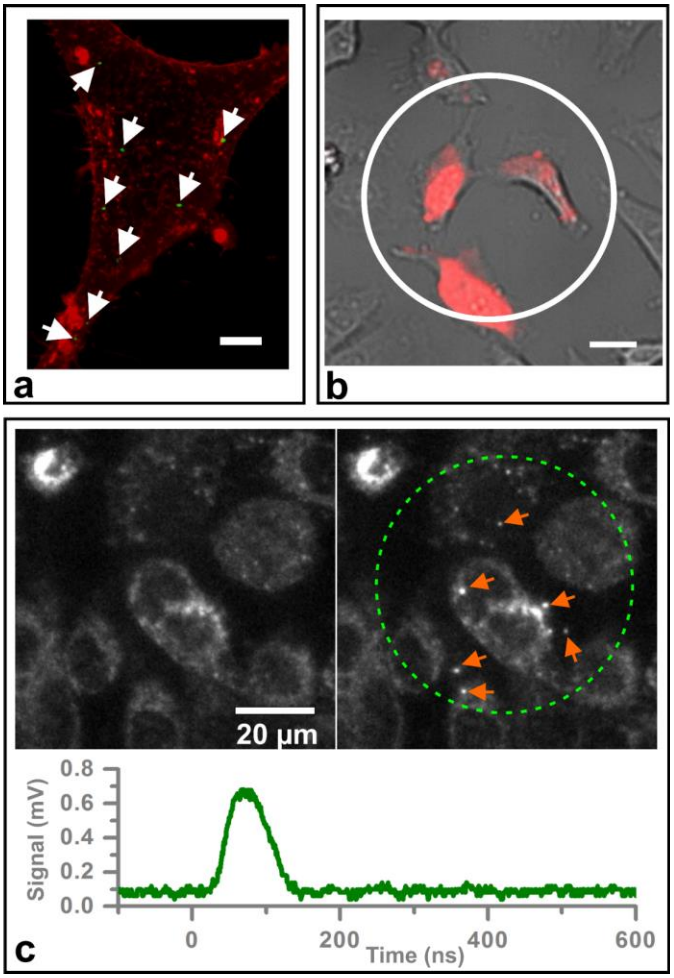

Figure S1. Characterization of SNAP. (a) AuNPs (false-colored in green) that remain adsorbed to the cell membrane (labeled with deep red plasma membrane stain after the washing step) can be detected by confocal microscopy in reflection mode. The image is a 3D projection of a confocal z-stack to visualize all AuNPs on the cell. Scale bare is 5 µm. (b) A single laser pulse was applied to HeLa cells in the indicated circular area. Subsequent influx of of propidium iodide (red) shows that only the irradiated cells become photoporated, while the neighbouring unirradiated cells remain unaffected. Scale bar is 20 µm. (c) Generation of VNB can be verified by dark field microscopy. VNB efficiently scatter light and are visible as transient dots of bright light (orange arrow heads). Alternatively, VNB can be detected in time-resolved mode by monitoring the change in transmitted light of a CW (continuous wavelength) laser focused on the sample. During the VNB lifetime (typically tens to a few hundreds of ns) the CW laser light focus is shifted due to a local change in refractive index, which is detected as a change in transmitted signal through a confocal pinhole in front of the detector.

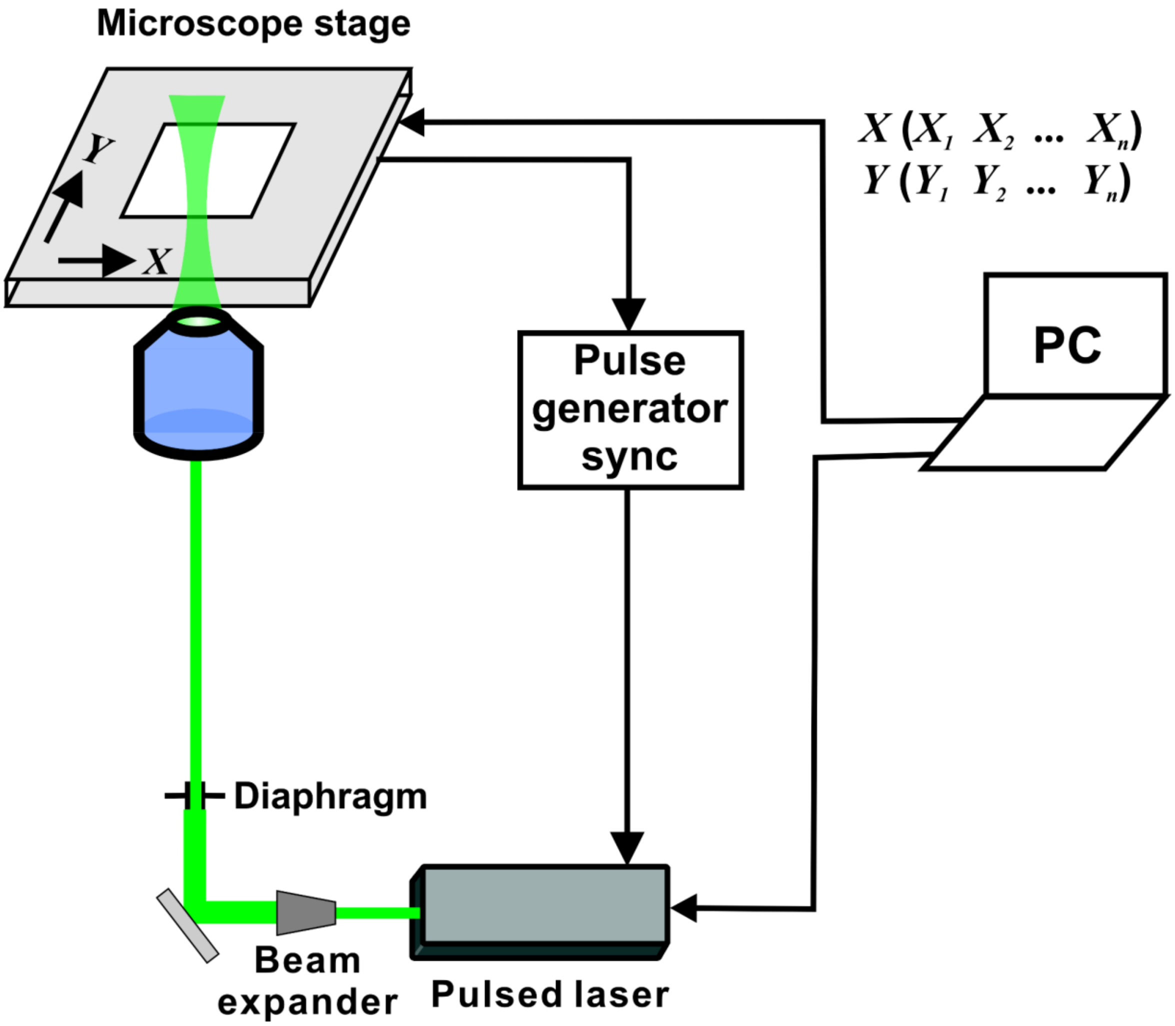

Figure S2. Schematic diagram of the SNAP platform. Laser light from a pulsed laser is directed to the sample through a beam expander, diaphragm and objective lens. The adjustable diaphragm is used as a simple means to adjust the laser beam diameter. Computer software drives the xy-translation stage and controls the laser pulse energy. Every time the xy-stage arrives at a targeted position it will send a trigger signal to the pulse generator, which in turn triggers the laser to send a single pulse to the sample at that location.

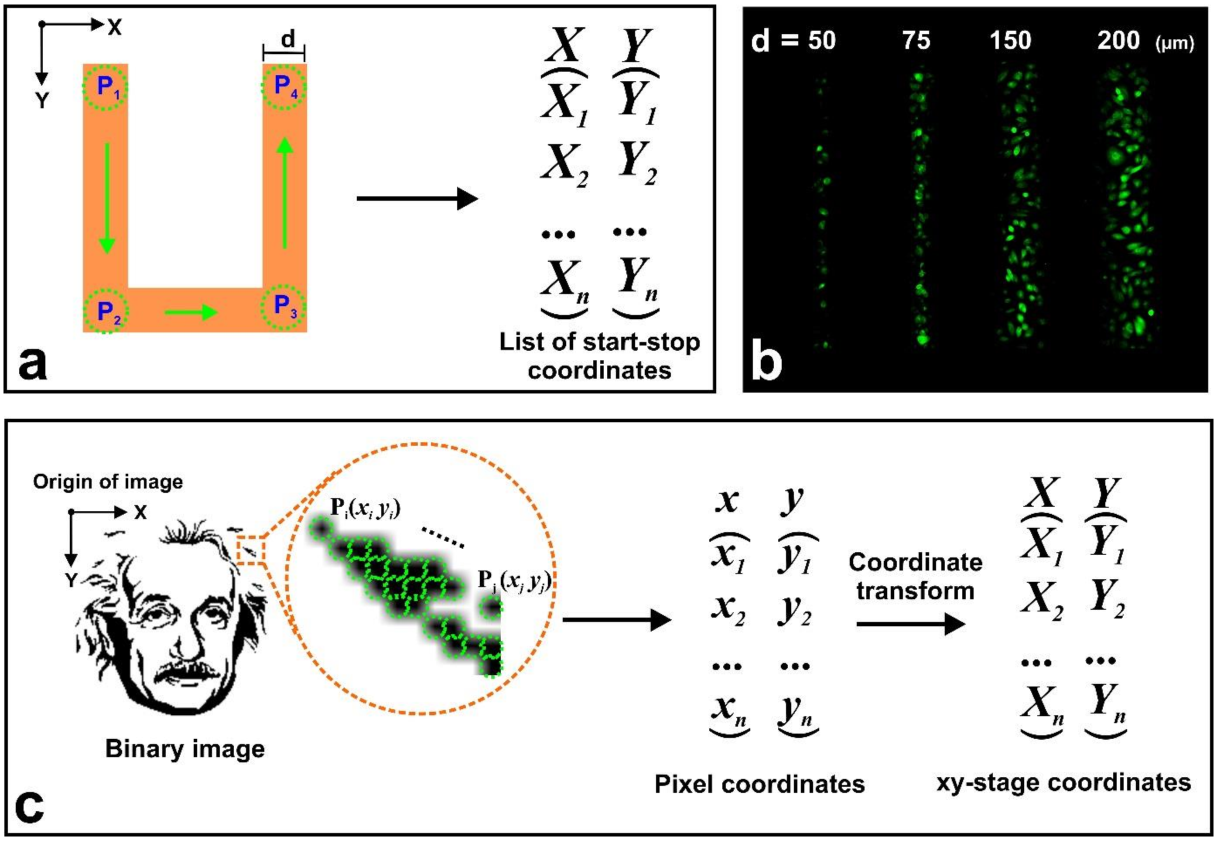

Figure S3. Cells can be photoporated according to pre-defined patterns. (a) In line-scanning mode one defines the start and stop coordinates of individual lines which together form a desired geometry. The line width is determined by the width d of the photoporation laser beam. (b) Demonstration that the photoporation line width can be controlled by changing the laser beam diameter d. Photoporation with FD10 was performed along single lines at neighbouring locations in a HeLa cell culture with different beam sizes (d = 50, 75, 150, 200 µm). (c) In the pixel-based mode one uses the pixels of a black-and-white image as a template to define the places in the sample that should receive a photoporation laser pulse. The selected size of the laser beam determines how the image pixels (*x*,*y*) will be mapped onto the sample (*X*,*Y*).

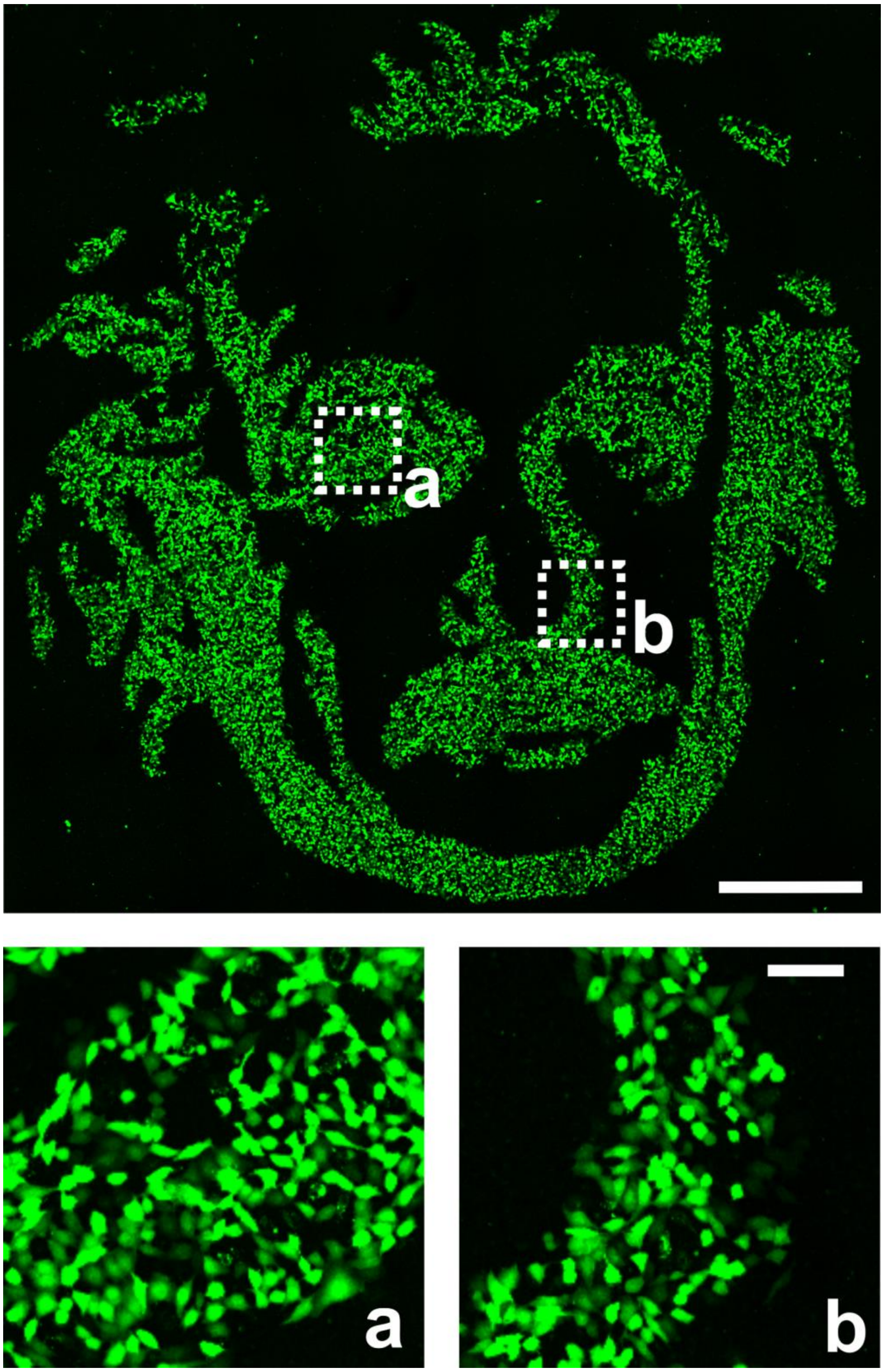

Figure S4. Zoom-in of Fig. 1b showing individual photoporated cells. The scale bars are 1000 µm (top) and 100 µm (bottom).

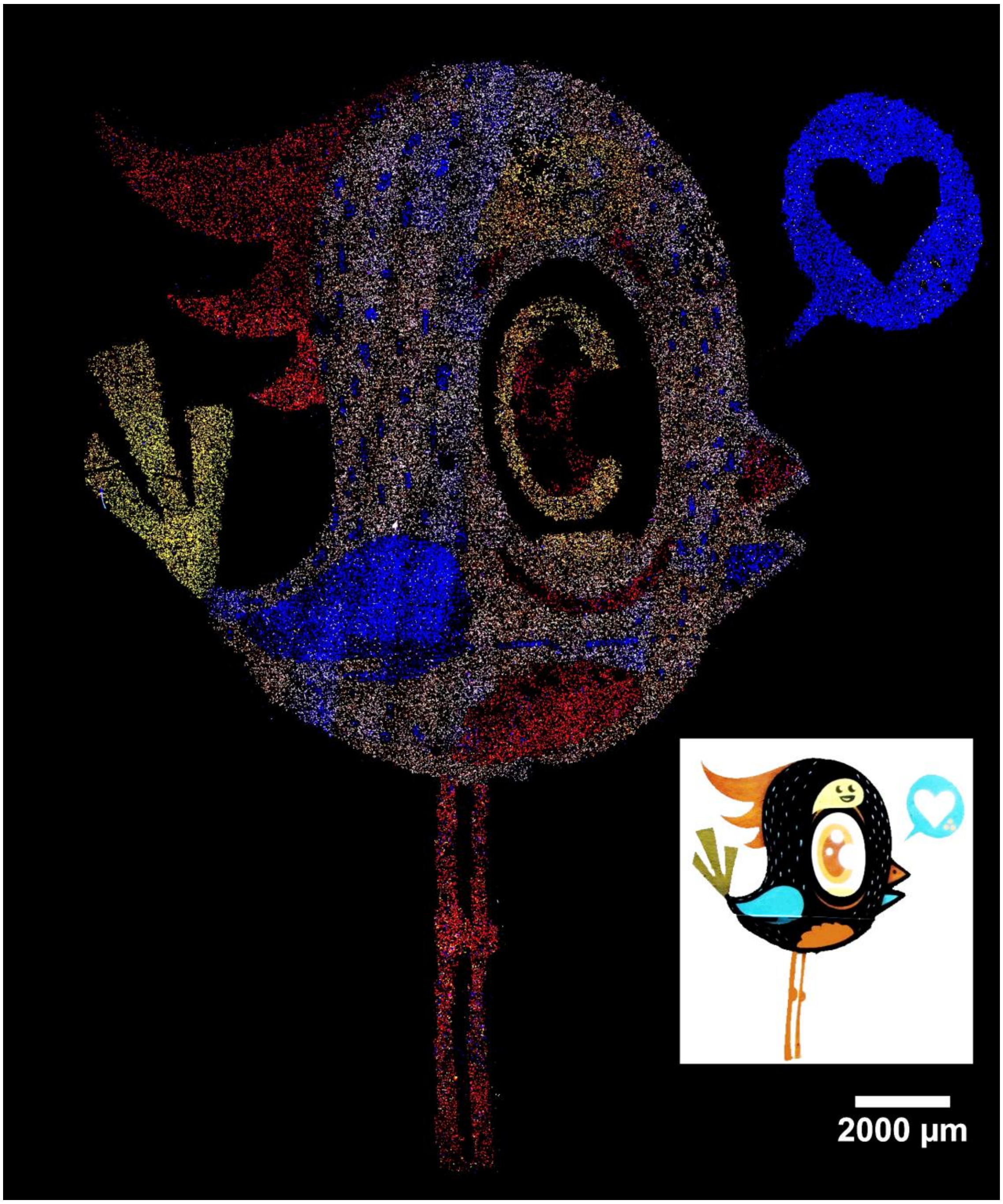

Figure S5. Delivery of multiple compounds into selected regions of a cell culture by repeated photoporation. The signature of the Ghent street artist BUE was used to create a painting in a culture of living HeLa cells with six colors: Alexa 647-dextran (AD; red), FITC-dextran (FD; green), cascade blue-dextran (CD; blue), mixture of FD with AD (yellow), and a mixture of FD with CD and AD (white).

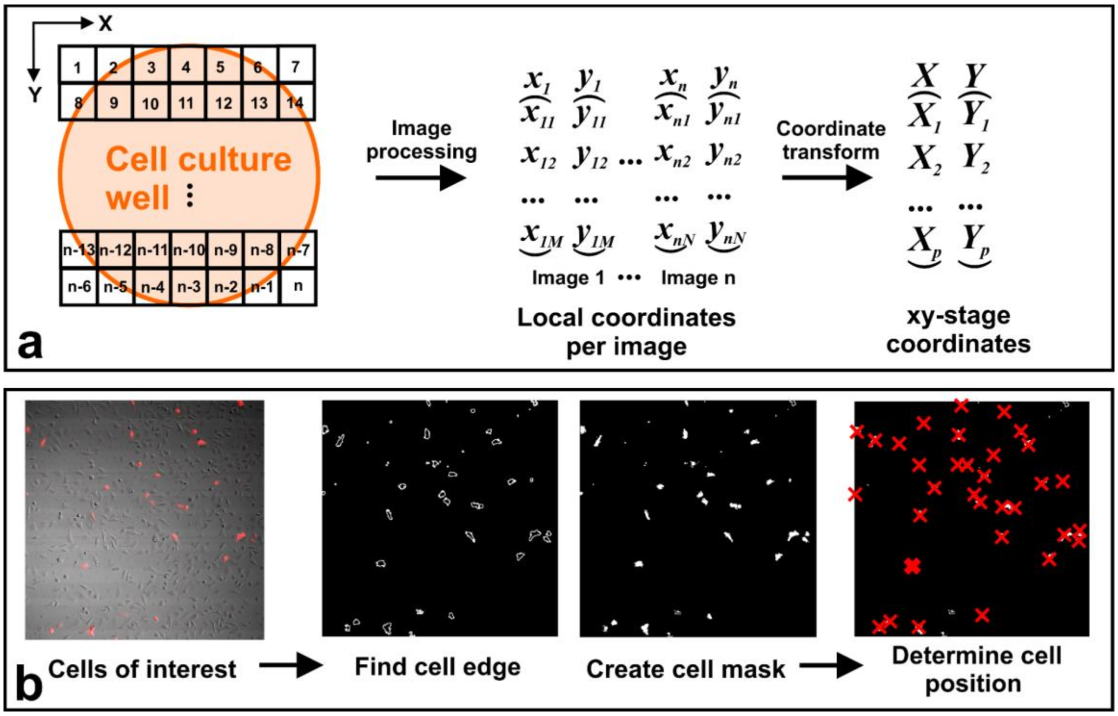

Figure S6. Automated image-guided SNAP of selected cells. (a) The cells in the region of interest (here the entire well) are imaged by capturing adjacent microscopy images. The locations of the cells of interest are determined by image processing for each image. These coordinates are transformed to stage coordinates for sequential photoporation of the selected cells. (b) Overview of the image processing procedure to define the location of fluorescently labeled cells of interest. Edge detection is used to delineate the cells of interest and to define cell masks. The cell coordinates are calculated as the local max. intensity in cell mask.

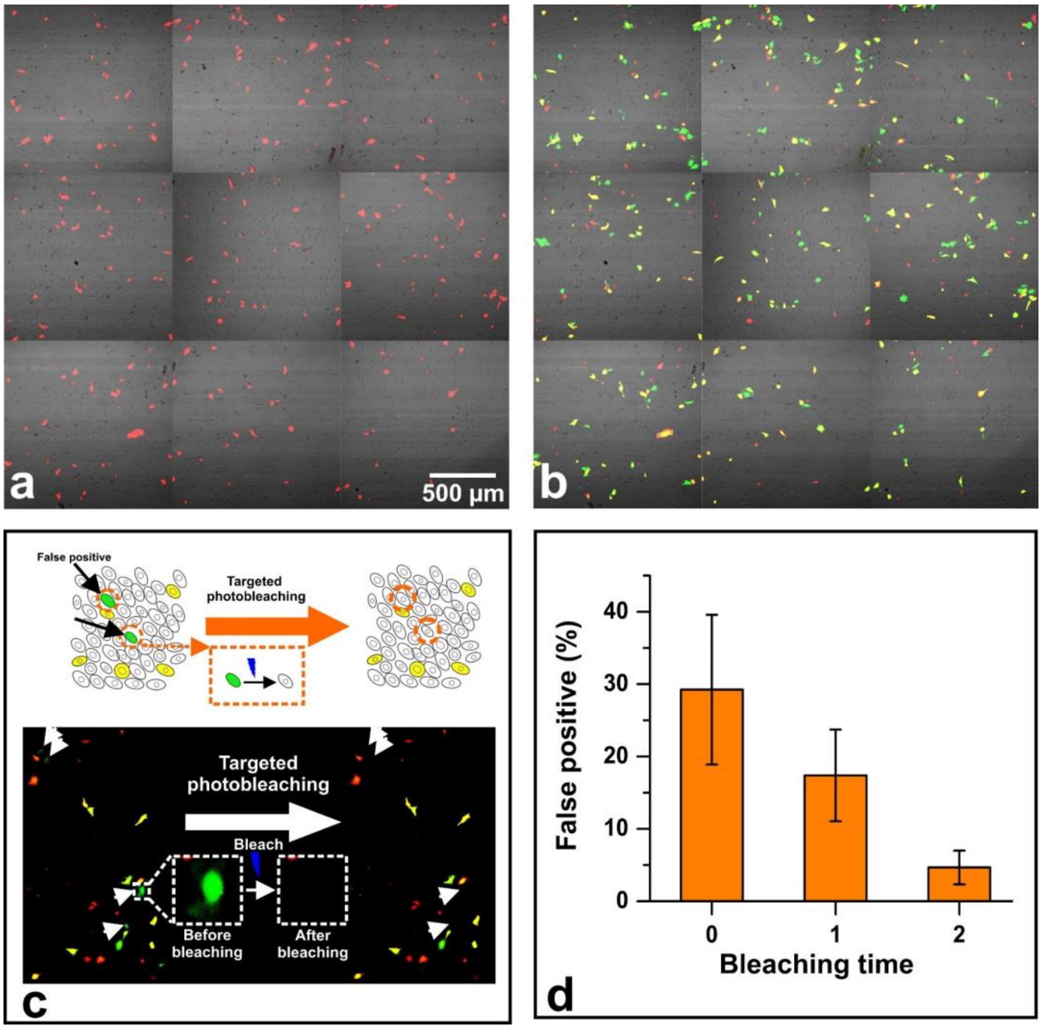

Figure S7. Validation of image-guided automated SNAP. (a) A culture of HeLa cells was prepared with labeled and unlabeled cells in a 1:5 ratio. The image shown is a stitched image consisting of 9 individual images covering a total area of 3.81 mm by 3.81 mm. This area contains 377 red fluorescent cells as determined by image processing. (b) The positions of the red fluorescent cells as determined by image processing are used as input to deliver a green fluorescent compound (FITC-dextran) into those cells by SNAP. More than 70% of the red cells were successfully loaded with the green fluorophore. (c) Of all green cells about 30% were false positives (calculated as the ratio of cells with only green dye over the number of targeted (red) cells). This comes from neighbouring cells which became photoporated too, as well as some dead cells into which the dye can penetrate. In case of fluorescent labels, these false positives can be largely removed by a subsequent photobleaching procedure targeting cells that only contain green dye. (d) After two rounds of targeted photobleaching the fraction of false positive cells could be reduced to 5%. The data shown comes from three independent repeats where n1=847, n2=416, and n3=633 cells were targeted (i.e. red fluorescent).

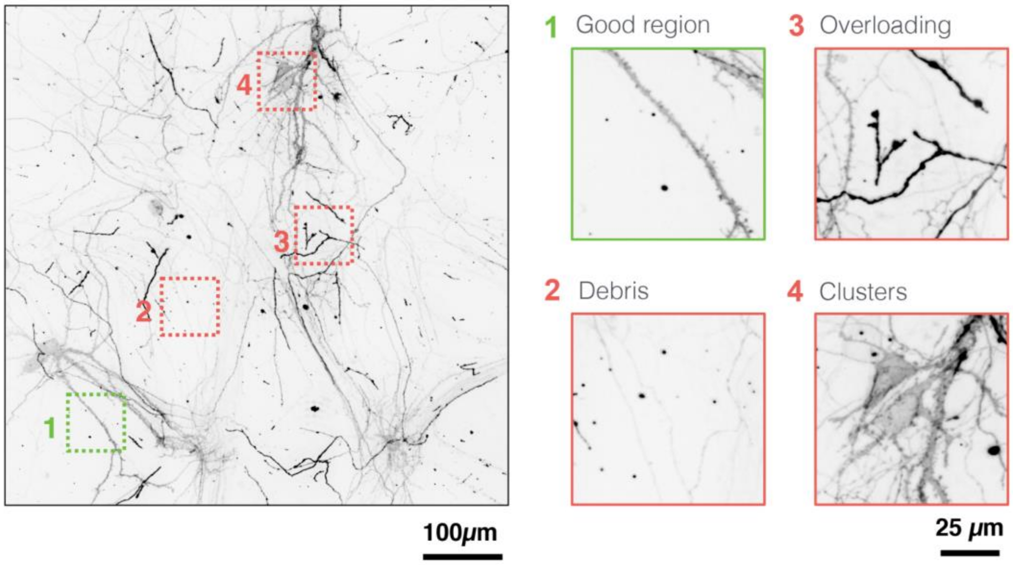

Figure S8. An example image of DiI-stained neurons with dendritic spines after 14 days in culture. Cells were fixed (4% paraformaldehyde in 0.1 M phosphate buffer, 10 min at room temperature) and stained with the carbocyanine dye CM-DiI (Life Technologies) at 1 µg/ml for 20 min at room temperature. The images were recorded at least 24 h post staining allowing the hydrophobic dye to spread throughout the plasma membrane. Images are shown in negative contrast for improved visualization. In such densely labeled cultures it is difficult to find regions that are suitable for quantitative morphological analysis, thus hindering high-throughput automated image analysis as required in screening assays.

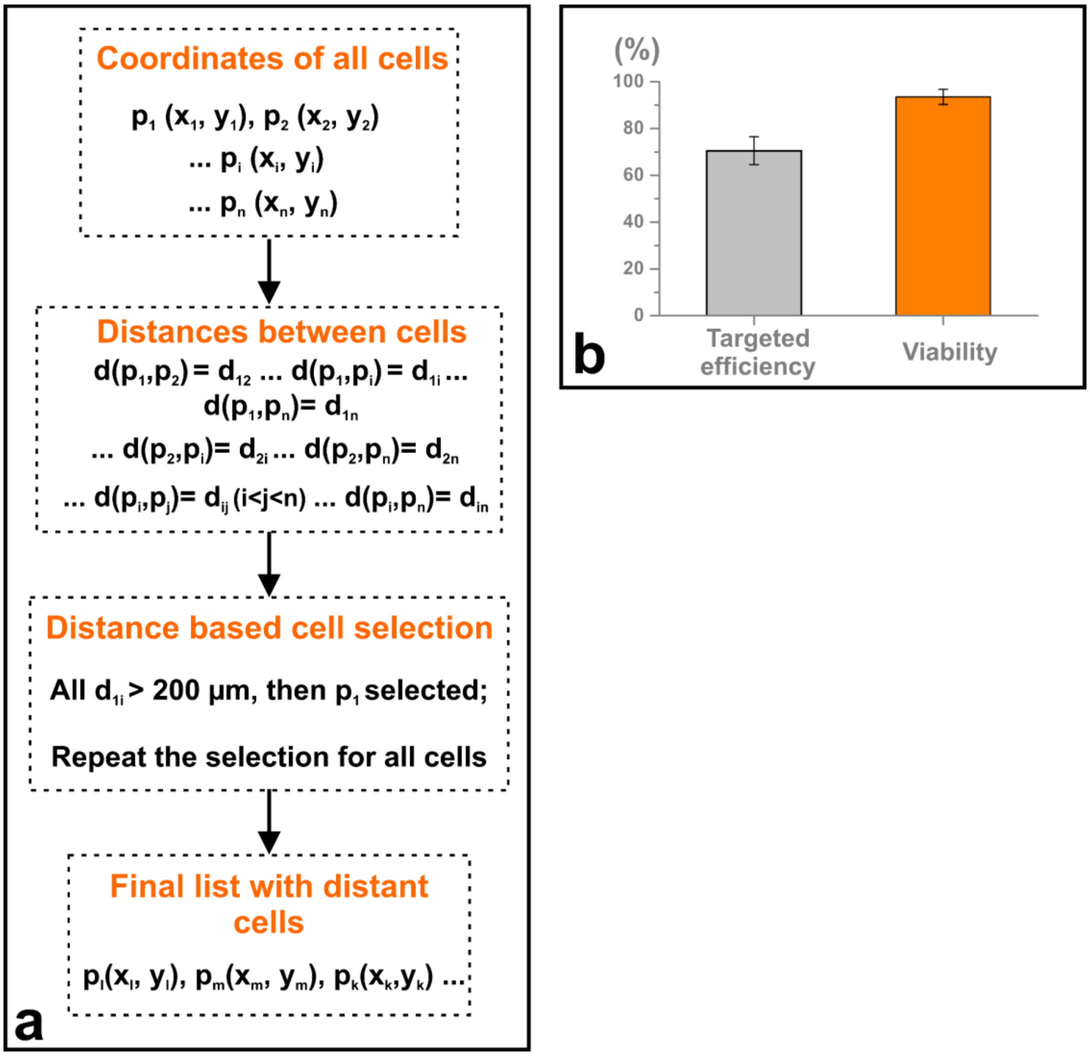

Figure S9. Automated selection of a sparse set of distant neuronal cells. (a) A simple algorithm was developed to randomly select individual cells that are at least 200 µm apart. After determining the cell positions by image processing (here based on the nuclear stain Hoechst), the distances between all cells are calculated. Next, a subset of cells is selected that are at least 200 µm apart. This list with coordinates is finally used for photoporation of the selected cells with phalloidin. (b) The target efficiency was quantified based on the labeling of hundreds of cells (n=3). To assess cell viability, the photoporation procedure was performed on an entire culture of hippocampal cells. Cell viability was measured by subsequent Propidium Iodide labeling (2 h after the photoporation procedure) for three independent biological repeats. Despite hippocampal cells being very sensitive cells, the near perfect cell viability shows that the optimized photoporation procedure is very gentle to the cells.

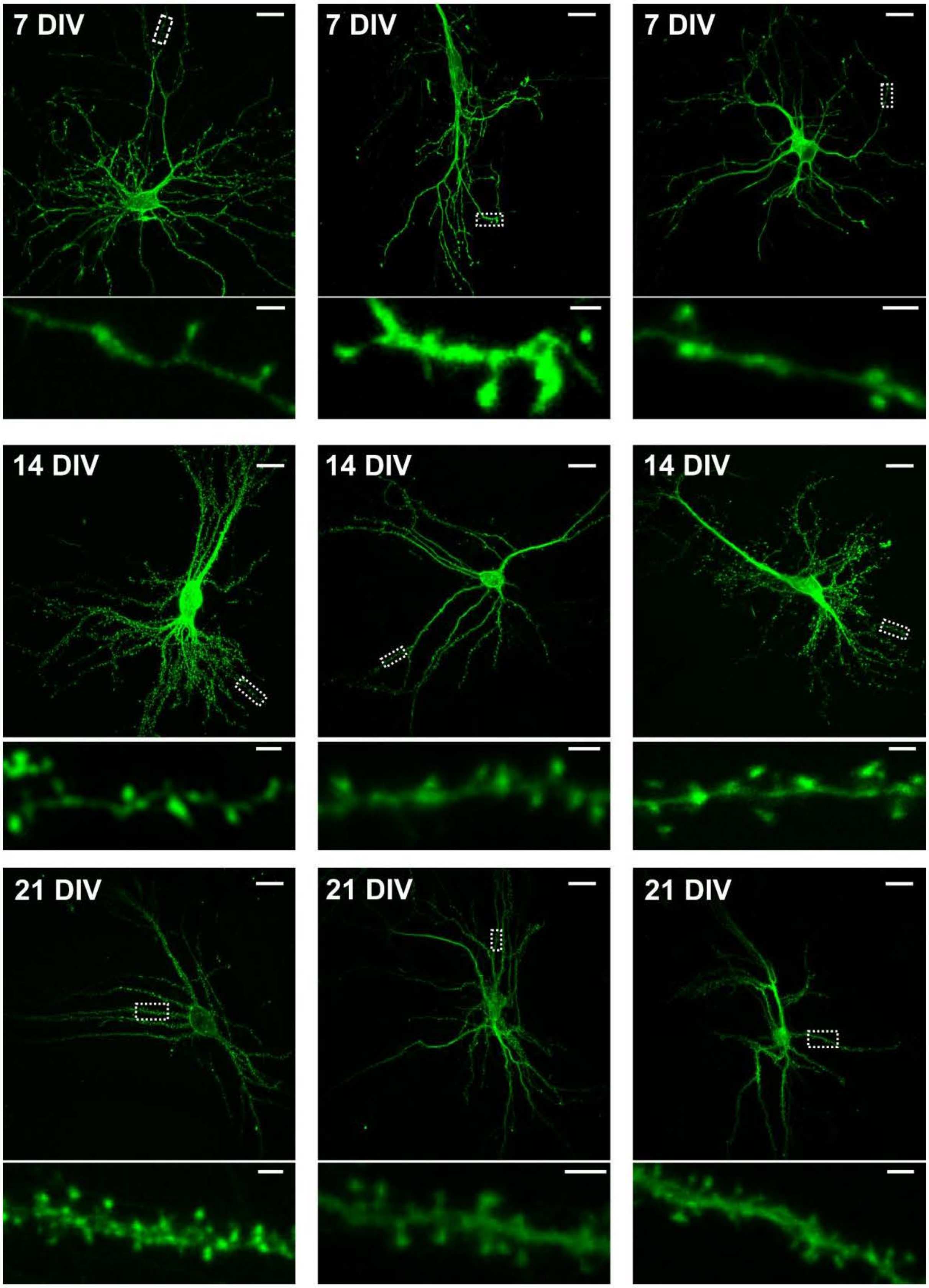

Figure S10. Labeling of selected neuron cells in primary mouse hippocampal cultures enables accurate imaging of dendritic spines. Exemplary images are shown of three different single neurons at 7 DIV, 14 DIV and 21 DIV (scale bars 20 µm). Below each image a magnified view of the indicated dendrite is shown (scale bar 2 µm). The images clearly show that the spine density along the dendrites increases over time.

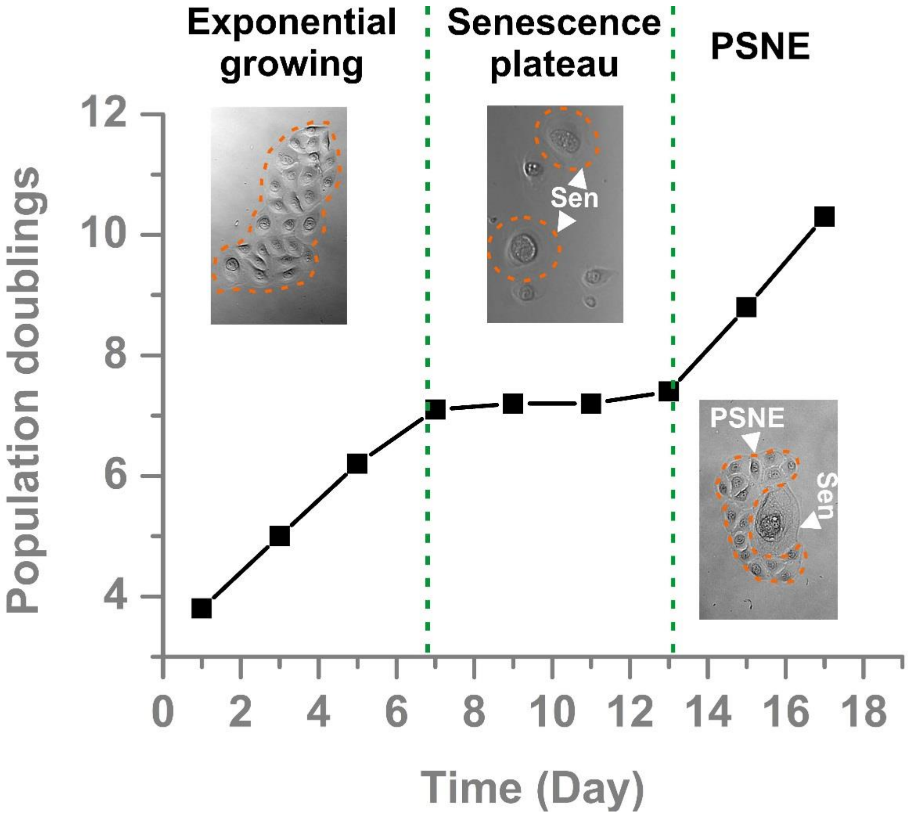

Figure S11. Growth curve of in vitro cultivated NHEKs. The growth curve of NHEKs starts with an initial exponential growth, followed by a senescence plateau characterized by cell cycle arrest. A small fraction of the senescent cells, however, re-enter the cell cycle, which is referred to as PSNE (post senescence neoplastic emergence). Transmission microscopy images are shown of typical cells in each phase. In the growth phase, the cells have their typical morphology of epithelial cells growing as islets. Cells in the senescence phase (Sen) typically become larger in size. In the PSNE phase there are senescent cells from which new daughter cells emerge, which are the PSNE cells.

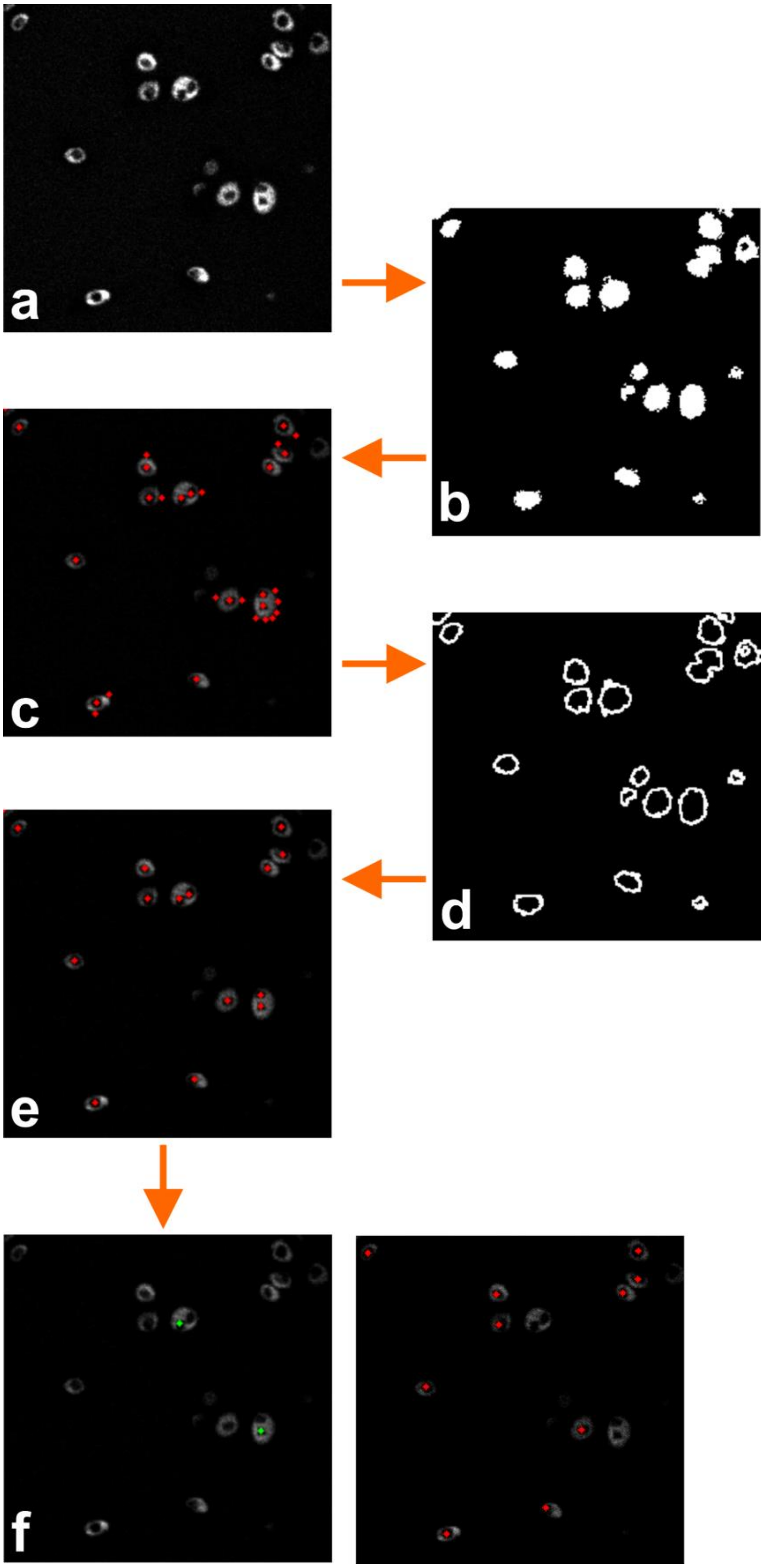

Figure S12. Image processing procedure for determining the location of mononuclear and polynuclear NHEK cells. (a) Nuclei are visible as dark areas by labeling the late endolysosomes in the perinuclear area. (b) Cell masks are defined by edge detection and subsequent filling using Matlab functions ‘edge’ and ‘imfill’. (c) Local minimal within each cell mask are identified, indicated by the red points. (d) Local minima close to the edge of the cell mask are removed. (e) The remaining red points demarcate the position of nuclei. (f) Polynucleated cells are identified based on two nuclei positions that within a short distance (15 µm) of each other. The polynucleated cells are indicated with a green dot, and those coordinates are subsequently used for selective photoporation of those cells. Alternatively the mononucleic cells can be identified (indicated by red dots) for subsequent photoporation.

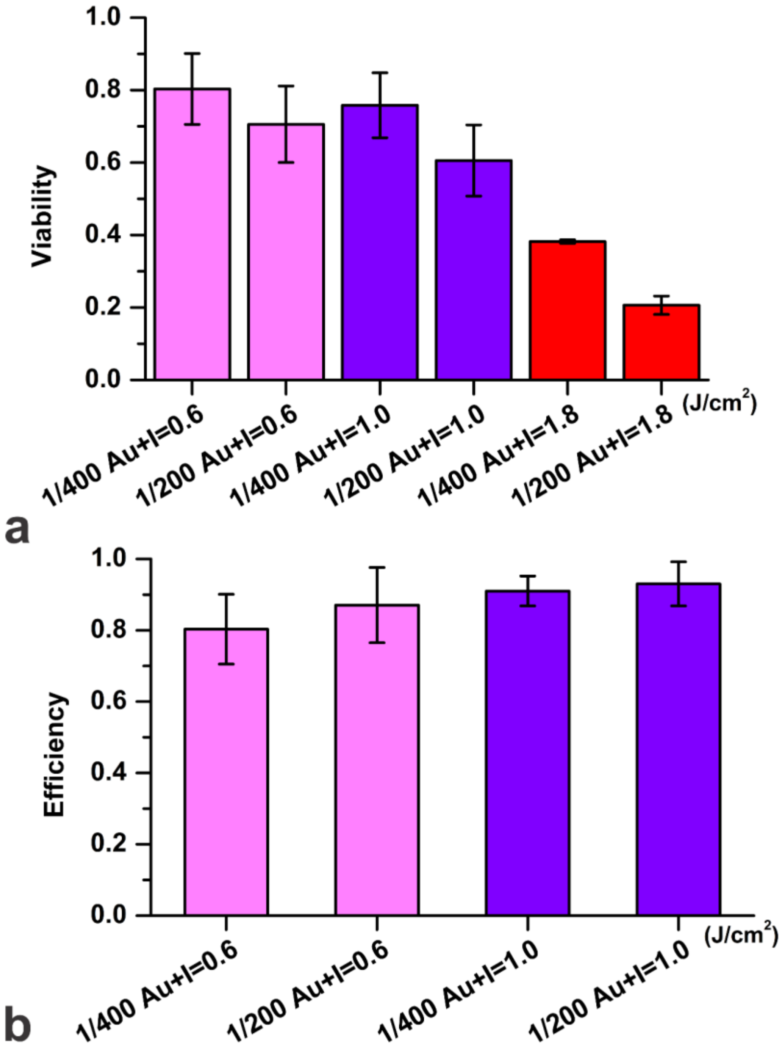

Figure S13. Optimization of cytotoxicity and labeling of NHEK with FITC-dextran. (a) Presenescent NHEKs were photoporated with FD10 using two different AuNP concentrations (concentration of 1/400 AuNPs is ~2.5 × 107 nps/ml, and 1/200 AuNPs is ~5.0 × 107 nps/ml) and 3 different laser fluence settings (I = 0.6, 1.0 and 1.8 J/cm2). Cytotoxicity was measured by MTT assay after 4 days to assess long-term cytotoxicity. (b) The labeling efficiency was measured in parallel for the two lowest laser fluence levels. Labeling efficiency was quantified as the fraction of positive cells, i.e. the cells containing a detectable FD10 signal above the background (untreated cells).

Supplementary Movies

Supplementary Movie 1. To validate selective delivery by SNAP, the cytoplasmic accumulation of cell impermeable dye of Propidium Iodide (PI) was in situ recorded by fluorescence microscopy before and after photoporation. Subsequent influx of of PI (red) shows that only the irradiated cells become photoporated, while the neighbouring unirradiated cells remain unaffected. (https://figshare.com/s/7cb6528a1d9c083dbcf3)

Supplementary Movie 2. Andy Warhol's painting of Einstein was reproduced by photoporating HeLa cells sequentially with cascade blue-dextran (blue), FITC-dextran (green) and Alexa 647-dextran (red). The cells in two specific region were imaged in a stage-top cell incubator (37 °C) with confocal microscopy for ~10 hours. (https://figshare.com/s/bf5166bd2163ad9d1fb8)

Supplementary Movie 3. The signature of the Ghent street artist BUE was used to create a painting in a culture of living HeLa cells with six colors: Alexa 647-dextran (AD; red), FITC-dextran (FD; green), cascade blue-dextran (CD; blue), mixture of FD with AD (yellow), and a mixture of FD with CD and AD (white). The cells in one specific region were imaged in a stage-top cell incubator (37 °C) with confocal microscopy for ~10 hours. (https://figshare.com/s/7db34274e973d00bc069)

Supplementary Movie 4. A neuron cell in primary mouse hippocampal cultures selectively labeled by SNAP and 3D imaged with confocal microscopy. (https://figshare.com/s/608dba9fabd24f043505)

Supplementary Matlab Code

The Matlab code source which was developed SNAP to determine cell positions can be downloaded via this link: https://figshare.com/s/227b20516d845711dbb2

PART II

SIZING NANOMATERIALS IN BIO-FLUIDS BY FRAP

Chapter 6

cFRAP sizing nanomaterials: introduction, theory and validation

This chapter is part of the publication:

Sizing nanomaterials in bio-fluids by cFRAP enables protein aggregation measurements and diagnosis of bio-barrier permeability

Ranhua Xiong[1,2], Roosmarijn E. Vandenbroucke[3,4], Katleen Broos[5], Toon Brans[1,2], Elien Van Wonterghem[3,4], Claude Libert[3,4], Jo Demeester[1], Stefaan C. De Smedt[1], Kevin Braeckmans[1,2], Nature Communications, 2016, doi:10.1038/ncomms12982

[1]Laboratory of General Biochemistry and Physical Pharmacy, Ghent University, Ghent, Belgium
[2]Centre for Nano- and Biophotonics, Ghent University, Ghent, Belgium
[3]Inflammation Research Center, VIB, Ghent, Belgium
[4]Department Biomedical Molecular Biology, Ghent University, Ghent, Belgium
[5]Anabiotec nv, Evergem, Belgium

ABSTRACT

FRAP is widely applicable in the biophysical, pharmaceutical and material sciences to study diffusion of molecules and nanoparticles on a micrometer scale. With an intense laser beam the fluorescence inside a micrometer sized area is photobleached, and the subsequent recovery of the fluorescence due to diffusion of the labelled molecules is imaged over time. To date, quantitative interpretation of FRAP data is based on analyzing the average intensity in the bleach area as a function of time. Consequently, the spatial information in the diffusion profiles remains largely unused, due to which interpretation of FRAP data is limited to a single average diffusion coefficient. Recently, our group developed a new and improved FRAP model, based on the photobleaching of a rectangular area (rFRAP), which allows analysis of the entire spatial diffusion profile in confocal recovery images. Although rFRAP was demonstrated to offer improved precision over standard FRAP, interpretation was limited to a single diffusion coefficient until now. Here we extend the capability of rFRAP to measuring polydisperse samples with a continuous distribution of diffusion coefficients (cFRAP). First we present the mathematical derivation of the cFRAP model. The influence of experimental parameters of a cFRAP experiment on the measurement is examined by simulations. We confirm through simulations that cFRAP can correctly analyze polydisperse systems with a continuous broad range of diffusion coefficients. Furthermore, we investigate what is the minimal SNR that is needed in the recovery images to perform meaningful cFRAP analysis. Finally, cFRAP is validated by performing FRAP experiments on solutions of FITC-dextran of different molecular weight and mixtures thereof, in comparison with DLS measurement. Thanks to including spatial information in the cFRAP model, we found that the apparent PDI of the distributions was significantly less compared to the PDI measured by DLS, which demonstrated the improved precicsion of this method thanks to taking the full tempo-spatial information into account.

1. INTRODUCTION

Fluorescence recovery after photobleaching (FRAP) has been used extensively to study mobility of molecules and nanoparticles on a micrometer scale in terms of an average local diffusion coefficient[1, 2]. Since its development in the 1970s[3, 4], FRAP has been widely applied to the biophysical, pharmaceutical and material sciences. For example, FRAP has been used to study the diffusion of molecules in living cells like the mobility of molecules in the cell membrane[5-10], cytoplasm[11-15] and nucleus[16-19]. Additionally, FRAP has also been applied to study the mobility of macromolecules in extracellular matrices[20-24] and pharmaceutical solutions and gels[25-31].

In a FRAP experiment, fluorescently labeled molecules in a micron sized area of the sample are photobleached by a powerful laser excitation pulse. Through this photochemical process, fluorescent molecules lose their fluorescence properties. After photobleaching, the photobleached fluorescent molecules will diffuse out of the beach area and are replaced by unbleached fluorescent molecules from the surrounding region. A gradual recovery of the fluorescence inside the area will occur due to this diffusional exchange, as can be observed from confocal time-lapse images. The rate of fluorescence recovery is proportional to the rate of diffusion of the fluorescently labeled molecules. Fitting a suitable FRAP model to the observed fluorescence recovery can yield the physical quantities describing the local diffusion in the sample, such as the average diffusion coefficient[29].

To date, quantitative interpretation of FRAP data is limited to the analysis of the average intensity in the bleach area over time, as it reduces the mathematical complexity of the diffusion model. As such the spatial information of the diffusion profiles is essentially lost, which results in limited precision of FRAP analyses. Recently, we developed a fast and straightforward FRAP model that makes use of the full temporal and spatial diffusion process after photobleaching of an arbitrary rectangular area (rFRAP)[32]. While it offers improved precision, rFRAP with least squares fitting still limits data interpretation to a single-component diffusion process, or a discrete multicomponent system at best. Generally, however, polydisperse systems have a continuous distribution of diffusion coefficients While some attempts have been made to apply FRAP to the measurement of polydisperse systems, success was very much limited as those methods still relied on analyzing the average intensity over time[33-35].

Here, we extend the rFRAP model to describe a continuous distribution of diffusion coefficients (termed as cFRAP). We make use of the Maximum Entropy Method (MEM) when fitting the cFRAP model to confocal recovery images to ensure that features, such as local extrema, in the resulting distribution of diffusion coefficients are statistically warranted by data[36-38]. First we will give an outline of the mathematical derivation that leads to the cFRAP model. Next, we will test the influence of experimental parameters on the distribution of diffusion coefficients by fitting the cFRAP model to simulated recovery images. Following, the ability of this method to recover continuous diffusion coefficients distributions will be evaluated. Furthermore, the minimal SNR that is needed in the recovery images to perform meaningful cFRAP analysis is tested. Finally, cFRAP analysis is validated in sizing single or mixture different FITC-dextran, and compared with DLS measurement.

2. THEORY OF CFRAP

We start from the rFRAP (rectangle FRAP) model developed before for measuring a single average diffusion coefficient according to Deschout et al., which makes use of both time and spatial information in the recovery images[32]:

$$F(x,y,t) = F_0 - F_0 \cdot \frac{K_0}{4} \cdot \left[erf\left(\frac{x + \frac{l_x}{2}}{\sqrt{r^2 + 4Dt}} \right) - erf\left(\frac{x - \frac{l_x}{2}}{\sqrt{r^2 + 4Dt}} \right) \right] \cdot \left[erf\left(\frac{y + \frac{l_y}{2}}{\sqrt{r^2 + 4Dt}} \right) - erf\left(\frac{y - \frac{l_y}{2}}{\sqrt{r^2 + 4Dt}} \right) \right] \quad (1)$$

where t is the time after photobleaching, K_0 the photobleaching parameter (which determines the extent of bleaching), D is the isotropic diffusion coefficient of diffusing species, l_x and l_y are the width and height of the rectangular photobleaching area, and r^2 is the mean square resolution of the bleaching and imaging point-spread function. In case of N independent diffusing components, we can simply make a superposition of the individual fluorescence recovery profiles:

$$F(x,y,t) = \sum_i \alpha_i \varepsilon_i F_i(x,y,t) \quad (2)$$

where α_i is the relative fraction of the i^{th} component and ε_i is the corresponding relative fluorescence brightness. Evidently, $\sum_{i=1}^{N} \alpha_i = 1$.

Defining:

$$k_i = \alpha_i \varepsilon_i K_{0i} \quad (3)$$

the multicomponent rFRAP model becomes:

$$F(x,y,t) = F_0 - F_0 \cdot \sum_i \frac{k_i}{4} \cdot \left[erf\left(\frac{x + \frac{l_x}{2}}{\sqrt{r_i^2 + 4D_i t}} \right) - erf\left(\frac{x - \frac{l_x}{2}}{\sqrt{r_i^2 + 4D_i t}} \right) \right] \cdot \left[erf\left(\frac{y + \frac{l_y}{2}}{\sqrt{r_i^2 + 4D_i t}} \right) - erf\left(\frac{y - \frac{l_y}{2}}{\sqrt{r_i^2 + 4D_i t}} \right) \right] \quad (4)$$

The multicomponent rFRAP model of Eq. (4) can be generalized to describe a continuous distribution of diffusion coefficients $a(D)$:

$$F(x,y,t) = \int \alpha(D) f\big(x,y,t,D,K_0(D),r(D)\big)\, dD \quad (5)$$

where $f(x,y,t,D,K_0(D),\varepsilon(D),r(D))$ describes the fluorescence recovery of a component with diffusion coefficient D. Inserting Eq. (1) and (2) into Eq. (5) yields:

$$F(x,y,t) = F_0 - \frac{F_0}{4} \int \alpha(D) \epsilon(D) K_0(D) f'\big(x,y,t,D,r(D)\big) dD \quad (6)$$

where $f'(x,y,t,D,r(D))$ is defined as:

$$f'\big(x,y,t,D,r(D)\big) = \left[erf\left(\frac{x + \frac{l_x}{2}}{\sqrt{r^2 + 4Dt}} \right) - erf\left(\frac{x - \frac{l_x}{2}}{\sqrt{r^2 + 4Dt}} \right) \right] \cdot \left[erf\left(\frac{y + \frac{l_y}{2}}{\sqrt{r^2 + 4Dt}} \right) - erf\left(\frac{y - \frac{l_y}{2}}{\sqrt{r^2 + 4Dt}} \right) \right] \quad (7)$$

For numerical computation according to the maximum entropy method (MEM) we now make the transition to the semi-continuous case. Let D be discretized in n components (e.g. with equal interval in $log(D)$ space) in the range of D_{min} to $D_{max.}$, Eq. (7) becomes:

$$F(x,y,t) = F_0 - \frac{F_0}{4} \sum_{i=1}^{n} k_i f'(x,y,t,D_i,r_i) \quad (8)$$

where we made use of Eq. (3). Eq. (8) can be used for direct fitting to the pixel values in the recovery images.

Alternatively, the recovery data can be analyzed based on the average intensities in ring areas (**Fig. 1b**). This considerably reduces computation time while retaining the essential spatial information. The average intensity in ring R_i is calculated as:

$$F_i(t) = \frac{1}{M_i} \sum_{(x,y)\epsilon R_i} F(x,y,t) \quad (9)$$

where *F(x,y,t)* is defined in Eq. (8) and M_i is the number of pixels inside ring R_i .

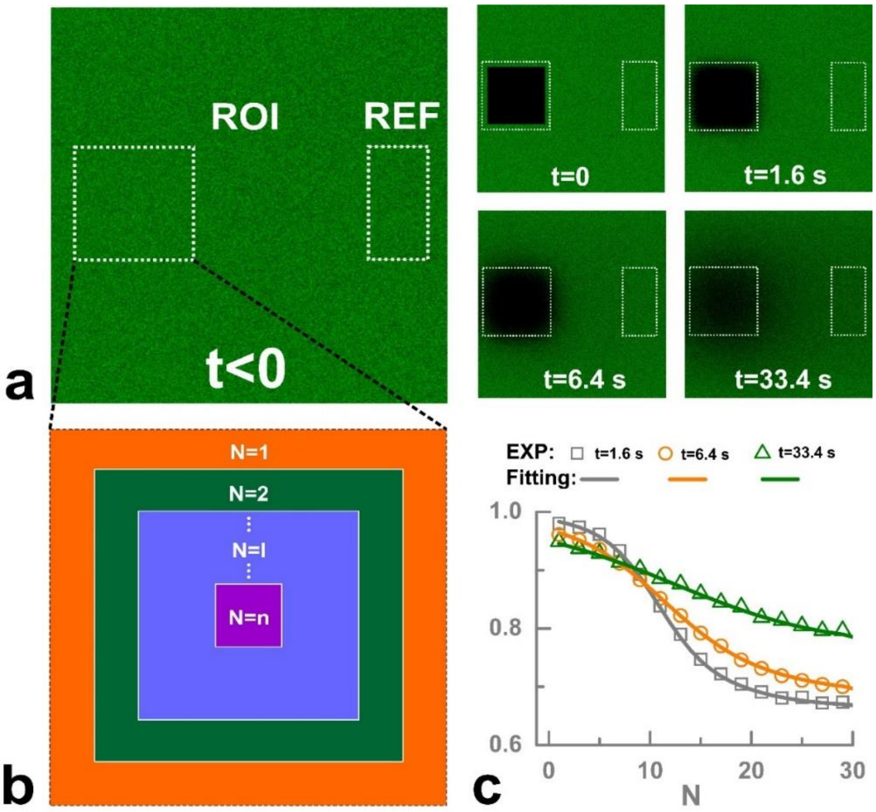

Figure 1. (a) Confocal images (field of view 153.6 μm by 153.6 μm) are shown of an cFRAP experiment in a FITC-dextran solution. Images are shown before (t < 0), during (t = 0) and after photobleaching (t > 0). cFRAP analysis is performed on the indicated Region of Interest (ROI). The REF region indicates the reference area that is used in the analysis to correct for potential laser fluctuations and bleaching during imaging. (b) For analysis according to the 'ring-based method', the ROI is divided into n equally spaced rectangular ring areas. (c) The normalized average intensity of each 'ring' is shown at time points t = 1.6, 10.6 and 50.6 s. The solid lines represent the best fit of the cFRAP model. Note that a single fit is done to all spatial profiles for all available time points in the data set simultaneously.

Instead of performing a standard least squares fitting of Eq. (9) to the experimental data, the Maximum Entropy Method (MEM) finds the 'best-fit' solution with maximum entropy. MEM ensures that the fitting result (i.e. the distribution of diffusion coefficients) contains the least possible information in order to avoid over-interpretation of noise due to limited sampling statistics. In other words, it looks for the smoothest best fit solution in the maximum entropy sense. The 'historic MEM' approach was implemented in this work, which means maximizing the Shannon-Jaynes entropy:

$$S = -\sum_{i=1}^{n} k_i log k_i \qquad (10)$$

under the least-squares condition of $\chi^2 = M$, where *M* is the total number of data points. For the pixel based fitting, the χ^2 statistic is calculated by:

$$\chi^2 = \sum_i \sum_j \sum_k \frac{[F_{ij}(t_k) - F'_{ij}(t_k)]^2}{\sigma_{ij}^2(t_k)} \qquad (11)$$

where $F_{ij}(t_k)$ is the normalized fluorescence at position x_i, y_j at time point t_k and $\sigma_{ij}^2(t_k)$ is the corresponding variance. $F'_{ij}(t_k)$ is the corresponding theoretical value calculated from Eq. (8).

On the other hand, for the ring analysis, the χ^2 statistic is calculated by:

$$\chi^2 = \sum_i \sum_k \frac{[F_i(t_k) - F'_i(t_k)]^2}{\sigma_i^2(t_k)} \qquad (12)$$

where $F_i(t_k)$ is the experimental average fluorescence in i^{th} ring at time point t_k and $\sigma_i^2(t_k)$ is the corresponding variance. $F'_i(t_k)$ is again the corresponding theoretical value calculated from Eq. (9). The variance can be calculated for simulated images according to:

$$\sigma_i^2(t_k) = \frac{\sigma^2}{M_i} \qquad (13)$$

where σ is the standard deviation on the pixel values used for simulating the FRAP recovery images. For experimental images it can be calculated from[39]:

$$\sigma_i^2(t_k) = \frac{aF_i(t_k) + b}{M_i} \qquad (14)$$

Where a and b are constant parameters that can be determined by a series of images with various laser intensities of a homogeneous fluorescent solution with identical instrumental settings as in the final FRAP experiment[40].

Based on the theory outlined above, a Matlab code was written for MEM analysis of the recovery images which results in a semi-continuous distribution of diffusion coefficients, which can be converted to a distribution of sizes by the Stokes-Einstein equation when required. The Matlab code source is online available: figshare.com/s/9d93ae06318911e58f3e06ec4bbcf141 and a user's guide is also available: figshare.com/s/cb38f1cc318911e5a4f706ec4bbcf141 (or see **Appendix A**). To ensure proper use of this method, it is important to stress two important experimental requirements. The theory is based on 2-D diffusion only. In 3-D extended samples (as is the case in this work) this means that bleaching should be performed with an objective lens of sufficiently low NA (typically <0.5) which produces a cylindrical laser beam in a substantial area above and below the focal plane. In that case, the bleaching will be quite uniform over an extended region along the optical axis, so that only 2-D radial diffusion effectively takes place[1]. Secondly, in the derivation of the rFRAP model according to Deschout et al.[32], the assumption is made of a linear photobleaching process. In reality, however, photobleaching rather follows an exponential type of decrease. This means that the model will only work perfectly for modest bleach depths, i.e. up to 50% photobleaching as demonstrated before[32]. This can be easily accommodated for by changing the bleach laser intensity appropriately.

3. MATERIASL AND METHODS

3.1 FRAP equipment and experimental procedure.

FRAP experiments were performed on a C1-si confocal microscope (Nikon, Japan) equipped with a 488 nm Ar-ion laser of 40 mW and acoustic optical tunable filter (AOTF) to modulate the laser intensity for bleaching and imaging (fastest imaging rate ~0.5 frame/s). Rectangular areas were photobleached and the fluorescence recovery was imaged using the Nikon NIS Elements AR software package. A 10× NA 0.45 plan apochromat objective lens was used for bleaching and imaging. The laser power was adjusted to obtain 25-50% bleaching, in accordance with the theoretical requirement of limited bleaching (due to the assumption of a linear photobleaching process in the derivation of Eq. (1)). The recovery time depends on the diffusion coefficient as well as the size of the bleach area. A particular benefit of our theoretical framework is that we can adjust the size of the bleach rectangle in a continuous fashion. The smallest component in our applications is FITC-dextran of 4 kDa (FD4), while the largest is FITC-dextran of 500 kDa (FD500). To capture the diffusion from the smallest to largest components we used a bleach area of 50 µm with a sampling time that starts at 0.5 s per frame and increases to 16 s per frame towards the end of the time lapse recording. As explained in detail in later, this ensures that the sampling was optimal over the entire experiment to capture the fastest and slowest component in one and the same measurement.

For FRAP experiments, 4 *uL* of the samples was 'sandwiched' between a microscope slide and a coverslip sealed by an adhesive spacer of 120 µm thickness (Secure-seal, Spacer, Molecular probes, Leiden, The Netherlands). This provides a 3D environment for diffusion while avoiding flow in the sample. All FRAP measurements were performed at room temperature (22.5 °C).

3.2 Simulation of FRAP images.

FRAP images were simulated using Eq. (2) in Matlab. Simulations were performed with the reported values of the diffusion coefficient(s) D_i, their relatively frequency a_i, photobleaching amount $K_{0,i}$ and resolution parameter r_i.

3.3 Viscosity measurement.

The measured distribution of diffusion coefficients can be converted to a corresponding distribution of hydrodynamic sizes (diameter), using the Stokes-Einstein equation $D = kT/3\pi\eta d$, where k is the Boltzmann constant, T the absolute temperature, η the dynamic viscosity of the solution and D the diffusion coefficient of the molecule. However, this requires accurate knowledge of the viscosity of the sample. While e.g. a capillary viscosimeter can be used for this in case of solutions prepared in the lab, it cannot be applied to the often minute samples retrieved from animal experiments. Therefore, we have made use of a viscosity probe with known size that can be added to the samples to inherently calibrate the viscosity of the sample under study. 10 kDa FITC-dextran (FD10) at a weight concentration of 20 mg/ml was added to the sample solution at a volume ratio of 1:20 so that the effect on the sample viscosity by adding the viscosity probe was considered neglectable.

3.4 cFRAP data analysis.

Before fitting of the data to the cFRAP model, the recovery data (**Fig. 1**) was normalized to the fluorescence before bleaching. Normalization to the pre-bleach intensity can be performed by dividing every pixel in the recovery images by the corresponding pixel in the pre-bleach image. To limit the corresponding amplification of noise, the pre-bleach image was smoothed first with a median filter with a kernel of 5×5 pixels. Correction for laser fluctuations and bleaching during imaging is performed by dividing the pixels of each recovery image by the average value from one reference background region in the same image (**Fig.1a**). The reference background region was placed sufficiently far from the bleach region so as to remain unaffected by the diffusion front during the observation time.

Data analysis is done by fitting of the cFRAP model (Eq. (8)) to the pixel values of the normalized recovery images. Alternatively, as detailed in later, the region of interested (ROI) can be divided into n equally spaced ring-shaped areas. In that case Eq. (9) is fitted to the average intensity values in each of the ring-shaped areas. The Maximum Entropy Method (MEM) was included into the analysis so as to obtain the smoothest distribution fulfilling the requirement of $\chi^2 = M$, where M is the total number of data points used for fitting. This is a well-known method to ensure that the final distribution does not contain more features than statistically warranted by the data[14]. In practice, using the function 'fmincon' in the Matlab Optimization tool box (The matworks, Natick, MA, USA) the entropy criterion according to Eq. (10) was maximized, while the constraint $\chi^2 = M$ in Eq. (12) was relaxed to the narrow interval $M - \sqrt{2M} \le \chi^2 \le M + \sqrt{2M}$.

3.5 Dynamic light scattering (DLS) size measurements.

DLS size measurements were performed on a Malvern Zetasizer Nano ZS (Malvern Instruments LTD., Malvern, UK) equipped with a 632 nm, 4 mW He-Ne laser source.

Instrument performance was verified by a system suitability test according to the manufacturer's IQ/OQ documentation and consisting of a measurement of 60 nm and 200 nm polystyrene beads from Thermo Scientific (Erembodegem, Belgium). For each measurement, 40 µL samples were transferred into a ZEN0040 Micro cuvette (Malvern Instruments LTD). Sample measurements were performed at 25°C with automatic attenuation. Samples were equilibrated for 180 seconds at 25°C. Measurement position was fixed at 4.65 by 'The seek for optimum position' option. The sample was measured 10 times using automatic measurement duration with a delay of 60 seconds between each measurement. Measurements were performed under a 173° backscattering angle. For data processing, the general purpose algorithm was used. The polydispersity index (PDI) was defined as $PDI=(\sigma/d)^2$, where σ is the standard deviation of the size distribution and d the mean diameter.

3.6 Fluorescent/dextran probes.

FITC-dextran (FD) or dextran (D) of various MW (FD4/D4: MW $=4\times10^3$ g/mol, FD10/D10: MW $=1\times10^4$ g/mol, FD40/D40: MW $=4\times10^4$ g/mol, FD150/D150: MW $=1.5\times10^5$ g/mol, FD500/D500: MW$=5\times10^5$ g/mol) were purchased from Sigma-Adrich (Bornem, Belgium). For the validation experiments of cFRAP, FITC-dextran solutions were prepared in HEPES buffer at pH7.0 and dextran solutions were prepared in distilled water. The concentration was always 0.5 mg/ml for DLS (Dynamic Light Scattering) measurements. For each type of FD, a concentration series was prepared in order to determine the linear fluorescence range as observed on the confocal microscope.

4. RESULTS AND DISCUSSION

4.1 Pixel-based fitting vs. ring-averaged method

The rFRAP model presented here provides a complete description of the recovery phase in time and space after photobleaching. Therefore, fitting of the model can be done to all pixel values in a confocal time-lapse recording of the fluorescence recovery. Direct fitting to all pixel values in the ROI (120 by 120 pixels), however, results in very long calculation times. In order to speed up the fitting procedure, we evaluated a slightly modified approach where the spatial information (pixel values within a particular confocal image) is averaged over rectangular ring areas as illustrated in **Fig. 1**. The ROI is divided into n rings according to $\Delta L=L/2n$, where ΔL is the spacing between each ring and L is the length of the ROI. We hypothesize that the same accuracy can be obtained as compared to fitting to all individual pixels on condition that the spatial increment of rectangular ring areas is sufficiently small. To evaluate this, we simulated recovery images of a single component system with a diffusion coefficient of 10 μm^2/s. As the results show in **Fig. 2**, the ring-averaged method has the same precision as pixel based fitting when the number of rings is larger than 10. Increasing the number of rings more did not result in more precision. Most importantly, the calculation time is reduced by 3 orders of magnitude when using the ring method (n=10) versus pixel-based fitting. An interesting special case is when a single ring is used, which corresponds to the most common way to analyse FRAP data where only the time-course of the average intensity in the bleach region is considered. As shown in Suppl. Fig. 2 (NC=1, where NC is the number of divided rectangle ring), while the apparent D-distribution is still centred at the expected D-value of 10 μm^2/s, it is much broader as compared to our new method where also the spatial information is included. This nicely demonstrates that cFRAP offers much better precision and resolution to analyse polydisperse samples as before.

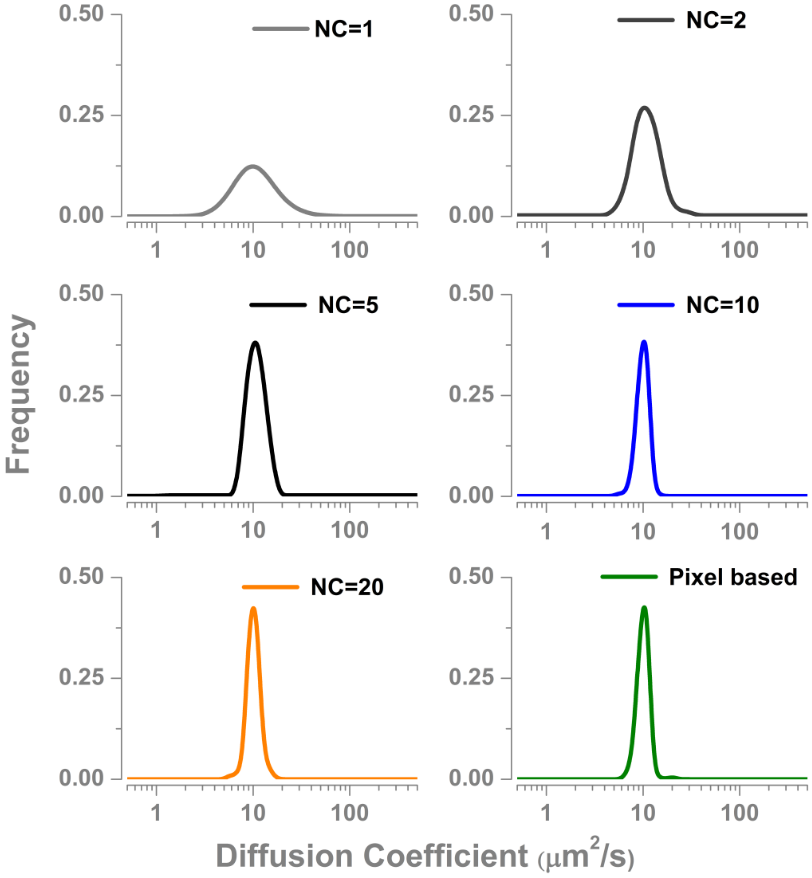

Figure 2. Recovery images were simulated according to Eq (2) for a single component system of D = 10 μm2/s. D-distributions are shown for the ring-based method for different numbers of equally spaced rings (NC=1, 2, 5, 10 and 20) and the pixel-based method.

4.2 Discretization of D-space

The cFRAP approach requires discretization of the D-space. Obviously, a finer discretization is expected to give a better description of the distribution, but comes at the expense of longer calculation times. Therefore, we evaluated the influence of the number of D-components (*ND*) on the fitting results. Recovery images were simulated for a single component system with D = 10 μm^2/s. The D-space was logarithmically discretized in *ND* components over 3 orders of magnitude. The results in **Fig. 3** show that increasing *ND* from 20 to 30 did not appreciably change the resulting distribution, while the calculation time increases more than two fold. Based on these results, we decided to use *ND* of 20 for further experiments.

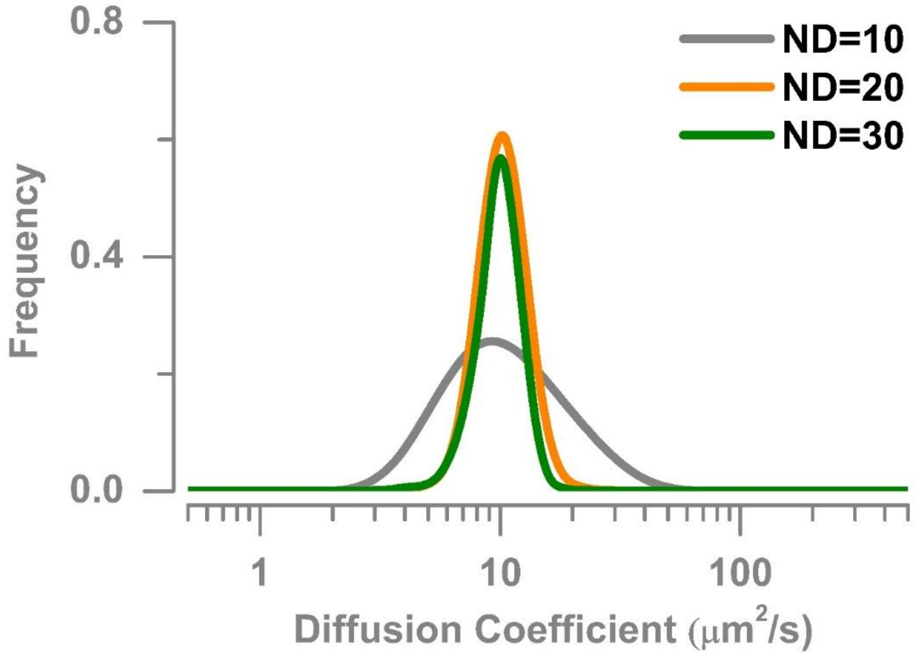

Figure 3. The influence of discretization of D-space is evaluated for a single component D=10 μm2/s. ND is the number of D values that are chosen over three orders of magnitude with logarithmic spacing. ND was varied from 10 to 30.

4.3 Optimization of the total measurement time and the time interval between recovery images

After photobleaching, time-lapse images are recorded of the recovery phase. The question then arises what is the most optimal time between subsequent images (Δt)? On the one hand it should be sufficiently short so as to capture all diffusion dynamics, while on the other hand one wants to limit total measurement recording time (T) by limiting total number of images to minimize (unwanted) photobleaching during imaging. To investigate what are suitable values for Δt and T, recovery images were simulated of a single component system with a diffusion coefficient of 10 μm^2/s. To allow to draw general conclusions, Δt and T will be expressed relative to the characteristic recovery time, defined as $\tau = (l/2)^2/4D$, where l is the length of the shortest side of the bleach rectangle and D is the diffusion coefficient. As shown in **Fig. 4a**, according to the single component system there is no improvement as soon as $T \geq \tau$. Looking at the result in **Fig. 4b**, we conclude that Δt should be smaller or equal to 0.5τ. To study the influence of these experimental parameters in more detail for a complex polydisperse systems, we also simulated recovery images of a two-component system consisting 50% of D_1=1.0 μm^2/s and 50% of D_2=10 μm^2/s. Here, we defined τ_{slow} and τ_{fast} as characteristic recovery time of the slow and fast component, respectively The results are shown in **Fig. 4c, d** for different *Δt* and *T.* Not unexpectedly the slow component cannot be accurately determined anymore when *T* becomes too short. Just as for the single component system we conclude that $T \geq \tau_{slow}$. Also regarding *Δt* we come to the same conclusion as from the single component system that $\Delta t \leq 0.5\tau_{fast}$.

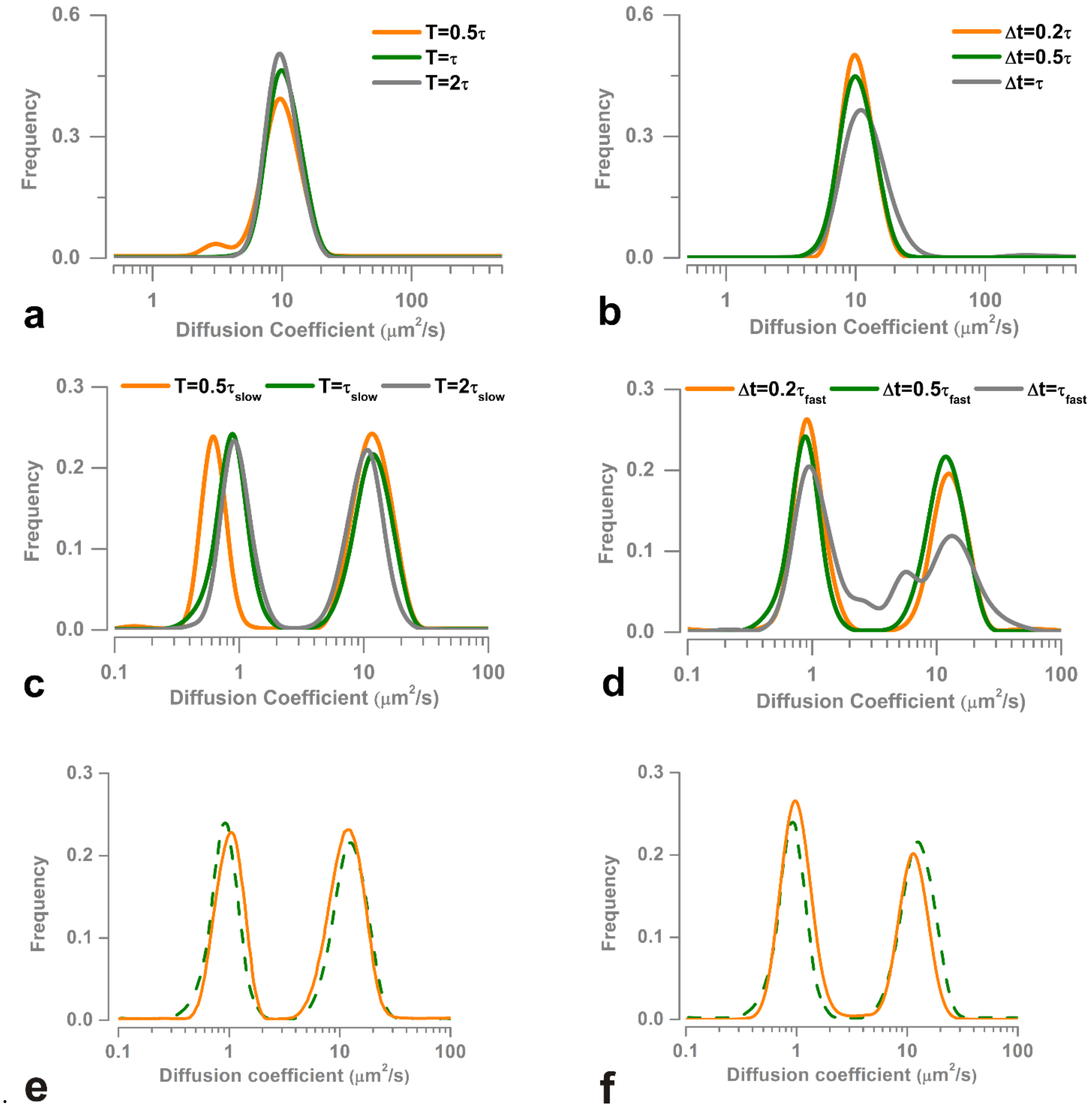

Figure S4. The influence of total measurement time (T) and time interval (Δt) is evaluated for (a, b) a single component (D=10 μm2 s-1) and (c, d) a two-component system (D1=1.0 μm2 s-1and D2=10 μm2 s-1). (e) To limit the number of recovery images, the time interval Δt can be increased with ~20% per recovery image or (f) with 100% per every 5 frames. For ease of comparison, the dashed lines in e and f show the distributions calculated for T =τ_{slow}, Δt =0.5 τ_{fast} from c and d.

Taken together, from these simulations we conclude that Δt should be at least 50% of the characteristic diffusion time of the fastest component, while the total measurement time should be at least equal to the characteristic diffusion time of the slowest component. For a fixed Δt this actually leads to over-sampling of the slower components so that more images are recorded than actually needed for the analysis, potentially leading to substantial photobleaching during imaging of the recovery phase. Therefore, we recommend the use of a linearly increasing of Δt with ~20% per image or, as in our case, a doubling of the time step per every 5 frames as shown in **Fig. 4e, f**, until the selected total imaging time T is reached.

4.4 Discriminating and quantifying subpopulations with different diffusion coefficients

Having optimized experimental and analysis parameters, it is of interest to determine the resolution of cFRAP with which it can distinguish between subpopulations with different diffusion coefficients. Recovery images were simulated for a two-component system with different ratios of the diffusion coefficients ($R_D = D_2/D_1$). Both components are present in the same concentration (50/50%). The results are shown in **Fig. 5a** for R_D=5, 3 and 2. For R_D=5 both components are found in the expected 50/50% ratio. Indeed, the area under the curve is 49.9% for the slow component and 50.1% for the fast component. Also at a ratio of R_D=3 both components are still well resolved, but at a ratio of 2 both populations could no longer be discriminated. Still this is an excellent result as compared to the standard approach of only taking the time-progression of the average intensity into account. This corresponds to n = 1 ring with our method, and in that case a ratio R_D at 8 is needed to discriminate both components as shown in **Fig. 5b**.

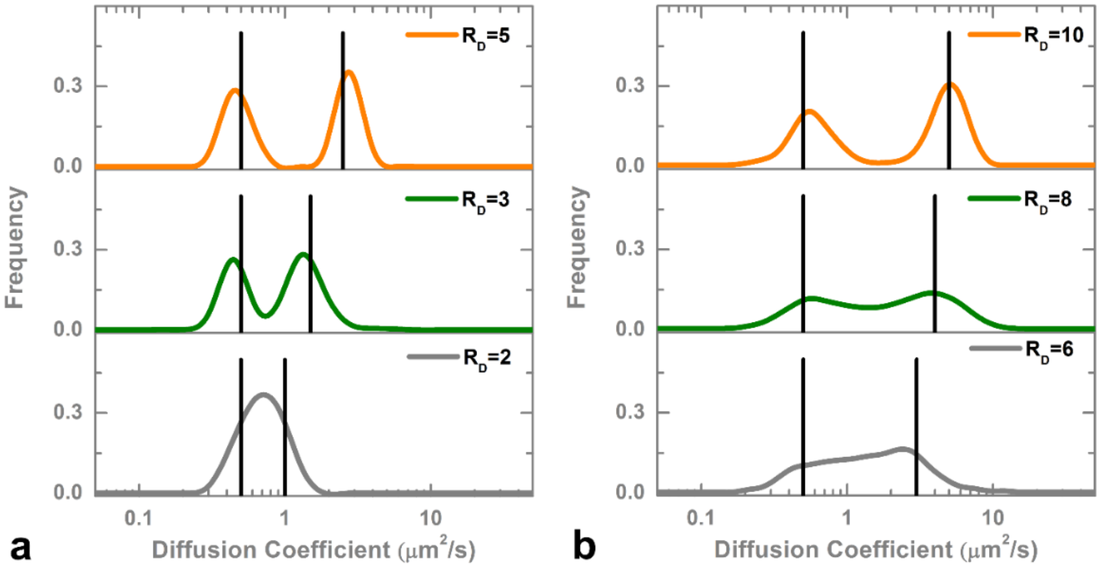

Figure 5. The ability of cFRAP to discriminate two components was investigated using simulated recovery images. Different ratios of diffusion coefficients were evaluated using (a) the full tempo-spatial information

vs. (b) using only time information as in standard FRAP analysis. R_D indicates the ratio of the two diffusion coefficients, where D_1=0.5 µm^2/s. The black lines indicate the diffusion coefficients used in the simulations.

4.5 Analysis of continuous *D* distributions

For parameter optimization and basic evaluation of the method until now we used single or double component systems. However, the cFRAP method was developed with the aim to analyze continuous distributions of diffusion coefficients. Therefore, we went on to simulate recovery images for a polydisperse sample with a continuous distribution of diffusion coefficients according to a lognormal distribution with location parameter μ = 1.4 $\mu m^2/s$ and varying scale parameter σ from 0.1 to 2 to simulate an increasingly polydisperse system (black bars in **Fig. 6a-c**). The orange curves are the result from cFRAP analysis and nicely corresponds to the expected distributions. Going one step further we also simulated a double lognormal distribution with μ_1=0.9 $\mu m^2/s$, σ_1 =1.5 and μ_2=8.7 $\mu m^2/s$ σ_2=1.5. As shown in **Fig. 6d**, again cFRAP is very well capable of retrieving the expected distribution. This demonstrates that cFRAP is very well suited for the intended task of analyzing complex polydisperse systems.

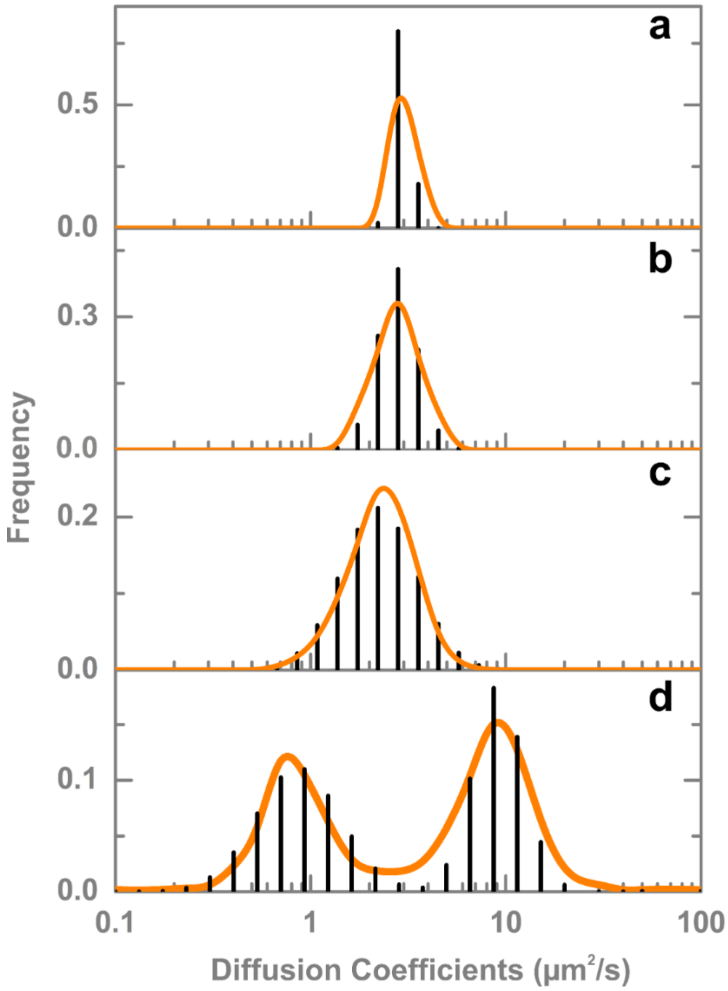

Figure 6. The ability of cFRAP analysis to recover continuous *D* distribution was tested for two simulated polydisperse systems. As indicated by the black bars, (a-c) the first system follows a lognormal distribution with location parameter μ = 1.4 $\mu m^2/s$ and scale parameter σ varying from 0.1 (a), 0.5 (b) to 2.0 (c)and (d) the second follows a double lognormal distribution with μ_1=0.9 $\mu m^2/s$, σ_1 =1.5 and μ_2=8.7 $\mu m^2/s$ σ_2=1.5.The orange curves are the result from cFRAP analysis and almost perfectly match with the true distributions.

4.6 Validation of cFRAP-sizing

The performance of cFRAP-sizing was compared experimentally to DLS (Dynamic Light Scattering) as a standard technique for measuring the size distribution of nanomaterial dispersions. Solutions of dextrans of various molecular weights were prepared and their size distribution was measured by DLS. FITC-labeled dextrans of similar molecular weights were used for sizing by cFRAP. In all cases the cFRAP size distributions corresponded very well with the ones obtained by DLS (**Fig. 7**). As could be expected, thanks to including spatial information in the cFRAP model, the PDI (polydispersity index) of the distributions was significantly less compared to the apparent PDI measured by DLS which only takes time information into account and, therefore, has more limited precision (**Fig. 8**).

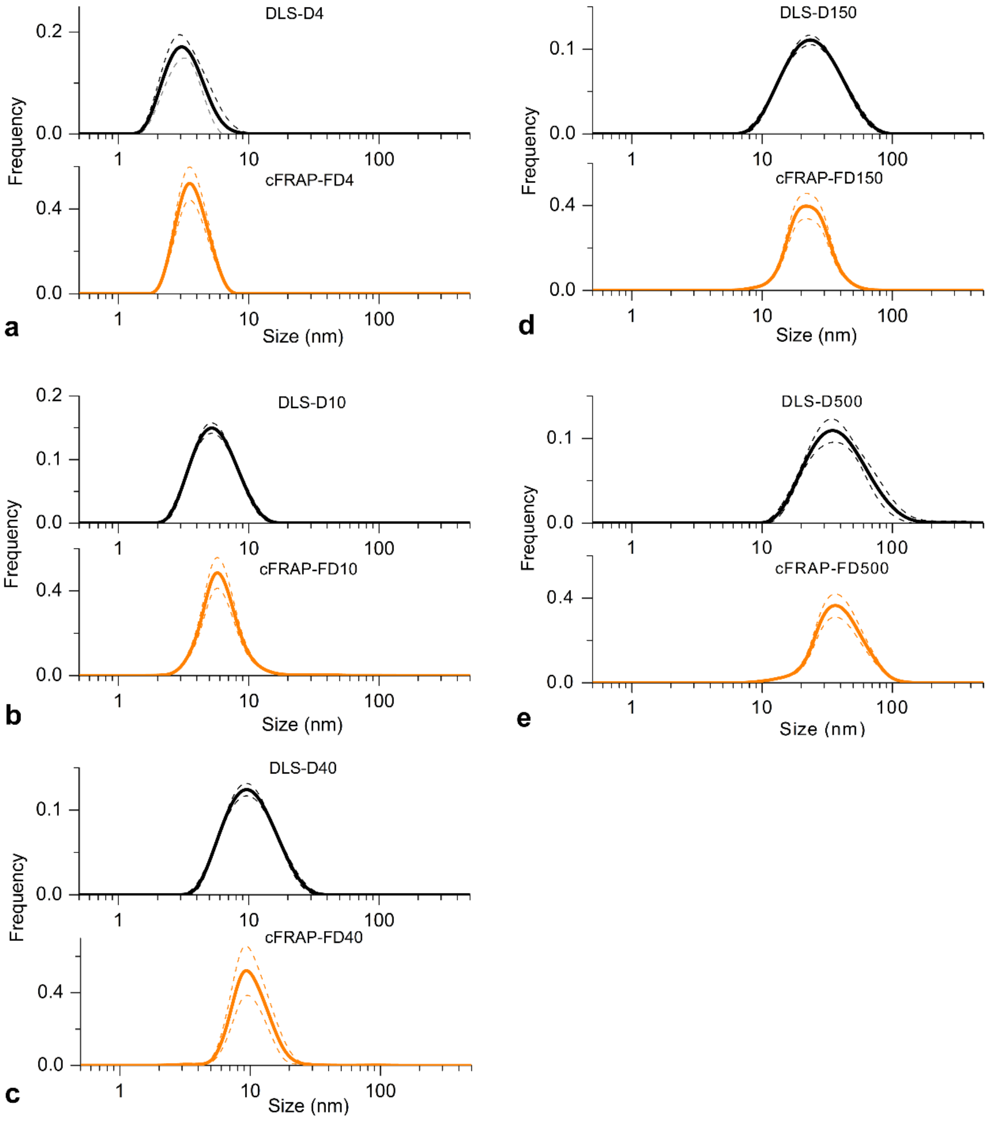

Figure 7. Experimental validation of cFRAP versus DLS as a standard sizing technique of nanomaterial dispersions. Measurements are performed on five types of dextrans each with a different nominal MW: (a) 4 kD, (b)10 kD, (c) 40 kD, (d) 150 kD and (e) 500 kD. For cFRAP the dextrans were labeled with FITC (FD), while they were unlabelled (D) for DLS. The orange lines correspond to the cFRAP measurements, and the black lines correspond to DLS results. The dashed lines indicate the standard deviation (n = 10).

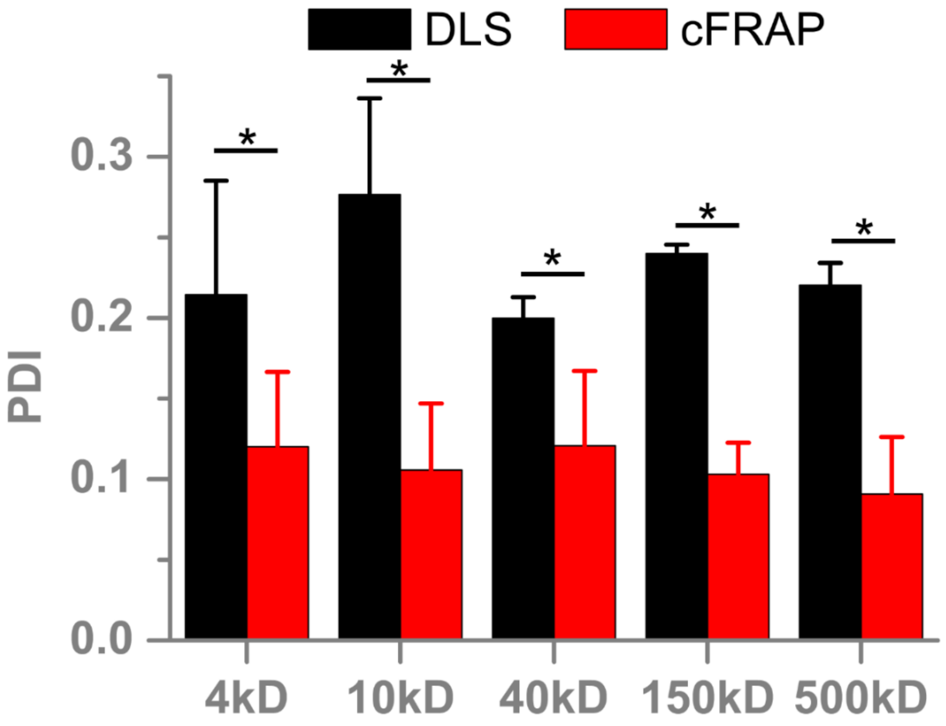

Figure 8. Comparison of the apparent size polydispersity measured by cFRAP compared to DLS. As DLS essentially only uses time information of the diffusion process, its precision is significantly less as compared to cFRAP which also takes spatial information into account. (n=10, one-way ANOVA analysis, *P<0.05).

Next, we wanted to prove experimentally that cFRAP is very well capable of analyzing broad size distributions of nanomaterials. Therefore, as a final validation step, we prepared mixtures of FD (FITC-dextran) with a gradually increasing range of MW to see if cFRAP can measure the full size distribution correctly. As the results in **Fig. 9** show, cFRAP can accurately retrieve the expected size distributions from ~2 to ~80 nm, in line with the aim to develop a method for nanomaterial sizing in this range.

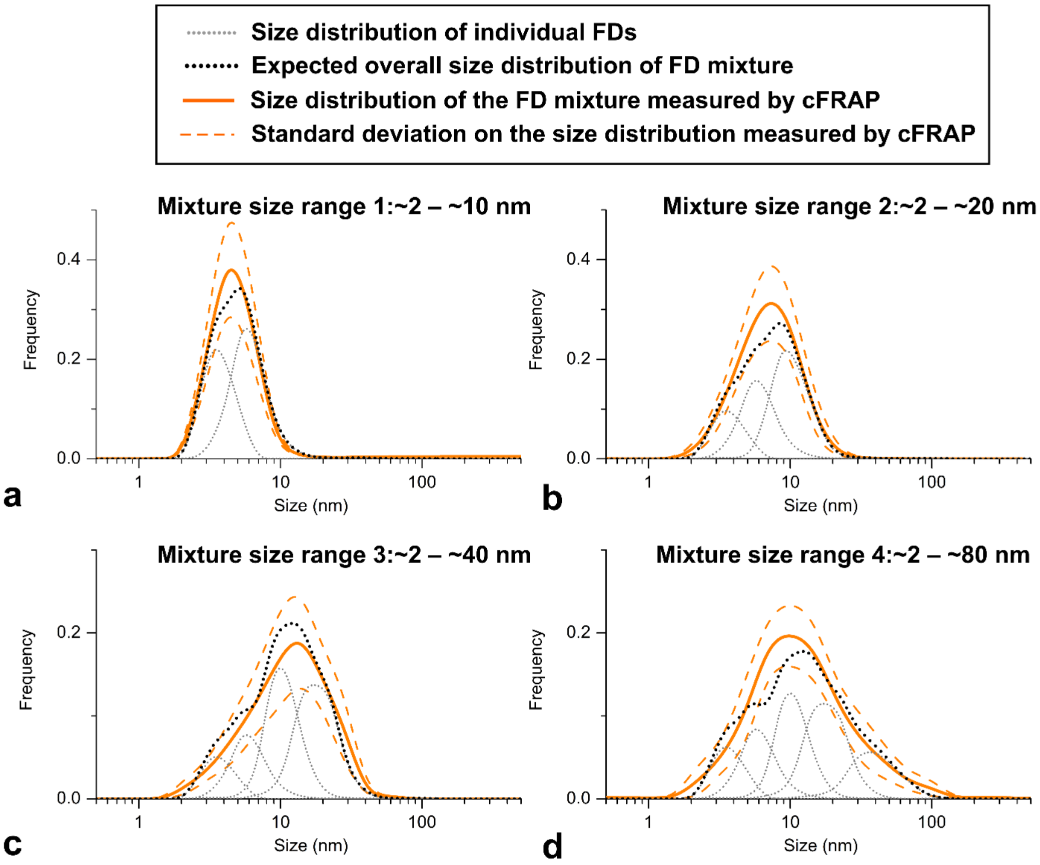

Figure 9. Experimental validation of cFRAP-sizing. Mixtures were prepared with a gradually increasing number of FITC-dextrans with different MW: (a) mixture of 1 mg/ml FD4 (4 kD FITC-dextran) and 0.5 mg/ml FD10 (10 kD FITC-dextran), (b) mixture of 1 mg/ml FD4, 0.7 mg/ml FD10 and 0.5 mg/ml 40 kD (40 kD FITC-dextran), (c) mixture of 1 mg/ml FD4, 0.7 mg/ml FD10, 0.3 mg/ml FD40 and 0.3 mg/ml FD150 (150 kD FITC-dextran), (d) mixture of 1 mg/ml FD4, 0.6 mg/ml FD10, 0.4 mg/ml FD40, 0.25 mg/ml FD150 and 0.25 mg/ml FD500 (500 kD FITC-dextran). The grey dotted lines indicate the size distribution of the individual FITC-dextrans measured by cFRAP. The black dotted lines are the sum of the grey dotted lines and represent the expected size distribution of the FD mixtures. The solid orange lines are the size distributions of the mixtures as experimentally measured by cFRAP, while the orange dashed lines indicate the SD (standard deviation). (n=10)

5. CONCLUSIONS

A new FRAP method of cFRAP has been developed here based on rFRAP model can precisely and straightforwardly measure the distribution of diffusion coefficients/size of a polydisperse systems. A rectangle is photobleached and the full tempo-spatial information available in the confocal recovery images is exploited using a dedicated theoretical recovery model to extract a continuous distribution of diffusion coefficients. cFRAP can distinguish two subpopulations of their diffusion coefficient differences by as small as a factor 3 in comparison with the differences by at least a factor of 8 for the classic FRAP (only the average fluorescence in the bleach area is considered as a function of time). It is confirmed through simulations that cFRAP can correctly analyze polydisperse systems with a continuous broad range of diffusion coefficients. Furthermore, it is investigated that cFRAP analysis can be performed down to SNR = 2.4. The performance of cFRAP was compared experimentally to DLS as a standard technique for measuring the size distribution of nanomaterial dispersions. Thanks to including spatial, information in the cFRAP model, the PDI of the distributions was significantly less compared to the apparent PDI measured by DLS which only takes time information into account and, therefore, has more limited precision.

6. REFERENCES

1. Braeckmans, K., Peeters, L., Sanders, N.N., De Smedt, S.C. & Demeester, J. Three-dimensional fluorescence recovery after photobleaching with the confocal scanning laser microscope. *Biophysical Journal* **85**, 2240-2252 (2003).
2. Braeckmans, K., Stubbe, B.G., Remaut, K., Demeester, J. & De Smedt, S.C. Anomalous photobleaching in fluorescence recovery after photobleaching measurements due to excitation saturation- a case study for fluorescein. *J Biomed Opt* **11** (2006).
3. Axelrod, D., Koppel, D.E., Schlessinger, J., Elson, E.L. & Webb, W.W. Mobility Measurements by Analysis of Fluorescence Photobleaching Recovery Kinetics. *Biophys J* **16**, A217-A217 (1976).
4. Peters, R., Peters, J., Tews, K.H. & Bahr, W. Microfluorimetric Study of Translational Diffusion in Erythrocyte-Membranes. *Biochim Biophys Acta* **367**, 282-294 (1974).
5. Chen, Y., Lagerholm, B.C., Yang, B. & Jacobson, K. Methods to measure the lateral diffusion of membrane lipids and proteins. *Methods* **39**, 147-153 (2006).
6. Edidin, M. in In The Structure of Biological Membranes. (ed. P.L. Yeagle, ed.) 539–572 (CRC Press, Boca Raton; 1992).
7. Ishihara, A. & Jacobson, K. A Closer Look at How Membrane-Proteins Move. *Biophys J* **65**, 1754-1755 (1993).
8. Koppel, D.E. Normal-Mode Analysis of Lateral Diffusion on a Bounded Membrane-Surface. *Biophys J* **47**, 337-347 (1985).
9. Lippincott-Schwartz, J. et al. Monitoring the dynamics and mobility of membrane proteins tagged with green fluorescent protein. *Method Cell Biol* **58**, 261-281 (1999).
10. Umenishi, F., Verbavatz, J.M. & Verkman, A.S. cAMP regulated membrane diffusion of a green fluorescent protein-aquaporin 2 chimera. *Biophys J* **78**, 1024-1035 (2000).
11. Lukacs, G.L. et al. Size-dependent DNA mobility in cytoplasm and nucleus. *J Biol Chem* **275**, 1625-1629 (2000).
12. Kao, H.P., Abney, J.R. & Verkman, A.S. Determinants of the Translational Mobility of a Small Solute in Cell Cytoplasm. *J Cell Biol* **120**, 175-184 (1993).
13. Seksek, O., Biwersi, J. & Verkman, A.S. Translational diffusion of macromolecule-sized solutes in cytoplasm and nucleus. *J Cell Biol* **138**, 131-142 (1997).
14. Elsner, M. et al. Spatiotemporal dynamics of the COPI vesicle machinery. *Embo Rep* **4**, 1000-1005 (2003).
15. Verkman, A.S. in In Biophotonics, Part A: Methods in Enzymology. (ed. a.I.P. G. Marriott) 635-648 (Academic Press, New York; 2003).
16. Braeckmans, K. et al. Line FRAP with the confocal laser scanning microscope for diffusion measurements in small regions of 3-D samples. *Biophys J* **92**, 2172-2183 (2007).
17. 9Braga, J., Desterro, J.M.P. & Carmo-Fonseca, M. Intracellular macromolecular mobility measured by fluorescence recovery after photobleaching with confocal laser scanning microscopes. *Mol Biol Cell* **15**, 4749-4760 (2004).
18. Karpova, T.S., Chen, T.Y., Sprague, B.L. & McNally, J.G. Dynamic interactions of a transcription factor with DNA are accelerated by a chromatin remodeller. *Embo Rep* **5**, 1064-1070 (2004).
19. Wedekind, P., Kubitscheck, U., Heinrich, O. & Peters, R. Line-scanning microphotolysis for diffraction-limited measurements of lateral diffusion. *Biophys J* **71**, 1621-1632 (1996).
20. Sanders, N.N., De Smedt, S.C. & Demeester, J. The physical properties of biogels and their permeability for macromolecular drugs and colloidal drug carriers. *J Pharm Sci* **89**, 835-849 (2000).
21. Olmsted, S.S. et al. Diffusion of macromolecules and virus-like particles in human cervical mucus. *Biophys J* **81**, 1930-1937 (2001).
22. Pluen, A. et al. Role of tumor-host interactions in interstitial diffusion of macromolecules: Cranial vs. subcutaneous tumors. *P Natl Acad Sci USA* **98**, 4628-4633 (2001).
23. Ramanujan, S. et al. Diffusion and convection in collagen gels: Implications for transport in the tumor interstitium. *Biophys J* **83**, 1650-1660 (2002).

24. Peeters, L. et al. Vitreous: A barrier to nonviral ocular gene therapy. *Invest Ophth Vis Sci* **46**, 3553-3561 (2005).
25. Hendrik Deschout, K.R., Jo Demeester, Stefaan C. De Smedt, Kevin Braeckmans FRAP in Pharmaceutical Research: Practical Guidelines and Applications in Drug Delivery. *Pharm Res-Dordr* (2013).
26. Alvarez-Mancenido, F. et al. Characterization of diffusion of macromolecules in konjac glucomannan solutions and gels by fluorescence recovery after photobleaching technique. *Int J Pharm* **316**, 37-46 (2006).
27. Van Tomme, S.R. et al. Mobility of model proteins in hydrogels composed of oppositely charged dextran microspheres studied by protein release and fluorescence recovery after photobleaching. *J Control Release* **110**, 67-78 (2005).
28. Burke, M.D., Park, J.O., Srinivasarao, M. & Khan, S.A. Diffusion of macromolecules in polymer solutions and gels: A laser scanning confocal microscopy study. *Macromolecules* **33**, 7500-7507 (2000).
29. Meyvis, T.K.L., De Smedt, S.C., Van Oostveldt, P. & Demeester, J. Fluorescence recovery after photobleaching: A versatile tool for mobility and interaction measurements in pharmaceutical research. *Pharm Res-Dordr* **16**, 1153-1162 (1999).
30. DeSmedt, S.C. et al. Diffusion of macromolecules in dextran methacrylate solutions and gels as studied by confocal scanning laser microscopy. *Macromolecules* **30**, 4863-4870 (1997).
31. Desmedt, S.C. et al. Structural Information on Hyaluronic-Acid Solutions as Studied by Probe Diffusion Experiments. *Macromolecules* **27**, 141-146 (1994).
32. Deschout, H. et al. Straightforward FRAP for quantitative diffusion measurements with a laser scanning microscope. *Opt Express* **18**, 22886-22905 (2010).
33. Periasamy, N. & Verkman, A.S. Analysis of fluorophore diffusion by continuous distributions of diffusion coefficients: application to photobleaching measurements of multicomponent and anomalous diffusion. *Biophys J* **75**, 557-567 (1998).
34. Hauser, G.I., Seiffert, S. & Oppermann, W. Systematic evaluation of FRAP experiments performed in a confocal laser scanning microscope - Part II: Multiple diffusion processes. *Journal of Microscopy* **230**, 353-362 (2008).
35. Tycon, M.A., Daddysman, M.K. & Fecko, C.J. RNA Polymerase II Subunits Exhibit a Broad Distribution of Macromolecular Assembly States in the Interchromatin Space of Cell Nuclei. *Journal of Physical Chemistry B* **118**, 423-433 (2014).
36. Livesey, A.K. & Brochon, J.C. Analyzing the Distribution of Decay Constants in Pulse-Fluorometry Using the Maximum-Entropy Method. *Biophys J* **52**, 693-706 (1987).
37. Skilling, J. & Bryan, R.K. Maximum-Entropy Image-Reconstruction - General Algorithm. *Monthly Notices of the Royal Astronomical Society* **211**, 111-& (1984).
38. Skilling, J. Data-Analysis - the Maximum-Entropy Method. *Nature* **309**, 748-749 (1984).
39. Smisdom, N. in School of Life Sciences, Vol. PhD 160 (Hasselt University, Belgium; 2011).
40. Dalal, R.B., Digman, M.A., Horwitz, A.F., Vetri, V. & Gratton, E. Determination of particle number and brightness using a laser scanning confocal microscope operating in the analog mode. *Microscopy Research and Technique* **71**, 69-81 (2008).

Chapter 7

cFRAP applied to the characterization of protein aggregation in bio-fluids and diagnosis of epithelial and vascular permeability

Part of this chapter is published as:

Sizing nanomaterials in bio-fluids by cFRAP enables protein aggregation measurements and diagnosis of bio-barrier permeability

Ranhua Xiong[1,2], Roosmarijn E. Vandenbroucke[3,4], Katleen Broos[5], Toon Brans[1,2], Elien Van Wonterghem[3,4], Claude Libert[3,4], Jo Demeester[1], Stefaan C. De Smedt[1], Kevin Braeckmans[1,2], Nature Communications, 2016, doi:10.1038/ncomms12982

[1]Laboratory of General Biochemistry and Physical Pharmacy, Ghent University, Ghent, Belgium
[2]Centre for Nano- and Biophotonics, Ghent University, Ghent, Belgium
[3]Inflammation Research Center, VIB, Ghent, Belgium
[4]Department Biomedical Molecular Biology, Ghent University, Ghent, Belgium
[5]Anabiotec nv, Evergem, Belgium

ABSTRACT

Sizing nanomaterials in complex biological fluids, such as blood, remains a great challenge in spite of its importance for a wide range of biomedical applications. In drug delivery, for instance, it is essential that aggregation of protein-based drugs is avoided as it may alter their efficacy or elicit immune responses. Similarly it is of interest to determine which size of molecules can pass through biological barriers in vivo in order to diagnose pathologies, such as sepsis. In this chapter, we report on continuous Fluorescence Recovery After Photobleaching (cFRAP) as a new analytical method enabling size distribution measurements of nanomaterials (1-100 nm) in undiluted biological fluids. We demonstrate that cFRAP allows to measure protein aggregation in human serum and to determine the permeability of intestinal and vascular barriers in vivo. cFRAP is a new analytical technique that paves the way towards exciting new applications that benefit from nanomaterial sizing in bio-fluids.

1. INTRODUCTION

Measuring the size of nanosized materials in complex biological fluids, such as blood or cerebrospinal fluid, is of great importance in a wide range of applications in the life sciences. In drug delivery, for instance, the effective size of nanomaterials in biofluids is important because it directly influences the biodistribution in the body[1-4]. Indeed, even though nanomedicine formulations may be stable under normal storage conditions, they may very well aggregate after administration into a biological fluid such as blood[5, 6]. Similarly, there is a growing appreciation that the colloidal stability of therapeutic proteins needs to be tested in blood as protein aggregation after intravenous administration will alter their functionality and may induce immunogenic responses[7, 8]. Yet, methods to investigate submicron protein aggregates in serum are virtually non-existent[9, 10]. Being able to size nanomaterials in biofluids is of interest to medical diagnosis as well, for instance to determine intestinal or vascular barrier permeability which is related to several pathologies, such as sepsis, liver disease, inflammatory bowel disease and neurodegenerative diseases[11-13]. Barrier permeability can be assessed by administering inert size probes, e.g. orally or intravenously, followed by quantification of the size and amount of probes that have leaked through the barrier.

Despite its relevance, measuring the size of molecules and nanomaterials in complex biological fluids remains a major challenge. A few years ago our group demonstrated that nanoparticles can be sized in undiluted biological fluids by fluorescence Single Particle Tracking (fSPT) microscopy[14-17]. However, as it is based on imaging the Brownian motion of individual, fluorescently labeled nanomaterials, it is mostly suited for nanoparticles with a size above ~0.1 µm. Therefore, a technique for measuring size distributions of nanomaterials in biofluids in the 1–100 nm range is still very much needed.

Here we report on the use of fluorescence recovery after photobleaching (FRAP) to measure size distributions of nanomaterials in biological fluids (**Fig.1**). In a FRAP experiment, the sample is placed on a confocal laser scanning microscope and the fluorescently labeled molecules or nanoparticles are photobleached in a micron sized area by a powerful excitation pulse. The fluorescence inside the bleach area will subsequently recover at a rate that is proportional to the diffusional rate of the fluorescent species. Until now, FRAP data have mostly been analyzed and interpreted in terms of a single average diffusion coefficient. Verkman and Periasamy were the first to develop a FRAP model for the measurement of continuous distributions of diffusion coefficients[18]. The method was based on measuring the fluorescence intensity as a function of time in a spot bleached by a stationary focused laser beam, as was common at that time. Consequently, since only time information was taken into account, the resolution to discriminate species with a different diffusion coefficient was rather limited (factor of 8). A similar approach was recently reported based on multi-photon spot beaching experiments for determining the size of macromolecular complexes in cells[19]. In the meantime, Hauser and colleagues showed that the resolution to discriminate two diffusing components could be substantially enhanced (factor of 3) by including spatial information into FRAP analysis[20]. Building forth on these concepts, here we propose an improved FRAP methodology that enables the measurement of continuous distributions of diffusion coefficients (cFRAP), which can be easily converted to equivalent size distributions. A rectangle is photobleached and the full tempo-spatial information available in the confocal recovery images is exploited using a dedicated theoretical recovery model to extract a continuous distribution of diffusion coefficients. The method is very flexible in that the rectangle can have any size, which conveniently allows to optimize the recovery time for a given diffusion coefficient so as to optimally match the sampling rate of the microscope used.

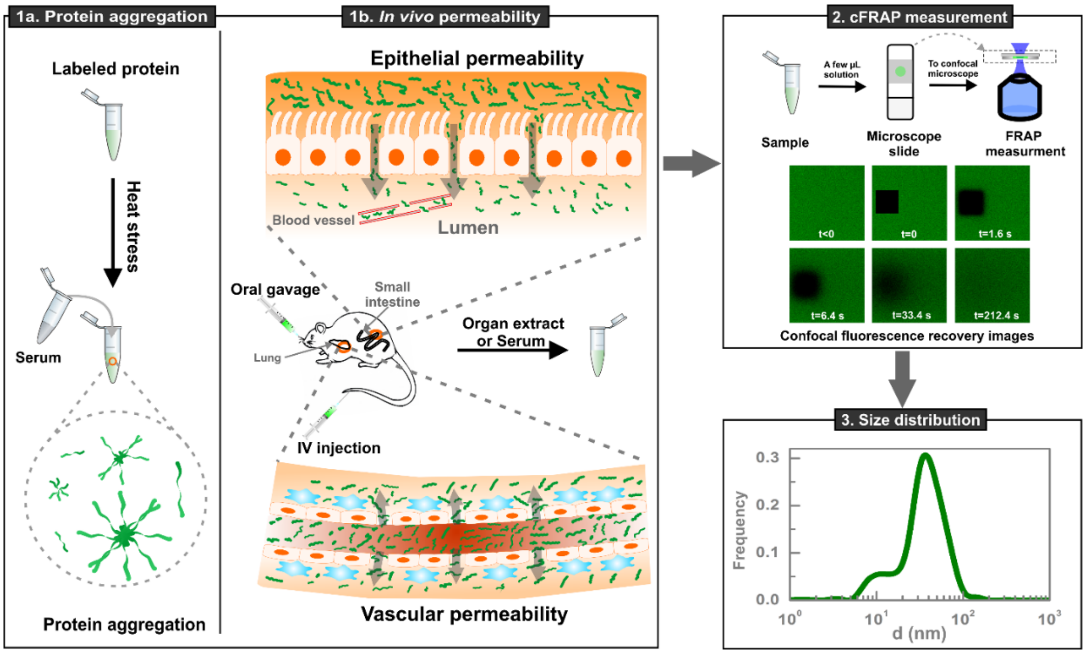

Figure 1 Schematic overview of cFRAP-sizing experiments. (1a) Measuring protein aggregates in serum and (1b) measuring the permeability of the small intestines and vasculature of mice following oral gavage or intravenous (IV) injection of fluorescent probes. (2) Only a few microliters of sample are required for cFRAP experiments on a standard confocal microscope (3) for retrieving the size distribution.

First we demonstrate that cFRAP-sizing enables accurate determination of protein aggregation in undiluted blood serum (**Fig.1a**). Next, in combination with the administration of a broad range of inert size probes, we show that cFRAP-sizing allows to characterize in great detail the intestinal and vascular permeability in mice (**Fig.1b**). Importantly, since a single measurement is sufficient to determine the full size distribution of probes that have leaked through the barrier, we find that the number of animals needed to assess the barrier permeability is reduced up to five times compared to classic approaches where probes of different size are administered and analyzed separately.

2. MATERIALS AND METHODS

2.1 Covalent protein labeling with an extrinsic fluorophore

A 10 mg/mL solution of bovine serum albumin (BSA) was prepared by dissolving BSA lyophilised powder ≥ 96 % (Sigma-Aldrich) in carbonate buffer pH 8.3. The free amine groups of BSA were covalently labeled by 5-6-carboxyfluoresceine succinimidyl ester (5(6) FAM, SE) (Life Technologies Corporation, Molecular Probes®, Eugene, USA). For this purpose, 100 µL of a 5 mg/mL fluorescein solution in dimethylsulfoxide (Life Technologies Corporation, Ghent, Belgium) was added to a 2 mL 10 mg/mL BSA solution and incubated for 1 hour under constant gentle stirring. The incubation was stopped by adding 200 µL of a 210 mg/mL hydroxylamine (Sigma-Aldrich) (stop solution) in ultrapure water adjusted to pH 8.5 with 4 M sodium hydroxide solution (Sigma-Aldrich). Next, the excess of free fluorescein labels was removed by dialysis overnight against 4 L 0.1 M phosphate pH 7.0 in a Slide-a-lyser 20 kDa MWCO (Thermo Scientific, Rockford, USA). The phosphate buffer was adjusted to pH by varying the amount of 0.1 M monobasic dihydrogen phosphate (WR, Leuven, Belgium) and 0.1 M dibasic monohydrogen phosphate (Merck, Darmstadt, Germany) solution. The buffer was filtered through a 0.2 µm PES filter (Novolab, Geraardsbergen, Belgium) before use.

Soluble protein concentration and labeling efficiency was determined by measuring the absorbance at 280 nm and at 495 nm respectively on a Spectramax M2 (Molecular devices, Sunnyvale, USA) with the SoftMax pro software version 6.1. For all measurements, samples were diluted 10-fold and 200 µL samples and buffer controls were transferred in triplicate to a 96-well plate (96 well pureGrade, non-sterile, transparent, F-bottom, Novolab).

The degree of labeling (DOL) was calculated using the measured absorbance of the dye at its absorbance maximum of 495 nm (blank corrected) and according to the following equation:

$$DOL = \frac{A_{\max dye}\ x\ \mathrm{MW}_{protein}}{[protein]\ x\ \varepsilon_{dye}}$$

with $\mathrm{MW}_{protein}$ for the molecular weight of the protein, ε_{dye} for the molar extinction coefficient of the dye (68000 $cm^{-1}M^{-1}$) at its absorbance maximum (494 nm), and the protein concentration (mg/mL). The Lambert-Beer law is used to calculate the protein concentration. For this application, the measured protein absorbance at 280 nm was corrected for the dye absorbance at 280 nm according to manufactures' instructions using the following equation: $A_{protein} = A_{280nm} - A_{max\ dye}$ (CF) with CF = $\frac{A_{280\ free\ dye}}{A_{\max free\ dye}}$.

2.2 Size exclusion chromatographic measurements.

The protein size distribution in the non-stressed and stressed samples for labeled and non-labeled BSA was further evaluated by size exclusion chromatography. For chromatographic separation, a Yarra SEC-3000 column (300 mm × 4.6 mm × 3.0 µm) attached to a Security cartridge GFC 3000 (4 × 3.0 mm) (Phenomenex, Utrecht, Netherlands) was installed on an Acquity H-Class UPLC BioSystem (Waters, Milford, MA, USA) equipped with a PDA detector with a 5 mm 1500 nL titanium flow cell. Empower 2 was used as operating system. The mobile phase consisted of 0.1 M phosphate pH 7.0 and the used Gel Filtration Standard was from Bio-Rad (Temse, Belgium). Before injection of the sample and standards on the column, the insoluble aggregates were removed by centrifugation in a 5424R centrifuge with FA-45-24-11 rotor (Eppendorf) for 10 minutes at 15000 rpm. The concentration of the soluble protein was determined on a spectramax M2 multi-detection reader using the Lambert-Beer equation with the measured absorbance at 280 nm and the theoretical absorbance at 280 nm for a 1% solution (being 0.66 for BSA). In addition, the absorbance at 320 nm was measured for background correction. During analysis, the autosample tray and column oven sample tray were both thermostated at 22 °C. The flow rate was set on 0.35 mL/min. After equilibration with the mobile phase, samples and standards were injected in triplicate. 20 µg was injected for each sample. Protein elution from the column was detected at 280 nm, while 320 nm was recorded as background control. The molecular weight standard was injected in triplicate. For the proteins within the molecular weight separation range of the column, a linear correlation between logarithm of the molecular weight and the elution time was established and used for size estimation of the aggregated and non-aggregated proteins.

2.3 Temperature stressed protein

Labelled and non-labelled BSA was diluted 10-fold to obtain a 1 mg/mL solution. Next, the sample was distributed over 1.5 mL Eppendorf tubes (Eppendorf, Hamburg, Germany) in 1 mL fractions and subjected to temperature stress upon incubation in a Thermomixer comfort (Eppendorf) for 6 hours at 75 °C. A non-stressed labeled and non-labelled sample was retained at 4 °C. During all manipulations over the different steps, the samples were kept protected from light.

To measure the size distribution of protein in biological fluids, blood was withdrawn on citrate from healthy volunteers under informant consent. Plasma was prepared by centrifugation. For analysis of proteins with the cFRAP method, mixtures of plasma and protein (90/10, v/v plasma/protein) were prepared. The same dilutions of protein in buffer were made to serve as a control.

2.4 Fluorescent/dextran probes.

FITC-dextran (FD) or dextran (D) of various MW (FD4/D4: MW $=4\times10^3$ g/mol, FD10/D10: MW $=1\times10^4$ g/mol, FD40/D40: MW $=4\times10^4$ g/mol, FD150/D150: MW $=1.5\times10^5$ g/mol, FD500/D500: MW$=5\times10^5$ g/mol) were purchased from Sigma-Adrich (Bornem, Belgium). For the validation experiments of cFRAP, FITC-dextran solutions were prepared in HEPES buffer at pH7.0 and dextran solutions were prepared in distilled water. The concentration was always 0.5 mg/ml for DLS (Dynamic Light Scattering) measurements. For each type of FD, a concentration series was prepared in order to determine the linear fluorescence range as observed on the confocal microscope. For the *in vivo* permeability measurements, different FDs were mixed at a weight ratio (FD4:FD10:FD40:FD150:FD500=40:25:15:10:10) and subsequently dissolved in PBS buffer, where the concentration of FD4 was 80 mg/ml. While this is outside the linear fluorescence range, such a high concentration was chosen to compensate for the dilution that occurs when the mixture is injected into mice.

2.5 Animals

C57BL/6J mice were housed in an SPF animal facility with *ad libitum* access to food and water. Both male and female mice (8–12 weeks old) were used. All experiments were approved by the ethics committee of the Faculty of Science of Ghent University. Mice were distributed randomly in different cages and mice from the same cage were randomly allocated to different experimental groups. They were injected intraperitoneally (i.p.) with 8.75 mg/kg body weight LPS from Salmonella enterica serotype abortus equi (Sigma), an LD_{100} dose for wild type C57BL/6J mice. No statistical method was used for sample size estimate.

2.6 *In vivo* experiments on intestinal permeability.

Control mice (injected with D-PBS) were sampled 7 h after injection. Septic shock mice were sampled 7 and 20 h after induction of peripheral inflammation. FITC-labeled dextran solution was administered to mice by gavage five hours before sampling. Blood obtained by heart puncture was collected in EDTA-coated tubes (Sarstedt) and plasma was prepared. Leakage of FITC-labeled dextran into the circulation was determined by measurement of the fluorescence with $\lambda_{ex}/\lambda_{em}$ = 488/520 nm. Values were normalized to the PBS control value. After fluorescence measurement, these samples were also measured by cFRAP in a similar fashion as for the vascular permeability experiments. No blinding was done for all of samples. The fluorescence intensity of these samples as measured by fluorimetry were compared by one-way analysis of variance (ANOVA). No samples or animals were excluded from the analysis

2.7 *In vivo* experiments on vascular permeability.

Control mice (injected with D-PBS) were sampled 7 h after injection. Septic shock mice were sampled 7 and 20 h after induction of peripheral inflammation. One hour before sampling, mice were injected intravenously (IV) with the relevant FITC-labeled dextran solutions. CSF was harvested from the fourth ventricle, centrifuged at 300 g to remove all cell debris, and CSF supernatant was collected and diluted 50-fold in D-PBS (Invitrogen) prior to analysis. Next, mice were transcardially perfused with D-PBS supplemented with heparin to remove all labeled dextran in circulation. Organs were isolated, cut into small pieces and incubated with formamide to extract the remaining FITC-labeled dextran from the tissues. After overnight incubation at 37°C, samples were centrifuged and supernatant was collected. Finally, the fluorescence of CSF and organ supernatant was measured at $\lambda_{ex}/\lambda_{em}$ = 488/520 nm by Fluostar Omega and values were normalized to the PBS control per tissue. Again, the samples of the fluorescence were compared by one-way ANOVA. The samples were subsequently analysed by cFRAP to determine the size distribution of FITC-dextrans in the various bodily fluids and organs.

3. RESULTS

3.2 Characterization of protein aggregation in biological fluids

As a first application, we used cFRAP-sizing to analyze protein aggregates in the sub 0.1 µm range in full serum. This is of current interest since protein aggregation has emerged as a key issue underlying multiple deleterious effects in the use of protein therapeutics, including loss of efficacy, altered pharmacokinetics, reduced stability and shelf life, and induction of unwanted immunogenicity[7, 8]. Fluorescently labeled bovine serum albumin (BSA) was used as a model protein, which could be analyzed by cFRAP down to a concentration of 4 µg/ml (60 nM) (**Fig. 2**). Protein aggregates were prepared by applying heat stress to the BSA monomers in a buffer solution. The unstressed and heat-stressed samples were first characterized in buffer solution by two standard techniques: DLS and SEC (Size Exclusion Chromatography). For the heat stressed sample, SEC showed both a monomer peak and the presence of aggregates (**Fig. 3a**). However, the SEC signal corresponding to aggregates was not very well resolved, so that the extent of aggregation was difficult to assess. On the other hand, DLS does show the size range of aggregates in the heat-stressed sample but failed to detect the monomers (**Fig. 3b**). Interestingly, cFRAP-sizing could discriminate both monomers and aggregates in a single measurement instead (**Fig. 3c**), with the size range of aggregates in excellent agreement with the DLS size distribution. This nicely demonstrates again the superior resolving power of cFRAP. Next, we addressed the main question if cFRAP is able to size protein aggregates directly in serum, which is difficult, if not impossible, to do by DLS or SEC. cFRAP was used to analyze samples prepared of BSA monomers and BSA aggregates in 90% serum. Comparison with the size distributions in buffer solution shows that both monomers and aggregates could be correctly sized in serum by cFRAP (**Fig. 3d**). We conclude that cFRAP-sizing is very well capable of accurately quantifying protein aggregates in a complex biological fluid like serum in the < 0.1 µm range with excellent resolving power.

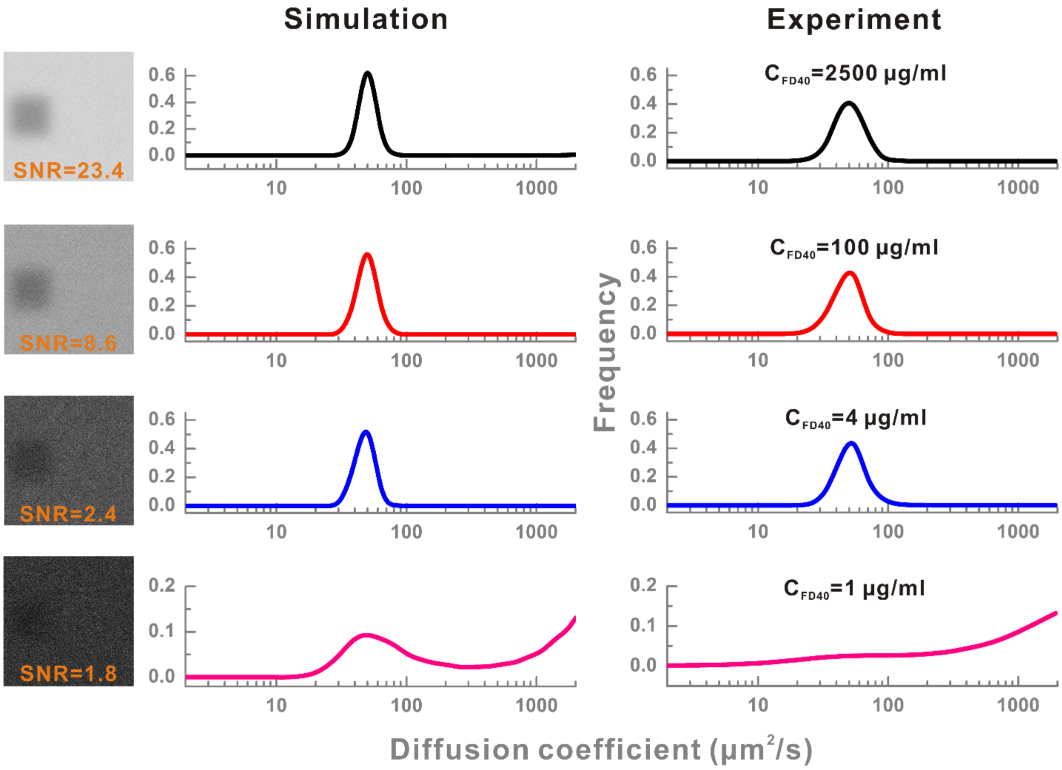

Figure 2. The influence of signal to noise ratio (SNR) on cFRAP analysis and determination of the lower concentration limit. cFRAP was performed on solutions with decreasing FD40 concentration and, therefore, deteriorating SNR. Experimental results are cross-checked with simulated experiments (single component system with D=50 µm^2 s^{-1}) having similar SNR. Even at a SNR as low as 2.4, the distribution of diffusion coefficients could be retrieved by cFRAP. On the confocal microscope used in this study, this corresponded to a lower concentration of 4 µg ml^{-1} FD40 (100 nM). It is to be noted that the exact value of the lower concentration limit depends on the type of confocal microscope used and the brightness of the labeled molecules.

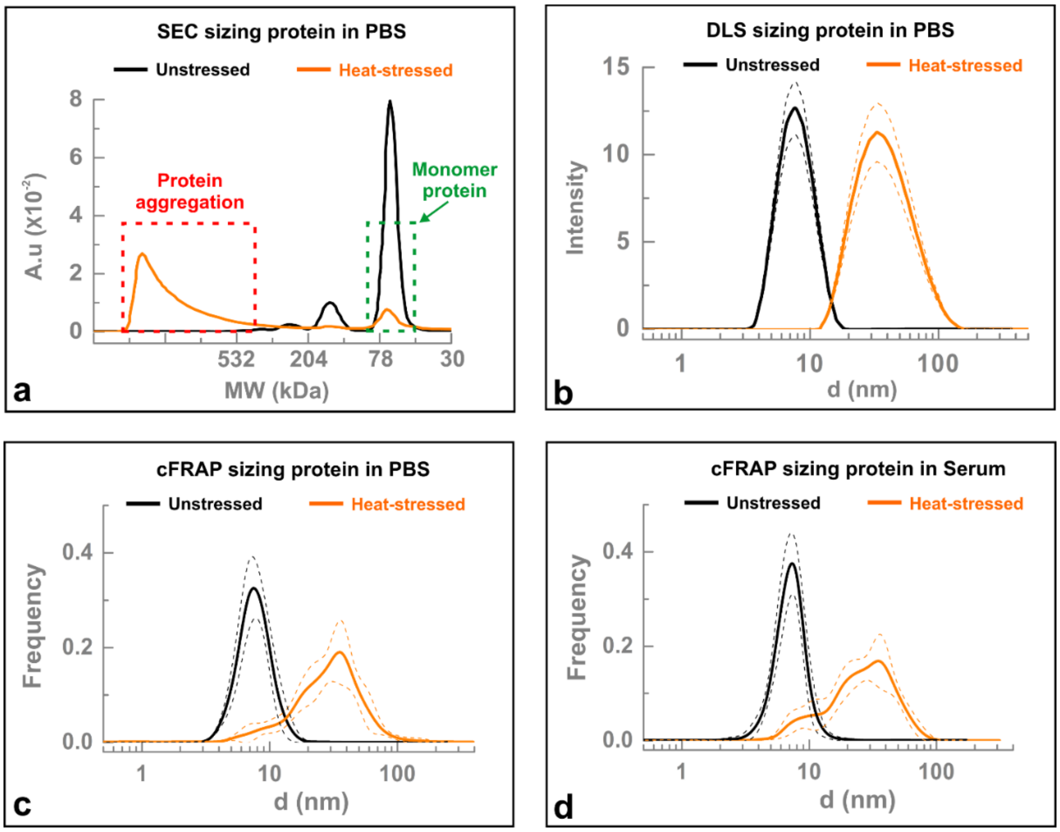

Figure 3 Sizing protein aggregates by SEC, DLS and cFRAP. Aggregates of fluorescently labeled BSA were prepared through heat-stress. (a-c) FITC-labeled BSA in buffer is measured before (black) and after (orange) applying 6 h heat stress by (a) Size Exclusion Chromatography, (b) Dynamic Light Scattering (DLS) and (c) cFRAP. (d) Unstressed (black lines) and heat-stressed (orange lines) samples were diluted in (90%) serum. The solid lines show the size distributions as measured by cFRAP while the dashed lines indicate the standard deviation on three independent repeats (with 10 cFRAP measurement per repeat). The size distributions as determined by cFRAP in serum nicely correspond to those in buffer. This demonstrates that cFRAP is very well capable of analyzing protein aggregates in (nearly undiluted) serum.

3.2 Assessing intestinal permeability in mice with septic shock

To further evaluate the potential of cFRAP-sizing we wondered to which extent cFRAP could be suitable for a detailed assessment of the permeability of the intestinal barrier in mice. The intestinal barrier is essential to prevent entry of the harmful intestinal content into the bloodstream. It consists of a single layer of epithelial cells that are sealed by tight junctions composed of claudins and other proteins in the junctional complex. Loss of intestinal barrier integrity is associated with various diseases, such as sepsis and inflammatory bowel disease. As there are indications that restoring intestinal integrity might ameliorate disease progression[21], there is great interest in finding pharmacological compounds, such as probiotics, that can safely strengthen the intestinal barrier. Therefore, methods are needed to accurately and quantitatively assess the intestinal barrier permeability. Inert fluorescently labeled dextrans of different molecular sizes (3–2000 kDa) can be used for this purpose. A probe of a particular size is administered orally and the quantity that leaks into the blood is measured by fluorimetry, potentially coupled to size exclusion chromatography[22]. To get information to which extent the barrier is compromised, this approach requires administering dextrans of various sizes sequentially – for which a new set of animals may be needed each time - and even then only discrete size information is obtained depending on the size of the probes used. In addition, these probes typically show some polydispersity so that the exact size that has leaked through is never certain.

To overcome these limitations, we propose the oral intake of a mixture of FITC-dextrans covering a wide range of sizes. cFRAP can then be used to analyze the size distribution of FITC-dextrans that have entered into the blood circulation after permeation through the intestinal barrier. A mixture of FITC-dextrans (FD) was prepared with a size ranging from ~2~80 nm. We verified that the entire size distribution could be measured by cFRAP, both in PBS buffer and in serum (**Fig. 4a**). The FD mixture was administered by oral gavage to mice treated with an intraperitoneal injection of PBS (control) or lipopolysaccharides (LPS) to induce septic shock. As schematically shown in **Fig. 4b**, blood was collected by cardiac puncture respectively 7 and 20 h after induction of septic shock and plasma was prepared. In each case, oral gavage of FDs was done 5 h before blood collection. Plasma fluorescence was measured by fluorimetry to determine the overall fraction of intestinal FD that had entered into the blood circulation (**Fig. 5**). These results confirm that septic shock results in loss of intestinal barrier integrity, as would be expected[23, 24]. cFRAP-sizing was subsequently performed on the plasma samples to determine the size distribution of FDs that had leaked through the epithelium (**Fig. 4b**). An exemplary cFRAP experiment is shown in **Fig. 6**. To correct for differences in concentration and molecular brightness between the various FDs in the mixture, all size distributions in serum were normalized to the reference measurement of the FD mixture in PBS buffer (**Fig. 4a**). As for the control mice with intact intestinal barrier (treated with PBS only), the amount of FD in plasma was insufficient to perform meaningful cFRAP experiments. In LPS treated mice we found that at 7 h after LPS injection FDs in the lower size range (up to 10 nm) had entered into the blood circulation. Twenty hours after LPS injection the distribution had not substantially changed, which suggests that the barrier integrity does not change noticeably from 7 h to 20 h after inducing septic shock. Note that subtle differences in the distributions may arise from the fact that the results at each time point are determined from a different set of animals.

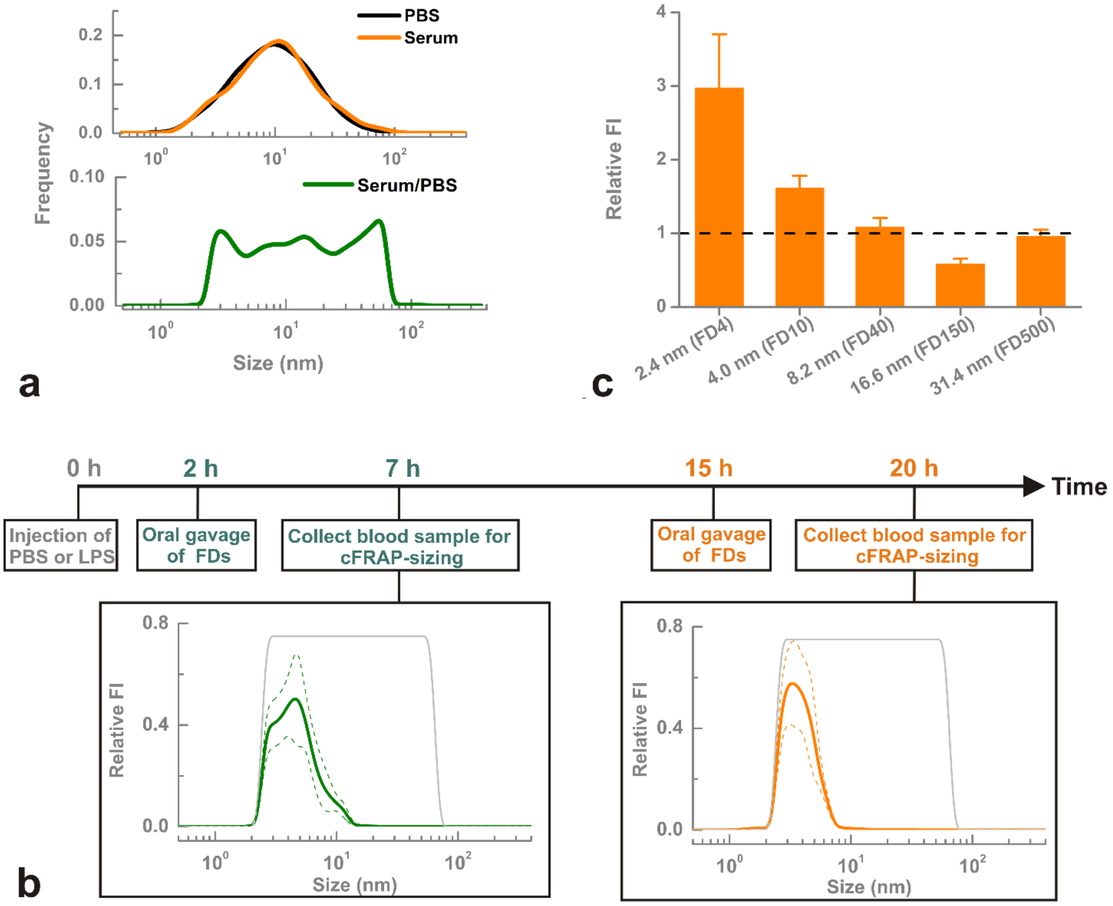

Figure 4. Assessing the permeability of the intestinal epithelium in mice. To assess the permeability of the intestinal barriers, a mixture of FITC-dextrans was prepared spanning a wide range of sizes from ~2 to ~80 nm. The mixture was prepared according to the weight ratio FD4 : FD10 : FD40 : FD150 : FD500 = 45 : 25 : 15 : 10 : 10. (a) The full size range can be measured by cFRAP in PBS buffer and (95%) serum. By normalizing the serum data to the results in PBS, these differences between FD components are cancelled out (since k_i is constant independent of the medium) and a virtually uniform distribution is obtained which is very well suited to interpret in a continuous fashion the size range of probes that can permeate through the barrier. (b) Following the induction of septic shock by intraperitoneal injection of LPS, a mixture of FDs covering a broad range of sizes (grey lines) was administered to mice by oral gavage, respectively 2 h and 15 h after LPS injection. Blood samples were collected respectively 7 h (green lines) and 20 h (orange lines) after LPS injection. Leakage of FDs through the intestinal epithelium in healthy mice (injected with PBS instead of LPS) was negligible and could not be measured by cFRAP. The data shown are average values obtained on 3 mice, with 10 cFRAP-sizing measurements per mouse. The solid lines are the average of all these results, while the dashed lines indicate the corresponding standard deviation. (c) To validate the cFRAP results on the intestinal barrier permeability, a classic experiment was performed where FITC-dextrans of various sizes are administered separately to mice by oral gavage. The fluorescence intensity values are shown relative to the values of control mice (indicated by black dashed line). Only the values for FD4 and FD10 are significantly higher than the control case ($P<0.05$).

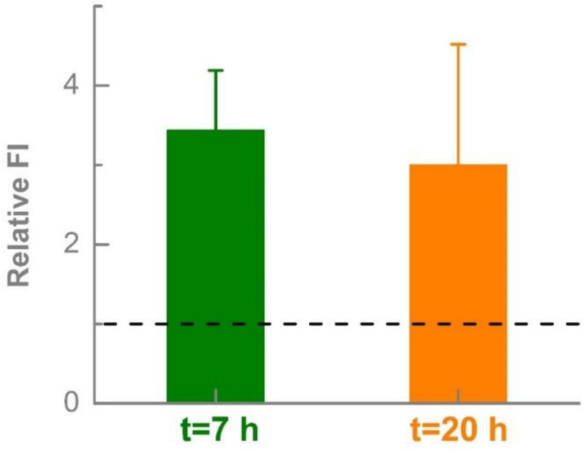

Figure 5. The total fluorescence of FDs in blood after oral gavage in mice with septic shock was measured by fluorimetry (λ_{ex}=488 nm and λ_{em}=520 nm). The values (n = 3) are expressed relative to the fluorescence in control mice (indicated by black dashed line), which were injected intraperitoneally with PBS only. Blood samples were collected at t = 7 h (green bar) and t=20 h (orange bar).

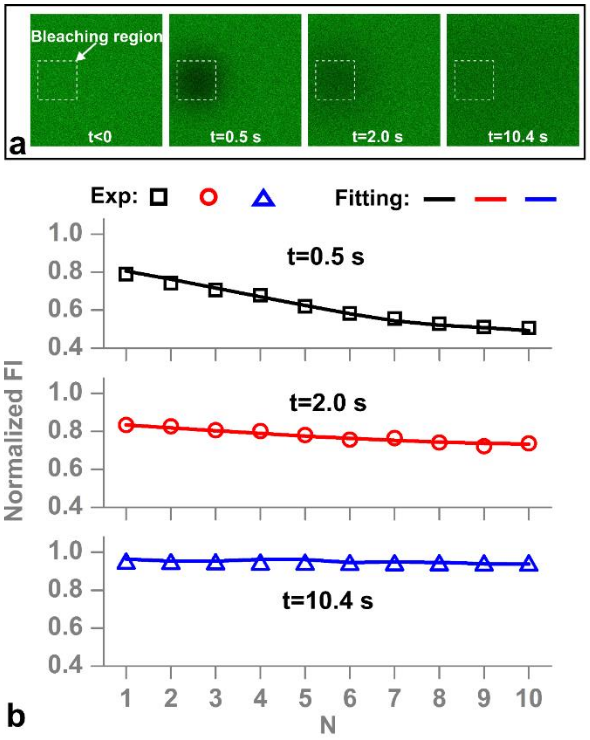

Figure 6. Example of a typical cFRAP experiment performed in blood. (a) The blood sample was collected at 7 h after LPS injection of a mixture of FDs covering a broad range of sizes. Confocal time-lapse series showing images before (t<0) and after bleaching (t = 0.5, 2.0 and 10.4 s). (b) Examples of spatial recovery curves at different time points are shown. N is the ring number as explained in Figure 1. The symbols denote the experimental data and the solid lines indicate the best fit solution of the cFRAP model to the data.

To validate these results, we performed extra experiments according to the classical approach of administering FITC-dextrans of different size separately in different mice and measuring the resulting fluorescence by fluorimetry in blood. In correspondence with the cFRAP experiments, we found that only FD with a nominal hydrodynamic size of ~2.4 nm (FD4) or ~4.0 nm (FD10) had entered the blood circulation, while larger FDs were not detected (**Fig. 4c**). Importantly, while ~30 mice were needed to determine the size cut-off of the intestinal barrier by the classical method of using different FD probes sequentially, microliter blood samples of only 6 mice were needed when cFRAP-sizing was used. This 5 fold reduction in the number of lab animals is one of the great advantages of cFRAP-sizing to measure barrier leakiness *in vivo*.

3.3 Assessing vascular permeability in mice with septic shock

Vascular permeability is essential for supplying tissues with nutrients and clearing waste products. Vascular permeability may be increased by diseases such as inflammatory disorders and cancer, as well as by wound healing. This hyperpermeable state is believed to influence the composition of the extravasate and the pathways that solutes follow in crossing the vascular endothelium[25]. Vascular hyperpermeability may also affect the barriers in the brain, including the endothelial blood-brain (BBB) and epithelial blood-CSF barrier (BCSFB)[26]. Disruption of the integrity of the BBB and BCSFB is believed to play a detrimental role in disease pathogenesis as protection of the delicate microenvironment of the brain from neurotoxic agents in the blood is compromised.

In order to quantify the size range of molecules that can leak through the vascular barrier, fluorescently labeled dextrans of different sizes can be injected intravenously, followed by analysis of fluorescence intensity in the relevant tissues. According to the classic protocol, each size of dextran is to be injected separately, each time in a different animal. Instead, by intravenous administration of a mixture of FDs covering a broad range of sizes, here we demonstrate that a single experiment is sufficient when combined with cFRAP-sizing. First we confirmed that the full FD size range could be analyzed in various organ fluids and CSF collected from control mice to which the FD mixture was added (**Fig. 7**). Next, as schematically shown in **Fig. 8**, mice were treated with an intraperitoneal injection of PBS (control) or LPS (septic shock). The mixture of FDs was injected intravenously 1 h before sample collection, which occurred respectively 7 and 20 h after PBS or LPS injection. CSF was collected using the cisterna magna puncture method. Kidney, brain, lung, spleen, ileum and liver were isolated after cardiac perfusion with PBS/heparin to remove all blood. Next, organ fluid was extracted from the different organs and total fluorescence was measured by fluorimetry after removing cellular debris, showing that there was a large increase in vascular permeability following septic shock (**Table 1**). From 7 to 20 h, the permeability increased further for CSF, kidneys, lung and ileum. Next, these samples were analyzed with cFRAP to determine the size distribution of FDs that had leaked through the vascular barrier. The size distributions (**Fig. 8**) were normalized to the relative fluorescence intensity as measured by fluorimetry (cfr. **Table 1**) so that the y-axis reflects the amount of FD that has leaked through relative to the control (healthy PBS injected mice) for CSF or each organ. The cFRAP-sizing results are shown in **Fig. 8** for CSF and kidney extract, while **Fig. 9** shows the cFRAP results obtained on extracts from brain, lungs, spleen, ileum and liver. Clearly, while no FD was found in the CSF of healthy control mice, FDs with a size below ~10 nm significantly permeated from the blood into the CSF in LPS treated mice. In kidneys the endothelium was found to become more permeable over time with FDs up to ~20 nm leaving the blood and entering the kidneys. Also here it is of note that 5 times less animals were needed as would have been the case for the classic fluorimetry method for which the size probes are to be administered separately in different animals. At the same time unprecedented detailed information is obtained on the continuous size range of probes that can leak through the barrier.

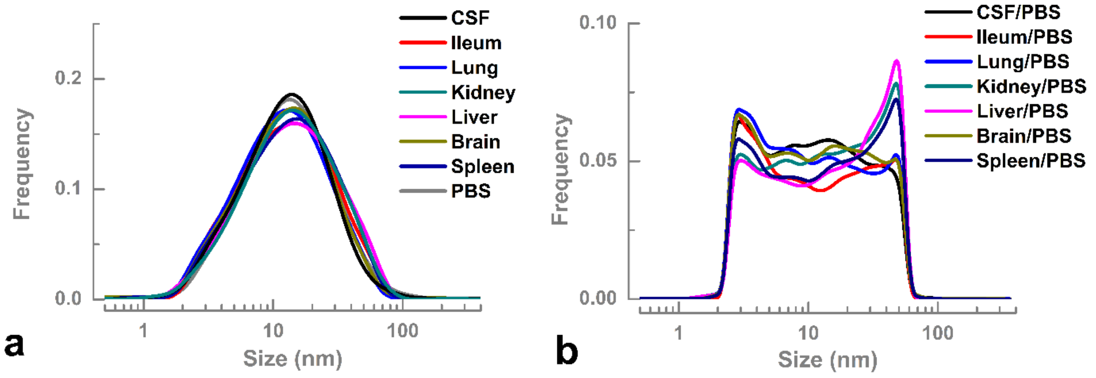

Figure 7. To assess the permeability of the vascular barrier, a mixture of FITC-dextrans was prepared spanning a wide range of sizes from ~2 to ~80 nm. (**a**) The FD mixture was measured by cFRAP in PBS, CSF and extracted organs fluids. (**b**) Normalization of the size distributions in CSF or organ fluids to the size distribution in PBS buffer corrects for differences in concentration and fluorescence brightness between the various probes in the mixture. All of above data are the average of 10 measurements.

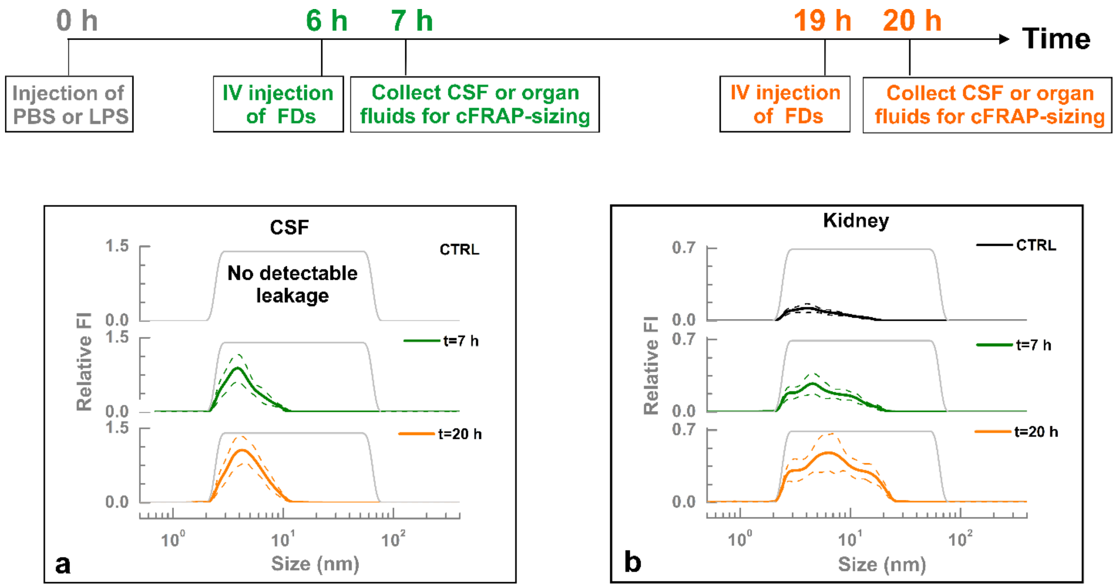

Figure 8. Assessing the vascular permeability in mice. Following the induction of septic shock by intraperitoneal injection of LPS, a mixture of FDs covering a broad size range (grey line) was intravenously injected respectively 6h and 19h after the LPS treatment. CSF and organs were collected respectively at 7 h (green lines) and 20 h (orange lines) after the LPS treatment. cFRAP-sizing was performed on (**a**) CSF and (**b**) kidney-extract. Control mice were injected with PBS (instead of LPS) to determine the leakage in healthy mice as a reference (black lines). Note that in healthy mice FDs did not appear in the CSF. The data shown are average values obtained on 3 mice, with 10 cFRAP-sizing measurements per mouse. The solid lines are the average of all these results, while the dashed lines indicate the corresponding standard deviation. Note that the Relative FI values can only be compared for the various time points per fluid. Comparison of Relative FI values should not be made between different sample types.

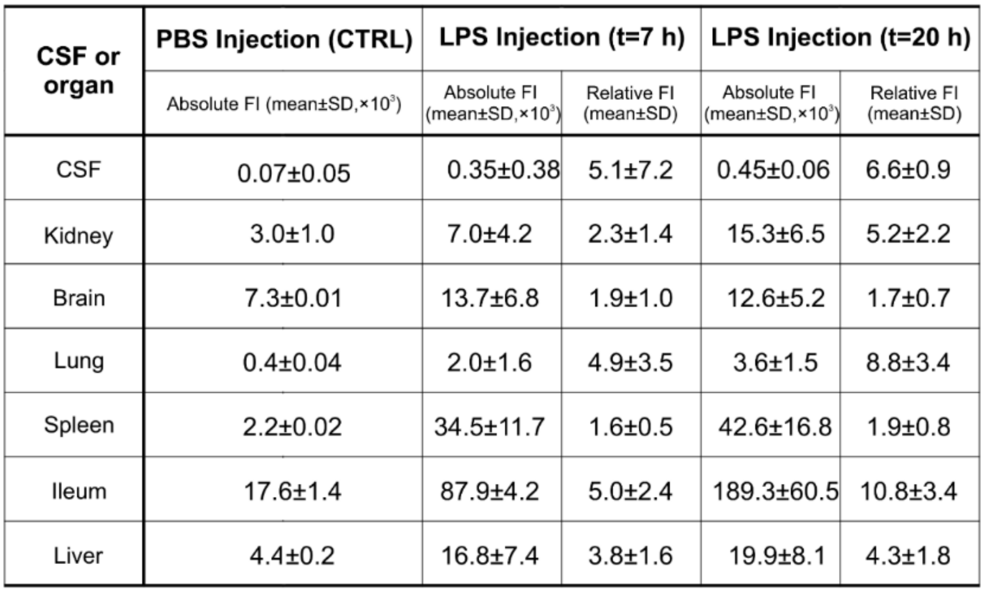

CSF or organ	PBS Injection (CTRL)	LPS Injection (t=7 h)		LPS Injection (t=20 h)	
	Absolute FI (mean±SD,×10^3)	Absolute FI (mean±SD,×10^3)	Relative FI (mean±SD)	Absolute FI (mean±SD,×10^3)	Relative FI (mean±SD)
CSF	0.07±0.05	0.35±0.38	5.1±7.2	0.45±0.06	6.6±0.9
Kidney	3.0±1.0	7.0±4.2	2.3±1.4	15.3±6.5	5.2±2.2
Brain	7.3±0.01	13.7±6.8	1.9±1.0	12.6±5.2	1.7±0.7
Lung	0.4±0.04	2.0±1.6	4.9±3.5	3.6±1.5	8.8±3.4
Spleen	2.2±0.02	34.5±11.7	1.6±0.5	42.6±16.8	1.9±0.8
Ileum	17.6±1.4	87.9±4.2	5.0±2.4	189.3±60.5	10.8±3.4
Liver	4.4±0.2	16.8±7.4	3.8±1.6	19.9±8.1	4.3±1.8

Table 1. The overall fluorescence intensity in CSF and organ fluids as measured by fluorimetry. Samples were collected at time points of t=7 h and t=20 h after intraperitoneal injection of PBS (control) or LPS (septic choc) in mice. The mixture of FDs was IV injected 1h before sample collection. The fluorescence intensity values are shown as absolute fluorescence intensity (FI, arbitrary units) and relative to the fluorescence in control mice, which were injected with PBS only.

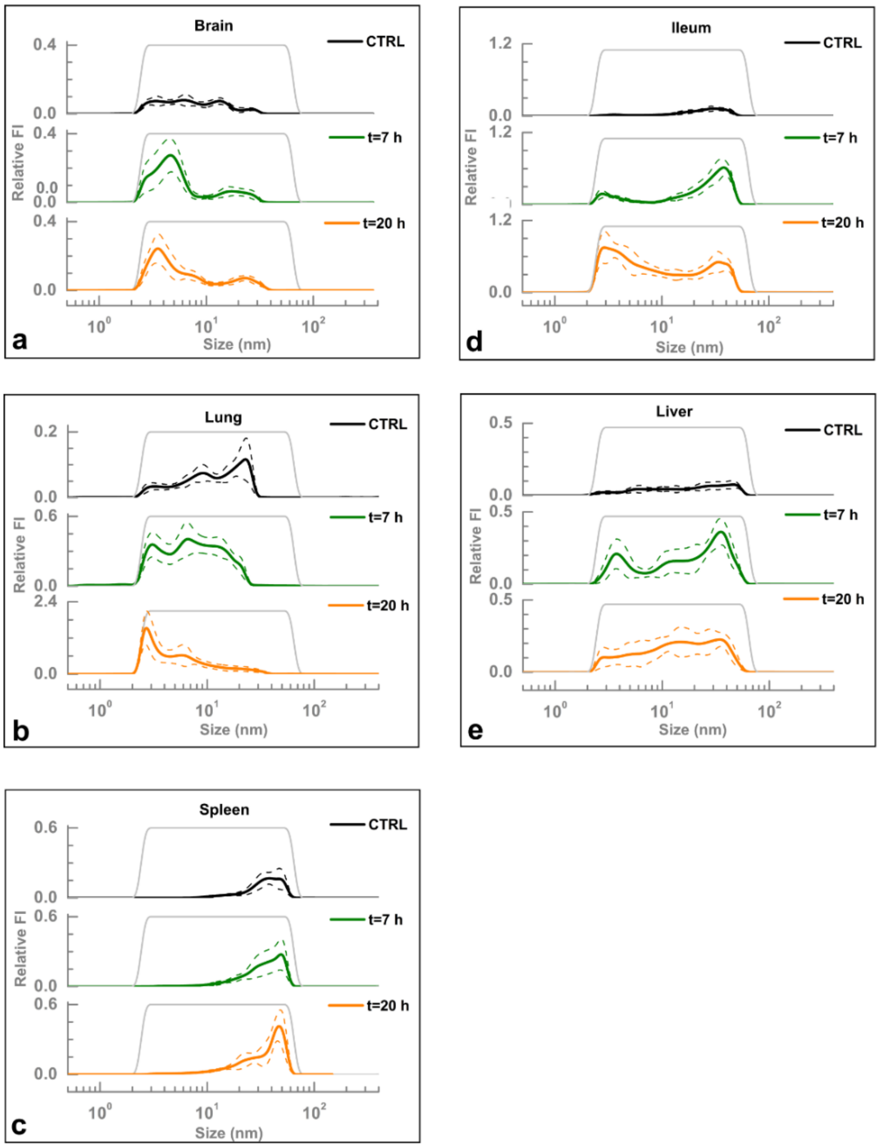

Figure 9. Assessing the vascular permeability in mice by measuring the range of probes that can permeate through the vascular endothelium in mice. cFRAP-sizing measurements were performed on (a) brain-, (b) lung-, (c) spleen-, (d) ileum- and (e) liver-fluids. Control mice were injected with PBS (instead of LPS) to determine the leakage in healthy mice as a reference (black lines). The data shown are the average from 3 mice, and for each mice 10 cFRAP measurements were performed. The solid line is the average of all these results and the dashed lines indicate the corresponding standard deviation. Note that direct comparison of the Relative FI values is only valid for the different time points of the same organ. Comparison of Relative FI values should not be made between organs. We could see brain an increase in the permeation of small molecules < 10 nm for LPS treated mice. The same is true for the lungs although they also contained a small fraction of large FDs (> 20 nm) after 20h. In the spleen there was only an increase in the permeation of large molecules (> 20 nm) while in the liver probes were found over the entire tested range (~2 - ~80 nm). The Ileum, finally, exhibits a bimodal distribution of probes in LPS treated mice with a marked increase in the permeation of small molecules (~2 - ~10 nm). These data show that the cFRAP method enables detailed analysis of vascular permeability in all tested organs.

4. DISCUSSION

FRAP has been used for decades to measure the average diffusion coefficient of fluorescently labeled molecules in various media, from cells and extracellular matrices to food products and drug delivery materials[27]. Instead, rather than measuring a single average diffusion coefficient, we succeeded in extracting the full distribution of diffusion coefficients from the recovery images using a dedicated theoretical framework that makes use of the full temporal and spatial information available in confocal recovery images. As the cFRAP method is compatible with standard laser scanning confocal microscopes, it is easily accessible and straightforward to apply. Although cFRAP surely can be used to perform detailed biophysical diffusion studies, instead we have evaluated this technique to measure the size of nanomaterials in biological fluids. Considering the capabilities of typical confocal microscopes in terms of sensitivity and image acquisition rate, cFRAP is perfectly suited to measure the diffusion of nanomaterials in the 1-100 nm size range in fluids. As such it nicely complements the fluorescence Single Particle Tracking (fSPT) method that was recently developed in our group for nanoparticle sizing primarily in the 0.1-1 µm range [17, 28].

When characterizing protein aggregation, we even found that a single cFRAP experiment produces the same size information as obtained by DLS and SEC combined. Furthermore, a major benefit of cFRAP is that microliter samples are sufficient. In principle even smaller volumes are very well possible since a single confocal image series typically probes a volume of 100 µm × 100 µm × 10 µm which corresponds to 0.1 nl. Assuming 10 measurements per sample this amounts to a probed volume of only 1 nl. Sizing by cFRAP, therefore, is perfectly compatible with miniaturization approaches like microfluidics.

As a first proof-of-concept application, we successfully demonstrated that cFRAP-sizing can be used to characterize protein aggregates directly in undiluted serum. This would be impossible to do by DLS due to strong light scattering by serum components. Also SEC is not without its problems since the high serum protein content may lead to interactions with the column matrix and altered elution profiles. Evidently the use of cFRAP comes at the expense of having to label the protein of interest. Yet, this is balanced by the fact that there are virtually no other techniques at this moment to characterize submicrometer protein aggregates in complex biological fluids.

Based on cFRAP-sizing we also devised a new approach to rapidly assess the integrity of the intestinal and vascular barriers which is related to disease pathogenesis. While disruption of tight junctions involved in cell–cell contact causes leakage of small molecules, the presence of epithelial apoptosis will allow permeation of larger molecules as well[29]. In the classic approach inert probes, such as FITC-dextrans, of a particular size are administered to lab animals. However, as the sequential administration and fluorimetric analysis of probes of different sizes requires each time a different set of animals, it is time-consuming, expensive and poses ethical issues. Instead, we have demonstrated the use of a single mixture of probes (FITC-dextrans) covering a very broad range of sizes. After sample collection of the relevant fluids, a single cFRAP experiment on a microliter sample can reveal the full size distribution of probes that have permeated through the barrier. The cFRAP-sizing method, therefore, reveals in a single experiment the full size distribution of probes that can leak through the barrier. Importantly, five times less animals were needed as compared to the classic fluorimetric method where FDs of (five) different sizes would have to be administered and analyzed separately. Although there is one report that has tried to assess endothelial barrier permeability with a mixture of FITC dextrans and fluorescence SEC analysis[30], cFRAP-sizing has the clear advantage of being able to work with tiny sample volumes, even down to nanoliters if required. It is also very fast and does not require calibration (other than an intrinsic viscosity measurement) as is needed for SEC to interpret the elution profiles. Using cFRAP-sizing we even succeeded in analyzing FD leakage in microliter samples of cerebrospinal fluid, notwithstanding that the fluorescence was very weak. To the best of our knowledge this would be impossible to do by SEC.

5. CONCLUSIONS

We conclude that sizing by cFRAP is a powerful and valuable new analytical technique for measuring the size of nanomaterials in complex biological fluids. While we have demonstrated its usefulness in proof-of-concept applications, the potential of cFRAP-sizing reaches much further and more valuable applications are expected to follow suit, potentially in combination with microfluidic approaches which enable accurate handling of small sample volumes.

6. REFERENCES

1. Nagayasu A, Uchiyama K, Kiwada H. The size of liposomes: a factor which affects their targeting efficiency to tumors and therapeutic activity of liposomal antitumor drugs. *Adv Drug Deliver Rev* **40**, 75-87 (1999).
2. Gaumet M, Vargas A, Gurny R, Delie F. Nanoparticles for drug delivery: The need for precision in reporting particle size parameters. *Eur J Pharm Biopharm* **69**, 1-9 (2008).
3. Koide H*, et al.* Particle size-dependent triggering of accelerated blood clearance phenomenon. *Int J Pharm* **362**, 197-200 (2008).
4. Decuzzi P*, et al.* Size and shape effects in the biodistribution of intravascularly injected particles. *J Control Release* **141**, 320-327 (2010).
5. Braeckmans K*, et al.* Advanced fluorescence microscopy methods illuminate the transfection pathway of nucleic acid nanoparticles. *J Control Release* **148**, 69-74 (2010).
6. Ragelle H*, et al.* Chitosan nanoparticles for siRNA delivery: Optimizing formulation to increase stability and efficiency. *J Control Release* **176**, 54-63 (2014).
7. Rosenberg A. Effects of protein aggregates: An immunologic perspective. *AAPS J* **8**, E501-E507 (2006).
8. Brinks V, Jiskoot W, Schellekens H. Immunogenicity of Therapeutic Proteins: The Use of Animal Models. *Pharm Res* **28**, 2379-2385 (2011).
9. Filipe V, Poole R, Kutscher M, Forier K, Braeckmans K, Jiskoot W. Fluorescence Single Particle Tracking for the Characterization of Submicron Protein Aggregates in Biological Fluids and Complex Formulations. *Pharm Res* **28**, 1112-1120 (2011).
10. Filipe V, Poole R, Oladunjoye O, Braeckmans K, Jiskoot W. Detection and Characterization of Subvisible Aggregates of Monoclonal IgG in Serum. *Pharm Res* **29**, 2202-2212 (2012).
11. Goldenberg NM, Steinberg BE, Slutsky AS, Lee WL. Broken Barriers: A New Take on Sepsis Pathogenesis. *Sci Transl Med* **3**, (2011).
12. Neurath MF. New targets for mucosal healing and therapy in inflammatory bowel diseases. *Mucosal Immunol* **7**, 6-19 (2014).
13. Wang L, Llorente C, Hartmann P, Yang A-M, Chen P, Schnabl B. Methods to determine intestinal permeability and bacterial translocation during liver disease. *Journal of Immunological Methods*, (2015).
14. Braeckmans K*, et al.* Sizing nanomatter in biological fluids by fluorescence single particle tracking. *Nano letters* **10**, 4435-4442 (2010).
15. Roding M, Deschout H, Braeckmans K, Sarkka A, Rudemo M. Self-calibrated concentration measurements of polydisperse nanoparticles. *J Microsc-Oxford* **252**, 79-88 (2013).
16. Deschout H*, et al.* On-chip light sheet illumination enables diagnostic size and concentration measurements of membrane vesicles in biofluids. *Nanoscale* **6**, 1741-1747 (2014).
17. Deschout H*, et al.* Precisely and accurately localizing single emitters in fluorescence microscopy. *Nat Methods* **11**, 253-266 (2014).
18. Periasamy N, Verkman AS. Analysis of fluorophore diffusion by continuous distributions of diffusion coefficients: application to photobleaching measurements of multicomponent and anomalous diffusion. *Biophysical journal* **75**, 557-567 (1998).
19. Tycon MA, Daddysman MK, Fecko CJ. RNA Polymerase II Subunits Exhibit a Broad Distribution of Macromolecular Assembly States in the Interchromatin Space of Cell Nuclei. *J Phys Chem B* **118**, 423-433 (2014).
20. Hauser GI, Seiffert S, Oppermann W. Systematic evaluation of FRAP experiments performed in a confocal laser scanning microscope - Part II: Multiple diffusion processes. *J Microsc-Oxford* **230**, 353-362 (2008).
21. Skilling J, Bryan RK. Maximum-Entropy Image-Reconstruction - General Algorithm. *Mon Not R Astron Soc* **211**, 111-& (1984).
22. Bischoff SC*, et al.* Intestinal permeability - a new target for disease prevention and therapy. *Bmc Gastroenterol* **14**, (2014).

23. Mehvar R, Shepard TL. Molecular-Weight-Dependent Pharmacokinetics of Fluorescein-Labeled Dextrans in Rats. *J Pharm Sci* **81**, 908-912 (1992).
24. Van Hauwermeiren F*, et al.* TNFR1-induced lethal inflammation is mediated by goblet and Paneth cell dysfunction. *Mucosal Immunol*, (2014).
25. Vandenbroucke RE, Vanlaere I, Van Hauwermeiren F, Van Wonterghem E, Wilson C, Libert C. Pro-inflammatory effects of matrix metalloproteinase 7 in acute inflammation. *Mucosal Immunol* **7**, 579-588 (2014).
26. Nagy J, Benjamin L, Zeng H, Dvorak A, Dvorak H. Vascular permeability, vascular hyperpermeability and angiogenesis. *Angiogenesis* **11**, 109-119 (2008).
27. De Bock M, Vandenbroucke RE, Decrock E, Culot M, Cecchelli R, Leybaert L. A new angle on blood-CNS interfaces: A role for connexins? *FEBS letters* **588**, 1259-1270 (2014).
28. Lorén N*, et al.* Fluorescence recovery after photobleaching in material and life sciences: putting theory into practice. *Quarterly Reviews of Biophysics*, (2015).
29. Zagato E*, et al.* Single-particle tracking for studying nanomaterial dynamics: applications and fundamentals in drug delivery. *Nanomedicine-Uk* **9**, 913-927 (2014).
30. Sengupta P, Garai K, Balaji J, Periasamy N, Maiti S. Measuring Size Distribution in Highly Heterogeneous Systems with Fluorescence Correlation Spectroscopy. *Biophysical journal* **84**, 1977-1984 (2003).
31. Arrieta MC, Bistritz L, Meddings JB. Alterations in intestinal permeability. *Gut* **55**, 1512-1520 (2006).
32. Mooradian AD, Haas MJ, Batejko O, Hovsepyan M, Feman SS. Statins ameliorate endothelial barrier permeability changes in the cerebral tissue of streptozotocin-induced diabetic rats. *Diabetes* **54**, 2977-2982 (2005).
33. Deschout H*, et al.* Straightforward FRAP for quantitative diffusion measurements with a laser scanning microscope. *Opt Express* **18**, 22886-22905 (2010).
34. Smisdom N. The dynamic behavior of the glycine receptor in the plasma membrane. In: *School of Life Sciences* (ed^(eds). Hasselt University (2011).
35. Dalal RB, Digman MA, Horwitz AF, Vetri V, Gratton E. Determination of particle number and brightness using a laser scanning confocal microscope operating in the analog mode. *Microsc Res Techniq* **71**, 69-81 (2008).
36. Braeckmans K, Peeters L, Sanders NN, De Smedt SC, Demeester J. Three-dimensional fluorescence recovery after photobleaching with the confocal scanning laser microscope. *Biophysical journal* **85**, 2240-2252 (2003).

Broader international context, relevance and future perspectives

Part I INTRACELLULAR DELIVERY OF BIOPHARMACEUTICALS AND CONTRAST AGENTS BY VAPOR NANOBUBBLE PHOTOPORATION

VNB photoporation is a relatively new method that is gradually receiving increasing interest in recent years to deliver nanomaterials into cells[1-4]. We report on a systematic comparison of two nanoparticle enhanced photoporation mechanisms in **Chapter 2**. Under condition of a single laser pulse per cell, we performed a systematic comparison of membrane permeabilization by photothermal heating vs. mechanical pore formation by vapor nanobubbles in terms of delivery efficiency and cytotoxicity. Despite the fact that it requires higher laser energies, we find that VNB photoporation allows more efficient cellular uptake of compounds due to the fact that larger pores could be formed. Yet, VNB photoporation did not induce extra cytotoxicity as compared to heating due to the fact that VNB generation is an almost purely mechanical effect that does not lead to heat diffusion into the surrounding tissue. Interestingly, by tuning the laser energy and hence the size of the VNBs, it seems possible (as we have no real proof of this) to tune the size of the pores that are created. This in turn allows to control the amount of molecules that are delivered into the cytosol, as well as the maximum size of molecules that are allowed to pass through. Although we are convinced that VNB photoporation is a promising alternative physical technique to efficiently deliver compounds into cells with little or no toxicity, further fundamental research is needed to fully understand the underlying mechanisms, like heat transfer from plasmonic nanoparticles to the environment, nanobubble dynamics and cell repair mechanisms. These aspects are explained in more detail below. A better understanding of these fundamental mechanisms will enable to better control and predict the influx of molecules into the cytoplasm.

Specifically, it is well known that in plasmonic nanoparticles like AuNPs, the optical absorption is enhanced by Localized Surface Plasmon Resonance (LSPR). Due to LSPR, a series of sequential energy transfer processes occur. First, the oscillating electrons become thermalized within a few hundreds of fs through electron-electron interactions. After that, the thermalized electrons transfer their energy to the nanoparticle phonons (i.e. lattice vibrations) by electron-phonon coupling, resulting in an increase of the nanoparticle temperature. Finally, thermal equilibration is achieved in ~100 ps inside the NPs. This laser-NP interaction has been extensively studied and is well known[5-8]. However, following thermal equilibration, the mechanisms of heat transfer from the particle to the environment remain unclear. Neither is it entirely clear how the heating of NPs induces the formation of vapor nanobubbles. When the NP temperature remains below the critical water evaporation temperature, heat transfers occurs through heat diffusion[9]. However, when water evaporation occurs around the NP surface, heat transfer is more complex. Normally, the heat transport from NPs to water is simply described by a single critical interface conductivity which is assumed to be uniform across the NP surface[10-12]. This assumption seems suitable when the vapor layer surrounding the NPs is formed in a homogenous manner. However, the Luo group recently showed that the vapor layer on the nanoscale is not homogenous on a nano-structured surface[13]. As a result, it seems logical that the heat transfer in case of a non-uniform vapor layer vapor will result in non-homogeneous heat transfer into the environment. Therefore, it is of interest to study how heat is transferred to water in case of a heterogeneous vapor layer formation in order to assess its contribution to membrane permeabilization and the impact of this heat transfer on cell viability.

More fundamental studies on water vapor nanobubble dynamics are needed as well. When the NP temperature is above the critical temperature to initiate water vaporization, water vapor nuclei are formed around the NP surface. These will grow and coalesce to form a nanobubble around the NP, which can further expand and collapse. Current research on the dynamics of nanobubbles assumes a symmetric expansion and collapse[11, 12]. This seems to be a reasonable assumption when NPs are suspended in liquid far from any obstacles. However, in NP enhanced photoporation, the NPs are necessarily close or even adsorbed to the cell membrane, which will affect the nanobubble dynamics. For bubbles on the microscale it has already been described that they collapse in an asymmetrical fashion near a surface, resulting in the formation of a liquid jet towards the surface[14, 15]. Furthermore, when two bubbles are in close proximity, asymmetric bubble deformation can occur with the formation of a microjet[16]. To better understand photoporation process it is of fundamental interest to investigate in further detail how water vapor nanobubbles interact with the cell membrane. Yet, clearly this is very challenging from an experimental point of view as nanobubbles are too small to be resolved by optical imaging, as is done for microbubbles. Instead it seems more reasonable to study this by numerical simulation tools like molecular dynamics simulations. Recently, Berkowitz's group applied coarse-grained molecular dynamics to study spontaneous nanobubble collapse and its mechanical effect on the cell membrane[17]. Although the 60 nm bubble was located closely to the membrane (~3 nm), it did not induce a pore in the membrane. This shows that the location of the nanoparticle relative to the membrane is essential for obtaining perforation of cell membrane. In the future, it would be of fundamental interest to try to better understand the interaction of nanobubbles of various sizes with the cell membrane and to determine how pores can be most efficiently formed. In particular it would be of interest to compare pore formation when the nanoparticles are attached on the cell membrane, slightly invaginated (i.e. onset of endocytosis), or completely enveloped inside an endosome.

Following pore formation in the cell membrane, the cell will try to repair the inflicted damage, which is quite essential to avoid cell death. The repair mechanism is reportedly based on Ca2+ influx that induces exocytosis of lysosomes for 'patching' of the pores[18, 19]. However, very little is known at this moment on whether or not size and lifetime of pores influence the repair processes . In some reports attempts have been made to estimate the pore lifetime, but the reported values range from tens of seconds to tens of minutes[20-22]. This is likely caused by differences in photoporation conditions, different cell types and different ways how the measurements are performed. Therefore, more systematic studies are needed to better understand and predict pore formation and repair, which in turn is needed to better understand the loading process for different types of cells and molecules. This will be especially useful to optimize photoporation of larger macromolecules, such as mRNA or plasmids.

In **Chapter 3** we showed that photoporation is a well-suited technology for the cytosolic delivery of nano-labels for long-term *in vivo* imaging of cells. It was shown that direct cytosolic delivery of nano-sized contrast agents by VNB photoporation opens up exciting avenues for improved long-term quantitative *in vivo* cell tracking. Apart from much more efficient cell loading and prolonged cell visibility *in vitro* and *in vivo* as compared to endocytic labeling, we show that asymmetric inheritance of labels can be avoided by delivering the labels directly into the cytosol through VNB photoporation. As VNB photoporation is independent of the cell type and contrast agent used, we expect that it will be an enabling technology that is of benefit for improved cell tracking studies. While in this thesis we focused on fluorescence labels, it will be of interest to evaluate in the future other contrast agents that are used for cell tracking, like superparamagnetic iron oxide nanoparticles or Gd-complexes for magnetic resonance imaging. Similar to the fluorescent labels, the most straightforward way to label cells with these contrast agents is also by simple incubation and endocytic uptake during *in vitro* culture. Yet, these MRI contrast agents suffer from similar disadvantages as the fluorescent labels when sequestered in endosomes. First, the endocytic labeling is a slow procedure that needs to be optimized for each combination of cell-type and contrast agent. This can be problematic especially for cells with a limited in vitro lifespan, such as pancreatic islets or cells which have little or no endocytic uptake, like T-cells. Second, asymmetric inheritance of labels over daughter cells leads to progressive label heterogeneity upon each cell division[23, 24]. Finally, it has been shown that sequestration of Gadolinium chelates in intracellular vesicles can result in quenching of the MRI T1 signal, interfering with accurate signal quantification[25-27]. Therefore, it will be of interest to see if these problems can be overcome by delivery of these NPs into cytosol by photoporation. The benefits of cytosolic delivery of contrast agents as found in **Chapter 3** were obtained with photoporation as delivery technology. It will be of future interest to find out if these benefits are uniquely linked to photoporation, or if the same benefits can be found when other delivery methods are used, such as electroporation[28] or the recently reported cell squeezing technology[29, 30].

In **Chapter 4**, we demonstrate that VNB photoporation is able to deliver functionalized QDs efficiently into the cytosol of cells for labeling of subcellular structures. In particular, we could show that antibody functionalized QDs could be targeted to the microtubules in living cells. While the final contrast was limited, likely due to the presence of too many unbound QDs, microtubules could be distinguished by confocal microscopy. While further work is certainly needed, it does show the potential of VNB photoporation to become a versatile tool for the delivery of exogenous labels for subcellular microscopic visualization. Future work should focus on getting better control over the amount of QDs that are delivered into the cells. More specifically, we recently found that graphene nanoparticles can be used to generate multiple VNB, while AuNP can only generate a single AuNP after which they are destroyed. This opens up the possibility to gradually increase the amount of nano-labels that are delivered in the cells by repeating generation of VNB. Obviously future work should also focus on delivering other fluorescent labels, like antibodies that are used for immunolabeling of fixed cells. If successful it would mean that a plethora of 'old-school' labels can be used for live cell imaging, which is currently limited to cell permeable constructs, or over-expression of proteins with the danger of associated artefacts.

In **Chapter 5**, we explored spatially resolved nanoparticle enhanced photoporation (SNAP) for fast and flexible delivery of nanomaterials into living cells with low toxicity. We developed an integrated platform that can be used to deliver nanomaterials into living cells in a spatially controlled manner, even down to single cell resolution. It offers very flexible cell-selective delivery according to pre-defined patterns or in an interactive image-guided manner. Our equipment can be used in a total of four working modes, which will meet most experimental requirements. Compared to traditional photoporation with a focused fs laser, or the recently developed system with laser-irradiated gold plasmonic nanotubes, the throughput of SNAP is more than one order higher[3, 31-34]. With our current SNAP set-up we achieved 20 cells/s, whereas only 1.7 cells/s has been reported as the fasted throughput with standard photoporation (i.e. without enhancing nanoparticles). We expect that the SNAP throughput can be increased by at least another factor of 10 when a laser is used with higher pulse repetition frequency. It is of note that other methods are also explored for cell-selective delivery. Microinjection can be used but it is a slow and technically demanding technique[35]. Spatially resolved electroporation has been explored as well, demonstrating that cells were selectively transfected with genes by an array of microelectrodes[28]. This method, however, is limited to the transfection of fixed patterns according to the design of the electrode array. Interactive image-guided delivery would be impossible with such a technology. In addition, the electrodes are too large for single cell selective delivery.

In this thesis we have shown many benefits of photoporation as a fast and flexible delivery technology in adherent cells. Clearly, there is great interesting in 3D cell cultures as well. A 3D cell culture is an artificially-created environment in which biological cells are permitted to grow or interact with their surroundings in all three dimensions. Unlike 2D culture, a 3D cell culture allows cells *in vitro* to grow in all directions, which is closer to the *in vivo* situation[36]. As such it is of interest to develop our technology further towards 3D cell selective delivery. One of the key questions is how to precisely deliver sufficient laser energy to the selected cells in 3D culture without affecting the cells above and below. Yet, it does not seem impossible since VNB generation is a threshold phenomenon. With a more tightly focused laser beam it could be possible to find conditions where the light intensity is only high enough near the focal region for effective photoporation. Another approach could be to make use of a multi-photon process with a fs laser with a wavelength outside the LSPR peak. As explained in **Chapter 1**, in such conditions there will be very little heating while in the laser focus plasma-mediated nanobubbles can be formed due to multiphoton ionization[37, 38]. In this way, heating of cells above and below the focal plane can be avoided and only the selected cells in the focal plane will be photoporated.

We illustrated the usefulness of SNAP in two exemplary applications in **Chapter 5**. First we demonstrated that a sparse set of distant neuronal cells can be selectively labeled in a primary rat hippocampal culture in high throughput and with little or no toxicity. Targeted labeling of spatially separated neurons in a dense neuronal network by SNAP facilitates research in two ways. First, it enables one to assess neuronal morphology with automated image analysis, without fluorescence from nearby neurons and their neurites that traditionally complicate the analyses. Secondly, the labeling can be directed to neurons that show geno- or phenotypic patterns of interest. These may be neuronal subtypes (e.g. pyramidal- or interneurons) or neurons that show intracellular accumulation of toxic proteins (e.g. alpha-Synuclein or Tau). While this study focused on dendritic spines through actin staining, several other membrane-impermeable dyes could be photoporated into single neurons, showing the wide range of potential applications of this technique. Next we demonstrated that a fluorescent label can be automatically delivered into morphologically distinct subpopulations of cells. This allowed us to purify polynuclear from mononuclear primary NHEK cells, which will be useful in the future to unravel the role of polynuclear NHEKs in PSNE. In particular it is of interest to further unravel the underlying molecular mechanisms of PSNE by downstream molecular and functional analysis like sequencing of DNA breaks[39].

Taken together we can conclude that VNB photoporation is a maturing promising technique for unprecedented flexible intracellular delivery of membrane impermeable substances that, thanks to its unique capabilities, will secure its place next to the more established intracellular delivery methods.

Part II SIZING NANOMATERIALS IN BIO-FLUIDS BY FLUORESCENCE RECOVERY AFTER PHOTOPOBLEACHING

FRAP is widely applicable in the biophysical, pharmaceutical and material sciences to study diffusion of molecules and nanoparticles on a micrometer scale. To date, most mathematical models quantitatively interpreted FRAP data based on the average intensity in the bleach area as a function of time. As spatial information is essentially lost in this process, FRAP analysis has been limited to measuring a single overall diffusion coefficient, even though the system might be very polydisperse. Extension of FRAP to investigate polydisperse diffusion could become possible by also including spatial information in the analysis.

In **Chapter 6**, we report on a new analytical FRAP method for measuring a continuous distribution of diffusion coefficients (cFRAP). We developed a dedicated mathematical framework that makes use of the full tempo-spatial information available in confocal fluorescence recovery images. Although the applications in **Chapter 7** have already shown that cFRAP is an exciting method, there are still some further improvements possible from a technical point of view. The mathematic model of cFRAP is derived on the assumption of compounds undergoing free diffusion in the system. While this is correct for viscous solutions, other systems like soft materials, the cell cytoplasm, mucosa or biofilms, have more complex properties. They have a heterogeneous structure in which obstacles and molecular interactions can cause a deviation from free diffusion. Instead, molecules will undergo anomalous diffusion, leading to a time- dependent diffusion coefficient. Therefore, to further broaden its application in these systems, the cFRAP model could be extended for anomalous diffusion. Since cFRAP makes use of the full tempo-spatial information it is expected to offer better accuracy and precision as compared to previous FRAP methods for anomalous diffusion that only take temporal information into account[40].

In **Chapter 7,** we made use of cFRAP to measure the size distribution of nanomaterials (1-100 nm) in undiluted biological fluids. Sizing nanomaterials in complex biological fluids, such as blood, remains a great challenge for a wide range of biomedical applications. First, we demonstrate that cFRAP allows to measure protein size for characterization of aggregation not only in buffer but also in human serum. Even in buffer, the SEC signal corresponding to aggregates was not very well resolved and DLS failed to detect the monomers, while cFRAP could discriminate both monomers and aggregates in a single measurement. In future research it would be of interest to further validate this technique for actual protein based drugs, rather than BSA which was used as a model protein. In theory, a therapeutic protein in biological fluids like serum should remain in the monomer state. However, unexpected interactions and aggregation may occur[41]. Due to a lack of methods studying and understanding protein aggregation in e.g. serum remains a challenge; cFRAP may thus offer new opportunities in this area in the future. A few years back, our group has shown that fluorescence single particle tracking (fSPT) is a powerful technique for the characterization of submicron protein aggregates in human serum, plasma and formulations containing human serum albumin (HSA). However, as it is based on imaging the Brownian motion of individual, fluorescently labeled nanomaterials, it is mostly suited for nanoparticles with a size above ~0.1 μm[42]. Therefore, cFRAP complements fSPT as it is perfectly suited to measure the diffusion of protein aggregates in the 1-100 nm size range in fluids. It is of note that very recently a microfluidic platform was developed for protein sizing that is based on the spatial analysis of diffusion profiles as well. It was shown to allow sizing of molecules/nanoparticles (from sub-nanometers to hundreds of nanometers) in buffer[43]. Although it was not applied to measure the size of protein aggregates in biological fluids, it would be quite interesting to see how this method compares to cFRAP in terms of precision and accuracy.

As a second application in **Chapter 7**, we measured the size distribution of fluorescent probes ranging from 2 to 80 nm before and after administration in mice to determine the permeability of intestinal and vascular barriers *in vivo*. Apart from revealing unprecedented detailed information on pore sizes, cFRAP needed 5 times less animals compared with the classic fluorimetry method for which the size probes are to be administered separately in separate animals. Instead, by intravenous administration of a mixture of five FDs covering a broad range of sizes from 2-80 nm, a single experiment was sufficient. Using cFRAP-sizing we even succeeded in analyzing FD leakage in microliter samples of cerebrospinal fluid. It could be of interest as well to try to implement cFRAP in a microfluidic set-up as it is naturally compatible with minute sample volumes.

We can conclude that cFRAP is a powerful and valuable new analytical technique for measuring the diffusion or size of molecules or nanomaterials in complex biological fluids. Undoubtedly there are many more potential applications in cell biology and pharmacy which are open to exploration.

References

1. Lukianova-Hleb, E.Y. et al. Intraoperative diagnostics and elimination of residual microtumours with plasmonic nanobubbles. *Nature Nanotechnology* **11**, 525-+ (2016).
2. Wu, Y.C. et al. Massively parallel delivery of large cargo into mammalian cells with light pulses. *Nat Methods* **12**, 439-+ (2015).
3. Messina, G.C. et al. Spatially, Temporally, and Quantitatively Controlled Delivery of Broad Range of Molecules into Selected Cells through Plasmonic Nanotubes. *Adv Mater* **27**, 7145-+ (2015).
4. Xiong, R.H. et al. Comparison of Gold Nanoparticle Mediated Photoporation: Vapor Nanobubbles Outperform Direct Heating for Delivering Macromolecules in Live Cells. *Acs Nano* **8**, 6288-6296 (2014).
5. Link, S., Burda, C., Nikoobakht, B. & El-Sayed, M.A. Laser-induced shape changes of colloidal gold nanorods using femtosecond and nanosecond laser pulses. *J Phys Chem B* **104**, 6152-6163 (2000).
6. Link, S. & El-Sayed, M.A. Spectral properties and relaxation dynamics of surface plasmon electronic oscillations in gold and silver nanodots and nanorods. *J Phys Chem B* **103**, 8410-8426 (1999).
7. Sun, C.K., Vallee, F., Acioli, L.H., Ippen, E.P. & Fujimoto, J.G. Femtosecond-Tunable Measurement of Electron Thermalization in Gold. *Physical Review B* **50**, 15337-15348 (1994).
8. Schoenlein, R.W., Lin, W.Z., Fujimoto, J.G. & Eesley, G.L. Femtosecond studies of nonequilibrium electronic processes in metals. *Physical Review Letters* **58**, 1680-1683 (1987).
9. Delcea, M. et al. Nanoplasmonics for Dual-Molecule Release through Nanopores in the Membrane of Red Blood Cells. *Acs Nano* **6**, 4169-4180 (2012).
10. Shao, J. et al. Near-Infrared-Activated Nanocalorifiers in Microcapsules: Vapor Bubble Generation for In Vivo Enhanced Cancer Therapy. *Angewandte Chemie International Edition* **54**, 12782-12787 (2015).
11. Siems, A., Weber, S.A.L., Boneberg, J. & Plech, A. Thermodynamics of nanosecond nanobubble formation at laser-excited metal nanoparticles. *New Journal of Physics* **13** (2011).
12. Pustovalov, V.K., Smetannikov, A.S. & Zharov, V.P. Photothermal and accompanied phenomena of selective nanophotothermolysis with gold nanoparticles and laser pulses. *Laser Physics Letters* **5**, 775-792 (2008).
13. Wang, W.R., Huang, S.H. & Luo, X.S. MD simulation on nano-scale heat transfer mechanism of sub-cooled boiling on nano-structured surface. *Int J Heat Mass Tran* **100**, 276-286 (2016).
14. Lentacker, I., De Cock, I., Deckers, R., De Smedt, S.C. & Moonen, C.T.W. Understanding ultrasound induced sonoporation: Definitions and underlying mechanisms. *Adv Drug Deliver Rev* **72**, 49-64 (2014).
15. Zhou, Y., Yang, K., Cui, J., Ye, J.Y. & Deng, C.X. Controlled permeation of cell membrane by single bubble acoustic cavitation. *J Control Release* **157**, 103-111 (2012).
16. Sankin, G.N., Yuan, F. & Zhong, P. Pulsating Tandem Microbubble for Localized and Directional Single-Cell Membrane Poration. *Physical Review Letters* **105** (2010).
17. Adhikari, U., Goliaei, A. & Berkowitz, M.L. Mechanism of Membrane Poration by Shock Wave Induced Nanobubble Collapse: A Molecular Dynamics Study. *J Phys Chem B* **119**, 6225-6234 (2015).
18. Defour, A., Sreetama, S.C. & Jaiswal, J.K. Imaging Cell Membrane Injury and Subcellular Processes Involved in Repair. *Jove-Journal of Visualized Experiments* (2014).
19. Andrews, N.W., Almeida, P.E. & Corrotte, M. Damage control: cellular mechanisms of plasma membrane repair. *Trends in Cell Biology* **24**, 734-742 (2014).
20. Yamane, D. et al. Electrical Impedance Monitoring of Photothermal Porated Mammalian Cells. *Jala* **19**, 50-59 (2014).
21. Palankar, R. et al. Nanoplasmonically-Induced Defects in Lipid Membrane Monitored by Ion Current: Transient Nanopores versus Membrane Rupture. *Nano Lett* **14**, 4273-4279 (2014).
22. Kalies, S. et al. Plasmonic laser treatment for Morpholino oligomer delivery in antisense applications. *Journal of Biophotonics* **7**, 825-833 (2014).

23. Soenen, S.J. et al. The effect of nanoparticle degradation on poly(methacrylic acid)-coated quantum dot toxicity: The importance of particle functionality assessment in toxicology. *Acta Biomaterialia* **10**, 732-741 (2014).
24. Summers, H.D. et al. Quantification of Nanoparticle Dose and Vesicular Inheritance in Proliferating Cells. *Acs Nano* **7**, 6129-6137 (2013).
25. Terreno, E. et al. Effect of the intracellular localization of a Gd-based imaging probe on the relaxation enhancement of water protons. *Magn Reson Med* **55**, 491-497 (2006).
26. Strijkers, G.J., Hak, S., Kok, M.B., Springer, C.S. & Nicolay, K. Three-Compartment T(1) Relaxation Model for Intracellular Paramagnetic Contrast Agents. *Magn Reson Med* **61**, 1049-1058 (2009).
27. Gianolio, E. et al. Photochemical Activation of Endosomal Escape of MRI-Gd-Agents in Tumor Cells. *Magn Reson Med* **65**, 212-219 (2011).
28. Xu, Y.C., Yao, H.F., Wang, L., Xing, W.L. & Cheng, J. The construction of an individually addressable cell array for selective patterning and electroporation. *Lab Chip* **11**, 2417-2423 (2011).
29. Kollmannsperger, A. et al. Live-cell protein labeling with nanometre precision by cell squeezing. *Nat Commun* **7** (2016).
30. Lee, J. et al. Nonendocytic Delivery of Functional Engineered Nanoparticles into the Cytoplasm of Live Cells Using a Novel, High-Throughput Microfluidic Device. *Nano Lett* **12**, 6322-6327 (2012).
31. Breunig, H.G., Uchugonova, A., Batista, A. & Konig, K. Software-aided automatic laser optoporation and transfection of cells. *Scientific Reports* **5** (2015).
32. Dhakal, K., Black, B. & Mohanty, S. Introduction of impermeable actin-staining molecules to mammalian cells by optoporation. *Scientific Reports* **4** (2014).
33. Barrett, L.E. et al. Region-directed phototransfection reveals the functional significance of a dendritically synthesized transcription factor. *Nat Methods* **3**, 455-460 (2006).
34. Tirlapur, U.K. & Konig, K. Cell biology - Targeted transfection by femtosecond laser. *Nature* **418**, 290-291 (2002).
35. Remaut, K., Oorschot, V., Braeckmans, K., Klumperman, J. & De Smedt, S.C. Lysosomal capturing of cytoplasmic injected nanoparticles by autophagy: An additional barrier to non viral gene delivery. *J Control Release* **195**, 29-36 (2014).
36. Fey, S.J. & Wrzesinski, K. Determination of Drug Toxicity Using 3D Spheroids Constructed From an Immortal Human Hepatocyte Cell Line. *Toxicol Sci* **127**, 403-411 (2012).
37. Lachaine, R., Boulais, E. & Meunier, M. From Thermo- to Plasma-Mediated Ultrafast Laser-Induced Plasmonic Nanobubbles. *Acs Photonics* **1**, 331-336 (2014).
38. Boulais, E., Lachaine, R. & Meunier, M. Plasma Mediated off-Resonance Plasmonic Enhanced Ultrafast Laser-Induced Nanocavitation. *Nano Lett* **12**, 4763-4769 (2012).
39. Lensing, S.V. et al. DSBCapture: in situ capture and sequencing of DNA breaks. *Nat Meth* **advance online publication** (2016).
40. Periasamy, N. & Verkman, A.S. Analysis of fluorophore diffusion by continuous distributions of diffusion coefficients: Application to photobleaching measurements of multicomponent and anomalous diffusion. *Biophys J* **75**, 557-567 (1998).
41. Filipe, V., Vol. PhD (Utrecht University, 2012).
42. Braeckmans, K. et al. Sizing Nanomatter in Biological Fluids by Fluorescence Single Particle Tracking. *Nano Lett* **10**, 4435-4442 (2010).
43. Arosio, P. et al. Microfluidic Diffusion Analysis of the Sizes and Interactions of Proteins under Native Solution Conditions. *Acs Nano* **10**, 333-341 (2016).

Summary

This thesis consists of two parts, which summarized separately below.

Part I INTRACELLULAR DELIVERY OF BIOPHARMACEUTICALS AND CONTRAST AGENTS BY VAPOR NANOBUBBLE (VNB) PHOTOPORATION

Cytosolic delivery of foreign materials into live cells is an important step for many applications in cell biology and pharmacy. For instance, intracellular delivery of DNA is required for studying gene expression, mutation analysis, and gene therapy. Similarly, mRNA delivery into live cells enables assessing cell biological functions, while small interfering RNA (siRNA) is introduced for sequence-specific gene silencing. Apart from biological molecules there is an equal interest in the intracellular delivery of contrast agents. Recently, the use of inorganic particles as imaging contrast labels is being investigated, such as superparamagnetic iron oxide nanoparticles (SPIONs) and Gadolinium complexes for MRI, and quantum dots (QD) and upconversion nanoparticles for fluorescence imaging. Some of those exogenous nanomaterials could be introduced into cells *via* a viral vector. But immunogenicity and toxicity are major concerns. On the other hand, the nanomaterials could be formulated into non-viral carriers, typically lipid or polymer based. As these are generally internalized by cells through endocytosis, escape from the endosomes into the cytosol is typically needed. Up to date, endosomal escape remains one of the major bottlenecks hampering safe and efficient delivery of nanomaterals into the cytosol. Physical approaches have been developed as well to deliver nanomaterials into the cytosol of cells by transient permeabilization of the cell membrane. Such physical methods have attracted considerable interest as they typically offer generic applicability to a variety of cell types and enable direct delivery of the exogenous materials into cytosol. Micro-injection, electroporation and sonoporation are typical examples of physical delivery methods. Laser-assisted photoporation is an alternative promising physical technique that is receiving increasing attention in the last decade. Especially in combination with enhancing nanoparticles like plasmonic NPs it seems to be a promising technology. By attaching plasmonic NPs such as gold nanoparticles (AuNPs), to the cell membrane, the photoporation effect can be achieved at lower laser intensities. This means that throughput can be increased since non-focused laser light can be used to illuminate a large amount of cells, leading to distinct phenomena such as heating of the cell membrane, acoustic shockwaves, and formation of water vapor nanobubbles (VNBs). Recently, it has been shown that VNBs can be used to permeate the plasma membrane and deliver cell impermeable compounds into the cytosol by the mechanical force induced by their expansion and collapse. A particular feature of VNB photoporation is that there is no neat heat transfer to the surrounding tissue as all energy is converted to mechanical energy. As VNB photoporation is still fairly new, the aim in **Part I** is to explore its usefulness for a number of applications, as detailed below.

In **Chapter 1**, an in-depth introduction is provided on photoporation to explain its fundamentals as well as its current applications. The various forms of laser-assisted photoporation are explained, with the two major classes being direct laser-induced photoporation and nanoparticle sensitized photoporation. The mechanisms responsible for cell membrane permeabilization are discussed, alongside technological advances and biological applications. This review chapter should give the reader the necessary background for a good understanding of the subsequent experimental chapters.

In **Chapter 2**, we report on a systematic comparison of AuNP mediated photoporation for delivering macromolecules in cells by heating of the membrane and VNB generation. While it has been shown that both heating of AuNPs and VNBs can be used to permeate the plasma membrane and deliver cell-impermeable compounds into the cytosol, it remains unclear which of both mechanisms are the most efficient. Despite the fact that it requires higher laser energies, surprisingly we find that VNBs allow more efficient cellular uptake of compounds with little or no cytotoxicity as compared to direct heating. This is attributed to the fact that bigger pores can be formed with VNB photoporation, allowing better entry of molecules that are present in the cell medium. Furthermore, we successfully show that VNB photoporation can transfect cells with siRNA more efficiently as compared to direct heating, resulting in enhanced gene silencing. Finally, we show that pores of different sizes can be created with VNB photoporation depending on the laser intensity, thus enabling size-selective delivery of macromolecules in cells.

In **Chapter 3**, we explore the use of VNB photoporation for the cytosolic delivery of contrast agents in a fast and non-toxic manner. Long-term *in vivo* imaging of cells is crucial for the understanding of cellular fate in biological processes in cancer research, immunology or in cell-based therapies such as beta cell transplantation in type I diabetes or stem cell therapy. Traditionally, cell labeling with the desired contrast agent occurs *ex vivo via* spontaneous endocytosis, which is a variable and slow process that requires optimization for each particular label-cell type combination. Following endocytic uptake, the contrast agents mostly remain entrapped in the endolysosomal compartment, which leads to label degradation, cytotoxicity and asymmetric inheritance of the labels upon cell division. We hypothesize that direct delivery of contrast agents into the cytosol by VNB photoporation can alleviate the many difficulties related to endocytic cell labeling. First, we demonstrate efficient and safe loading of fluorescent dextran and QD in different cell types by photoporation. Compared to endocytic uptake, cell loading with photoporation was 50 and 3 times more efficient for FD and QD, respectively. Combined with reduced toxicity, this enabled extended cell visualization *in vitro* over 10 cell generations for FD and 3 generations for QD. This shows that old-school labeled dextrans are excellent inexpensive and bio-compatible labels for cell tracking when delivered by photoporation as compared to much more expensive and often toxic QDs. We demonstrate for the first time that asymmetric inheritance of fluorescent labels can be avoided by cytosolic delivery *via* photoporation. As a result, the cell intensity polydispersity remains identical over multiple cell divisions, while it rapidly increases for endocytic loading (already factor 10 after 6 divisions). Finally, we show extended *in vivo* imaging of an insulin producing cell line (INS-1E cell line) labeled with Cy5.5-dextran by photoporation. Cells labeled by photoporation could be imaged up to two months instead of only two weeks in case of endocytic labeling.

In **Chapter 4**, VNB photoporation is applied to deliver antibody funcationlized QDs in living cells for subcellular labeling. The application of QDs as subcellular labels for microscopic investigation of living cells remained virtually impossible until now due to a lack of means to deliver QDs unambiguously into the cytosol of cells. We first confirmed highly efficient delivery of PEG-coated QDs into living cells. We obtained more than 80% of positive cells while the cell viability remained as high as ~85%. As a first proof-of-concept, we delivered antibody functionalized QDs in HeLa cells targeted at the microtubules. Successful labeling of the microtubules was achieved, although the contrast was rather limited likely due to the presence of too many unbound QDs in the cytosol. Although further work is needed to get better control on the quantity of QDs that are delivered into the cells, it shows that photoporation has the long-awaited capability to deliver antibody-targeted QDs into living cells for live cell microscopic visualization.

In **Chapter 5** we explored one of the most unique features of photoporation, which is to deliver exogenous materials into selected cells within a large population of cells. We developed the soft- and hardware to perform cell-selective intracellular delivery by spatially resolved nanoparticle enhanced photoporation (SNAP). Cells can be photoporated according to pre-defined patterns or in an interactive image-guided manner. The unique technological capability to deliver compounds quickly and flexibly into selected cells was applied to two challenging application. Applying SNAP to cell-selective photoporation of single neurons in automated image-guided mode, we labeled and highlighted single neurons for accurate morphological analysis. On the other hand, we used SNAP to deliver a non-toxic fluorescent marker into morphologically distinct primary normal human epidermal keratinocytes. In particular, polynucleated or mononucleated senescent cells are separately targeted so that they can be purified for further downstream molecular and functional analysis in relation to cancer research.

Part II SIZING NANOMATERIALS IN BIO-FLUIDS BY FLUORESCENCE RECOVERY AFTER PHOTOPOBLEACHING (FRAP)

FRAP is advanced well-known fluorescence microscopy method for measuring molecular mobility in biomaterials, cells and tissues. FRAP has been widely applied in the biophysical, pharmaceutical and material sciences. In a FRAP experiment, the sample is placed on a microscope and the fluorescently labeled molecules or nanoparticles are photobleached in a micron sized area by a powerful excitation pulse. The fluorescence inside the bleach area will subsequently recover at a rate that is proportional to the diffusional rate of the fluorescent species. Typically the average fluorescence intensity inside the bleach area is quantified as a function of time. A suitable mathematical model is used to fit the fluorescence recovery data, from which an average local diffusion coefficient follows. However, by calculating the average fluorescence in the bleach area, the special information is effectively lost and only the time-progression of the average intensity is taken into account. Instead, by also analyzing the spatial diffusion profile in function of time one can expect much better precision of FRAP experiments. In **Part II** we develop such a new and improved tempo-spatial FRAP model and show that it can be used for diffusion analysis of polydisperse systems. In particular the method is used to measure the hydrodynamic size of molecules in biological fluids, as explained below.

In **Chapter 6**, we describe the improved FRAP methodology that enables the measurement of continuous distributions of diffusion coefficients (cFRAP). A rectangular area is photobleached and the full tempo-spatial information available in the confocal recovery images is exploited using a dedicated theoretical recovery model to extract a continuous distribution of diffusion coefficients. It is found from simulations that cFRAP can distinguish two subpopulations if their diffusion coefficient differs by as small as a factor 3 in comparison with at least a factor of 8 for traditional FRAP methods which only consider the average fluorescence as a function of time. It is confirmed through simulations that cFRAP can correctly analyze polydisperse systems with a broad range of diffusion coefficients. The performance of cFRAP was compared experimentally to DLS as a standard technique for measuring the size distribution of polydisperse nanomaterial dispersions. Thanks to including spatial, information in the cFRAP model, the PDI of the distributions was significantly less compared to the apparent PDI measured by DLS.

In **Chapter 7**, we demonstrate the strength and versatility of cFRAP in a number of challenging sizing applications. As a first application, we used cFRAP-sizing to analyze protein aggregates in the sub 0.1 µm range in full serum. This is of current interest since protein aggregation has emerged as a key issue underlying multiple deleterious effects in the use of protein therapeutics, including loss of efficacy, altered pharmacokinetics, reduced stability and shelf life, and induction of unwanted immunogenicity. Fluorescently labeled BSA was used as a model protein, which could be analyzed by cFRAP down to a concentration of 4 µg/ml (60 nM). cFRAP-sizing could discriminate both monomers and aggregates in a single measurement, not only in buffer but also in undiluted serum. As a second application cFRAP was used to study the permeability of the intestinal and vascular barriers in mice in unprecedented detail. The classic protocol requires the separate

administration of dextrans of different molecular weights, each time in a different animal. The leakiness of the barrier is then evaluated by quantifying the fluorescence intensity for each dextran size in the relevant fluid (prepared from the receptor tissue). Instead, by intravenous administration of a mixture of five FDs covering a broad range of sizes from about 1-100 nm, here we demonstrate that a single experiment is sufficient when combined with cFRAP-sizing. This results in 5 times less animals compared with the classic fluorimetry method. At the same time unprecedented detailed information is obtained on the continuous size range of probes that can leak through the barrier. Using cFRAP-sizing we even succeeded in analyzing FD leakage in microliter samples of cerebrospinal fluid, notwithstanding that the fluorescence was very weak. Both applications show that cFRAP is a promising new method to measure the size distribution of molecules and nanomaterials in undiluted biological fluids.

Samenvatting

Deze scriptie bestaat uit twee afzonderlijke delen zoals hieronder beschreven.

Deel I INTRACELLULAIRE AFGIFTE VAN BIOFARMACEUTICA EN CONTRASTAGENTIA D.M.V. WATERDAMP NANOBUBBEL FOTOPORATIE

Afgifte van exogene materialen in het cytosol van levende cellen is een belangrijke stap voor vele toepassingen in celbiologie en farmacie. Zo is de intracellulaire afgifte van DNA noodzakelijk voor het bestuderen van genexpressie, de analyse van mutaties en gentherapie. Analoog is de aflevering van mRNA in cellen van belang voor het onderzoeken van celbiologische functies, terwijl small interfering RNA (siRNA) geïntroduceerd wordt voor sequentie-specifieke genonderdrukking. Naast biologische moleculen is er evenzeer interesse in de intracellulaire afgifte van contrastagentia. Zo wordt het gebruik van anorganische nanopartikels onderzocht als contrastagentia voor beeldvorming, waaronder superparamagnetische ijzeroxide nanopartikels en gadolinium complexen voor MRI, naast quantum dots en opconversie nanopartikels voor beeldvorming op basis van fluorescentie. Een aantal van dergelijke exogene materialen kunnen via een virale drager in cellen binnengebracht worden. Daarbij zijn echter immunogeniciteit en toxiciteit een concrete zorg. Niet-virale dragers, gebaseerd op lipiden of polymeren, vormen daartoe een alternatief. In het algemeen zorgen die echter voor opname in de cellen via endocytose zodat ontsnapping uit endosomen een noodzakelijke stap is. De ontsnapping uit endosomen blijft echter tot op vandaag een van de belangrijkste hinderpalen voor niet-virale dragers, wat efficiënte afgifte in het cytosol verhindert. Er zijn ook fysische methodes ontwikkeld voor intracellulaire afgifte van exogene nanomaterialen d.m.v. een transiënte permeabilisatie van de celmembraan. Dergelijke fysische methodes hebben heel wat interesse gewekt doordat ze algemeen toepasbaar zijn op een grote variëteit aan celtypes. Welbekende voorbeelden hiervan zijn microinjectie, electroporatie en sonoporatie. Een alternatief hierop dat recent aan populariteit wint is laser-geïnduceerde fotoporatie. Voornamelijk in combinatie met versterkende nanopartikels, zoals plasmonische nanomaterialen, lijkt het een bijzonder beloftevolle technologie. Door plasmonische NP, zoals goud nanopartikels (AuNP), aan de celmembraan te koppelen kan het fotoporatie-effect bekomen worden bij lagere laserintensiteit. Daardoor kan de 'throughput' toenemen aangezien niet-gefocust laserlicht gebruikt kan worden om vele cellen tegelijkertijd te belichten waarbij fenomenen optreden zoals opwarming van de celmembraan, acoustische schokgolven en de vorming van waterdamp nanobubbels (VNB). Recent werd aangetoond dat VNB gebruikt kunnen worden om poriën te vormen in de celmebraan d.m.v. de mechanische kracht veroorzaakt door hun expansie en implosie, zodat cel-impermeabele componenten vervolgens tot in het cytosol kunnen doordringen. Een bijzondere eigenschap van VNB fotoporatie is dat er geen netto transfer is van warmte in de omgeving doordat alle energie omgezet wordt tot mechanische energie. **Deel I** van deze scriptie heeft tot doel om VNB fotoporatie als relatief nieuwe technologie verder te exploreren in verscheidene applicaties, zoals hieronder in meer detail besproken wordt.

In **Hoofdstuk 1** wordt een gedetailleerde introductie gegeven op zowel de basisprincipes van fotoporatie als de toepassingen van deze techniek. Hierbij komen de verschillende vormen van laser-gemedieerde fotoporatie aan bod, met als belangrijkste categorieën de zogenaamde directe laser-fotoporatie en NP-versterkte fotoporatie. De mechanismen worden besproken die betrokken zijn bij permeabilisatie van de celmembraan, naast technologische ontwikkelingen en biologische applicaties. Dit hoofdstuk heeft zodoende tot doel de lezer een degelijke achtergrond te geven van een aantal basisconcepten die een goed begrip van de daaropvolgende experimentele hoofdstukken moeten geven.

In **Hoofdstuk 2** rapporteren we over een systematische vergelijking van AuNP gemedieerde fotoporatie voor de intracellulaire aflevering van macromoleculen d.m.v. opwarming van AuNP versus VNB generatie. Hoewel aangetoond werd dat beide fotoporatiemechanismes kunnen gebruikt worden, blijft het onduidelijk welke van beide het meest efficiënt is. Ondanks dat hogere laserintensiteit benodigd is, vinden we VNB fotoporatie de meest efficiënte afgifte van moleculen in het cytoplasma mogelijk maakt met bijna verwaarloosbare cytotoxiciteit. Dit feit is toe te schrijven doordat grotere poriën gevormd worden met VNB fotoporatie waardoor de inwaartse flux van moleculen vergroot. Bijkomend wordt aangetoond dat VNB fotoporatie efficiëntere transfectie van cellen met siRNA mogelijk maakt met verhoogde genonderdrukking. Tenslotte tonen we aan dat poriën van verschillende groottes gevormd kunnen worden met VNB fotoporatie afhankelijk van de laserintensiteit. Dit maakt grootte-afhankelijk intracellulaire afgifte van moleculen mogelijk.

In **Hoofdstuk 3** exploreren we het gebruik van VNB fotoporatie voor de cytosolaire aflevering van contrastagentia op een snelle en niet-toxische manier. Langdurige *in vivo* beeldvorming van cellen is van cruciaal belang voor een goed begrip van de rol van cellen bij biologische processen in kanker en immuun respons, maar ook voor celtherapieën zoals stamceltherapie of transplantatie van betacellen i.g.v. diabetes type I. Traditioneel gebeurt het labelen van cellen met contrastagentia *ex vivo* d.m.v. spontane endocytische opname, hetgeen een variabel en traag proces is dat geoptimaliseerd dient te worden voor iedere combinatie van label en celtype. Na endocytose zitten de contrastagentia grotendeels vast in endosomen, hetgeen uiteindelijk kan resulteren in afbraak van het label, cytotoxiciteit en asymmetrische verdeling van de labels over dochtercellen na celdeling. Onze hypothese is dat directe aflevering van contrastagentia in het cytosol met VNB fotoporatie een oplossing kan bieden voor deze problemen bij endocytische opname. In dit hoofdstuk tonen we eerst de intracellulaire afgifte aan van fluorescent dextraan (FD) en QDs in verschillende celtypes met fotoporatie. In vergelijking met endocytische opname blijkt fotoporatie te resulteren in een 50 en 3 keer hogere opname van respectievelijk FD en QD. Gecombineerd met gereduceerde cytotoxiciteit resulteert dit in substantieel verlengde tijd waarover de cellen gevisualiseerd kunnen worden, zijnde 10 celgeneraties voor FD gelabelde cellen, terwijl dit 3 generaties is voor QD gelabelde cellen. Dit toon dat de welgekende fluorescente dextranen excellente en relatief goedkope biocompatibele labels zijn voor celvisualisatie indien afgeleverd via fotoporatie. Bijkomend tonen we in dit hoofdstuk voor het eerst aan dat asymmetrische verdeling van labels over dochtercellen vermeden kan worden met fotoporatie. Een belangrijk gevolg hiervan is dat de polydispersiteit van celintensiteiten identiek gelijk blijft over opeenvolgende celgeneraties, terwijl dit snel toeneemt i.g.v. endocytische opname (toename met factor 10 na 6 celgeneraties). Tenslotte tonen we verlengde in vivo beeldvorming aan van een insuline producerende cellijn (INS-1E cellijn) met Cy5.5 dextraan d.m.v. fotoporatie. Deze cellen konden gevisualiseerd worden tot twee maand na transplantatie, terwijl dit beperkt bleef tot twee weken bij endocytische labeling.

In **Hoofdstuk 4** wordt VNB fotoporatie toegepast om QD gefunctionaliseerd met antilichamen af te leveren in cellen voor subcellulaire labeling. Het gebruik van QD als subcellulaire merkers in levende cellen bleef tot nog toe onmogelijk door een gebrek aan een methode om QD in het cytosol af te leveren. Vooreerst bevestigen we dat gepegyleerde QD in HeLa cellen kunnen afgeleverd worden d.m.v. VNB fotoporatie. Daarbij bereiken we >80% positieve cellen met een celviabiliteit van ~85%. Vervolgens brengen we antilichaam gefunctionaliseerde QD in de cellen gericht tegen de microtubuli. De microtubuli werden succesvol gelabeld hoewel het contrast eerder beperkt was, vermoedelijk door een overmaat van ongebonden QD in het cytosol. Hoewel verdere optimalisatie nodig is om de hoeveelheid afgeleverde QD beter te controleren, tonen deze preliminaire resultaten aan dat fotoporatie de langverwachte mogelijkheid biedt om QDs als subcellulaire labels in levende cellen te gebruiken.

In **Hoofdstuk 5** exploreren we één van de meest unieke eigenschappen van fotoporatie, namelijk het intracellulair afleveren van exogene materialen in een selectie van cellen binnen een grote celpopulatie. We ontwikkelen hard- en software om cel-selectieve aflevering te realiseren d.m.v. spatiaal geresolveerde nanopartikel versterkte fotoporatie (SNAP). De technologie laat toe om cellen te fotoporeren volgens vooraf gedefinieerde patronen of volgens een beeld-gebaseerde interactieve manier. De unieke mogelijkheid om materialen snel en flexibel in geselecteerde cellen af te leveren wordt toegepast op twee uitdagende applicaties. Geselecteerde neuronale cellen worden selectief gefotoporeerd met een fluorescente merker om accurate morfologische analyse van deze cellen mogelijk te maken. Daarnaast gebruiken we SNAP om een niet-toxische merker in een morfologisch te onderscheiden subpopulatie te brengen van primaire normale humane epidermale keratinocyten. Meer bepaald werden hetzij de polynucleaire of mononucleaire cellen selectief gelabeld voor purificatie. Dit is noodzakelijk om bijkomende functionele en moleculaire analyses te kunnen uitvoeren op deze subpupulaties van cellen om zo hun rol in de vorming van neoplasmen en kanker te kunnen ontrafelen.

Deel II HET METEN VAN DE GROOTTE VAN NANOMATERIALEN IN LICHAAMSVOCHTEN D.M.V. FLUORESCENTIEHERSTEL NA FOTOBLEKING (FRAP)

FRAP is een gekende fluorescentie microscopiemethode om de mobiliteit van moleculen te meten in biomaterialen, cellen en weefsels. FRAP is doorheen de jaren frequent toegepast in biofysisch, farmaceutisch en materiaalkundig onderzoek. In een FRAP experiment wordt het staal op een microscoop geplaatst waarin vervolgens in een micrometer grote regio de fluorescent gelabelde moleculen gefotobleekt worden met een krachtige lichtpuls. Na fotobleking zal de fluorescentie zich geleidelijk herstellen in de gebleekte zone met een snelheid die proportioneel is met de diffusiesnelheid van de gelabelde moleculen. Traditioneel wordt daarbij de gemiddelde fluorescentie-intensiteit in de gebleekte zone gekwantificeerd in functie van de tijd. Met een passend mathematisch model wordt vervolgens het fluorescentieherstel geanalyseerd om zodoende de lokale diffusiecoëfficiënt te bepalen. Doordat echter de gemiddelde fluorescentie-intensiteit berekend wordt, gaat de spatiale informatie van het diffusieprofiel grotendeels verloren. Het gevolg is dat FRAP analyses weinig precies zijn en daardoor niet geschikt om polydisperse systemen te analyseren. We stellen ons daarom in dit deel van de thesis tot doel een FRAP methode te ontwikkelen die gebruik maakt van de volledige temporele en spatiale informatie in FRAP experimenten. Dit moet een hogere precisie toelaten en zodoende de analyse van polydisperse systemen. In het bijzonder wensen we daarmee een methode te bekomen waarmee, via diffusie-analyse, de groottedistributie van nanomaterialen in biologische vloestoffen bepaald kan worden van 1 tot 100 nm.

In **Hoofdstuk 6** beschrijven we de ontwikkeling van deze verbeterde FRAP methodologie waarmee polydisperse systemen geanalyseerd kunnen worden in termen van een continue distributie van diffusiecoëfficiënten (cFRAP). De methode is gebaseerd op de fotobleking van een rechthoekige regio waarvoor we een theoretisch model ontwikkeld hebben waarmee de spatiale diffusieprofielen geanalyseerd kunnen worden in functie van de tijd. Vertrekkend van simulaties blijkt dat cFRAP twee componenten van mekaar kan onderscheiden als hun diffusiecoëfficiënt een factor 3 verschillend is. Ter vergelijking, met traditionele FRAP gebaseerd op louter tijdsinformatie is dit een factor 8. Verdere simulaties en experimenten tonen aan dat cFRAP geschikt is om continu-polydisperse systemen te analyseren van 1-100 nm grootte. De performantie van cFRAP wordt vergeleken met DLS als standaardtechniek voor het meten van groottedistributies van polydisperse nanomaterialen. Daarbij wordt gevonden dat cFRAP distributies een kleinere PDI vertonen dan bij DLS wegens de verhoogde precisie dankzij tempo-spatiale analyse van het diffusieproces.

In **Hoofdstuk 7** tenslotte tonen we de sterke en veelzijdigheid van cFRAP aan via toepassing van de techniek in enkele uitdagende applicaties. Vooreerst gebruiken we cFRAP om sub 0.1 µm proteïneaggregaten te analyseren in vol serum. Dit is van belang aangezien proteïneaggregatie tegenwoordig beschouwd wordt als één van de belangrijke nadelen van eiwittherapeutica. Aggregatie van therapeutische eiwitten kan namelijk leiden tot verlies van het therapeutisch effect, gewijzigde farmacokinetiek, kortere bewaartijd en immunogeniciteit. We gebruiken fluorescent gelabeld BSA als model, waarbij concentraties vanaf 4 µg/ml (60 nM) geanalyseerd kunnen worden met cFRAP. Met cFRAP kunnen we monomeren van aggregaten onderscheiden in een enkele meting, niet alleen in buffer maar zelfs in onverdund vol serum. Vervolgens passen we cFRAP toe om de permeabiliteit van de intestinale en vasculaire barrière te bepalen in muizen. Het klassieke protocol vergt administratie van afzonderlijke FD met verschillend moleculair gewicht, telkens in andere proefdieren. De permeabiliteit van de barrière wordt dan gekwantificeerd door de intensiteit van elk van de FD te meten in de relevante vloeistoffen (geprepareerd van het relevant receptorweefsel). Met cFRAP daarentegen kan het mengsel van al deze FD tegelijk in éénzelfde proefdier ingebracht worden, om vervolgens de volledige groottedistributie van FD te bepalen in de vloeistof van het receptorweefsel. Concreet betekent dit dat 5 keer minder proefdieren benodigd zijn i.v.m. de klassieke methode. Tegelijkertijd wordt continue informatie verkregen over de grootte van FD die door de barrière doorgekomen zijn, daar waar de klassieke methode enkel informatie geeft over de discrete groottes. Met cFRAP zijn we zelfs in staat analyses te doen op microliter stalen van cerebrospinaal vocht, hoewel de fluorescentie bijzonder zwak was. Beide toepassingen tonen aan dat cFRAP een beloftevolle nieuwe methode is om de groottedistributie van moleculen en nanomaterialen mogelijk te maken in onverdunde biologische vloeistoffen.

Appendix A

User’s guide of cFRAP matlab code

User's guide for Matlab code

In this guide it is explained how to use the custom written Matlab code for analysis of FRAP recovery images and to obtain the diffusion coefficient or size distributions. The user's guide includes the following sections: description of the structure of the main code, the procedure for adding the cFRAP code to the Matlab program, examples on simulated and experimental FRAP images.

1. Structure of code

The cFRAP code consists of a main routine which is used to call three main subroutines: the image loading routine, rFRAP and cFRAP fitting routines, and the data output and saving routines. Each routine is written as a separate M-file:

Main routine M-file : rFRAP_MEM_GUI.m . A flow chart of the main routine is presented in **Fig. 1**. When the main routine is running, a window named 'rFRAP_MEM_GUI' will open (**Fig. 3**). The FRAP image files and parameters are required to be filled out in this window (for details please refer to the examples further on). The main routine calls the subroutines to load the FRAP images and starts with performing a one component least squares fitting to obtain reasonable initial values for D, K_0, k and r^2 that are needed for further cFRAP analysis. Before cFRAP analysis, it is verified if χ^2 can arrive at a value $<M+\sqrt{2M}$ when performing a classic least-squares fit of the multi-component rFRAP model. If so, the main routine continues by calling the subroutine for cFRAP analysis. Otherwise, it stops and asks for a different set of parameters or better quality FRAP movies. After finishing cFRAP analysis, the resulting distributions of the diffusion coefficient is saved in 'csv' format.

Image loading M-files: bfopen.m, importdata.m and load_image.m. These functions are used to load the FRAP images that should be either in Nikon '.nd2', '.mat' or '.tif' format.

One component rFRAP fitting M-file: rFrapFit.m. This M-file is needed to perform a classic least-squares fitting of the FRAP images according to the one component rFRAP model as reported earlier.

Multicomponent rFRAP fitting M-file: FRAP_leastsquare.m. The function is used to perform a classic least-squares fit of the FRAP images with the multicomponent rFRAP model.

cFRAP fitting M-file: FRAP_MEM.m. This function performs cFRAP analysis of the FRAP images. First the recovery data is normalized to the fluorescence intensity before bleaching. Correction for laser fluctuations and bleaching during imaging is performed by dividing the pixels of each recovery image by the average value from one or more reference background regions in the same image. Data analysis is done by fitting of the cFRAP model (Eq. (12)) to the average fluorescence intensity values in rectangular ring-shaped areas of into which the ROI is divided. To accelerate convergence of the fitting routine, initial values of the parameters D, K_0, k and r^2 are set according to the results from the 1 component least square fitting. The cFRAP procedure then continues with maximizing the entropy according to Eq. (10) under the constraint $M - \sqrt{2M} \leq \chi^2 \leq M + \sqrt{2M}$. cFRAP analysis is performed on the values of all ring-shaped in the ROI over the entire time lapse movie.

Data saving M-file: mat2csv_wheaders.m. This function is able to output the data as a 'csv' file.

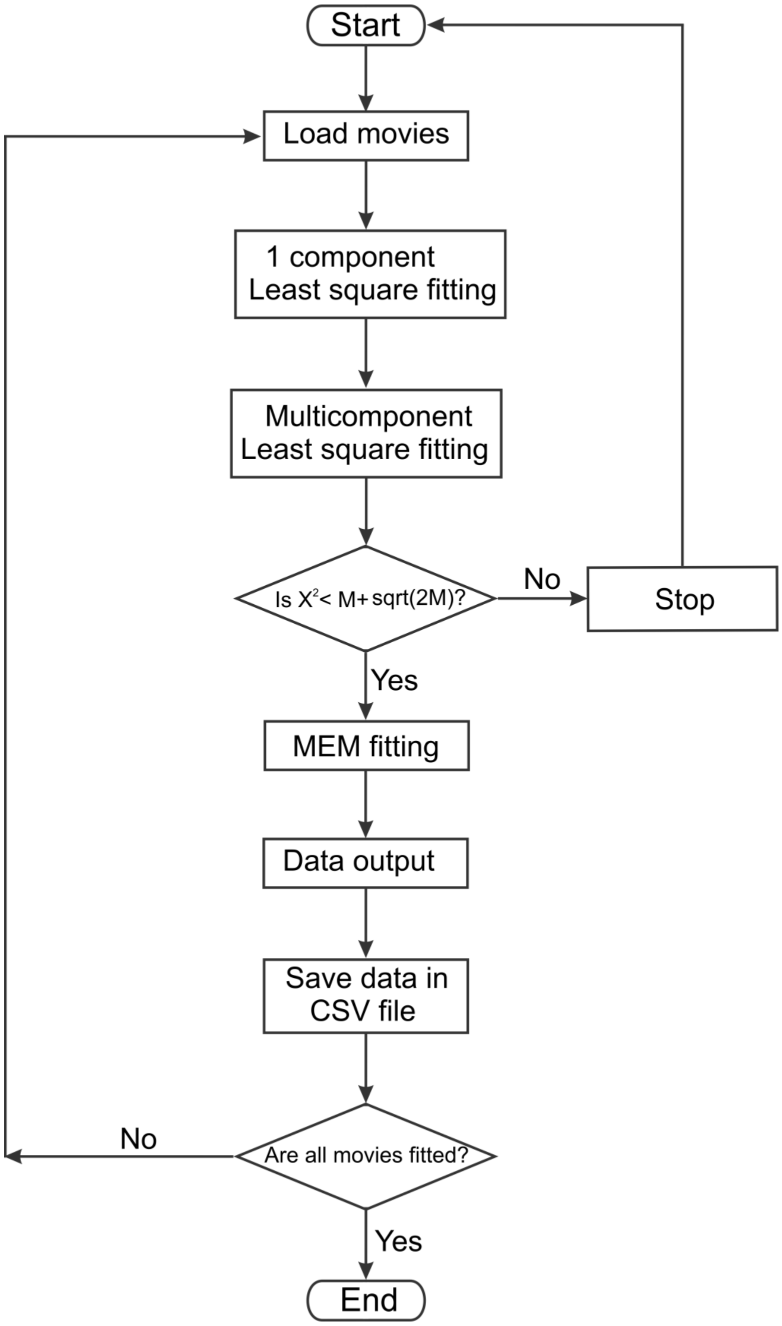

Figure 1. Flow chart of the cFRAP Matlab code.

2. Adding the cFRAP source code to Matlab

Matlab software version of R2010b or above is required. Uncompressing the zip file of "matlab code soure package.zip" and copy the fold of "cFRAP-v3.0" , to e.g. "C:\Program Files\MATLAB\R2010b\". Run Matlab and add this folder to the Matlab search path (e.g. File->Set Path->Add Folder->Save) .

3. Examples of analysing FRAP images by cFRAP

3.1 Example 1: analyse simulated rFRAP images with the cFRAP code

Step 1: Simulate rFRAP images

Start Matlab software and input "sim_rFRAP_Im" in the command window to open the GUI for the simulation of rFRAP images (**Fig. 2a**).

Note : the "Simulate" button will start calculation of the simulated images; "Display" can be used to display the selected images. The slider can be used to display a particular frame number.

Clicking the 'Simulate' button will open a window where the desired parameters of the simulated images can be filled out (**Fig. 2b**). By clicking 'OK' the simulated images will be calculated according to Eq. (2). For the example shown in **Fig. 2b**, an rFRAP time lapse movie will be calculated for single component system with a diffusion coefficient of 5 μm^2/s. The movie will consist of 30 recovery frames and with 1s intervals. The simulated image can be viewed by clicking the 'Display' button.

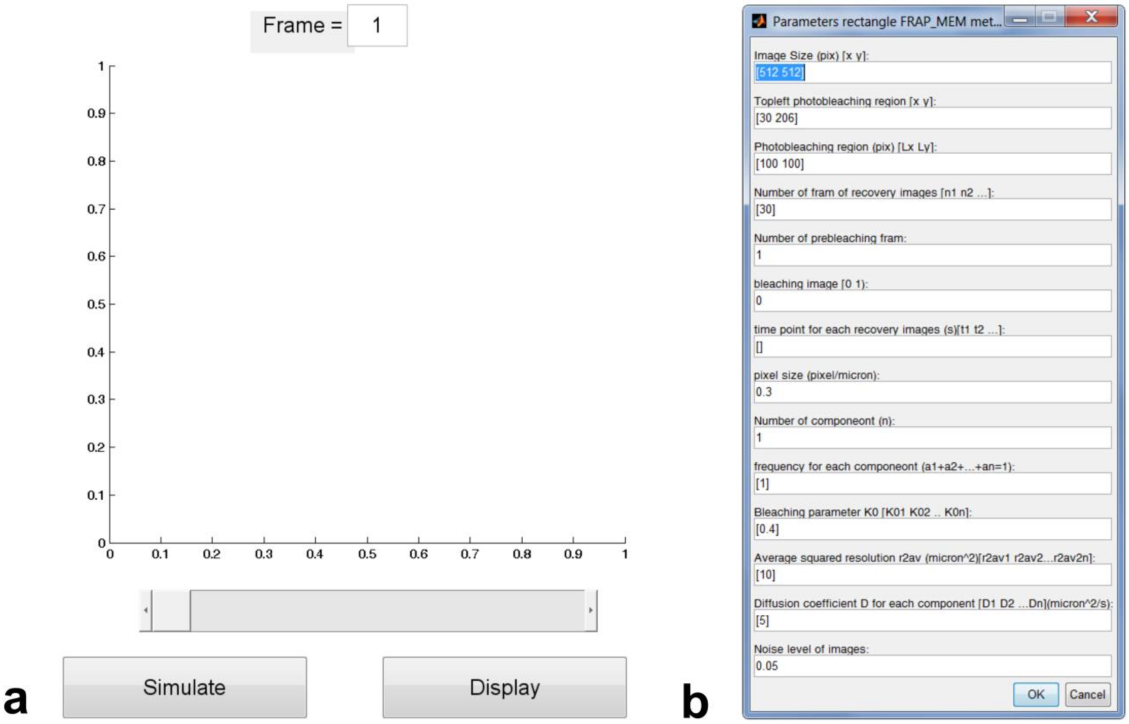

Image Size (pix) [x y]: [512 512]
Topleft photobleaching region [x y]: [30 206]
Photobleaching region (pix) [Lx Ly]: [100 100]
Number of fram of recovery images [n1 n2 ...]: [30]
Number of prebleaching fram: 1
bleaching image [0 1): 0
time point for each recovery images (s)[t1 t2 ...]: []
pixel size (pixel/micron): 0.3
Number of componeont (n): 1
frequency for each componeont (a1+a2+...+an=1): [1]
Bleaching parameter K0 [K01 K02 .. K0n]: [0.4]
Average squared resolution r2av (micron^2)[r2av1 r2av2...r2av2n]: [10]
Diffusion coefficient D for each component [D1 D2 ...Dn](micron^2/s): [5]
Noise level of images: 0.05

Figure 2. GUI for simulation and viewing of FRAP images (**a**). This window will pop up when clicking the 'Simulate' button and is designed to input all parameters that are required for the simulation of FRAP images (**b**).

Step 2: Analysis of simulated rFRAP images

A. Type "rFRAP_MEM_GUI" in the Matlab command window to open the main GUI for cFRAP analysis (**Fig. 3a**).

B. Select the recovery images simulated in previous step by clicking 'Select Files' and the name of the file will be shown in list box after selection.

C. The radio button "Simulated Images" should be selected for analyzing simulated recovery images. A noise level should be filled out as the percentage of Gaussian noise that will be added to the simulated images before applying cFRAP analysis. The radio button "Is Multicomponent LS fitting" should be selected to check if χ^2 can reach the required small value (see above).

D. Click the 'Analyse' button to open the input window shown in **Fig. 3b**. The required parameters should be filled out before clicking 'OK' to start the analysis.

E. After finishing the calculation, the data is saved as 'csv' file. The diffusion coefficient distribution can be displayed by selecting the csv file in the list-box as shown in **Fig. 3c**.

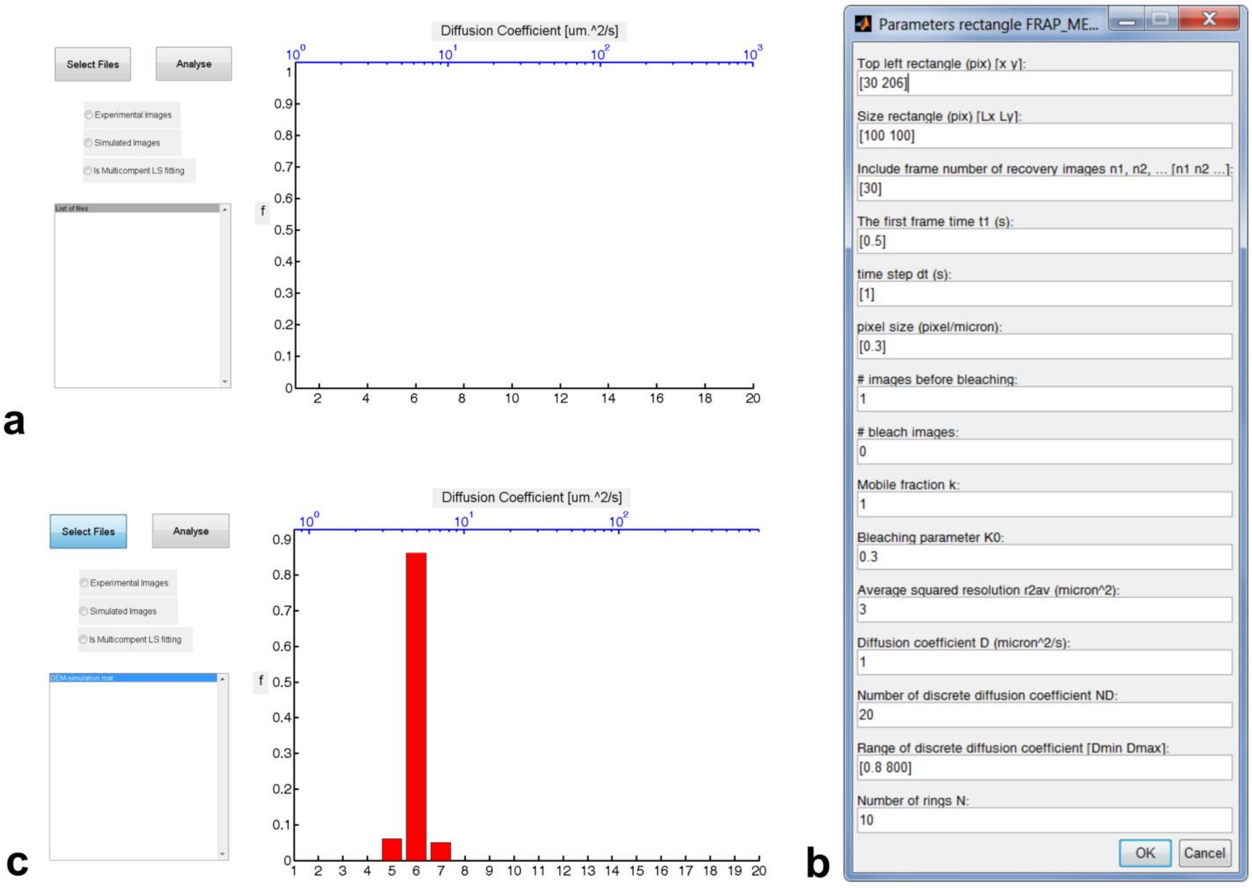

Top left rectangle (pix) [x y]: [30 206]

Size rectangle (pix) [Lx Ly]: [100 100]

Include frame number of recovery images n1, n2, ... [n1 n2 ...]: [30]

The first frame time t1 (s): [0.5]

time step dt (s): [1]

pixel size (pixel/micron): [0.3]

images before bleaching: 1

bleach images: 0

Mobile fraction k: 1

Bleaching parameter K0: 0.3

Average squared resolution r2av (micron^2): 3

Diffusion coefficient D (micron^2/s): 1

Number of discrete diffusion coefficient ND: 20

Range of discrete diffusion coefficient [Dmin Dmax]: [0.8 800]

Number of rings N: 10

Figure 3. Main GUI window for cFRAP analysis (**a**). A pop-up window is used to input the required parameters for cFRAP analysis (**b**). The diffusion coefficient distribution is displayed in the GUI window when cFRAP analysis is complete (**c**).

3.2 Example 2: cFRAP analysis of experimental rFRAP images

A. Type "slop_intercept" in the Matlab command window to open the GUI for calculation of fluorescence intensity variance as a function of average fluorescence intensity (required for Eq. (14)) to calculate the variance of each ROI divided ring region. In the equation, a and b are constant parameters and they can be determined by a series of images with various laser intensities in a homogeneous solution of the fluorescent species with identical instrumental settings as will be the final FRAP experiment as described before. The average and variance of fluorescence intensity for each ring can be calculated and plotted as variance as a function of the average of fluorescence of intensity. The slope (a parameter) and intercept (b parameter) of a linear fit through the data points will yield the constant of a and b. The program will yield the slope and intercept values which are used to calculate the variance of each ring region into which the ROI is divided (**Fig. 4a**).

B. Load the movies recorded with different laser intensities and calculate the parameters slope and intercept by clicking the ‘calculate’ button.
C. Type “rFRAP_MEM_GUI” in the Matlab command window to open GUI for rFRAP_MEM analysis (**Fig. 3a**) and load the experimental FRAP recovery images. Select the ‘Experimental images’ radio button and fill out the slope and intercept values into the pop-up interface window. Select the radio button “Is Multicompent LS fitting” to check if χ^2 can reach the required small value (see above). .
D. When cFRAP analysis is complete, the result is saved as a ‘csv’ file. The diffusion coefficient distribution can be displayed by selecting the file in the list-box as shown in **Fig. 4b**.

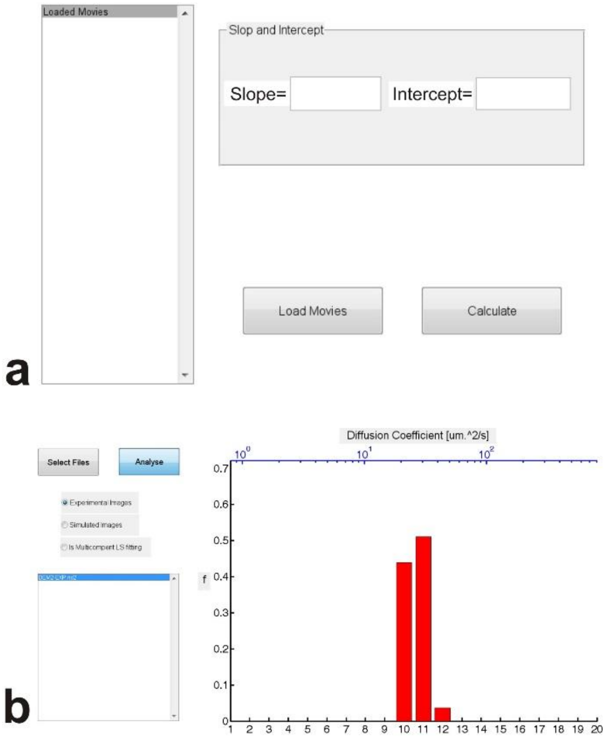

Figure 4. GUI for calculating the slope and intercept in Eq. (14). (**a**) These two parameters are required for subsequent cFRAP analysis. (**b**) The diffusion coefficient distribution can be displayed by selecting the file in the list-box.

Appendix B

Curriculum Vitae

Ghent University
Department of Pharmaceutics
Ottergemsesteenweg 460
Gent, Flanders, 9000
Belgium

ranhua.xiong@gmail.be
Phone: +32 (0)9 264.80.74
Mobile: +32486137408
Fax: +32 (0)9 264.81.89
Website: www.biofys.ugent.be

Name: Ranhua Xiong
Gender: Male
Date of birth: October 20, 1983
Place of birth: Jiangxi, China
Nationality: Chinese

Education

Mar 2012 – Present **Ghent University**
PhD, Pharmaceutics, Biophotonic
Ghent, East Flanders, Belgium

Oct 2010 – Feb 2012 **Ghent University**
PhD, Low temperature plasma
Ghent, East Flanders, Belgium

Sep 2007 – Jun 2010 **University of Science and Technology of China**
MS, Fluid Mechanics
Hefei, Anhui, China

Sep 2003 – Jun 2007 **Anhui University of Science and Technology**
BSc, Mechanics
Huainan, Anhui, China

Research Experience

Mar 2012 – Present	**PhD Candidate** Ghent University, Department of Pharmaceutics Ghent, East Flanders, Belgium Intracellular delivery by nanoparticle sensitized photoporation and sizing nanomaterials in bio-fluids by FRAP
Oct 2010 – Feb 2012	**PhD Candidate** Ghent University, Department of Applied Physics Ghent, East Flanders, Belgium Low temperature plasma in experiment and numerical simulation.
Sep 2007 – Jul 2010	**Master's Student** University of Science and Technology of China, Department of Modern Mechanics Hefei, Anhui, China Multiphase flow in experiment and simulation.

Publication Highlights

Ranhua Xiong, Roosmarijn E Vandenbroucke, Katleen Broos, Toon Brans, Elien Van Wonterghem, Claude Libert, Jo Demeester, Stefaan C De Smedt, Kevin Braeckmans: *Sizing nanomaterials in bio-fluids by cFRAP enables protein aggregation measurements and diagnosis of bio-barrier permeability*. **Nature Communications** 09/2016; 7. DOI:10.1038/ncomms12982 (**IF$_{2015}$=11.329**)

Ranhua Xiong, Freya Joris, Sayuan Liang, Riet De Rycke, Saskia Lippens, Jo Demeester, Andre G Skirtach, Koen Raemdonck, Uwe Himmelreich, Stefaan C. De Smedt, Kevin Braeckmans: *Cytosolic delivery of nano-labels prevents their asymmetric inheritance and enables extended quantitative in vivo cell imaging*. **Nano Letters** 09/2016; DOI:10.1021/acs.nanolett.6b01411 (**IF$_{2015}$=13.779**)

Ranhua Xiong, Koen Raemdonck, Karen Peynshaert, Ine Lentacker, Ine De Cock, Joseph Demeester, Stefaan C De Smedt, Andre G Skirtach, Kevin Braeckmans: *Comparison of Gold Nanoparticle Mediated Photoporation: Vapor Nanobubbles Outperform Direct*

Heating for Delivering Macromolecules in Live Cells. **ACS Nano** 05/2014; 8(6). DOI:10.1021/nn5017742 (**IF$_{2015}$=13.334**)

Journal Publication List

1. **Ranhua Xiong**, Roosmarijn E Vandenbroucke, Katleen Broos, Toon Brans, Elien Van Wonterghem, Claude Libert, Jo Demeester, Stefaan C De Smedt, Kevin Braeckmans: *Sizing nanomaterials in bio-fluids by cFRAP enables protein aggregation measurements and diagnosis of bio-barrier permeability*. Nature Communications 09/2016; 7. DOI:10.1038/ncomms12982
2. **Ranhua Xiong**, Freya Joris, Sayuan Liang, Riet De Rycke, Saskia Lippens, Jo Demeester, Andre G Skirtach, Koen Raemdonck, Uwe Himmelreich, Stefaan C. De Smedt, Kevin Braeckmans: *Cytosolic delivery of nano-labels prevents their asymmetric inheritance and enables extended quantitative in vivo cell imaging*. Nano Letters 09/2016; DOI:10.1021/acs.nanolett.6b01411
3. **Ranhua Xiong**, Sangram Keshari Samal, Jo Demeester, Andre G. Skirtach, Stefaan C. De Smedt, Kevin Braeckmans: *Laser-assisted photoporation: fundamentals, technological advances and applications*. Advances in Physics: X 09/2016; DOI:10.1080/23746149.2016.1228476
4. **Ranhua Xiong**, Koen Raemdonck, Karen Peynshaert, Ine Lentacker, Ine De Cock, Joseph Demeester, Stefaan C De Smedt, Andre G Skirtach, Kevin Braeckmans: *Comparison of Gold Nanoparticle Mediated Photoporation: Vapor Nanobubbles Outperform Direct Heating for Delivering Macromolecules in Live Cells*. ACS Nano 05/2014; 8(6). DOI:10.1021/nn5017742
5. **Ranhua Xiong**, Hendrik Deschout, Jo Demeester, Stefaan C De Smedt, Kevin Braeckmans: *Rectangle FRAP for Measuring Diffusion with a Laser Scanning Microscope*. Methods in molecular biology (Clifton, N.J.) 01/2014; 1076. DOI:10.1007/978-1-62703-649-8_18
6. **Ranhua Xiong**, Stefaan J Soenen, Kevin Braeckmans, Andre G Skirtach: *Towards Theranostic Multicompartment Microcapsules: in-situ Diagnostics and Laser-induced Treatment*. Theranostics 02/2013; 3(3). DOI:10.7150/thno.5846
7. **Ranhua Xiong***, Qing Xiong, Anton Yu. Nikiforov, Patrick Vanraes, Christophe Leys: *Influence of helium mole fraction distribution on the properties of cold atmospheric pressure helium plasma jets*. Journal of Applied Physics 08/2012; 112(3). DOI:10.1063/1.4746700
8. **Ranhua Xiong***, Anton Yu. Nikiforov, Patrick Vanraes, Christophe Leys: *Characteristics of an underwater direct current discharge in bubbles and the temperature distribution in the bubbles*. Physics of Plasmas 02/2012; 19(2). DOI:10.1063/1.3680615
9. **Ranhua Xiong***, Anton Nikiforov, Patrick Vanraes, Christophe Leys: *Hydrogen Peroxide Generation by DC and Pulsed Underwater Discharge in Air Bubbles*. Journal of Advanced Oxidation Technologies 01/2012; 15(1).
10. Dawei Hua, Zhongche Liu, Fang Wang, Buhong Gao, Fei Chen, Qilu Zhang, **Ranhua Xiong**, Jingquan Han, Sangram Keshari Samal, Stefaan C. De Smedt, Chaobo Huang: *pH Responsive polyurethane (core) and cellulose acetate phthalate (shell) electrospun fibers for intravaginal drug delivery*. Carbohydrate Polymers 06/2016; 151. DOI:10.1016/j.carbpol.2016.06.066

11. Wenjing Ma, Qilu Zhang, Dawei Hua, **Ranhua Xiong**, Juntao Zhao, Weidong Rao, Shenlin Huang, Xianxu Zhan, Fei Chen, Chaobo Huang: *Electrospun fibers for oil-water separation*. RSC Advances 01/2016; 6(16). DOI:10.1039/C5RA27309A
12. Rita S Santos, George R Dakwar, **Ranhua Xiong**, Katrien Forier, Katrien Remaut, Stephan Stremersch, Nuno Guimarães, Sílvia Fontenete, Jesper Wengel, Marina Leite, Céu Figueiredo, Stefaan C De Smedt, Kevin Braeckmans, Nuno F Azevedo: *Effect of Native Gastric Mucus on in vivo Hybridization Therapies Directed at Helicobacter pylori*. Molecular Therapy - Nucleic Acids 12/2015; 4(12). DOI:10.1038/mtna.2015.46
13. Xiaoyun Yang, Lennert Steukers, Katrien Forier, **Ranhua Xiong**, Kevin Braeckmans, Kristien Van Reeth, Hans Nauwynck: *A Beneficiary Role for Neuraminidase in Influenza Virus Penetration through the Respiratory Mucus*. PLoS ONE 10/2014; 9(10). DOI:10.1371/journal.pone.0110026
14. Miaomiao Zhu, Jingquan Han, Fang Wang, Wei Shao, **Ranhua Xiong**, Qilu Zhang, Hui Pan, Yong Yang, Sangram Keshari Samal, Feng Zhang, Chaobo Huang, *Electrospun Nanofibers for Effective Air Filtration*. Macromolecular Materials and Engineering (Accepted)

*Corresponding author

Patent

K. Braeckmans, S. De Smedt, J. Demeester, S.K. Samal, ***R. Xiong****, S. Szunerits, R. Boukherroub*

Carbon-based particles for vapor bubble generation

Submission number: EP15176560.9

Priority Date: 14.07.2015

Filling date: 14/07/2015

UGent ref.: P2015/032 - GOBA

Conference Proceedings

Ranhua Xiong, Koen Raemdonck, Karen Peynshaert, Ine Lentacker, Ine De Cock, Jo Demeester, Stefaan C. De Smedt, Andre G. Skirtach, Kevin Braeckmans,2015, *Laser-induced vapor nanobubbles for efficient delivery of macromolecules in live cells*. SPIE. Photonics WEST BIOS 2015, San Francisco, USA (Invited oral presentation, represent Prof. Kevin Braeckmans)

Ranhua Xiong, Stefaan C. De Smedt, Kevin Braeckmans，2014，Comparison of Gold Nanoparticle Mediated Photoporation: Vapour Nanobubbles Outperform Direct Heating for Delivering Macromolecules in Live Cells，NB-Photonics Annual Meeting 2014, Ghent, Belgium (Highlight oral presentation)

Ranhua Xiong, Freya Joris, Ine De Cock, Jo Demeester, Stefaan C. De Smedt, Andre G. Skirtach, Kevin Braeckmans, 2015, *Efficient delivery of quantum dots in live cells by* *gold nanoparticle mediated photoporation*. SPIE. Photonics WEST BIOS 2015, San Francisco, USA (Oral presentation)

R. Xiong, J. Demeestera, S. C. De Smedta, K. Braeckmans, 2015, Efficient and Spatial-Selection Delivery of Quantum Dots in Live Cells by Gold Nanoparticle Medicated Photoporation, NANOTECH FRANCE 2015, Paris, France (Oral presentation)

Ranhua Xiong, Peter Verstraelen, Winnok De Vos, Stefaan C. De Smedt, Kevin Braeckmans, 2015, Spatial selection-delivery of nano-agents into cells by target-VNB-perforation, NB-Photonics Annual Meeting 2015, Ghent, Belgium (Highlight poster)

Ranhua Xiong, Kevin Braeckmans, Stefaan C. De Smedt, Cytosolic delivery of nanomaterials into live cells by vapour nanobubble photoporation, 2016, Controlled Release Society Annual meeting & exposition, Seattle, USA (Poster)

Ranhua Xiong, Roosmarijn Vandenbroucke, KatleenBroos, Jo Demeester, StefaanC. De Smedt, Kevin Braeckmans, 2015, FRAP for measuring molecular size distributions in biological fluids: from sizing proteins to analyzing intestinal and vascular barrier integrity, Focus on Microscopy 2015, Göttingen, Germany (Poster)

Ranhua Xiong, Stefaan C. De Smedt, Kevin Braeckmans, 2014, Gold nanoparticle mediated photoporation for delivering macromolecules in live cells, NanoBioTech Montreux 2014, Montreux, Switzerland (Poster)

Ranhua Xiong, Koen Raemdonck, Karen Peynshaert, Ine Lentacker, Ine De Cock, Jo Demeester, Stefaan C. De Smedt, Andre G. Skirtach, Kevin Braeckmans, 2014, EFFICIENT DELIVERY OF MACROMOLECULES INTO LIVING CELLS BY LASER EXCITED GOLD NANOPARTICLES, 13th European Symposium on Controlled Drug Delivery, Egmond aan Zee, The Netherlands (Poster)

Ranhua Xiong, Hendrik Deschout, Jo Demeester, Stefaan C. De Smedt, Kevin Braeckmans, 2013 RECTANGULAR FRAP WITH MAXIMUM ENTROPY METHOD FOR MEASURING CONTINUOUS DISTRIBUTIONS OF DIFFUSION COEFFICIENTS, Focus on Microscopy 2013, Maastricht, The Netherlands (Poster)

R. Xiong, H. Deschout, J. Demeester, S. De Smedt, K. Braeckmans, 2013, Rectangular FRAP with Maximum Entropy analysis for measuring continuous distributions of diffusion coefficients, 13th International Symposium on Colloidal and Molecular Electrooptics, Ghent, Belgium (Poster)

R. Xiong, K. Forier, S. J. Soenen, A. G. Skirtach , K. Braeckmans, 2012, Vapour nanobubbles as novel agents for triggered cytosolic nanoparticle delivery in target cells and for biofilm inactivation, NB-Photonics Annual Meeting 2012, Ghent, Belgium (Poster)

Awards & Grants

Nov 2014	Grant: FWO conference travel grant
Nov 2009	Scholarship: Guanghua Education Scholarship
Jan 2009	Grant: Funded by the graduate and innovative research project of USTC
Nov 2006	Scholarship: Outstanding Student Scholarship (Grade 2) of Anhui University of Science and Technology
Nov 2005	Scholarship: Outstanding Student Scholarship (Grade 2) of Anhui University of Science and Technology

Acknowledgements

I would like to use this opportunity to express my sincere gratitude to all people who have helped me on almost 5 years journey of my PhD research.

First of all, I have to thank my promotor **Prof. Dr. Kevin Braeckmans**. Without your hard working and great contributions to the work, my accomplishments would not be possible. Here, I want to show how is intensity of our communications. Only in last year of 2016, there are as many as 1781 emails which are relevant with us and 561 emails that you sent to me. It means that every day we have more than 5 emails in contact and you directly sent me more than 1.5 emails every day. I also have to thank for bringing me the chance to work on life science. Without your ideas on VNB and FRAP, the thesis doesn’t exist. I would cite an old Chinese Sayings to express my sincere gratitude to you “一日为师，终身为父” (Once a mentor, always a father).

Next, I would like to also thank my promotor **Prof. Dr. Stefaan De Smedt**. In 2010, when I met you for first time in your garden, you made me know what is big science and where I should go in future in my academic career. You are my first teacher to initiate me into a scientist who should do something more useful to our life. I would also appreciate your powerful of spirit and faith. It always encourages us to keep going ahead when we meet with difficulties. Thank you, Stefaan!

I think my another promoter **Prof. Dr. Andre Skirtach**. Thanks for the fruitful discussion with you when I started my doctoral research. And also thanks for invitation me to give presentation in your group.

Following, I would like to thank all of my colleagues from Lab. General Biochemistry & Physical Pharmacy of Ghent University. Thanks for **Prof. Dr. Jo Demeester** guidance on FRAP project and also your correction of the manuscript. Thank, **Prof. Dr. Koen Raemdonck** , for the great cooperation with you on VNB project. Appreciate the discussion with **Dr. Ine Lentacker** and **Prof. Dr. Katrien Remaut**. Thank, **Dr. Bart Lucas** and **Ms. Hilde Verhaeghe**. The projects won’t have progressed so smoothly without your efficiently ordering of optics and materials. Thanks for useful discussion with **Dr. Sangram Keshari Samal**. Thank, **Dr. Toon Brans**, for your great contribution to the FRAP project and also your excellent management of microscopes Thank, **Karen**. You are very helpful for my first time of cell culture. Thank, **Freya**, for the help on cell tracking project and also much appreciate you drove me to Leuven for the experiment. I also need to thank my previous and current officemates, **Hendrik**, **Ine**, **Oliwia**, **George**, **Rein**, **Peterjan**, **Juan** and **Thijs**. You always create cordial and friendly working atmosphere. I also appreciate very much your help or suggestions on my personal life like Peterjan help me do translation of document for my VISA application. I would also thank my other previous and current kind colleagues, **Laura**, **Koen**, **Katrien**, **Thomas**, **Lynn**, **Heleen**, **Stephan**, **Félix**, **Joke**, **Lotte**,

Elisa, **Eline**, **Rita**, **Silke**, **Heyang**, **Jing, Molood, Jelter, Aranit, Roberta,** and **Laurens**. Thanks a lot for all of you to organize the great lab activities like Christmas event and Lab weekend. Also thank you very much for your kind attention and care to my family. Thanks, **Ms. Ilse Dupon** and **Ms. Katharine Wullaert**, for your big help on document work and also the bookings of my conferences.

I am also deeply indebted to the other cooperators I have worked with during my Ph.D studies. Thank **Prof. Uwe Himmelreich** and **Dr. Sayuan Liang** from University of Leuven for supporting on in vivo imaging experiment. Thanks for **Dr. Saskia Lippens** and **Dr. Riet De Rycke** help and suggestion on TEM and SEM imaging. Thanks for **Prof. Corinne Abbadie** and **Dr. Claire Drullion** discussion and support on the experiment of ploy-nuclei cell labelling. Thanks for **Prof. Winnok H. De Vos** and **Dr.Peter Verstraelen** suggestions and supporting on the experiment on neuron labelling. Also thank **Prof. Roosmarijn Vandenbroucke**, **Dr.Katleen Broos**, **Dr. Elien Van Wonterghem** and **Prof. Claude Libert**, for the great cooperation on FRAP project.

I would also express my gratitude to my Chinese friends. Without you, I am sure that my life in Ghent would lost so much funny and happy. Also thanks a lot for your help on my public defense reception. Here, I would appreciate one of my special Chinese friends, **Prof. Dr. Chaobo Huang**. Without your help and introduction, I probably never know Stefaan and further know Kevin. Then, the thesis presented here could be neither not existence. You look like a “gold bridge" of mine. Thank you, Chaobo.

Most importantly, I want to thank my family. 首先感谢我的父母，谢谢你们的生育、养育之恩。正如古语所言：“谁言寸草心，报得三春晖”（Who says the tiny inch-tall blade of grass. Can e’er repay the warm sunshine of spring?)。感谢我已故的奶奶，您总是那么无私奉献于您的子孙！岁月流逝，也无法让我忘怀儿时牵着您的衣襟讨要零花钱。感谢我的弟弟、妹妹，谢谢你们照顾父母当我远在万里之外求学。感谢我的爱人**王芳**，谢谢你陪伴我风雨共济12年；谢谢你持家有道、相夫教子；谢谢你给我生育了一对女儿。还要感谢我亲爱的女儿**熊莉辰**，你带给爸爸快乐总是无与伦比的、发至内心的。每次我听到你用那儿语般的童音叫“爸爸”，我心中快乐与幸福总是油然而起。谢谢你给我带来的幸福和快乐！

Finally, I would thank the jury members for examination of the thesis and also your suggestion on improvement of the thesis. I gratefully acknowledge the financial support from China Scholarship Council (CSC) and Financial support by the Ghent University Special Research Fund (Centre for Nano- and Biophotonics).

Ranhua, February, 2017, Ghent

结束语 / END：

“故天将降大任于是人也，必先苦其心志，劳其筋骨，饿其体肤，空伐其身行，行弗乱其所为，所以动心忍性，曾益其所不能。”

“When Heaven is about to place a great responsibility on a great man, it always first frustrates his spirit and will, exhausts his muscles and bones, exposes him to starvation and poverty, harasses him by troubles and setbacks so as to stimulate his spirit, toughen his nature and enhance his abilities.”

《孟子・告子下》

Mencius